Dipl.-Ing. Boris R. Scherwitzl

Studies on the Deposition, Adsorption, Film Growth and Desorption Behavior of Large Organic Molecules on SiO_2

DOCTORAL THESIS

to achieve the university degree of

Doktor der technischen Wissenschaften

Doctoral Programme of Technical Sciences
Technical Physics

Graz University of Technology

Supervisor:

Univ.-Prof. Dipl.-Ing. Dr.techn. Adolf Winkler

Institute of Solid State Physics

Graz, August 2015

Deutsche Fassung:
Beschluss der Curricula-Kommission für Bachelor-, Master- und Diplomstudien vom 10.11.2008
Genehmigung des Senates am 1.12.2008

EIDESSTATTLICHE ERKLÄRUNG

Ich erkläre an Eides statt, dass ich die vorliegende Arbeit selbstständig verfasst, andere als die angegebenen Quellen/Hilfsmittel nicht benutzt, und die den benutzten Quellen wörtlich und inhaltlich entnommene Stellen als solche kenntlich gemacht habe.

Graz, am ……. ……..
(Unterschrift)

Englische Fassung:

STATUTORY DECLARATION

I declare that I have authored this thesis independently, that I have not used other than the declared sources / resources, and that I have explicitly marked all material which has been quoted either literally or by content from the used sources.

……. ……..
date (signature)

Abstract

The present work investigates fundamentals of initial film formation, adsorption and desorption behavior of large organic molecules. In addition to disc-shaped rubicene, the H-bonded and rod-like organic semiconductors indigo, quinacridone and epindolidione were studied on carbon covered and sputter cleaned silicon dioxide substrates. Thin films in a thickness range from 0.1 – 100 nm were prepared via physical vapor deposition from Knudsen and Knudsen-like evaporation cells under well-defined ultra-high vacuum conditions and subsequently analyzed with thermal desorption spectroscopy (TDS), Auger electron spectroscopy (AES), atomic force microscopy (AFM), X-ray diffraction (XRD), grazing incidence X-ray diffraction (GIXS) and Raman spectroscopy. It is demonstrated that rubicene forms two full wetting layers on differently prepared SiO_2 substrates which fully re-orientate into 3D-islands at higher coverages. The initial sticking coefficient was determined to be 0.2, which is remarkably low for organic molecules of this size. Indigo molecules on the other hand, displayed a strong wetting layer formation on sputtered silicon dioxide and a subsequent molecular re-orientation into highly mobile dimers. Once a certain coverage was reached, the molecules started to dewet and form more strongly bonded island structures. A similar metastable initial state and island formation was also observed on carbon covered substrates, although no dimer formation was apparent in this case. Detailed investigations on quinacridone film formation revealed idiosyncrasies in the deposition process upon usage of evaporation cells of the Knudsen-type. Partial dissociation was observed in the cell and by using thermal desorption spectroscopy it could unambiguously be demonstrated that at least two different molecular species were present in the grown films. In addition to quinacridone, indigo and carbazole were unveiled as main decomposition products. Epindolidione thin films exhibited a single thermal desorption peak attributable to fully upright

standing molecules, as verified by XRD. The gathered results and drawn conclusions in this thesis are of significant relevance for the application of organic molecules in novel organic electronic devices.

Kurzfassung

Die vorliegende Arbeit beschäftigt sich mit grundlegenden Aspekten des Dünnschichtwachstums und des Adsorptions- sowie Desorptionsverhaltens von organischen Molekülen. Neben dem plättchenförmigen Rubicen wurden die über Wasserstoffbrücken gebundenen, stäbchenförmigen organischen Halbleiter Indigo, Chinacridon und Epindolidione untersucht. Als Substratmaterialien kamen sowohl mit Kohlenstoff bedeckte als auch mittels Sputter-Reinigung präparierte Siliziumdioxidproben zur Anwendung. Dünne Schichten mit Dicken zwischen 0,1 nm und 100 nm wurden mit Hilfe eines physikalischen Aufdampfverfahrens im Ultrahochvakuum hergestellt und anschließend mittels thermischer Desorptionsspektroskopie (TDS), Auger Elektronenspektroskopie (AES), Rasterkraftmikroskopie (AFM), Röntgenbeugung (XRD bzw. GIXD) und Raman Spektroskopie vermessen. Es konnte gezeigt werden, dass Rubicen auf unterschiedlich präparierten Substraten zwei vollständig ausgebildete Benetzungsschichten bildet, welche sich bei höheren Bedeckungen in Inselstrukturen umorientieren. Der Anfangshaftkoeffizient wurde auf einen Wert von 0,2 bestimmt, was für organische Moleküle dieser Größe ungewöhnlich klein ist. Des Weiteren wurde untersucht, wie Indigo Moleküle zuerst bei sehr niedrigen Bedeckungen eine stark gebundene Benetzungsschicht bilden und anschließend bei geringfügig höherer Bedeckung fast frei bewegliche Dimere formen. Nach weiterer Bedeckungserhöhung bildeten sich darauffolgend dreidimensionale Inselstrukturen. Ähnliche Beobachtungen konnten auch für Indigo Filme auf mit Kohlenstoff bedeckten Substraten gemacht werden, eine Dimer-Bildung konnte in diesem Fall jedoch nicht nachgewiesen werden. Detaillierte Untersuchungen des Wachstums von dünnen Chinacridon Schichten führten zur Erkenntnis, dass Chinacridon Moleküle teilweise thermisch dissoziieren, sofern die Aufdampfung aus einer Knudsenzelle erfolgt. Mittels thermischer Desorptionsspektroskopie konnten eindeutig mehrere unterschiedliche Moleküle auf

der Probenoberfläche nachgewiesen werden. Neben Chinacridon wurden sowohl Indigo- als auch Carbazolstrukturen in den dünnen Schichten gefunden. Epindolidione Dünnschichtproben zeigten einen einzigen Desorptionspeak, welcher, wie durch XRD nachgewiesen wurde, einer Anordnung von aufrecht stehenden Molekülen entspricht. Die im Zuge dieser Dissertation gesammelten Ergebnisse und die daraus gezogenen Schlussfolgerungen sind von großer Relevanz für die direkte Anwendung organischer Moleküle in aktuellen und zukünftigen organischen Halbleiterbauelementen.

Acknowledgements

This Ph.D. thesis was performed under the supervision of Prof. A. Winkler at the Institute of Solid State Physics. Without his help, constant support and patience this work would not have been possible. For this I am deeply thankful.

Furthermore, I would like to thank my work group consisting of R. Lassnig, L. Tümbek and M. Hollerer. They always had an open ear to discuss experimental results and their valuable support and expertise helped me out whenever things did not work as planned.

I want to thank all members of the Institute of Solid State Physics, most notably Prof. G. Leising, Prof. R. Schennach, Prof. R. Resel and the whole X-ray diffraction group for their assistance with multiple experiments and many stimulating discussions. My special thanks go to B. Kunert, H. Kerschbaumer, M. Kornschober as well as our secretary E. Stern for their helpful support.

I also gratefully thank the Helmholtz Zentrum Berlin for the allocation of synchrotron radiation beam time and acknowledge experimental support by I. Salzmann and D. Többens.

Moreover, I thankfully acknowledge the experienced support of K. Krenn from Karl Franzens University Graz for the Micro-Raman experiments.

I would like to thank E. Głowacki and the whole Institute for Organic Solar Cells at Johannes Kepler University Linz for many interesting conversations. Their pioneering work on H-bonded semiconductors was truly inspiring.

Special thanks go to Prof. N. Sariciftci from Johannes Kepler University Linz for acting as second referee and examiner.

Finally, I want to thank my family and the most important person in my life, Hollie. Without their constant support throughout my years of studying I would have never made it this far.

Contents

List of Symbols and Abbreviations

OTFT	Organic Thin Film Transistor
OFET	Organic Field Effect Transistor
UHV	Ultra-High Vacuum
QMS	Quadrupole Mass Spectrometer
TDS	Thermal Desorption Spectroscopy
AES	Auger Electron Spectroscopy
AFM	Atomic Force Microscopy
XRD	X-Ray Diffraction
GIXD	Grazing Incidence X-Ray Diffraction
E_a	Adsorption Energy
Θ	Surface Coverage, X-ray Incidence Angle
ML	Monolayer
amu	Atomic Mass Units (1 amu = 1.66×10^{-27} kg)
s	Sticking Coefficient
r_a	Adsorption Rate
I_z	Total Flux of Molecules onto a Surface
D	Diffusion Coefficient
E_{diff}	Diffusion Energy
k_B	Boltzmann Constant (1.38×10^{-23} J/K)

T_m	Temperature at the Maximum of the Desorption Peak
T_{ad}	Substrate Temperature during Adsorption
a	Lattice Constant
ΔE_{ES}	Ehrlich-Schwoebel Barrier
i	Critical Island Size
n	Desorption Order
DLA	Diffusion-Limited Aggregation
ALA	Attachment-Limited Aggregation
R	Desorption Rate
E_{des}	Desorption Energy
ν	Pre-Exponential or Frequency Factor
N_{ML}	Monolayer Coverage
TST	Transition State Theory
β_H	Heating Rate
d	Distance between Lattice Plains, Thickness
Δf	Frequency Change of a Quartz Microbalance

List of Figures

List of Tables

1 | Introduction

The idea to use organic materials as semiconductors in electronic devices dates back as far as the late 1940s.[1] However, such devices failed to have a significant practical impact until many years later, despite a considerable amount of experimental and theoretical studies. The tremendous increase of industrial and scientific interest did not start until the early 1990s when it was discovered that organic and polymeric materials can be used as potential electroactive elements in thin-film transistors (OTFT or OFET).[2, 3] The scientific pursuit is driven by the increasing interest in flat-panel-display applications, for which organic and polymeric materials offer strong promise.[4] Organic transistors are by no means expected to replace high-performance silicon devices in terms of output characteristics and charge density but instead are aimed at applications where easier fabrication steps, large area coverage, mechanical flexibility and low process temperatures are of particular importance.[5] The latter characteristic in particular enables a large number of applications that are not achievable using the entrenched technology, most notably the ability to process devices at room temperature which are therefore compatible with transparent plastic substrates.[6] Organic devices do not only offer the possibility to use ultra-thin and lightweight substrates with extreme bending stability [7–9] but also combine low-cost [10] with a high biocompatibility. Organic thin-film transistors are of course just one class of organic devices, of which electroluminescent diodes, either consisting of conjugated polymers or of small organic molecules, light-emitting diodes, photodetectors, lasers, sensors and solar cells are other representative examples.[11–17]

Initially, most organic semiconducting materials were based on linear thiophenes and thiophene oligomers with mobility values of 10^{-1}–10^{-2} cm^2/Vs and source-drain current on/off ratios of up to 10^6.[4, 18] Only few materials were able to meet the high industrial

demands [19, 20] until the rod-like pentacene and other fused aromatic molecules emerged as workhorse materials for organic electronics. Especially pentacene showed unique properties sufficient for proper transistor operation and has been the focus of a large number of scientific publications ever since.[21–26] This sudden focus in research provoked significant device improvements over the recent years [27] and subsequently led to a number of solution processable and/or vapor depositable organic semiconductors with charge carrier mobilities and on/off ratios exceeding those of amorphous silicon.[22, 28–31]

While the potential of these molecules is exciting, the processing of these materials into high performance and reliable transistor arrays remains challenging. It was shown that besides the nucleation rate, the growth mode of organic semiconductors is of vital importance for high performance OTFTs.[32] Thin organic films can be deposited by sublimation in a variety of vacuum deposition systems, utilizing techniques in which the deposition parameters vary widely. For once, the base pressure of the deposition system is a crucial parameter since it determines the mean free path of the sublimed organic semiconductor molecules and the presence of residual gas atoms and molecules in the vicinity of the substrate surface during film formation, essentially making ultra-high vacuum deposition indispensable for controlled thin film growth. Other important parameters that can significantly influence thin film morphology and charge transport characteristics are substrate temperature, deposition rate, purity of the organic source material and substrate cleanliness.[21, 33–37] The latter is especially important since it is well established that carrier accumulation mainly occurs in the first few monolayers of the organic semiconductor at the interface with the insulator. Impurities in that region can affect mobility, on/off ratio and in some cases even the polarity of the OTFT.[19, 20] Thus, the growth and crystalline order of these interfacial semiconducting layers dictate device performance and need to be studied and controlled accordingly. Moreover, the electronic structure of the bulk of conjugated systems (single crystals, thin films) can be strongly tuned by the crystallographic packing of single molecules with respect to each other.[38]

What kind of growth mode occurs for a certain adsorbate / substrate system is determined by an interplay of interlayer interaction energies and adsorbate-substrate interaction energies. Typically higher mobility semiconducting films exhibit layer-by-layer growth as compared to the less favorable 3D island growth.[24, 39] Is it important to note that the interaction between each type of semiconductor and substrate surface is unique and can typically not be predicted. It was shown that simplified models which are purely based on surface energy arguments are not able to properly describe film formation parameters.[25] Precise control of the deposition setup can strongly affect device characteristics, as it was studied experimentally for a number of systems.[23, 40, 41] For example, by controlling the thin film growth of the organic semiconductor and minimizing the detrimental grain boundaries high charge carrier mobilities have been achieved.[42]

Now that the significance of deposition specifications and film growth characteristics has been extensively demonstrated, it should come as no surprise to the reader why this dissertation focuses on those parameters so extensively. In addition to the disc-shaped rubicene molecule, the focus of my work was clearly on the film formation, adsorption and desorption behavior of H-bonded organic pigments on silicon dioxide. Many H-bonded molecules have, especially in comparison with a lot of other organic semiconductors, only sparsely been investigated despite showing great promise for cheap and high-mobility OTFTs.

1.1. H-bonded Organic Semiconductors

In the constant search for new high-performance organic semiconductors for the application in organic electronics, optimum materials should combine high charge carrier mobilities, low cost and stable long term operation under ambient conditions as well as a low ecological impact. Especially if one wants to achieve good charge transport and close intermolecular stacking, a high degree of intramolecular π-π conjugations is considered to be necessary.[43] H-bonded organic semiconductors such as indigo, tyrian purple, quinacridone, epindolidione etc. exhibit, although limited by a weak intramolecular conjugation, a multitude of desired properties, most notably low production costs, high carrier mobilities and strong intermolecular interactions. Maximizing intermolecular bonding in the form of strong hydrogen-bonds may therefore turn out to be sufficient to create powerful electronics without the necessity to maximize intramolecular π-conjugations.

One thing that distinguishes indigoids, quinacridones and other natural dyes from more well-known organic semiconductors is the formation of intermolecular hydrogen bonds during stacking.[44] Each molecule is hydrogen bonded to some of its neighbors, while adjacent molecules are also π-stacked to each other, leading to π-π interactions that are reinforced by hydrogen bonds.[45] However, organic pigments are, contrary to organic dyes, generally insoluble. Current literature research unveils a formidable amount of publications elucidating how adding various kinds of solubilizing groups to, for example, the quinacridone molecule gives rise to a number of new applications, most notably as photodetectors [46] and both donor and acceptor molecules in organic solar cells.[47–49] The general insolubility of H-bonded pigments, in turn, makes physical vapor deposition the method of choice for manufacturing thin layers, which was the employed deposition method in this work.

Despite recent reports of air-stable organic field-effect transistors of quinacridones, indigoids and other amine/carbonyl dye molecules with relatively high carrier mobilities of 0.2 cm^2/Vs [50], good operational stabilities [43, 51–53] and other functionalities inaccessible to conventional organic semiconductors, there is still a lack of knowledge concerning the kinetics of vacuum deposition and film formation on industrially relevant silicon dioxide

substrates. Comparable investigations on the kinetics of adsorption, layer growth and desorption exist, as shown above, for a number of organic molecules, while the focus has only recently shifted to H-bonded semiconductors.[54–57]

In this dissertation three hydrogen bonded molecules (indigo, quinacridone and epindolidione) have been studied, which all exhibit intermolecular hydrogen bonds between the N−H and H···O entities (i.e. the amine and carbonyl groups), while indigo and epindolidione may additionally exhibit weak intramolecular H-bonds. This is not possible for quinacridone due to the distribution of C=C double bonds in the benzene rings. The combination of these bonds forms highly-ordered molecular solids with formidable lattice energies. Highly-ordered structures promote good field-effect mobilities, which were reported to vary between 0.2 and 1.5 cm^2/Vs for quinacridone and epindolidione.[43] However, the formation of highly-ordered layers and bulk structures may, especially for thin films, indubitably depend on the underlying substrate and its preparation conditions and makes it necessary to study this trait in detail.

Table 1.1 summarizes properties such as density, lattice vectors and lattice angles for the four organic semiconductors that were used throughout this thesis.

Table 1.1.: Fundemental properties of the used organic semiconductors

	Rubicene	Indigo	Ref.
Stoichiometric formula	$C_{26}H_{14}$	$C_{16}H_{10}N_2O_2$	
Color	bright red	dark blue	
Molecular mass (amu)	326.3894	262.2628	[58]
Density (g/cm^3)	1.381	1.50	[59]
Band gap (eV)		1.7	[60]
Crystallographic phases	A	A, B	
Lattice	monoclinic	monoclinic	
Space group	$P2_1/n$	$P2_1/c$	
Lattice vectors a, b, c (nm)	16.16, 5.12, 19.11	9.24, 5.77, 12.22 (A)	[61]
		10.84, 5.89, 12.28 (B)	[62]
Lattice angles α, β, γ (°)	90, 97.22, 90	90, 117, 90 (A)	[61]
		90, 130.02, 90 (B)	[62]

	Quinacridone	Epindolidione	Ref.
Stoichiometric formula	$C_{20}H_{12}N_2O_2$	$C_{16}H_{10}N_2O_2$	
Color	red or pink	yellow or orange	
Molecular mass (amu)	312.3215	262.2628	[58, 63]
Density (g/cm^3)	1.47		
Sublimation temperature[1] (°C)	535°	404°	[43]
Band gap (eV)	2.5	2.7	[43, 64]
Crystallographic phases	α, α', β, γ	A, B	[34]
Lattice	monoclinic	/	
Space group	$P2_1/c$	/	
Lattice vectors a, b, c (nm)	3.80, 6.61, 14.49 (α)		[34]
	5.69, 3.98, 30.02 (β)		[34]
	13.70, 3.84, 13.35 (γ)		[65]
Lattice angles α, β, γ (°)	100.68, 94.40, 102.11 (α)		[34]
	90, 96.77, 90 (β)		[34]
	90, 100.09, 90 (γ)		[65]

[1] from thermogravimetric analysis

1.2. The SiO_2 Surface

In a time where conventional silicon and germanium electronics is still at its prime, silicon dioxide has ever since been the most prominent and well-studied insulating oxide available. The list of its desirable properties and advantages is long and does not only include a suitable band gap, well understood defect phenomena and easy process steps, but also helps silicon retain its supremacy in microelectronic devices. Especially with the development towards thinner oxides that are grown at lower temperatures, questions such as oxide structure and stoichiometry, transport processes, defect behavior and its consequences, etc. need to be well understood and controlled. Further studies imply that there is most likely a difference between the oxide stoichiometry close to the silicon and the one at the outer surface. This difference is caused by the necessity of arriving oxygen molecules to diffuse through the SiO_2 layer to get to the silicon in order to react as its thickness starts to build up. Strong influences can be found upon varying stress levels as well as roughness and defect accumulation.[66] However, for device fabrication it is more the oxide quality than the oxide structure which matters.

As surface scientist the main focus of this work lies on the surface, its reactivity and roughness and how it changes the growth behavior of thin organic films and subsequently the device characteristics of OTFTs. Chemical impurities can play an important role in this case, even if only 0.1% of the available surface sites are different than the rest. Therefore, carbon impurities as well as the cleaning procedure may influence the surface characteristics and its roughness substantially.[67] Figure 1.1 depicts this very well as it compares the surface roughness of a 10 min Ar^+ sputter cleaned sample (roughness <1 nm) with a sample that has some carbon residue, which remained after multiple incomplete desorption processes of organic layers, on top. These two sample preparations were used throughout the course of this thesis and significant differences were found regarding the initial film growth of organic molecules on either of the two preparations.

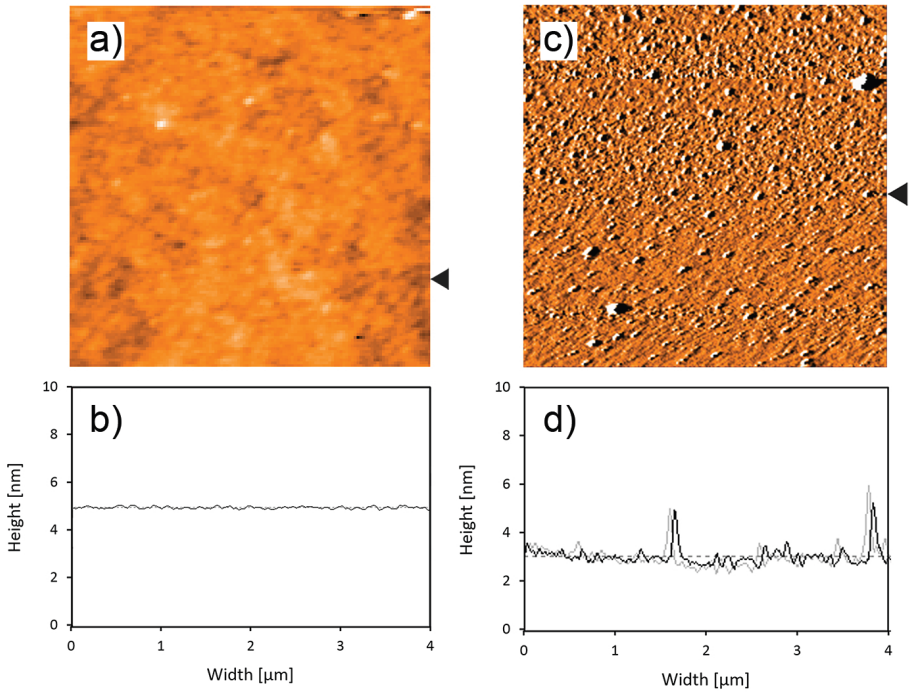

Figure 1.1.: Roughness of an Ar^+ sputtered SiO_2 substrate (left) versus a substrate with carbon residue on top (right)

1.3. Organization of this Thesis

In this dissertation the film growth behavior and adsorption/desorption phenomena of four organic molecules on silicon dioxide will be thoroughly illustrated and described. In addition to the plate-like rubicene molecule, three different H-bonded organic semiconductors will be addressed: indigo, quinacridone and epindolidione. Measurements on each of the four molecules include thermal desorption spectroscopy, specular and grazing-incidence X-ray diffraction, atomic force microscopy and Raman spectroscopy. The organization of this thesis is as follows. Chapter 2 outlines the basic physical principles necessary to understand the experimental results, namely adsorption, diffusion, island nucleation and desorption. Chapter 3 then introduces the employed analytical methods in detail. Chapter 4 provides a brief description of the measurement setup as a whole. Characteristics and capabilities as well as experimental limitations are explained together with the sample setup and sample preparations. Chapter 5 describes the residual gas composition in the vacuum chamber, illustrates reproducibility and sensitivity of the in-situ measurement system and also explains the preparation of carbon covered substrate samples.

The following chapters then explain experimental results on film growth, adsorption and

desorption behavior of the different molecules, respectively. Chapter 6 for rubicene, chapter 7 for indigo, chapter 8 for quinacridone and chapter 9 for epindolidione. All experiments were performed on differently treated SiO_2 substrates. Finally, chapter 10 provides a short summary and conclusion.

1.4. List of enclosed Publications

Paper I (Ref. [57])

Initial Steps of Rubicene Film Growth on Silicon Dioxide
B. Scherwitzl, W. Lukesch, A. Hirzer, J. Albering, G. Leising, R. Resel and A. Winkler
Journal of Physical Chemistry C **117 (8)**, pp. 4115-4123 (2013).

Author Contribution: In this paper results on the rubicene thin film growth on SiO_2 are extensively described. Film growth and subsequent TDS, AES and AFM measurements as well as additional investigations on sticking coefficients, desorption energies, etc. were performed by B. Scherwitzl. W. Lukesch performed initial TDS experiments which are not included in the final version of the publication. Prof. G. Leising, A. Hirzer and J. Albernig performed IR spectroscopy measurements shown in the supporting information. Prof. R. Resel and his work group performed XRD experiments and helped with their interpretation. The publication was written by B. Scherwitzl in accordance with input and corrections from Prof. A. Winkler, who supervised this project.

Large parts of this publication were used in chapter 6.

Paper II (Ref. [68])

Film growth, Adsorption and Desorption Kinetics of Indigo on SiO_2
B. Scherwitzl, R. Resel and A. Winkler
Journal of Chemical Physics **140 (18)**, 184705 (2014).

Author Contribution: This second publication was submitted to the Journal of Chemical Physics after experiments on the film formation and desorption behavior of indigo on SiO_2 led to a number of interesting and previously unpublished results. Film growth and subsequent TDS, AES and AFM measurements as well as additional investigations on sticking coefficients, desorption energies, etc. were performed by B. Scherwitzl. Prof. R. Resel and his work group performed XRD experiments and helped with their interpretation. The publication was written by B. Scherwitzl in accordance with input and corrections from Prof. A. Winkler, who supervised this project.

Large parts of this publication were used in chapter 7.

Paper III (Ref. [69])

Idiosyncrasies of Physical Vapor Deposition Processes from Various Knudsen Cells for Quinacridone Thin Film Growth on Silicon Dioxide

B. Scherwitzl, C. Röthel, A. O. F. Jones, B. Kunert, I. Salzmann, R. Resel, G. Leising and A. Winkler

accepted in Journal of Physical Chemistry C (August 2015)

Author Contribution: Quinacridone deposition, film growth and desorption experiments led to a number of results which hinted at the occurrence of thermal decomposition processes both in the evaporation source and on the surface. This initial suspicion was verified with further experimental investigation employing additional spectroscopic methods. Following the initial referee report and a number of discussions it was decided that the results should be divided into two separate publications, one describing the molecular dissociation in the evaporation source and its ramifications, while the other focuses on the film growth and desorption characteristics of quinacridone and its cracking products (see below). Film preparation employing various evaporation sources, TDS, AES and AFM measurements as well as additional investigations on sticking coefficients, desorption energies, etc. were performed by B. Scherwitzl. Prof. R. Resel, C. Röthel, A. Jones, I. Salzmann and B. Kunert performed multiple XRD and GIXD experiments both at Graz University of Technology and BESSY II. They additionally provided assistance in understanding and interpreting the obtained data. Prof. G. Leising supervised Micro-Raman experiments performed at Karl-Franzens University Graz. The publication was written by B. Scherwitzl in accordance with input and corrections from Prof. A. Winkler, who supervised this project.

Large parts of this publication were used in chapter 8.

Paper IV

Adsorption, Desorption and Film Formation of Quinacridone and its Cracking Products on Silicon Dioxide

B. Scherwitzl and A. Winkler (in preparation)

Author Contribution: As described above, a fourth publication is currently in preparation, focusing on the desorption behavior and desorption analysis of thin quinacridone films grown on differently prepared SiO_2 samples. It will feature TDS data as well as sticking coefficient and desorption energy analysis done by B. Scherwitzl.

Parts from chapter 8 will be used in this publication.

Part I.

Prerequisites

2 | Theoretical Background

2.1. Adsorption Kinetics

Adsorption is the binding process of atoms or molecules[1] from the gas phase or from solution onto a solid surface due to interatomic attractive forces (compare Lennard-Jones potential in Fig. 2.1). An atom/molecule can adsorb on the surface, becoming an adatom or admolecule, if the adsorption process is energetically favorable. The first monolayer (the so called wetting layer) is thereby in direct contact with the substrate and forms a physical or chemical bond to the surface. Typical monolayer densities vary between 10^{14} and 10^{15} molecules/cm^2, meaning that very few molecules are needed to form a monolayer.[70] Subsequent layers will interact strongly with each other and only experience weak interactions with the substrate. Generally, two types of adsorption can be distinguished:

- **Chemisorption**, if the molecules electronic structure is *significantly* perturbed upon adsorption (i.e. through chemical bonds). This phenomenon is characterized by chemical specificity and often involves an activation energy. Binding energies are in the range of several eV, even for small atoms.
- **Physisorption**, if the adsorption happens without the molecules undergoing *significant* changes of their electronic structure (e.g. van der Waals forces). Binding energies vary between a few meV for light gases up to several eV for large organic molecules.

However, a clear distinction between chemisorption and physisorption is not possible in every case. Molecules can distort upon adsorption on solid surfaces while their chemical bonds

[1] For simplicity reasons some explanations in the following chapters will only be made for atoms. Of course, any described processes are equally applicable to the adsorption and diffusion of molecules.

may (dissociative adsorption) or may not (nondissociative or molecular adsorption) break. Additionally, a mixture between physisorption and chemisorption may exist if a molecule first physisorbs and then converts to a chemisorbed state.

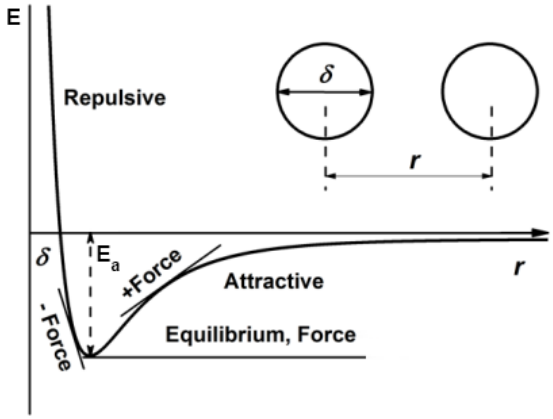

Figure 2.1.: Lennard Jones potential between two atoms. Attractive forces lead to an energy minimum at a certain distance which is followed by strong repulsive forces upon further approach. (adapted from Ref. [71])

One should always keep in mind that significant differences exist between the initial or wetting layer and any subsequent adsorbate layers. Many theories (e.g. the Langmuir model of adsorption isotherms [72]) only describe chemisorption under specific conditions, most notably on a homogenous surface with a finite amount of energetically identical adsorption sites and for monomolecular layers, i.e. each adsorption site can only be occupied once. Each adatom is then considered to adsorb with an adsorption energy E_a at a well-defined adsorption site on the surface. Therefore, any chemisorption models are only applicable to monolayer formation and are valid up to a maximum coverage of

$$\Theta_{\max} = 1 \text{ monolayer (ML)} \qquad \text{(Chemisorption)} \tag{2.1}$$

The situation is very different for higher coverages, i.e. if the second, third and any following layers (physisorption) are added into consideration. Van der Waals and other interactions (such as hydrogen bonds) between adjacent particles become the main driving force and different adsorption behaviors might emerge when compared to the monolayer. These differences are of course the focus of research in the field of surface science.

From continuous studies in the field of surface science it is known that, depending on certain parameters such as surface roughness, temperature, molecule size, deposition rate, binding energies etc. the adsorbate is able to diffuse more or less unhindered across the surface, especially in the monolayer and sub-monolayer regime. The preparation of highly ordered adsorbate wetting layers requires ultra-clean surfaces with large, atomically smooth

terraces and suitable flat molecules [73], while the arrangement of the second and any other following layers depends, as mentioned, on different parameters such as intermolecular interactions (see below). If the substrate is very reactive the molecules may (partially) dissociate or may simultaneously be bound in various orientations at sites where they impinge on the surface. If the substrate is inert the molecules form monolayers with structures that are determined by intermolecular forces and the substrate acting as a two-dimensional basis. Hence, long-range order is often observed but hardly influenced by the symmetry of the substrate. If several layers are deposited, they will usually show polycrystalline growth. The homogeneity of the layers and the size and orientations of the microcrystallites are essentially determined by the properties of the organic crystals. However, true expitaxial growth is very rarely observed, since the requirements of commensurability between the organic layer and the substrate surface as well as a highly ordered interface with similar or equal geometric structure compared to the deposited film and a layer-by-layer growth mechanism are generally not met. Thus the very different lattice properties of organic crystals when compared to metallic or semiconductor crystals usually inhibit expitaxial growth.

Very interesting observations can be made for weakly chemisorbed particles. In this case the particles remain intact and may diffuse over large distances along the surface to form huge, ordered islands. The adsorbate superstructures will be determined by the substrate surface. Only in a very few cases have homogeneous films with large domains and true organic epitaxy been found.[74, 75] Optimal structures are typically achieved at very low adsorption rates (i.e. less than one monolayer per minute).[73]

Another important aspect when talking about adsorption is the sticking coefficient or sticking probability s, defined as the probability that a molecule is adsorbed on an available surface site

$$s = \frac{\text{Number of molecules that adsorb}}{\text{Number of molecules that impinge on the surface}} \tag{2.2}$$

The rate of adsorption r_a is related to the sticking probability by

$$r_a = s\ I_z \tag{2.3}$$

where I_z is the total flux of molecules onto the surface in molecules/(cm^2 sec). The sticking coefficient is strongly dependent on the geometrical structure of the surface, the coverage of already adsorbed atoms and the temperature. Additionally, the relation can be misleading in certain cases. Impinging molecules that do not instantly adsorb may enter a so called precursor state where they diffuse along the surface in a weakly bonded state until either a vacant site is located for adsorption to occur or until the molecule reevaporates into the gaseous phase. The latter is different from an elastic collision of non-adsorbing molecules due to the fact that molecules lose all information on kinetic energy, scattering angle etc.

upon entering the precursor state and will desorb into the gas phase randomly rather than being scattered elastically. Real time X-ray observation revealed lifetimes of precursor states in the picosecond range.[76]

2.2. Surface Diffusion

As it was mentioned earlier, adsorbed molecules can diffuse along potential wells on the surface with a diffusion coefficient (or diffusivity) D and diffusion energy E_{diff}. Both values depend on multiple parameters of the adsorbate/substrate system. The activation energy of diffusion E_{diff} is the difference in potential energy of the atom in the equilibrium adsorption site and the transition saddle point between two adsorption sites. It is generally smaller than E_a, in some cases even significantly smaller. Adatom diffusion is derived from considering a random walk in two dimensions and the 2D diffusion coefficient is given by [77]

$$D = \frac{\nu_d \ a^2}{4} \ \exp(-\frac{E_{diff}}{k_B \ T}) \tag{2.4}$$

with a as the lattice constant and the pre-exponential factor for diffusion ν_d. Similarly, the adatom lifetime before diffusion can be written as

$$\tau_d = \frac{1}{\nu_d} \ \exp(\frac{E_{diff}}{k_B \ T}) \tag{2.5}$$

Indeed, one of the difficulties of studying surface diffusion is that there are so many mechanisms which may need to be considered.[78–81] The probability of a single hopping (or in some cases tunneling) process is dependent on the relation between the thermal energy (k_BT) of the atom versus the potential barrier height E_{diff} and the attempt frequency ν_d to overcome that barrier (oscillation frequency of the particle in the potential well). If $E_{diff} \ll k_BT$, a situation that is typically given for very smooth substrates with shallow potential wells and/or high temperatures, then the atoms are free to move in two dimensions and the ideal 2D gas law can be applied. On the other hand, some translation degrees of freedom may not exist anymore for $E_{diff} > k_BT$. Diffusion in this case becomes erratic and is referred to as *hopping diffusion*.[82]

Of course the whole situation becomes significantly more complicated if interactions between multiple adsorbed atoms are to be considered. A two-atom Lennard-Jones-potential is added to the periodic lattice potential and each adsorbed atom modifies the effective potential of a neighboring atom and vice versa. The surface becomes energetically inhomogeneous.

Ehrlich *et al.* [83] and Schwoebel *et al.* [84] described, independent of each other, an active

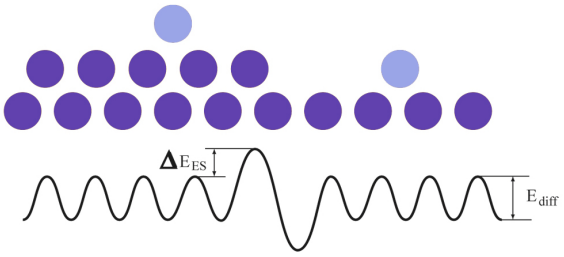

Figure 2.2.: Ehrlich-Schwoebel barrier (from Ref. [77])

barrier for interlayer diffusion across step edges. Atoms and molecules get reflected from step edges rather than crossing them. This increased barrier for adatom hopping across a step edge compared to adatom diffusion on a terrace is called Ehrlich-Schwoebel-barrier (ΔE_{ES}) and outlined in Fig. 2.2. It can be explained as follows: An adatom has less nearest neighbors on a step edge and therefore an energetically disfavored location when hopping across. Reflected adatoms diffuse along the original terrace until they will meet other adatoms to form an island. Systems with a large Ehrlich-Schwoebel barrier commonly exhibit terraced growth mounds with deep trenches inbetween.[85]

2.3. Island Nucleation and Film Growth Modes

If a particle reaches its destined spot, either by not having any more surface sites available it can jump to or by meeting other molecules and forming islands (Fig. 2.3), it suddenly becomes way less mobile and film growth can occur. Two growth regimes can be distinguished: First, an increase in island density is observed, which can be described by classical nucleation theory in the so called nucleation regime. This initial nucleation process has a big influence on the morphology and properties of the thin film, even if multiple layers are grown on top of it.[85] Islands can nucleate either in a 2D or a 3D configuration and the total number of generated islands defines the coarseness of the resulting film. The nucleation regime is followed by the aggregation regime at coverages of more than 0.2 monolayers. Here the number of islands stays nearly constant, only their size increases with coverage.

Once the adsorbate coverage exceeds one full monolayer the classification changes from wetting layer to thin film and the growth behavior of the latter can be divided into three different modes (compare Fig. 2.4):

- **Frank van der Merwe (FM)** or layer-by-layer growth
- **Volmer-Weber (VW)** or island growth
- **Stranski-Krastanov (SK)** or layer plus island growth

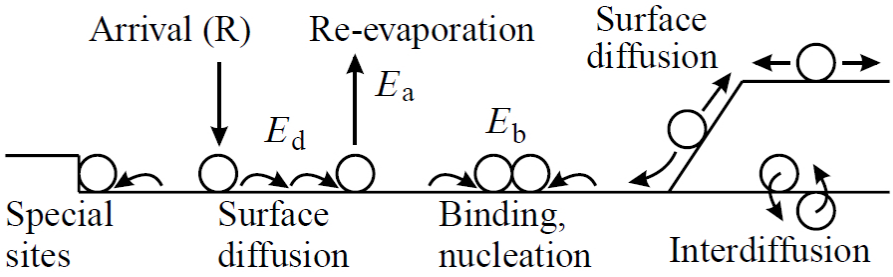

Figure 2.3.: Different processes on surfaces (from Ref. [86])

Which growth mode is present on the adsorbate / substrate system at hand is controlled by an interplay of thermodynamic (energetic) and kinetic processes and the relative bond-strength between adsorbate particles and adsorbate-substrate bonds.[77, 87] From an energetic point of view the requirement of minimizing the total free energy holds up at all times and different growth modes can be explained, under the assumption of a thermodynamic equilibrium, by an interplay between the substrate surface energy γ_a, the adsorbate surface energy γ_b and the interface energy γ.[88] If, for example, the surface tension of the substrate is equal or larger than the surface tension of the thin film and of the film-substrate interface combined ($\gamma_a \geq \gamma_b + \gamma$), typically the case for weak intermolecular interactions between adsorbate particles and/or a strong bonding of the initial layer to the substrate surface, then layers are able to fully close prior to additional island nucleation on top and Frank van der Merwe growth occurs. However, if intermolecular interactions are large and adsorbate to substrate interactions small enough for the surface tension of the substrate to be smaller than the one of film plus interface ($\gamma_a < \gamma_b + \gamma$), then islands will form and their shapes will be influenced by factors such as diffusion coefficients and Ehrlich-Schwoebel-barriers (see the following chapter). Particles will get trapped at step edges and the islands will grow in height while the zone in-between such islands simultaneously gets depleted of adsorbate particles. This is known as Volmer-Weber growth. Additionally, systems - such as PTCDA on Si(100) [89] - exist, which show layer-like growth for low substrate temperatures that switches to island growth for higher substrate temperatures. As a third and probably most common option Stranski-Krastanov growth may be observed. A finite number of wetting layers are strongly bonded to the substrate, while any additional molecules form islands on top. Examples for such film formations include para-hexaphenyl on Au(111)[90] and mica(001)[91–93], pentacene on Au(111)[94] and Si(111)[95], as well as quaterphenyl on Au(111)[96] and PTCDA on Ag(111)[97].

However, the question still remains at what point the island nucleation starts and when do two atoms or molecules collide with each others just to part again and continue diffusing along the surface separately? To address this issue, we need to introduce another parameter:

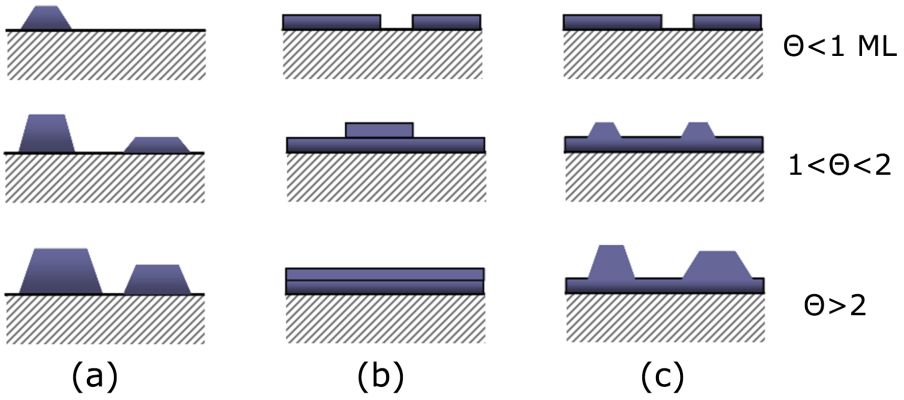

(a) Volmer-Weber growth

(b) Frank van der Merwe growth

(c) Stranski-Krastanov growth

Figure 2.4.: The three primary modes of thin-film growth (from Ref. [77])

the critical island size i. The critical island size is an integer value that defines the largest *non-stable* cluster. If only isolated adatoms are mobile on the surface, we can consider all clusters of size $> i$ to be 'stable', i.e. that another adatom arrives before the cluster decays (on average).[86] The reverse is true for clusters of below critical size. The coverage Θ_i with clusters containing i atoms is described by the *Walton relation*; [98]

$$\Theta_i = (\Theta_1)^i \ \exp(\frac{E_i}{k_B\ T}) \tag{2.6}$$

under the condition

$$0 \leq \Theta \leq 1 \tag{2.7}$$

Θ_1 denotes the ratio of the sample surface which is covered by clusters containing one atom, i.e. by single particles. The energy term E_i is positive because of the formation of bonds between the atoms. The number of bonds depends on the size and shape of the cluster. Critical cluster size are typically large at high temperatures.

2.4. Island Shapes

Depending on growth conditions, islands may be of fractal, dendritic or compact shape (see. Fig. 2.5) and may also consist of flat-lying or upright standing molecules if the respective molecules are rod- or plate-like. Due to energetic reasons, diffusing molecules and small

islands are always in a flat-lying configuration. If larger islands show an upright-standing configuration, then it means that the re-orientation happened at a specific, sufficiently high coverage. A standing configuration is initially unstable and metastable (energetically unfavorable) for medium sizes. For example, para-hexaphenyl on ion-bombarded mica shows energetically favorable clusters of standing molecules only at cluster sizes of $n > 14$.[99] In general, it can be said that a stronger substrate/molecule interaction favors clusters of lying molecules due to the large adsorption energy and a weak substrate/molecule interaction leads to energetically favored islands of standing molecules due to a lower energy being needed to overcome to create a large surface.

A further distinction in terms of growth behavior can be made between two-dimensional (2D) and three-dimensional (3D) islands. The former are by definition exactly one monolayer high and and should rather be viewed as not yet fully closed layers. 3D-islands on the other hand are a result of Volmer-Weber or Stranski-Krastanov growth and have heights of multiple layers.

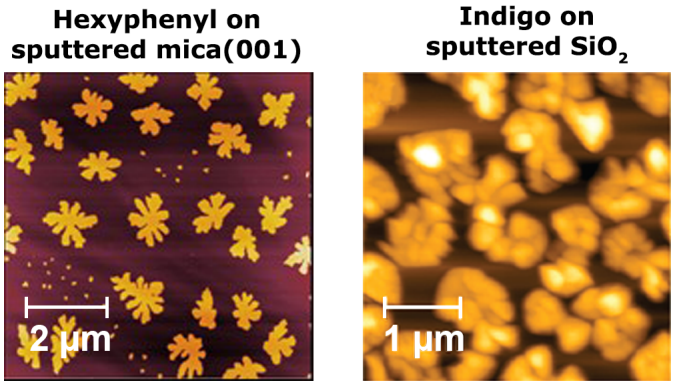

Figure 2.5.: Examples of dendritic (left, adapted from Ref. [100]) and compact (right, adapted from Ref. [68]) island shapes

The compactness of the island is largely controlled by the temperature dependent ability of the captured adatom to diffuse along island edges and to cross corners, where two edges meet.[77] Typically, the formation of fractal or dendritic islands takes place at relatively low temperatures, when the edge diffusion is slow. In the ultimate case of a *hit-and-stick* regime, an adatom sticks to an island edge and stays immobile at the impact site. The diffusion-limited-aggregation (DLA) model [101] can be applied for this case, under the assumptions that condensation is complete, i.e. no desorption of the monomers is allowed, and the attachment probability at the island edge is unity. The model predicts that under these conditions fractal islands with average branch thicknesses of about the width of one atom will be formed, irrespective of lattice geometry. However, the classic DLA mechanism will not occur in reality, since adatoms that reach an island always diffuse a certain path,

depending on the temperature T, to find an energetically more favorable site. The higher the edge diffusion rate, the greater the branch thickness.

A second aggregation model [102] was proposed for scenarios where the incorporation of the approaching monomers at the island edge is hindered. These kinds of island edge barriers may exist for surfactant mediated growth, where the island edge atoms have first to be removed in order to attach further approaching atoms.[103] Hence, the attachment probability and overall capture number of islands will not only depend on the edge diffusion, but also on the relative orientation between approaching molecules and the molecule arrangement at the rim of the island, leading to an effective barrier for attachment.[104] This scenario is known as attachment-limited-aggregation (ALA).[102, 105] The aggregation mode and the critical island size can be experimentally determined by the measurement of the island density N_{x} as a function of the deposition rate R.

If adatoms are easily able to cross island corners, for example at higher temperatures, then the growth will result in the formation of compact islands. The shapes of growing islands might differ from the equilibrium shape due to kinetic limitations of the many rate processes involved.

2.5. Thermal Desorption

If adsorbate particles gain enough energy from the thermal vibrations of the surface atoms to escape from the adsorption well, they will leave the surface in a so called *thermal desorption* process. The principle of microscopic reversibility demands that a reaction passes through exactly the same states irrespective of whether it proceeds forward or backward. Adsorption and desorption can therefore be described by the same set of rate equations. The equation describing the desorption rate of non-interacting particles is referred to as Polanyi-Wigner equation.[77] In the Langmuir desorption picture (Θ_{max}=1) it can be written as

$$\boxed{R(T) = -\frac{\mathrm{d}N(T)}{\mathrm{d}t} = \nu_n \; \Theta^n \; N_{ML}^n \; \exp(-\frac{E_{des}}{k_B \; T})} \tag{2.8}$$

Θ denotes the surface coverage, ν_n the pre-exponential factor of the desorption process, n the desorption order (comprehensively described in chapter 3.1), N_{ML} the monolayer coverage and E_{des} the activation energy for desorption. E_{des} is equal to E_a if the adsorption is not activated.

Eq. (2.8) is, however, only valid for first and higher order desorption (n≠0) and needs to be rewritten for the case of zero order or multilayer desorption (N_{max}=const.), where the desorption energy is equivalent to the heat of evaporation and the desorption rate becomes

coverage independent.

$$\boxed{R(T) = \nu_0 \; N_{ML} \; \exp(-\frac{E_{des}}{k_B \; T})} \tag{2.9}$$

One should also note that generally the desorption energy may depend on the adsorbate coverage ($E_{des}(\Theta)$), resulting in relationships exceedingly more complicated than equations (2.8) and (2.9).

The angular distribution of the desorption rate is a cosine law and the velocity distribution is Maxwellian under ideal conditions, i.e. for a sticking coefficient of unity. Once again, substantial deviations might occur, depending on the specific adsorbate/substrate system.

2.6. Applying Transition-State-Theory to Thermal Desorption

As we have learned from the Polanyi-Wigner equation, both an activation energy E_{des} and a prefactor ν has to be used to characterize the desorption dynamics. In a lot of cases ν is assumed to have its "typical" value of 10^{13} s^{-1}. In this section it will briefly be explained why this assumption is not valid in general and why the prefactor can be substantially larger for large molecules.

In transition-state-theory (TST) the desorption rate for adatoms at equilibrium on the surface is given as a canonical average of the flux of desorbed molecules passing through the transition state to the vacuum above.[106] It can be written as [107]

$$R(T) = \sigma_a \kappa \frac{k_B T}{h} \frac{q^{\ddagger}}{q_{ads}} \exp(-\frac{E_{des}}{k_B T}) \tag{2.10}$$

with $q^{\ddagger}$ being the partition function of the transition state, q_{ads} the partition function of the adsorbed state, σ_a the surface concentration of the adsorbate, κ a transmission coefficient which defines the probability of an activated complex to proceed into the product channel ($\kappa \leq 1$) and T the surface temperature.

The pre-exponential factor ν is then given by

$$\nu = \kappa \frac{k_B T}{h} \frac{q^{\ddagger}}{q_{ads}} \tag{2.11}$$

If one assumes a transmission coefficient of unity and no change in the partition function between the adsorbed phase and the transition state ($\frac{q^{\ddagger}}{q_{ads}} \approx 1$), as it is the case for desorption of small atoms that are able to freely move across the surface prior to desorption, then

the whole term reduces itself to $\frac{k_B T}{h}$, which is in the order of 10^{13} s^{-1} for typical desorption temperatures of 500 K. This has been experimentally verified for many mono-atomic and molecular adsorbates under a certain size.[108] However, this condition only holds if the adsorbates are non-interacting and if no changes in the vibrational, rotational and translational degrees of freedom occur. These assumptions are therefore not applicable for the large molecules that were investigated in this thesis and the partition function ratio needs to be analyzed more thoroughly. $\frac{q^{\ddagger}}{q_{ads}}$ may be represented as a product of the ratios of the translational, rotational and vibrational contributions. In detail, the two-dimensional translational, rotational and vibrational partition functions for a linear molecule can be written as [109]

$$\frac{l^2 2\pi m k_B T}{h^2} \qquad \text{(translational)} \tag{2.12}$$

$$\frac{8\pi^2 k_B T I}{h^2 \sigma} \qquad \text{(rotational)} \tag{2.13}$$

$$\frac{1}{1-\exp(-\frac{\hbar\omega}{k_B T})} \qquad \text{(vibrational)} \tag{2.14}$$

with $l^2 \approx 10^{-15}$ cm^2 the area of an elementary cell, m the molecule mass, I and ω the moment of inertia and vibrational frequency of a molecule, respectively, and σ a symmetry number. One should note that the values of vibrational partition functions are close to unity in many practical cases due to a high vibrational energy $\hbar\omega$. However, this consideration needs to be disregarded once again if large molecules are to be considered.

If the pre-exponential factor for desorption now exceeds values of 10^{13} s^{-1}, then it is a clear indication, still under the assumption that $\kappa \approx 1$, that the ratio $\frac{q^{\ddagger}}{q_{ads}}$ is larger than unity. This means that the transition state has degrees of freedom that are more easily excited by thermal energy than the adsorbed phase.[107] To further discuss contributions from rotational and translational partition functions, a clear distinction between monoatomic and molecular desorption needs to be made. The main differences arise due to two characteristic features of molecular adsorbates.[110] First, molecules have internal degrees of freedom which are absent in atomic systems. In addition, molecules exhibit rotational modes (surface-adsorbate bending modes) strongly coupled to the surface but which become pure rotational modes in the activated state. Motions that are free in the gas phase (e.g. translation, internal vibration and rigid-body rotation) are hindered on the surface. The rigid-body rotation for example is strongly coupled to the surface, so that the total potential which the adsorbed molecule feels has a large component due to this mode. Hence, parameters like molecule size and chemical bond type can have significant influence on the partition functions and may therefore lead to relatively large contributions to the prefactor. In general, rotational and translational partition functions are in the order of 10^1-10^3 for $T = 500$ K for most molecules.

Of course, there are some concerns with TST. The main difficulty involves the definition of the transition state for the desorbing species. The most common choice is to assume that the transition state is located at an infinite adsorbate-surface separation, essentially making the partition function equivalent to a free atom moving in a direction normal to the surface.[110] This is generally a reasonable assumption. Either way, values obtained via TST represent only upper limits of the rate constants, due to multiple assumptions and the fact that no precursor states are taken into account. However, the existence of such states does not change the obtained values considerably. If the sticking probability is unity up to the desorption temperature, then the TST description is exact.[111]

2.7. Coarsening and Ripening

The phenomena where the mean island size increases over time at the expense of decreasing the number of islands is referred to as *coarsening*. Further distinctions are being made between coalescence (the merging of islands upon contact) and ripening (the growth of larger islands due to the diffusion flux of adatoms that are detached from smaller islands). In the former case, the resulting island shape depends on the edge mobility of atoms. In practice this mobility is often sufficient to allow newly formed islands to recover their equilibrium shape. The ripening process described earlier is typically referred to as *Ostwald ripening*. It is a thermodynamically driven process to reduce free energies associated with island edges. Contrary to that, *Smoluchowski ripening* is the process of mobile islands encountering each other and coalescing into larger islands.[77]

3 | Analytical methods

3.1. Thermal Desorption Spectroscopy

The determination of adsorption states, desorption kinetics and desorption energies as well as getting a general understanding of the behavior of adsorbed molecules in thin film phases was one of the focal points during my research. A very powerful method to assess the mentioned processes is temperature-programmed desorption, also known as thermal desorption spectroscopy (TDS). The basic idea of this method goes back to Redhead [112] and other publications in the 1960s (e.g. Ehrlich [113]) and can be summarized as a continuous heating of a substrate with a simultaneous mapping of the desorption rate as a function of temperature. The rate at any time will be determined by the temperature and the remaining amount of material on the surface. It will feature a maximum at one point, when the increased desorption due to the temperature rise is equal to the decrease from the diminished coverage.[108] The quantity and mass of the desorbing atoms and/or molecules is subsequently analyzed in a quadrupole mass spectrometer or pressure gauge and plotted versus either time or temperature.

If non-condensable materials (gases) are studied, then the desorption process can directly be mapped by an increase in partial pressure of the UHV system. The general relationship for non-condensable gases between the adsorbate desorption rate and the partial pressure increase is described by the equation

$$-A\,\frac{\mathrm{d}\Theta}{\mathrm{d}t} = \frac{V}{k_B T}\,\left(\frac{\mathrm{d}p}{\mathrm{d}t} + \frac{S}{V}\,p\right) \tag{3.1}$$

with A the sample surface area, $\frac{\mathrm{d}\Theta}{\mathrm{d}t}$ the desorption rate, V the volume of the UHV chamber,

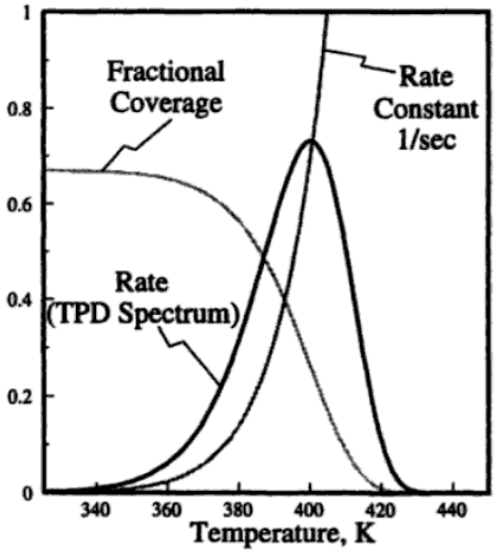

Figure 3.1.: Evolution of the coverage and rate constant for desorption during heating resulting in a characteristic desorption peak (adapted from Ref. [70])

p the partial pressure of the adsorbate and S the pumping speed. Now, if the pumping speed is sufficiently high, as it is generally the case for most UHV systems, the pressure becomes directly proportional to the desorption rate

$$p \propto \frac{\mathrm{d}\Theta}{\mathrm{d}t} \tag{3.2}$$

If a linear heating rate β_H

$$T(t) = T_0 + \beta_H \; t \tag{3.3}$$

is used, equation (3.2) can be written as

$$p \propto \frac{\mathrm{d}\Theta}{\mathrm{d}T} \; \beta_H = \nu_n \; \Theta^n \; \exp(-\frac{E_{des}}{k_B \; T}) \tag{3.4}$$

under consideration of equation (3.3) and equation (2.8) on page 21. Upon visualizing this relationship one can see, that the exponential term is negligible at low temperatures, hence the negligible desorption rate. With further heating the desorption rate increases rapidly, following the growth of the exponential term at sufficiently high temperatures. However, the inevitable decrease in adsorbate coverage during the desorption process slows down the desorption rate until it reaches zero once the adsorbate is depleted. As a result, the pressure versus time dependence displays a peak at a certain characteristic temperature T_m (compare Fig. 3.1).

If one wants to study larger molecules or condensable gases, then it is not sufficient to

map the desorption rate with a pressure gauge. An in-line quadrupole mass spectrometer needs to be installed directly in front of the studied sample. Although the detected intensity is directly proportional to the desorption rate, several problems can arise and need to be addressed. First, large molecules will likely fragment upon contact with the QMS leading to a potentially large number of cracking and reaction products. The selection of a proper cracking mass to map the desorption signal of the primary molecule can be tricky and should be addressed carefully. Additionally, the angular distribution (see page 22) and the dependence of the detected intensity on the kinetic energy of the desorbing particles need to be kept in mind when interpreting thermal desorption spectra.

From a certain desorption peak one can now draw a number of conclusions. Primarily, the peak temperature is an important aspect and dependent on multiple parameters, e.g. desorption energy, desorption order and adsorbate coverage. T_m will be higher at larger heating rates and for higher desorption energies and will decrease with larger pre-exponential factors (higher attempt frequency to leave the surface). Additionally, the amount and relative positions of different peaks may yield valuable information about different molecule configurations (i.e. wetting layer, structures with flat-lying or upright standing molecules, island formation etc.), while the peak shape and the change of T_m with varying initial adsorbate coverage is directly related to the desorption order. Each peak may represent a different kinetic process. As an example, Fig. 3.2 shows a set of ideal TDS spectra for zero, first and second order desorption kinetics.

Zero order desorption

Zero order desorption is observed for condensable gases which form multiple layers upon adsorption. Desorption kinetics in this case are characterized by curves with a common leading edge for all coverages and a rapid drop beyond T_m. The peak temperature moves to higher values with increasing initial coverage Θ_0. Zero order desorption can be described by eq. (2.9), as the desorption rate $R(T)$ is directly proportional to $\exp(-\frac{E_{des}}{k_B T})$ and therefore coverage independent. The desorption energy and pre-exponential frequency factor can be acquired by a simple $\ln(R(T))$ vs. $1/T$ plot. The slope is then equivalent to $-E_{des}/k_B$ and the intercept with the y-axis can be used to determine ν.

First order desorption

First order desorption appears primarily for monolayer desorption of non-condensable gases and is described by the Langmuir adsorption model ($\Theta_{max} = 1$). Peaks have an asymmetric shape and the peak maximum remains at a constant temperature with increasing initial coverage Θ_0. The desorption rate is directly proportional to the surface coverage

($R(T) \sim \Theta \exp(-\frac{E_{des}}{k_B T})$, see eq. (2.8)), which needs to be considered if one wants to obtain E_{des} and ν. E_{des} for first order desorption is obtained from the slope of an Arrhenius plot of $\ln(R/\Theta)$ vs. $1/T$.

Second order desorption

Second order desorption appears if two individual atoms or molecules need to recombine before they are able to leave the surface. Peaks have a symmetric shape and the peak temperature moves to lower values with increasing coverage due to an increasing amount of recombination partners becoming available.

In all three cases the integrated area under a desorption peak is proportional to the initial coverage Θ_0.

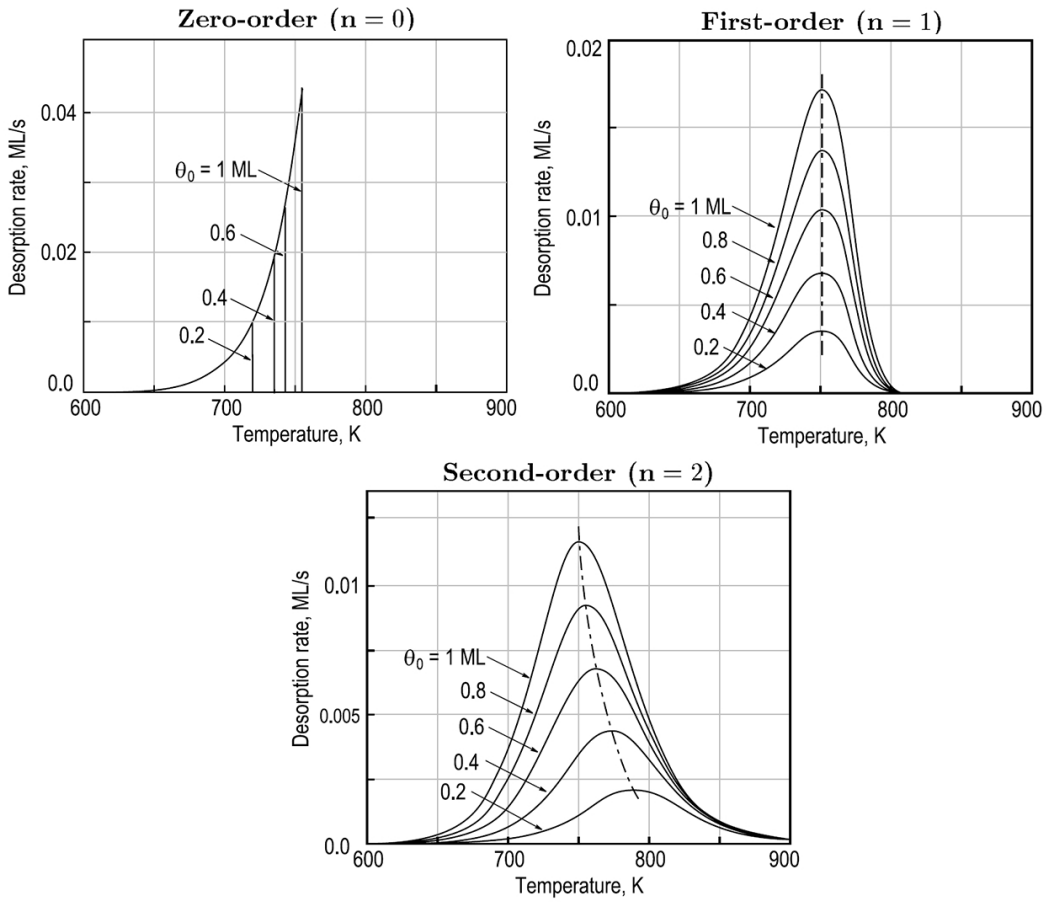

Figure 3.2.: Thermal desorption spectra for zero, first and second order desorption kinetics and various initial coverages Θ_0 (from Ref. [77])

According to King [114] one is able to calculate the activation energy of desorption as

a function of coverage from different thermal desorption spectra taken at different initial coverages via the construction of an Arrhenius plot. This derivation is based upon the fact that the area under a TDS curve integrated from temperature T to ∞ is proportional to the coverage at that temperature $\Theta(T)$

$$\Theta(T) = C_1 \int_T^\infty \frac{R_d(T)}{\beta_H} \, \mathrm{d}T \tag{3.5}$$

$R_d(T) = \frac{\mathrm{d}\Theta(T)}{\mathrm{d}t}$ is the desorption rate at temperature T and C_1 a constant which can be calculated by integrating the TDS curve for a saturated monolayer, assuming Θ=1 in that case. In the initial slope or Habenschaden-Küppers method [115] only the leading edge of the TDS curve is examined. This method can be used as a convenient way to obtain the kinetic parameters E_{des} and ν from a simple Arrhenius plot of $\ln(R)$ versus $1/T$ while omitting the coverage dependency in equation (2.8). In a simple approximation it is assumed, that the change of adsorbate coverage is negligible at the beginning of the desorption process.

Thermal desorption spectroscopy is of course not limited to obtaining peak temperatures, desorption order and desorption energies, but rather an efficient method to acquire full information about the adsorption and desorption behavior of different particles. Different molecular states as well as different molecular orientations can be distinguished in a thermal desorption spectrum and mapped upon varying coverage, substrate temperature, heating rate etc. to analyze dewetting processes and decomposition reactions. Furthermore, the initial and coverage dependent sticking coefficients may be obtained from a coverage versus exposure plot, providing insight to precursor states and adsorbate/adsorbant reactions.

3.2. Auger Electron Spectroscopy

Auger electron spectroscopy (AES) is a very surface sensitive technique to determine the chemical composition of the outermost few atomic layers of materials. Due to contamination, residue from various chemical and physical reactions and oxidation this composition can be quite divergent from the bulk phase of the studied material. In AES a specimen is probed either by photons or by electrons with energies in the keV-range. Atoms in the top layers (up to a maximum depth of a few nm) change from their ground state into an excited state, resulting in the ejection of core level electrons. The core hole causes a contraction of the outer shells and the vacancy quickly gets filled by an outer level electron in a transition process. The energy difference between the two electron states, known as excess energy, is then transferred either to another electron which is then ejected from the atom (Auger

electron, see Fig. 3.3) or used to emit X-ray radiation. In either case, the final state is a doubly ionized atom.

The surface sensitivity of AES is caused by strong inelastic scattering processes of low-energy electrons in solid specimens. Only electrons from the outermost layers can leave the sample without energy loss and contribute to the Auger peaks in a spectrum. Scattered electrons that have lost energy on their way to the detector may also appear in the spectrum as an additional background signal at lower kinetic energies. Every measured Auger electron has a kinetic energy that is specific for the probed element, due to the discrete binding energy levels of the involved electron states. Therefore, measuring the Auger kinetic energies is used to identify chemical compositions at the surface of various materials. Hydrogen and helium can obviously not be detected by AES due to the necessity of three different electrons. All emitted Auger electrons will appear as peaks on a continuous background of secondary (below 50 eV) and backscattered (above 50 eV) electrons. The relative concentration of elements can be semi-quantitatively determined from the intensities of the Auger peaks.

In a lot of cases the kinetic energy of the electrons leaving the sample is plotted versus the first derivative of the number of emitted electrons, using a lock-in amplifier, rather than the total number of emitted electrons itself. This is done to enhance the visibility of Auger peaks and to suppress the slow variations of the background signal as much as possible. In modern Auger setups the primary electron beam can be focused down to sizes of around 50 nm and subsequently scanned across the sample surface to accurately probe nanostructures.[116] The setup that was used in this thesis featured a diameter of the incident beam of roughly 1 mm, thus only providing an averaged signal over a large surface area.

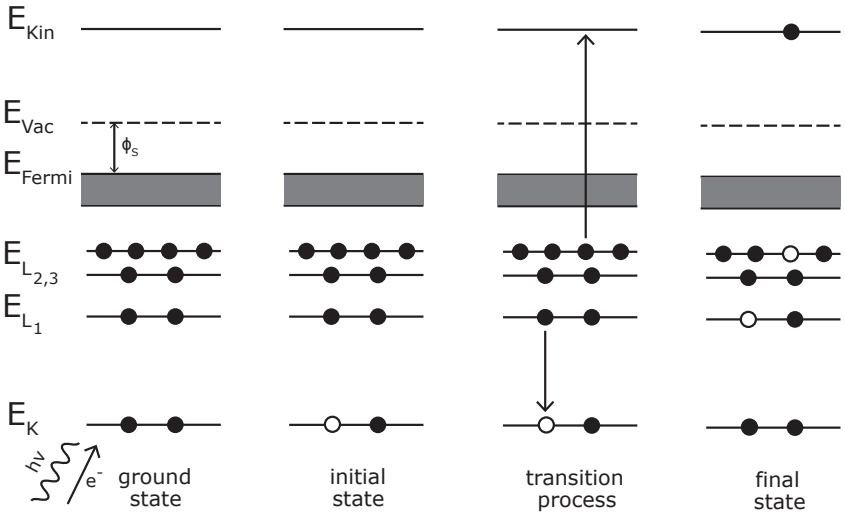

Figure 3.3.: Schematic representation of the Auger transition process in a solid (adapted from Ref. [77])

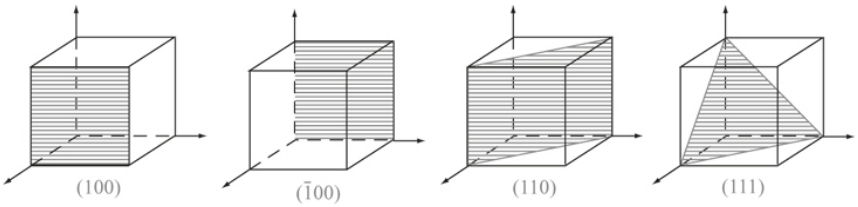

Figure 3.4.: Some important crystallographic planes and their corresponding Miller indices (adapted from Ref. [77])

3.3. X-ray Diffraction

X-Ray diffraction is a technique used to determine the crystalline structure in thin films and powder samples. Due to limitations of available X-ray detection systems certain scattering intensities are required to receive signals above the noise level, which in turn require certain minimum film thicknesses. The organic films that were investigated in this work required a minimum film thickness for XRD analysis of at least 20 nm, essentially restricting this technique to investigations of the bulk structure, opposed to the surface-sensitive AES technique.

Miller Indices

Crystallographic planes are defined as a group (or family) of planes that intersect all lattice points in a Bravais lattice. Within the same family, all planes are parallel to each other and equally spaced with the interplanar distance d. Each family of crystallographic planes is described with three integer values, h, k and l, which are commonly referred to as Miller indices. Miller indices indicate that the planes that belong to the family (hkl) divide lattice vectors (unit cell edges) a, b and c into h, k and l equal parts, respectively.[117] Is a plane parallel to a crystallographic axis, then the corresponding Miller index is set to 0. In addition, directions in the crystal lattice are defined as lines that pass through the lattice origin and are parallel to the direction of interest. Therefore, a crystallographic direction is indicated by referring to the coordinates of the first point the line intersects on its way from the origin. All Miller indices are enclosed in parentheses when referring to a crystallographic plane and enclosed in square brackets when referring to a crystallographic direction. Schematics of a few crystallographic planes that are important in surface science and their corresponding Miller indices are shown in Fig. 3.4.

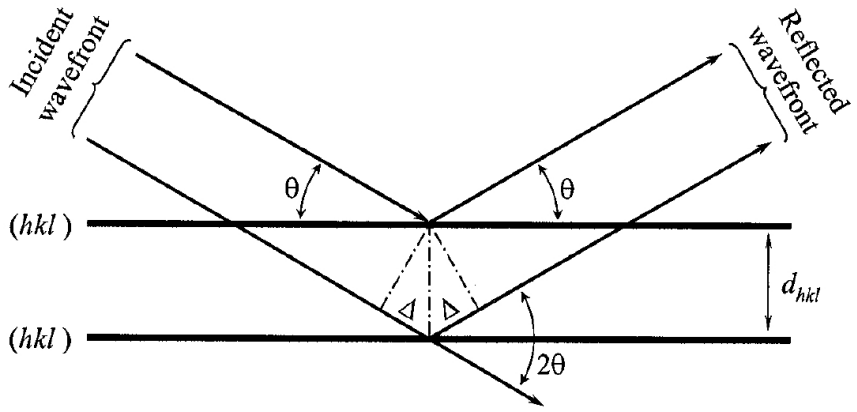

Figure 3.5.: Graphical representation of Braggs' law upon reflection of an incoming wavefront (from Ref. [117])

Single Crystal Diffraction

Diffraction from a set of equally spaced objects (i.e. crystallographic planes) is only possible at specific angles, as it is described by Braggs' law and geometrically derived in Fig. 3.5. If we consider an incident wave front with parallel propagation vectors that hit the (hkl) plane family with an angle of θ and assume a mirror reflection, then we can easily see that the reflected wavefront also consists of parallel waves, which form the same angle θ with all planes. The path difference between a pair of wavefronts before and after reflection is then determined by the interplanar distance and constructive interference is observed when

$$2\ d_{hkl}\ \sin\theta_{hkl} = n\lambda \tag{3.6}$$

with n an integer value and λ the incident wavelength. This formula is known as Braggs' law.

An alternative approach that describes diffraction in the reciprocal space for better visual representation and easier understanding was introduced 1969 by Ewald [118]. If an incident wave with a propagation vector $\mathbf{k}_0$ is selected with a length identical to the inverse of its wavelength λ

$$|\boldsymbol{k_0}| = \frac{1}{\lambda} \tag{3.7}$$

then the entire wave can be fully characterized by $\mathbf{k}_0$, its wavevector. The length of the wavevector of the incident wave remains constant upon elastic scattering, meaning that the scattered wave is characterized by a different wavevector $\mathbf{k}_1$ with the same length as $\mathbf{k}_0$. The angle between $\mathbf{k}_0$ and $\mathbf{k}_1$ is 2θ. If we overlap these two wavevectors with a reciprocal crystal lattice in such a way, that the end of $\mathbf{k}_0$ coincides with the origin of the lattice, then

diffraction in the direction of $\mathbf{k}_1$ can only occur when its end coincides with a point in the reciprocal lattice. Thus, considering that both wavevectors have identical lengths, the ends of $\mathbf{k}_0$ and $\mathbf{k}_1$ are equidistant to a common point and all possible orientations of $\mathbf{k}_1$ delineate a sphere in three dimensions (see Fig. 3.6). This sphere has a radius of $1/\lambda$ and is named Ewald's sphere.

Diffraction can only be observed when a reciprocal lattice point, other than the origin, intersects with the surface of the Ewald's sphere (as it is the case for the point $(\bar{1}3)$ in Fig. 3.6). Thus, only a few, if any, points of the reciprocal lattice will coincide with the surface of the Ewald's sphere when a randomly oriented single crystal is irradiated by monochromatic X-rays. Parameters that influence the amount of lattice points that coincide with the Ewald's sphere are (a) the wavelength of the incident beam (determines the radius of the sphere) and (b) the lattice parameters and orientation of the crystal (determines the distribution of the reciprocal lattice points). Additionally, if the crystal is set in motion, for example by rotating around an axis, many more reciprocal lattice points will be placed on the surface of the sphere. The rotation changes the orientation of the reciprocal lattice, however, the origin will stay aligned with the end of the incident wavevector. Hence, all reciprocal lattice points with $\mathbf{d^*} \leq 2/\lambda$ will coincide at some angular position with the surface of the Ewald's sphere.

Diffraction from Powder or Polycrystalline Samples

In the case of diffraction from powders or polycrystalline specimens, i.e. when multiple single crystallites are irradiated simultaneously by a monochromatic X-ray beam, a different situation is observed. If the number of grains in the irradiated volume is large enough and if they are completely randomly orientated, then those properties can be transferred onto the reciprocal lattice as well. Thus, the ends of the identical reciprocal lattice vectors $\mathbf{d^*}_{hkl}$ become arranged on the surface of the Ewald's sphere in a circle perpendicular to the incident wavevector $\mathbf{k}_0$. The corresponding scattered wavevectors $\mathbf{k}_1$ will then be aligned along the surface of a diffraction cone. For the desirable case of an infinitely high number of differently orientated crystallites the density of the scattered wavevectors becomes constant, leading to a diffracted intensity that is constant around the circumference of the cone base or, when measured by a planar area detector, around the ring, which the cone base forms with the plane of the detector. Hence, in a typical powder diffraction experiment, the measurements are performed only along a narrow rectangle centered at the circumference of the equatorial plane of the Ewald's sphere. Because of this only one variable axis is required in powder diffractometry. The scattered intensity is usually represented as the total number of the accumulated counts plotted as a function of a single independent variable, namely the Bragg angle 2θ. This type of plot is called a powder diffraction pattern.

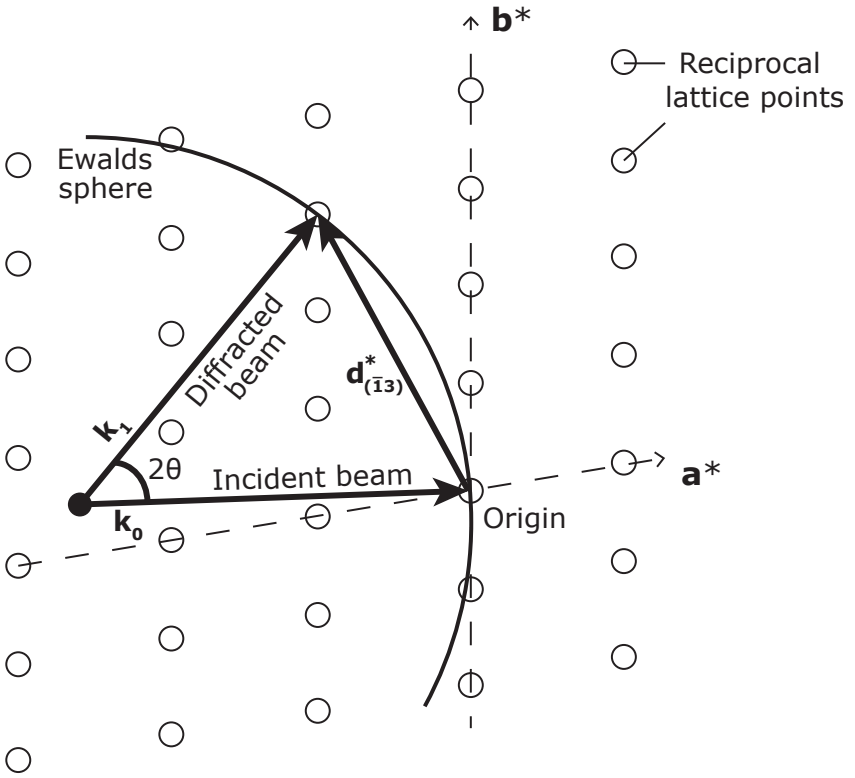

Figure 3.6.: Illustration of the Ewalds sphere and Braggs' law in reciprocal space. The incident ($\mathbf{k}_0$) and diffracted ($\mathbf{k}_1$) wavevectors originating from a common point are overlapped with the two-dimensional reciprocal lattice of a crystal. The origin of the reciprocal lattice is chosen at the end of ($\mathbf{k}_0$). When diffraction occurs from a point in the reciprocal lattice, e.g. the point ($\bar{1}3$), the corresponding reciprocal lattice vector $\mathbf{d^*}_{hk}$ (e.g. $\mathbf{d^*}_{\bar{1}3}$) extends between the ends of ($\mathbf{k}_0$) and ($\mathbf{k}_1$). (adapted from Ref. [117])

In reality the situation might prove to be slightly different from theoretical diffraction values, namely due to the finite thickness of the Ewald's sphere (caused by wavelength aberrations) and the slight diffuse behavior of reciprocal lattice points. The resulting Bragg peaks will therefore not have infinitely narrow diffraction maxima, but rather exhibit non-zero widths as functions of 2θ. A more comprehensive description of theoretical and practical X-ray diffraction processes can be found in Ref [117].

When performing a θ/2θ scan one has to keep in mind that the observed scattered intensity variation is not only associated with reflections in the sample, but also depends on the distance from the sample to the detection system. Therefore, X-ray diffraction experiments are preferably facilitated in such a way, that the space around the sample can be scanned while keeping the sample-detector distance constant. The detector should accordingly move on a sphere with constant radius with the sample in the center of it. In practice the sphere

reduces to a hemisphere above the sample, since only the surface layer is of interest. Data collection is then performed in reflection mode.[119]

Pole Figures

As it is extensively described in Ref. [120], so called 'poles' are the imaginary lines perpendicular to different Miller planes of a crystal. If we now imagine the crystal in the center of the reflection sphere upon irradiation, then it is clear that the poles meet the surface of the imaginary sphere. Those intersections are the spherical projection of the poles and their corresponding crystal planes (see Fig. 3.7a). When the base of the poles on the spherical surface is projected on a plane kept perpendicular to the diameter of the sphere, then this stereographic projection is called a pole figure. A (111)-pole figure for example means that the plane on which pole figures are stereographically projected is taken perpendicular to one of the (111)-poles. For perfect single crystals this projection will only meet at the center of the plane, as all (111)-planes are parallel and the poles of other planes will be distributed symmetrically onto the plane. During the measurement the angle θ remains fixed at a definite value that corresponds to a strong Bragg reflection and which was determined in advance by a specular $\theta/2\theta$ scan. To assess the orientation distribution of the crystallites, the sample is rotated and tilted by certain angles φ and ψ, respectively, (see Fig. 3.7b) until constructive interference appears. Pole figures are generally used to find the preferred crystallite orientations in textured polycrystalline materials. Even before finding the actual texture one can know whether the sample is textured or not: For random polycrystalline samples poles of an (hkl) reflection will be evenly distributed on the pole figure, whereas it will be clustered in specific regions for textured samples.

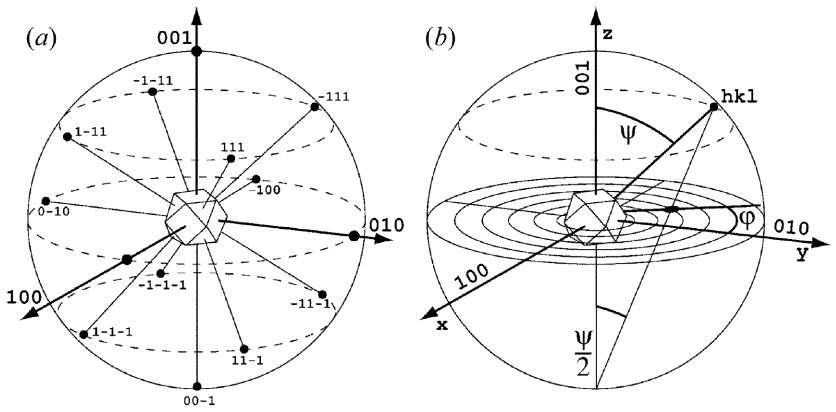

Figure 3.7.: (a) Spherical projection of crystal plane normals onto the unit sphere; (b) Illustration of the polar coordinates φ and ψ that are used to describe any given point (hkl) at the sphere (from Ref. [121])

Rocking Curves

The rocking curve technique may provide substantial information on dislocation density, mosaic spread, curvature, misorientation and inhomogeneity of thin film samples. During a rocking curve measurement the detector remains fixed at a specific Bragg angle (θ_0), which was determined by an earlier $\theta/2\theta$ scan. The sample is then tilted on the θ-circle in vicinity of the θ_0-angle. Both circles are thus decoupled and the θ-angle is generally referred to as ω. The result of the rocking curve analysis is a set of intensities which describe the 'crystal quality'. The smaller the full width at half maximum is for certain diffraction peaks, the less crystal defects, lattice mismatches, etc. exist in the crystal. A perfect crystal will produce a very sharp peak, observed only when the crystal is properly tilted. Defects will create disruptions in the perfect parallelism of atomic planes, which are observed by a broadening of the rocking curve.

3.4. Grazing Incidence Small Angle X-Ray Diffraction

Specular X-ray diffraction reaches its limits for thin-film investigations with thicknesses that are substantially less than the penetration depth of X-rays, typically 10-100 μm if the attenuation coefficient μ is in the order of 10^4-10^5 m^{-1}.[119] In this case a large fraction of the diffractogram as measured in a symmetric $\theta/2\theta$ configuration stems from the substrate and only negligible structural information can be gained in this measurement configuration - the path traveled by the X-rays in the sample, which is in the order of $\sin(\theta/\mu)$, is simply too short for typical Bragg angles to deliver reflections of sufficient signal-to-noise ratio. To address this issue, alternative X-ray diffraction techniques have been developed for which the primary beam enters the sample at very small angles of incidence. In its simplest form this configuration is known as GIXD: grazing incidence X-ray diffraction. The path traveled by the X-rays within the sample increases significantly due to the small entrance angle and causes any structural information contained in the diffractogram to stem primarily from the thin film. The maximum traveled path within the layer calculates to $l = t/\sin(\alpha_i)$ and can be a high multitude of the thicknes t if the entrance angle α_i is chosen very flat (typically in the 1.0-1.5° range and slightly above the critical angle of total reflection).

The principle of GIXD is schematically shown in Fig. 3.8. The surface of the sample defines the (x,y)-plane with the x-axis orientated along the X-ray beam direction and the y-axis being thus perpendicular to the scattering plane given through the incident angle α_i and the exit angle α_f.[122] The z-axis is representing the surface normal. The scattering process is called specular scattering if $\alpha_i = \alpha_f$ and diffusive scattering if $\alpha_i \neq \alpha_f$. The

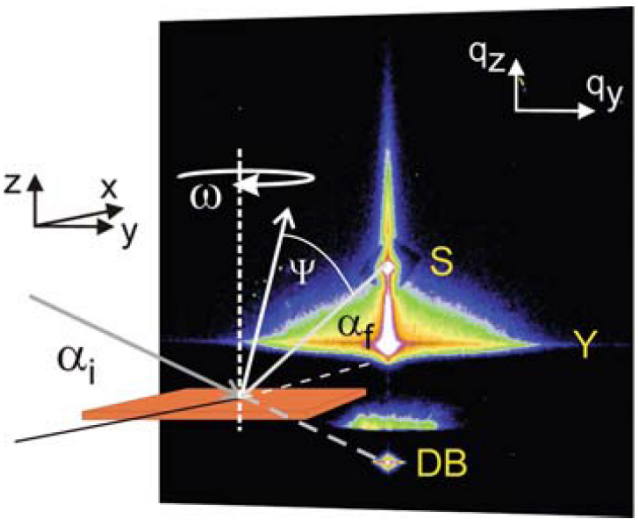

Figure 3.8.: Schematic picture of the GIXD scattering geometry. The sample (orange) is positioned with respect to the spatial coordinates x, y and z as well as by its azimuthal orientation ω. The incident angle is denoted α_i, the exit angle α_f and the out-of-plane angle ψ. The color coding visualizes differences in the scattered intensity on the two-dimensional detector. DB denotes the direct beam, S the specular peak and Y the Yoneda peak. (from Ref. [119])

direct beam and the specular reflected beam are often suppressed by a beam stop to avoid detector saturation as several orders of magnitude in intensity separate the diffuse scattering from the specular reflectivity.[123] The GIXD signal is then measured with a 2D-detector, which records an out-of-plane (wave vector q_z) versus in-plane (wave vector q_{xy}) scattering pattern that is symmetric with respect to the scattering plane. When the exit angle of the scattered beam is close to the critical angle, signal enhancement due to the Vineyard effect [124] occurs, resulting in a bright band of intensity at the critical angle. This is also referred to as the Yoneda peak.[125]

GIXD measurements performed at laboratory sources are typically very limited. Full structural information can only be obtained upon using a synchrotron radiation source. Besides the flux and collimation also the wavelength can be chosen accordingly in order to avoid fluorescence or to perform anomalous measurements.

3.5. Micro-Raman Spectroscopy

If monochromatic light with a frequency of $\tilde{\nu}_0$ is irradiated onto a transparent solid, most of it is transmitted unchanged. However, some part of it will interact with the molecules or atoms of the solid, distort the cloud of electrons around the nuclei and get inelastically

scattered. If the scattered radiation is analyzed, frequencies with values of $\tilde{\nu}_0 \pm \tilde{\nu}_M$ can be observed (Fig. 3.9). In the case of molecular systems, the frequency jumps $\tilde{\nu}_M$ can be attributed to changes in rotational, vibrational or electronical excitations. Scattering generally occurs in all directions and both the intensity and polarization of the scattered radiation depend on the direction of observation. Additionally, the scattered radiation usually has polarization characteristics different from the incident radiation. The whole scattering process is inherently incoherent and as a result, the intensity of scattering from a material system of N non-interacting molecules is simply N times that from one molecule and it is therefore independent of the bulk structure of the material system. This characteristic can be used for chemical material probing without the need to produce films with certain thickness or quality.

Scattering where the incident and the scattered beam have different frequencies is called Raman scattering (in contrast to Rayleigh scattering, where no frequency change occurs) and all the new frequencies are termed Raman bands and constitute a Raman spectrum. Raman lines at frequencies that are smaller than the incident frequency (i.e. of the type $\tilde{\nu}_0 - \tilde{\nu}_M$) are referred to as Stokes bands and those at frequencies greater than the incident frequency (i.e. of the type $\tilde{\nu}_0 + \tilde{\nu}_M$) as anti-Stokes bands.[126]

Contrary to for example Auger electron spectroscopy, the kinetic energy of the primary irradiation source does not promote an electron to any one excited state of the static molecule. All states are involved to different extents and are mixed together to create scattering photons. The energy of the short-lived excited state and subsequently the frequency of the scattered photon is dependent on the energy of the laser used and the shape of the distorted energy alignment is dependent on the electronic properties of the molecule, as well as on the energy of the laser. Rayleigh scattering occurs if the electron cloud relaxes without any nuclear movement. However, when the nuclei moves during the interaction between the light and the electrons, then the whole molecule will change its energy state. Once again, a change to a vibrationally excited state is known as Stokes Raman scattering and a relaxation to the ground state from a vibrationally excited state is known as anti-Stokes scattering. Most molecules at rest prior to interaction with the laser and at room temperature are likely to be in the ground vibrational state. Therefore the majority of Raman scattering will be Stokes Raman scattering.[127] The entirety of the recorded frequency changes makes up a Raman spectrum, which can be interpreted as a chemical fingerprint of the investigated material (i.e. a C=C double bond causes different Raman lines than a C-C single or a C-H bond).

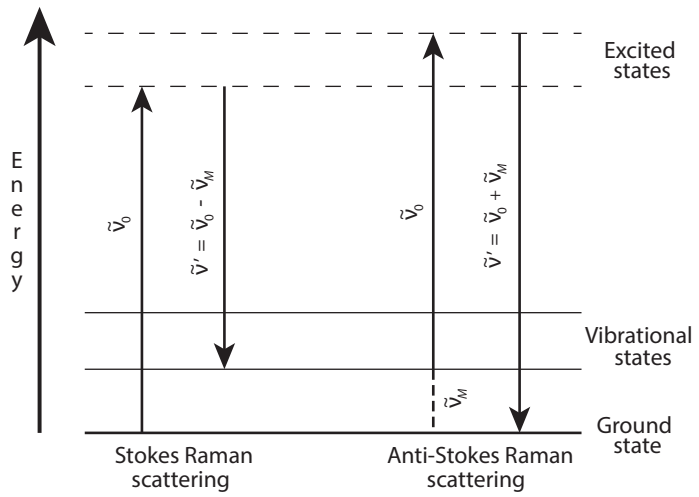

Figure 3.9.: Energy level changes for Stokes and anti-Stokes Raman scattering of an incident photon with the frequency $\tilde{\nu}_0$ (adapted from Ref. [127])

3.6. Atomic Force Microscopy

Atomic force microscopy (AFM) is, as the name already suggests, a scanning probe technique to map surfaces at an atomic level. A sharp tip with a length of a few microns is located at the free end of a cantilever (typically 100-200 µm long, see Fig. 3.10) and scanned across the sample surface. Interatomic forces between the tip and the sample causes the cantilever do deflect

$$F = C \cdot \Delta z \tag{3.8}$$

with C the spring constant and z the distance between sample surface and AFM tip. The small deflection of the cantilever can be detected with various techniques, but it is usually done optically with a laser diode and a four-segment photo detection sensor. Deflection detections down to 10^{-2} Å are possible.[77] The surface topography of a large area is mapped by measuring the cantilever deflection while either the tip is scanned over the sample or while the sample is moved under the tip. The evident advantage of atomic force microscopy, especially when the comparison with scanning tunneling microscopy is made, is the possibility to study any type of surface, independent of its conductivity.

A closer look at the physics between tip-sample interaction reveals, that the cantilever is weakly attracted to the sample for relatively large distances, but this attraction quickly increases with decreasing distance. The net force approaches zero at a distance in the order of the length of a chemical bond (i.e. a few Å) and electrostatic repulsion becomes dominate afterwards. The range of tip-to-sample separation during the measurement defines the AFM mode of operation, namely contact, non-contact or tapping mode. All microscopic

images that are shown at a later point in this thesis were recorded using tapping mode. Tapping mode has a lot of similarities to non-contact mode, namely a tip-sample separation and a constant vibration of the stiff cantilever near its resonance frequency. However, the cantilever tip touches (taps) the sample surface at the bottom point of its oscillation. This mode generally does not provide atomic resolution but has proven to be advantageous for imaging rough surfaces with high topographical corrugations. A photograph of the used AFM measurement system is shown in Fig. 3.12.

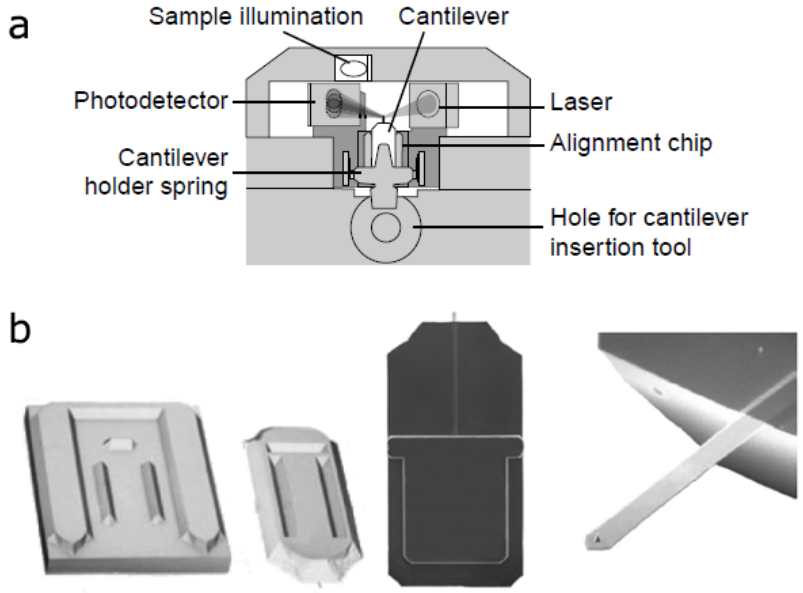

Figure 3.10.: Detailed look on the AFM measurement setup (from Ref. [128])

(a) Schematic diagram of the scan head.

(b) Photographs of the used cantilever, cantilever holder and the piezo-electric mounting platform.

Figure 3.12.: The Nanosurf easyScan 2 atomic force microscope

4 | Instrumentation

As far as the analytical methods over the course of this thesis are concerned, two distinctions can be made: in-situ and ex-situ measurements. In-situ spectroscopy has been performed with thermal desorption spectroscopy (TDS) and Auger electron spectroscopy (AES) under UHV conditions. Additionally, the quadrupole mass spectrometer (QMS) that was used for TDS was utilized to measure mass spectra of the flux of desorbing particles and/or the residual gas in the chamber and furthermore to analyze the deposition flux from the Knudsen cell. Sample cleaning was done via dry etching with argon ions. The second group of experiments were carried out under ambient conditions: atomic force microscopy (AFM), X-ray diffraction (XRD) and Raman spectroscopy analysis. Films grown via Langmuir deposition from a glass evaporation cell were created in a HV-system and subsequently transferred to an UHV system for analysis. All measurements were performed in the laboratories of Graz University of Technology, except the Raman analysis, which was carried out at Karl-Franzens University Graz.

4.1. The Necessity of Ultra-High-Vacuum

The characterization of a solid surface and possible adsorbate layers on an atomic level implies unambiguously that the surface composition remains essentially unchanged over the duration of the experiment. This essentially means that the rate of arrival of atoms and molecules from the surrounding gas phase needs to be low enough to not influence the surface. Table 4.1 illustrates how important vacuum parameters, such as molecular density, mean free path and monolayer arrival time change with pressure.

Table 4.1.: Changes in molecular density, arrival time, mean free path and monolayer arrival time with decreasing pressure. This example is for nitrogen molecules at room temperature with an assumed sticking coefficient of unity. (from Ref. [77])

Pressure p (Torr)	Molecular density n (cm^{-3})	Arrival rate I (cm^{-2} s^{-1})	Mean free path λ	Monolayer arrival time τ
760	2×10^{19}	3×10^{23}	700 Å	3 ns
1	3×10^{16}	4×10^{20}	50 µm	2 µs
10^{-3}	3×10^{13}	4×10^{17}	5 cm	2 ms
10^{-6}	3×10^{10}	4×10^{14}	50 m	2 s
10^{-9}	3×10^{7}	4×10^{11}	50 km	1 hour

We learn from this table that if one requires clean surfaces for the duration that is needed to perform an experiment (usually about one hour), then the amount of molecules adsorbed on the surface from the gas phase should not exceed the accuracy of current surface sensitive techniques, i.e. a few percent of a monolayer. A vacuum of the order of 10^{-9} Torr or better is required to fit this criterion. In reality and also in this work pressures in the order of 10^{-8} Torr were deemed to be sufficient due to a sticking coefficient of residual gas molecules of lower than unity.

4.2. Description of the UHV system

TDS and AES experiments have been carried out under UHV conditions at base pressures between 10^{-8} and 10^{-9} Torr. A schematic drawing of the UHV chamber is depicted in Fig. 4.1, including details of the pumping system. A rotary pump generates a prevacuum of roughly 10^{-2} Torr, while an adsorption trap prevents any oil regurgitation from contaminating the chamber. Two turbomolecular pumps connected in series generate the ultra-high vacuum and can be sealed from the chamber with a gate valve. The sample is placed in the center of the chamber on a stainless steel sample holder, which is in turn connected to a rotary sample stage. The sample stage can be moved horizontally and also rotated around 360° to access different components. Furthermore, it can be cooled via liquid nitrogen (LN_2) cooling to a temperature of 150 K. A computer-controlled heating stage makes it possible to maintain both a constant sample temperature and a linear heating procedure if required. A second stationary sample holder is available to utilize different deposition mechanisms (Fig. 4.5d). Residual pressures in the chamber are measured with a hot filament ionization gauge.

Two different AES systems have been used over the course of this thesis. The first

system by Varian consisted primarily of a coaxial integral electron gun to generate a primary electron beam with 2 kV beam energy, a cylindrical mirror analyzer and a SEV detector. The analyzer contained two concentric cylindrical electrodes, a dynode electron multiplier, a magnetic shield and a tungsten ribbon filament. Detection sensitivities were usually set to 25-100 μV. The diameter of the focused electron beam was roughly 100 μm. This system was employed during measurements of rubicene (Chap. 6) and indigo (Chap. 7) thin films.

Another system by Staib Instruments was prevalently used during analysis of quinacridone thin films (Chap. 8). The electron source was held at a voltage of 2 kV and featured a filament current I_F of 1.4 A and an emission current I_E of 1.4 μA. The detector voltage was set to 1900 V. For the shown measurements the energy resolution dE was set to 10 eV with a 50 ms dwell time. The Auger beam diameter (ca. 1 mm) was significantly larger than in the first system.[129]

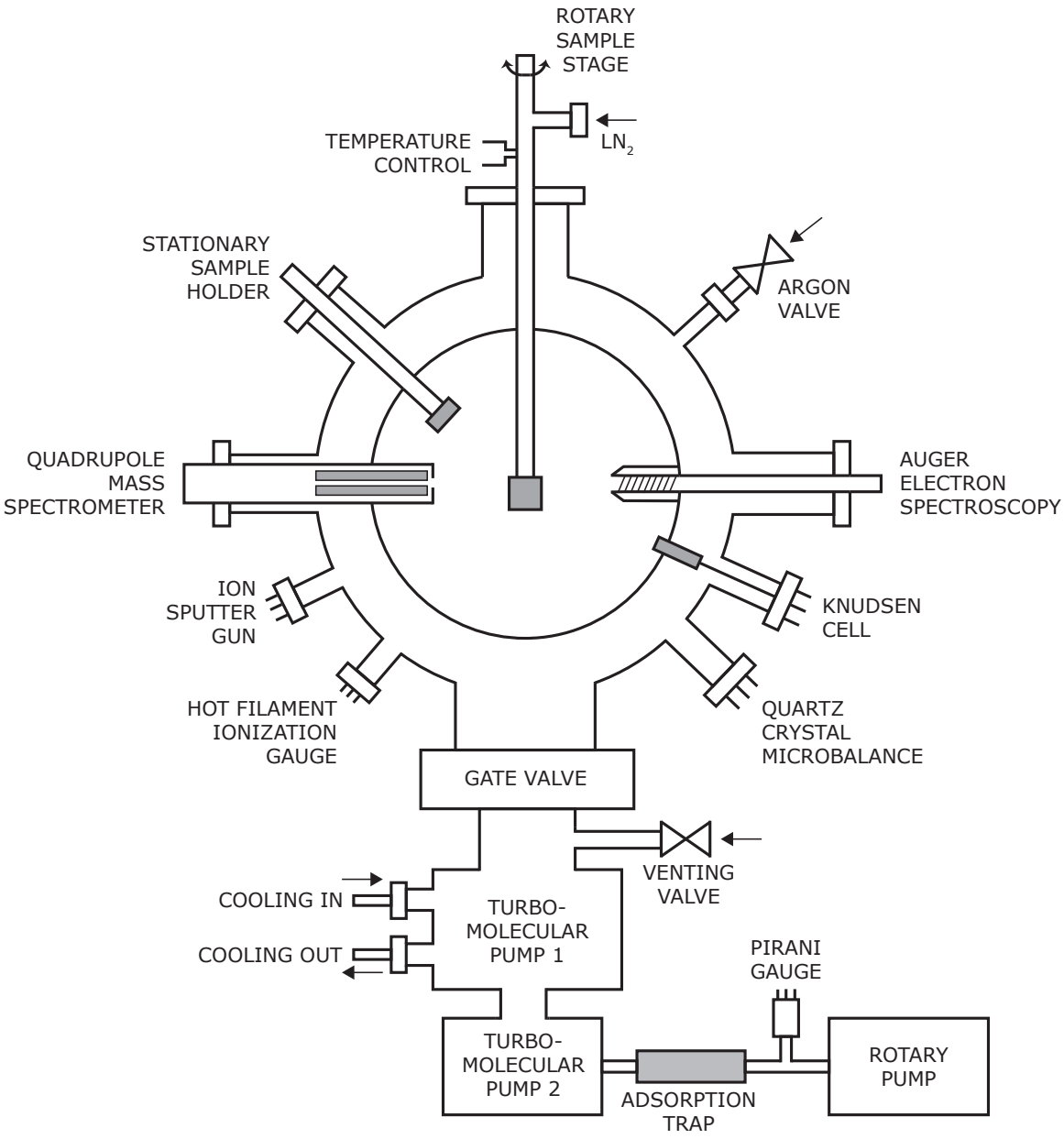

Figure 4.1.: Schematic overview of the experimental setup showing the main components and measurement methods

4.3. Quadrupole Mass Spectrometer

For residual gas analysis and thermal desorption spectroscopy, a quadrupole mass spectrometer (QMS) was used. A schematic overview of its operating principle is shown in Fig. 4.2. In the first section of the spectrometer the incoming gas particles are ionized, just like in a hot-filament ionization gauge. The ions are then accelerated and focused into the second section, the actual mass filter. It consists of four bars which set up an electrical quadrupole field, driven by the superposition of a DC and a radio frequency AC voltage. The filter works such that only ions with the same q/m ratio can pass it. The last element of the spectrometer is the ion detector which contains an electron multiplier. Signals are then plotted in intensity versus q/m ratio (compare Fig. 5.1). The lower limit of partial pressures which can be detected with such an instrument is about 10^{-14} mbar.[130]

Throughout this work, TDS experiments were performed with either a Pfeiffer QMS 200 (1-200 amu range) or a Pfeiffer QMA 400 (1-500 amu range) inline quadrupole mass spectrometer with a cross-beam ion source equipped with a secondary electron multiplier (Faraday) detector. The QMS was set to 2.00 mA emission current with potential differences of 90 V to the cathode and 65 V to the extractor, respectively. Secondary electron multiplier voltages were set to 1600 V for the QMS 200 and 1800 V for the QMA 400 system. According to the manufacturer, unit resolutions (valley, full mass range) for the deployed systems were smaller than 10%.

One should note that a QMS evaluates masses via ion counts per second, therefore the sensitivity will depend on the distance between the desorption source and the QMS sensor. This distance varied slightly throughout all conducted experiments due to slight chances in sample mounting and positioning. Consequently, absolute intensity values of the TDS measurements are not comparable between different measurement series.

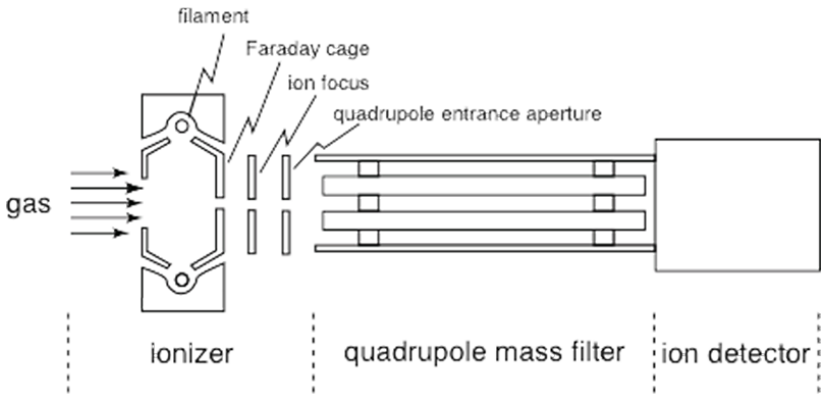

Figure 4.2.: Build-up of a quadrupole mass spectrometer

4.4. Physical Vapor Deposition

A lot of different evaporation cells were utilized for the experiments, all of which can be described via physical vapor deposition theory. The standard stainless steel cell (Fig. 4.5c, schematic overview in Fig. 4.3) uses Knudsens technique [131], namely evaporation occurring as effusion from an isothermal enclosure with a small orifice. The evaporating surface within the enclosure is large compared to the orifice and maintains the equilibrium pressure inside. The diameter of the orifice must be about one-tenth or less of the mean free path of the gas molecules at equilibrium pressure and the wall around must be thin enough so that gas particles leaving the enclosure are not scattered or adsorbed and desorbed by the orifice wall.[132] The cell is surrounded by heating wires and an insulating shielding, while the temperature is being held constant and monitored by a thermocouple. Provided the aperture is small enough, the depositing material will emerge from the cell in a cosine distribution. Other Knudsen-like cells were also used and will be described in details at a later stage. Additionally, Langmuir evaporation was employed, which is simply the isotropic evaporation from a directly heated free solid surface. The main shortage in the latter case are geometrical limitations and the quite unstable deposition rate.

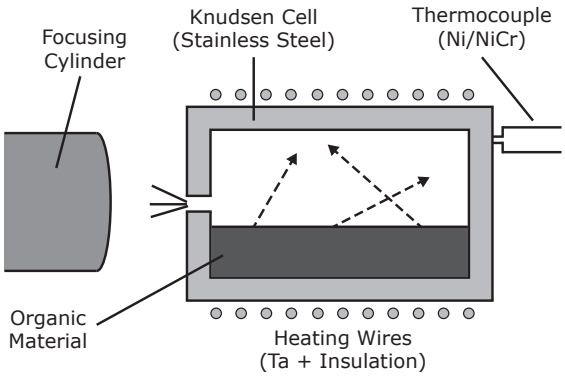

Figure 4.3.: Schematic overview of the Knudsen-type stainless steel evaporation cell. The employed cell featured an inner diameter of 7 mm, a length of 20 mm and an effusion hole diameter of 1 mm.

4.5. Deposition Monitor

Deposition rate and final film thickness are crucial parameters for any deposition process. A quartz crystal thickness monitor is the most prevalent instrument for measuring these

characteristics. This high frequency reference oscillator is especially important for rapid measurements, low deposition rates and low density materials due to its ability to resolve small mass-induced frequency shifts. It consists of an AT-cut quartz crystal which vibrates at an eigenfrequency f_0. This fundamental frequency is not only dependent on the crystal thickness, but also changes upon deposition of foreign layers.[133] The frequency change due to mass accumulation via a foreign layer is thereby indistinguishable from a frequency change that is caused by a layer with the same mass as the crystal (the crystal oscillation has only shear character and is therefore mass independent). The measured frequency change Δf is explained by the Sauerbrey equation [133]

$$\Delta f = -\frac{2f_0^2}{A\sqrt{\rho_q \mu_q}}\Delta m \tag{4.1}$$

with f_0 the quartz frequency (roughly 6 MHz), A the deposition area, ρ_q the density of the quartz crystal (2.643 g/cm^3), μ_q the shear modulus of an AT-cut quartz crystal (2.947 $\times$ 10^{11} g/(cm^2 s)) and Δm the deposition induced mass change. Rewriting the mass change Δm to a thickness change Δd via

$$\Delta m = \rho_a A \Delta d \tag{4.2}$$

with ρ_a the density of the deposited material leads to

$$\Delta d = -\frac{\sqrt{\mu_q \rho_q}}{\rho_a}\frac{\Delta f}{2f_0^2} \tag{4.3}$$

Equation (4.3) can equivalently be written as

$$\boxed{\Delta d = -\frac{\Delta f}{S f_0^2 \rho_a}} \tag{4.4}$$

where various quartz parameters are combined into the so called sensitivity S. S has a value of 2.26 $\times$ 10^{-6} cm^{2}s/g for the used quartz.

Of course this relation is based on a few simple assumptions, most importantly that the crystal receives exactly the same deposition as the substrate and that the sticking coefficient is identical on both surfaces. These assumptions were proven to be accurate enough for the given vacuum system and the used molecules. Additionally, it is important that the sensor temperature does not vary during the measurement, considering that this also induces a frequency change. An illustration of the employed system is shown in Fig. 4.4. The microbalance is coated with gold electrodes and designed to simulate an infinitely extended crystal. Energy of the traveling acoustic wave is not reflected back to the center where it can interfere with other newly launched waves, essentially ensuring the correctness of equation (4.3).[134] No geometry corrections were necessary, since the quartz crystal could

be intermittently placed at the sample position during deposition rate measurements.

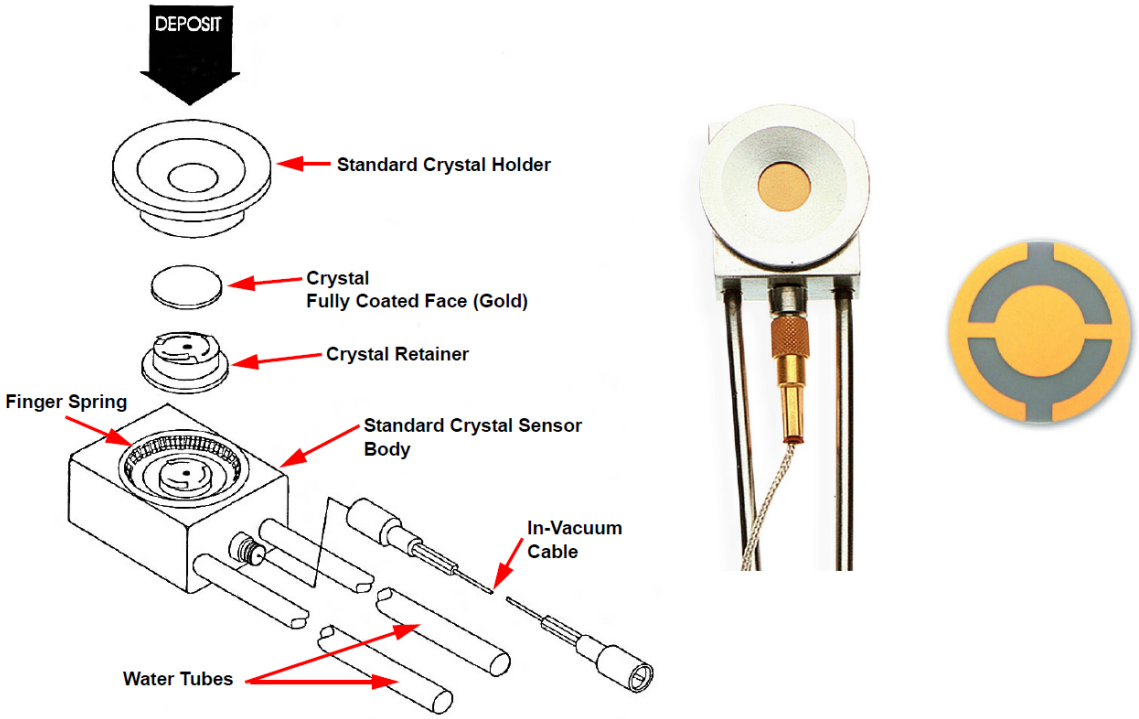

Figure 4.4.: Schematic diagram and photograph of the quartz deposition monitor

4.6. Sample mounting

The 1×1 cm^2 large and 525 µm thick Si/SiO_2 samples from Siegert Wafer (Fig. 4.5b) were mounted onto a stainless steel sample holder (10 mm × 10 mm, 1 mm thick) via four tantalum clamps (see Fig. 4.5a). Attached to the steel plate are two tantalum wires for resistive heating and a Ni/NiCr thermocouple to complete the feedback loop. Attributable to the poor heat conductivity of SiO_2 and the thermal contact resistance between the silicon wafer and the steel plate, a significant temperature lag between the sample surface and the heating plate was observed during the heating process. The measured temperatures on the backside of the steel plate did not represent the temperature on the sample surface properly and therefore the temperature scale had to be corrected. The applied first-order temperature correction will be discussed at a later point.

A second stationary sample holder (Fig. 4.5d) consisted of a stainless steel plate with four identical Ta mounting clamps. Samples that were installed with this setup could not be heated or cooled and neither a temperature measurement nor a sputter-cleaning process were possible. This setup was used during quinacridone measurements to desorb and subsequently

re-adsorb specific molecular phases from one sample to another. It will be explained in detail at a later stage.

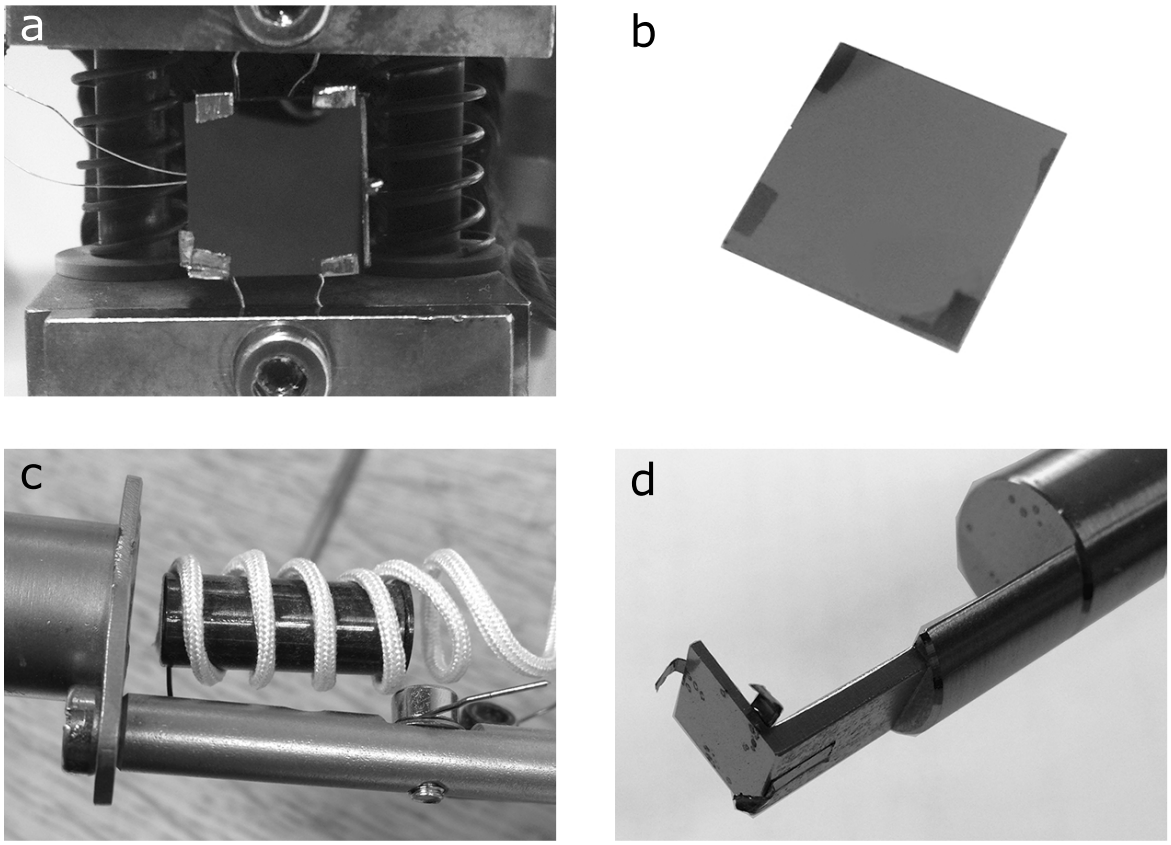

Figure 4.5.: Photographs of some of the used UHV components

(a) Sample stage with two Ta wires for resistive heating, a Ni/NiCr thermocouple to the side and four Ta clamps that mount the sample onto a stainless steel backplate

(b) Typical 1x1 cm^2 Si/SiO_2 sample with a thin organic film grown on top. The unexposed area under the mounting clamps is clearly visible.

(c) The metal Knudsen cell that was typically used for physical vapor deposition wrapped in electrically insulated Ta resistive heating wires

(d) Stationary sample holder with four Ta mounting clamps

4.7. Ion Sputtering

Carbonaceous contamination layers can be sputtered off together with the substrate top layers by bombardment of the surface with Ar^+ ions. To produce an ion beam, argon gas was admitted through a leak valve directly into the UHV chamber (Ar pressure: 5×10^{-5} Torr). Ionization of the gas atoms proceeded via electron impact in the ionizer of the ion gun. The produced ions were then accelerated to the desired energy (1-1.5 keV) and directed towards the sample. Ion sputtering is a very effective cleaning technique with the side effect of a degradation of the surface structure. The SiO_2 substrate is significantly more stable than any organic overlayers, although it is affected by decomposition processes as well. Hofman *et al.* [135] have shown that bond reorientations happen in SiO_2 upon ion sputtering, while Hattori *et al.* [136] proved a preferential sputtering of the more volatile oxygen atoms, resulting in a metal enriched surface. The conclusions were not affected by the initial contamination of the oxide film. It is believed that two mechanisms occur during ion bombardment: surface reduction to elemental Si due to preferential sputtering of oxygen and bond distortion as well as strain within the ion penetration length. The reduced surface layer has a thickness of the order of the Si-O bond length.[137]

However, sputter times prior to all experiments in this thesis were usually 10 min and did not exceed 20 min. It is therefore assumed that all organic contaminations were etched away within this period while the underlying silicon dioxide structure remained mostly unchanged.

4.8. Sample Preparation

All samples (10.0 × 10.0 mm ± 0.1 mm) were cut from a single 100 ± 0.3 mm large B-doped (p-type) wafer (Siegert wafer). Prior to installation into the UHV chamber a chemical cleaning procedure was performed. The samples were dropped in toluol (C_7H_8) and left in an ultrasonic bath for 16 minutes. Subsequently, any remaining toluol residue was cleared with pressurized CO_2 gas. Cleaning processes involving pressurized CO_2 beams are considered very efficient in literature and show no evidence of residues or chemical reactions on the cleaned surfaces.[138] An AFM image of a chemically cleaned sample (Fig. 4.7a) showed no visible contamination and a mean roughness of 0.16 nm. However, SiO_2 has a roughness close to the AFMs resolution limit and is therefore difficult to image.

Upon installation, the sample featured a clear carbon peak in the Auger spectrum (Fig. 4.8). This remaining amount of contamination was removed by one-time heating to 800 K followed by Ar^+ sputtering until no carbon signal could be observed anymore. Fig. 4.9 shows different Auger signals which were measured on a similar UHV apparatus and with an identical sputter setup than the one employed in this thesis. It clearly demonstrates the

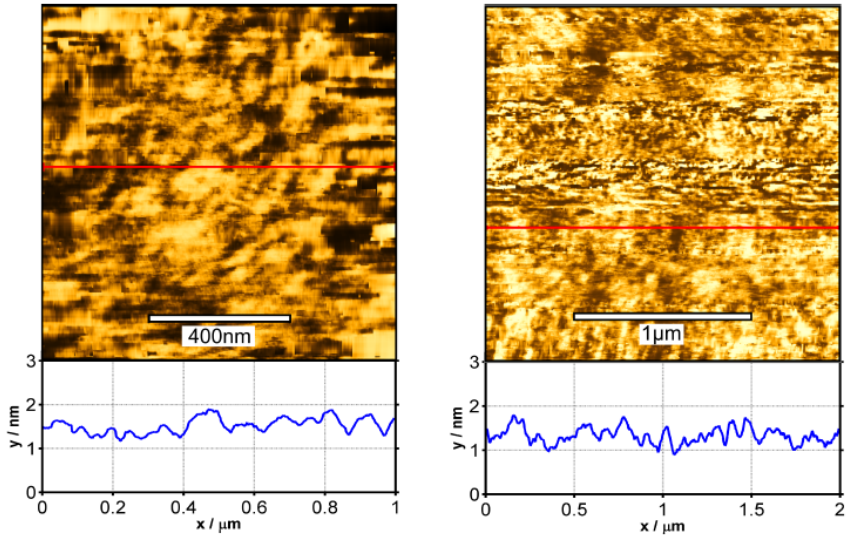

(a) $R_a = 0.16\,\mathrm{nm}$ (b) $R_a = 0.20\,\mathrm{nm}$

Figure 4.7.: AFM topography images of untreated SiO_2 (a) and after 30 min sputter cleaning (b) with corresponding roughness values (from Ref. [139])

sufficiency of a 10 minute sputter period for the removal of any kind of carbon residue, either after installation into the vacuum system or after a thermal desorption cycle.

A sputtered sample is indistinguishable from a non-sputtered sample under the atomic force microscope (Fig. 4.7b), although this might be due to the fact that additional carbon may have deposited once more on the sample upon exposure to ambient conditions. I want to note at this point, that both images contain measurement artifacts which artificially increase the roughness value. It is therefore hard to verify a surface roughening due to sputter-cleaning which is, if present at all, marginal. Another indication for little influence by sputter-cleaning on SiO_2 is observed when performing intense longtime sputtering, yielding an almost unchanged SiO_2 layer.[139]

Up to now, only few attempts have been made to quantify the exact level and consistency of carbonaceous contaminations on SiO_2. Seah and Spencer [141] conducted both a theoretical and experimental evaluation of the environmental carbonaceous contamination that builds up on surfaces and found that their data agreed considerably well with data from average polymers (saturated hydrocarbons) and deviated from measurements on glassy carbon. In general small carbon films on SiO_2 appear to be well described by an average polymer layer with thicknesses between 0.5 and 2 nm [142] and a binding energy of the C_{1S} electrons of 285.0 eV.[143]

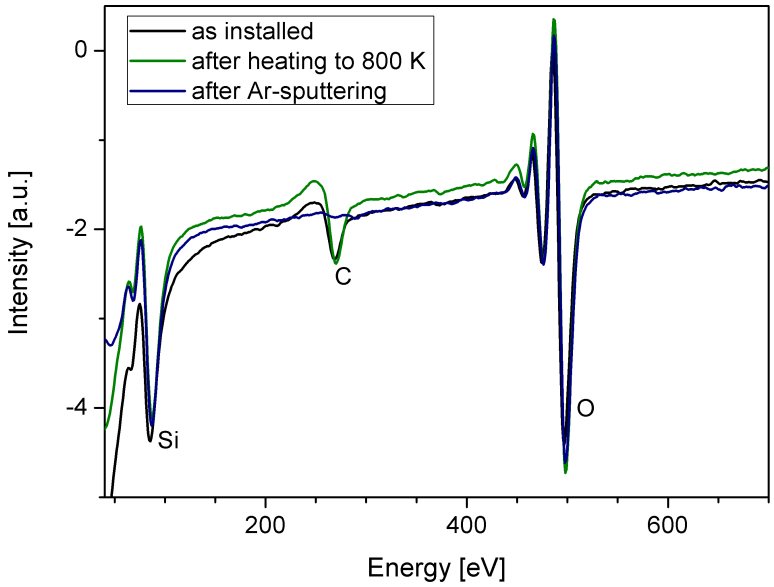

Figure 4.8.: Auger Electron Spectra of SiO_2 immediately after installation (black), after heating to 800 K (green) and following the sputter process (blue)

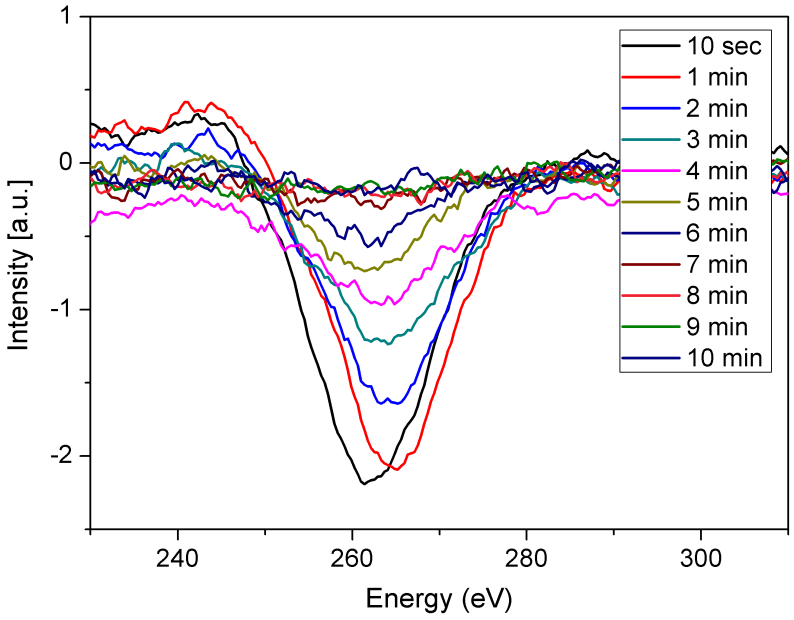

Figure 4.9.: Decrease of the carbon AES-signal after deposition of 4 nm pentacene and subsequent thermal desorption up to 800 K with increasing sputter time [140]

4.9. Ex-Situ Setup

Specular X-ray diffraction (SXRD) measurements have been performed in the laboratories of Graz University of Technology on two different diffractometers. First, indigo samples were analyzed with a SIEMENS D501 diffractometer using the radiation of a sealed copper tube. X-ray diffraction pole figures were collected with a Philips X'Pert system equipped with an ATC3 cradle, using the radiation of a chromium tube. In both cases a Bragg-Brentano focusing geometry was used in combination with a flat graphite monochromator at the secondary site. Additionally, a PANalytical EMPYREAN diffractometer fitted with a Cu sealed tube and a multilayer mirror (λ = 1.54 Å) on the primary side was used for quinacridone and epindolidione XRD analysis. The secondary side was equipped with a slit system and intensities were recorded using a PANalaytical PIXCcel detector in 1D mode. A photograph of the setup can be seen in Fig. 4.10.

Grazing incidence X-ray diffraction (GIXD) measurements were conducted at the KMC-2 beamline at BESSY II (Berlin, Germany) using X-rays with a wavelength of 1.00 Å and a 2D cross-wire detector (BRUKER).[144] An incident angle of $\alpha_i = 0.13°$ was chosen to enhance the scattered intensities of the adsorbate. Reciprocal space maps were calculated with the xrayutilities library for Python.[145]

The micro-Raman experiments in Chap. 8 and Chap. 9 were performed at Karl-Franzens University Graz with a HeCd-laser excitation wavelength of 325 nm on a LABRAM HR-800 (HORIBA Jobin Yvon) Raman-spectrometer using gratings of 2400 lines/mm and providing a spectral resolution of 3.92 cm^{-1}. As detection system a liquid nitrogen cooled CCD-Spectrometer was used.

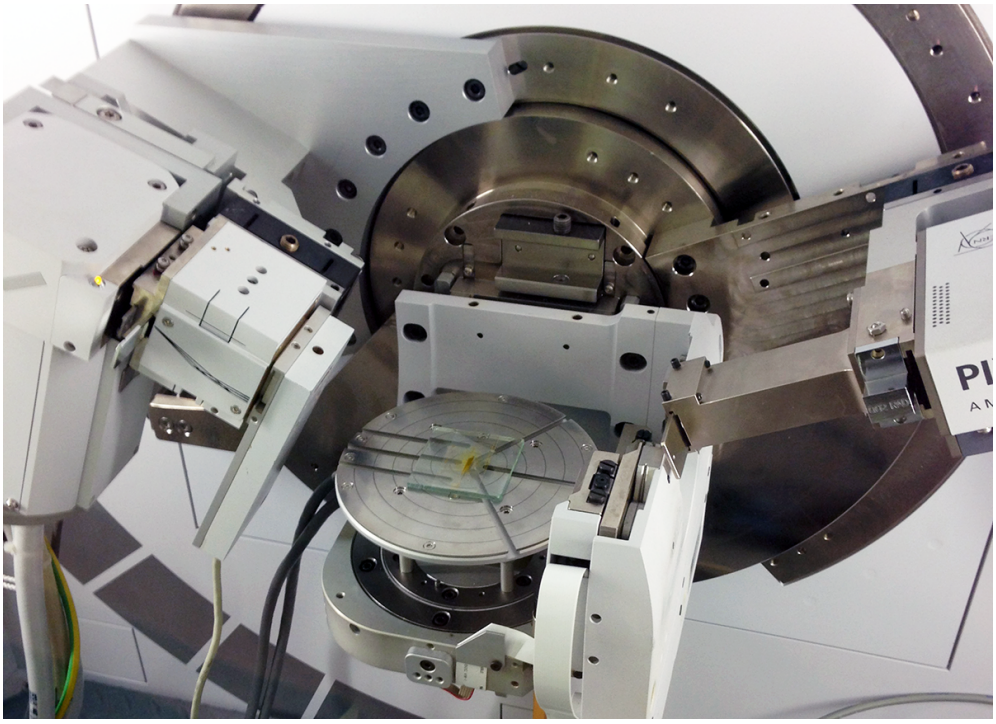

Figure 4.10.: Photograph of the PANalytical EMPYREAN diffractometer during a XRD powder measurement

Part II.

Experimental Results

5 | General Results

5.1. Residual Gas Spectrum

As already mentioned in the introduction, the pressure and residual gas composition of an UHV system is immensely important to achieve the desired thin film formation. Mean free path and consequentially the thin film quality and impurity level are directly dependent on the pressure level of the vacuum chamber, which needs to be precisely controlled and monitored to ensure the growth of reproducible films of sufficient quality. When looking at a residual gas spectrum, it is important to note that the criterion for rest gas molecules to pass the mass spectrometer is the right q/m and not simply the right mass m. This means that doubly charged ions appear as particles with half the mass in the spectrum. CO does for example not only give a peak at m/z=28 but also one at m/z=14 due to double ionization. The gases are also dissociated in the spectrometer such that one does not only find one peak for single-ionized water at m/z=18 but also peaks at m/z=16, 17 and 2 for its fragments. This molecular dissociation is even more prominent for larger organic molecules, leading to cracking patterns with a multitude of cracking masses (e.g. [146]).

Without any bakeout, the pressure of a vacuum system is usually dominated by a high partial pressure of water. After the bakeout of the system, this will be strongly reduced and the total pressure will be determined by CO and hydrogen.[130] Additional pressure decrease may be achieved via liquid nitrogen or liquid helium cooling. If there is an air leak in the system this would show up mainly as peaks of 28 (N_2) and 32 (O_2). The trouble, however, is that a peak at 28 is always present due to CO and a small peak of 32 might even be present in a leak-tight chamber.

A mass spectrum of the residual gas present in the evacuated chamber of the employed

UHV setup (pressure about 10^{-9} Torr) is shown in Fig. 5.1. One can see that this spectrum differs from a typical residual gas spectrum. This is attributable to a history of many years of physical vapor deposition of large organic molecules and the resulting hydrocarbonic residue at the inner walls of the vacuum chamber. However, residue levels are so small that any influence on thin film evaporation and growth can be eliminated.

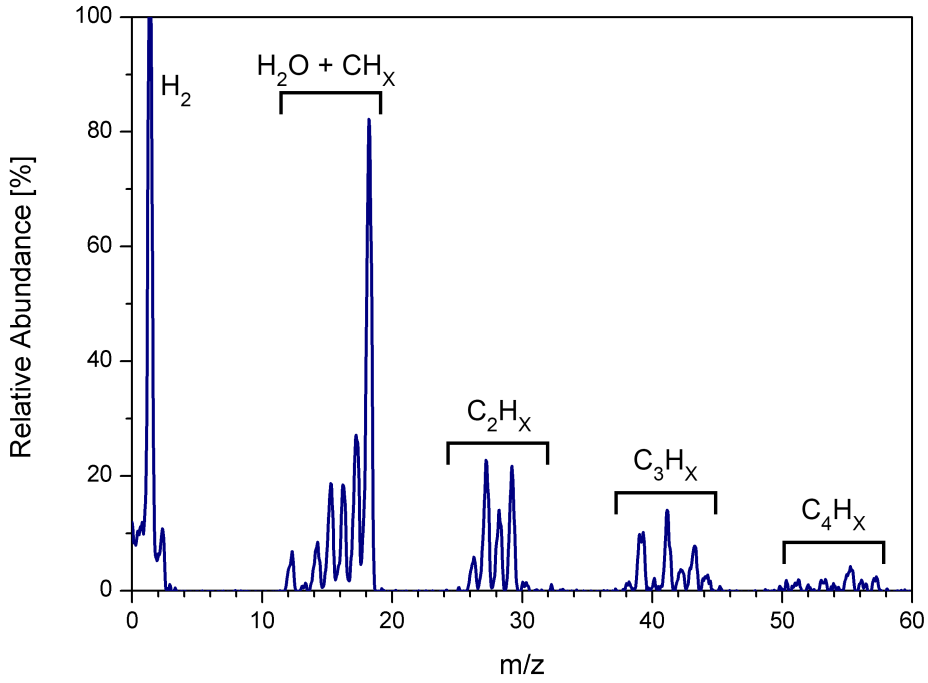

Figure 5.1.: Residual gas spectrum measured at 10^{-9} Torr with H_2, H_2O and various hydrocarbon peaks

5.2. Reproducibility and Sensitivity

Resolution and reproducibility are two fundamentally important parameters that directly determine the reliability and validity of experimental results. Both parameters were tested in the employed QMS detection system via repeated adsorption and subsequent desorption of roughly 0.85 Å thick indigo films, as it is shown in Fig. 5.2. One is clearly able to distinguish the desorption signal from the background noise for the shown material deposition of less than one Ångström. Furthermore, repeating the experiment leads to almost identical curve progressions, illustrating how the QMS detection system shows both very high repeatability and reproducibility, even for exceedingly low film thicknesses.

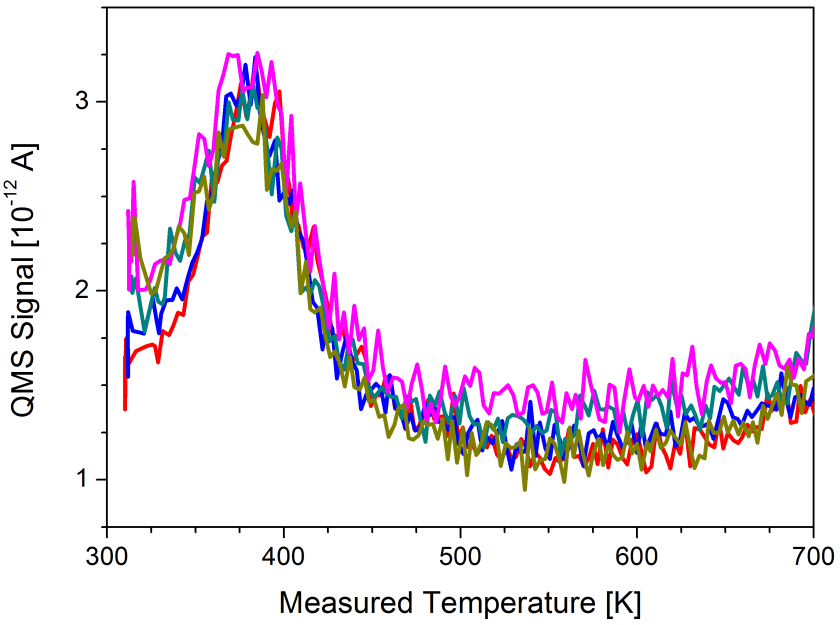

Figure 5.2.: Demonstration of reproducibility and QMS resolution in the example of repeated adsorption and subsequent desorption of 0.85 Å thick indigo films at room temperature

5.3. Carbon covered Substrates

As it was already briefly mentioned in chapter 1.2 and shown in Fig. 1.1, substrates with carbon residue on top were used for a number of adsorption and desorption experiments. The samples in question were initially sputter cleaned after their installation into the UHV system and subsequently underwent multiple adsorption and desorption cycles without any sputter procedures in-between. The procedure was repeated until a stable carbon signal in the AES spectrum was reached (see Fig. 5.3). However, it cannot be completely ruled out that the carbon layer changes even after this point, the only thing that can be said for sure is that the Auger signal remains constant once a certain number of adsorption and desorption cycles is reached. The accumulated carbon forms either island structures or only a single wetting layer on the surface, due to the fact that both the silicon and the oxygen Auger peaks are clearly visible, even after multiple adsorption and desorption cycles. When also taking AFM measurements into account, the former seems to be more likely as multiple small islands are visible on the substrate surfaces.

Depending on the molecule employed in the Knudsen cell at that time, it is however possible that the carbon residue may vary in shape and thickness. Especially for quinacridone a peculiar situation was found as a fixed amount of carbon remained on the surface after every desorption cycle, independent of previous sample treatment. Figure 5.4 shows a 4×4 µm AFM micrograph of a SiO_2 substrate that experienced a very high number (50+) of thermal desorption cycles. Carbon islands reach up to 50 nm height in this case with a mean height of at least 10 nm. This argument is backed up by sticking coefficient evaluations that will be shown at a later point in this work (see chapter 8.7).

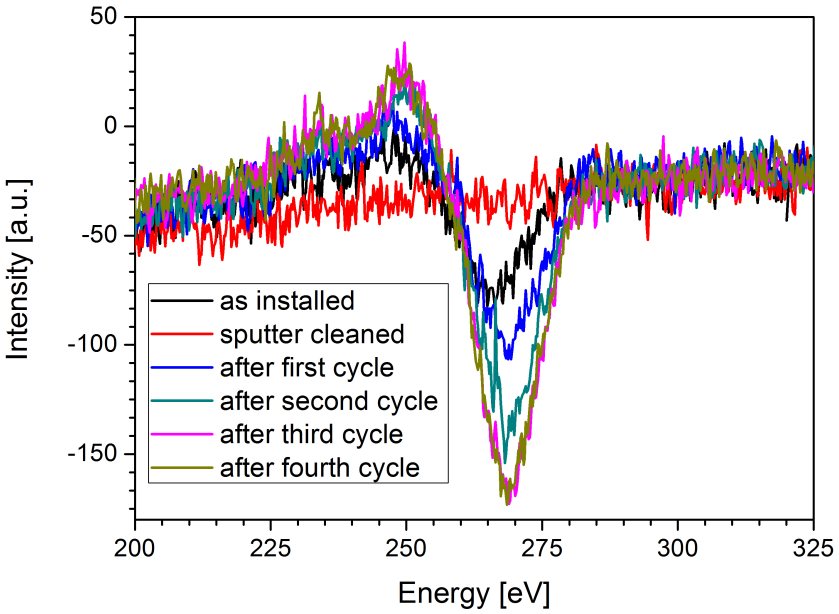

Figure 5.3.: Changes in the carbon Auger signal upon repeated adsorption and desorption cycles of 8.5 nm thick quinacridone films after an initial sputter process

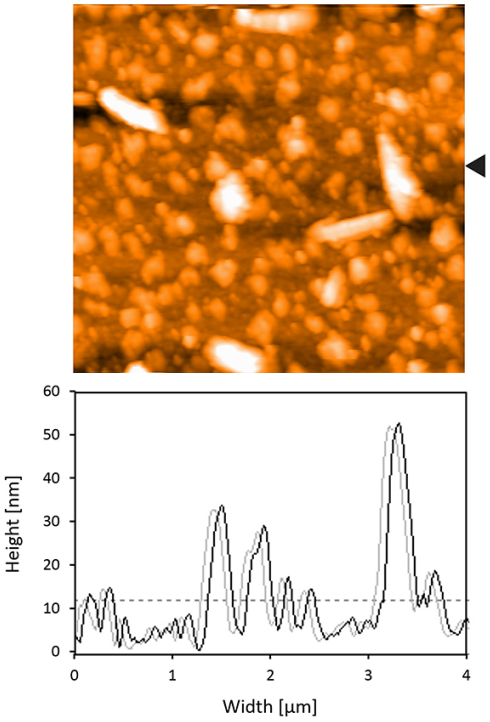

Figure 5.4.: AFM image of a thick carbon layer created after a multitude of quinacridone adsorption / desorption cycles

6 | Rubicene

6.1. Introduction

Rubicene (RU, $C_{26}H_{14}$, see Fig. 6.1) is a polycylic hydrocarbon consisting of five benzene rings with three linearly fused rings and one benzene ring at each diagonal side. It is a stiff and planar semiconducting molecule with a molecular weight of 326.4 amu, a density of 1.392 g/cm^3 , and a melting point of 581 K. Interestingly, this material is poorly investigated and only a limited amount of publications are available (e.g. [147]). So far nothing is known about the crystallography of condensed rubicene and the formation of rubicene thin films. One important aspect is that rubicene films can be produced both from solution and by thermal evaporation under vacuum conditions. In order to investigate initial steps of film formation, adsorption as well as desorption characteristics of rubicene on/from silicon dioxide, high purity single crystals were first prepared from solution for their structural identification and then used to grow thin films via physical vapor deposition under ultra-high vacuum conditions. These films were subsequently analyzed in-situ with TDS and AES and ex-situ with AFM, which was additionally used to monitor thermal and air stability of the ultra-thin films.[1]

[1] As mentioned in section 1.4, large parts of this chapter emanate from a publication (Paper I, Ref. [57]) to which I have contributed as the leading author. For reasons of legibility I will avoid constant citation of this work in the following sections.

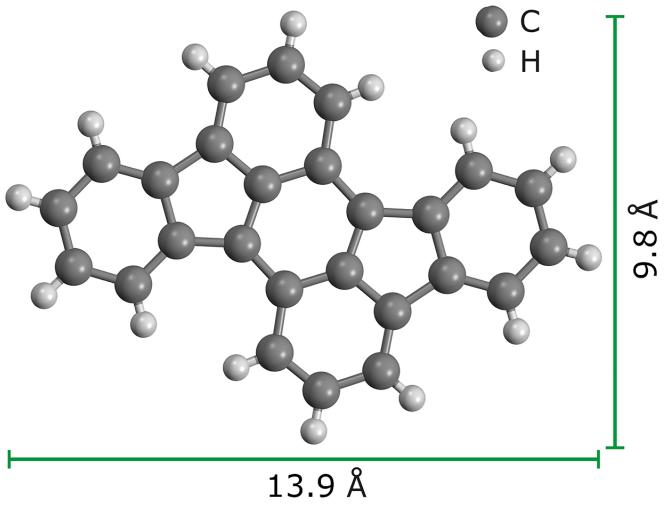

Figure 6.1.: Structure and van der Waals dimensions of the rubicene molecule [57, 148]

6.2. Purification

The rubicene starting material was purchased from Acros Organics having a purity of 98%. A quantity of about 1.4 g of the purchased powder was firstly purified by an Argon gas transport sublimation technique under laminar gas flow. Subsequently, a quantity of about 1 g of the firstly purified rubicene was purified in a second purification procedure by the same Argon gas transport sublimation technique resulting in highly pure rubicene powder.

6.3. Single Crystal Structure

So far no structural characterization for rubicene single crystals existed in the literature. Single crystal XRD characterizations and crystal structure calculations, which were carried out at different temperatures by earlier members of the work group (see supporting information in Ref. [57]), revealed a monoclinic crystal system with a primitive monoclinic Bravais lattice (space group $P2_1/n$). Figure 6.2 depicts the package of the molecules in the rubicene crystal. Within the asymmetric unit of rubicene two crystallographically independent molecular units were found. Each represents the half of a rubicene molecule and is located around a center of symmetry. Thus, the unit cell contains four rubicene units and the density calculates to $\rho = 1.381$ g/cm^3. This in in good agreement with literature data.[149] The molecules are stacked along the b-axis of the unit cell forming rubicene piles, which are held together by π-stacking interactions (Fig. 6.3). The distances between the individual molecules (333.1 pm and 334.7 pm at 100 K and 336.2 pm and 338.6 pm at 250 K) are in

the same range like e.g. in the crystal structure of graphene (interlayer distance: 335 pm). The rubicene stacks of different molecules form a fishbone-like arrangement (Fig. 6.4). The observed molecular packing is typical for aromatic molecules with disc-like shape.[150]

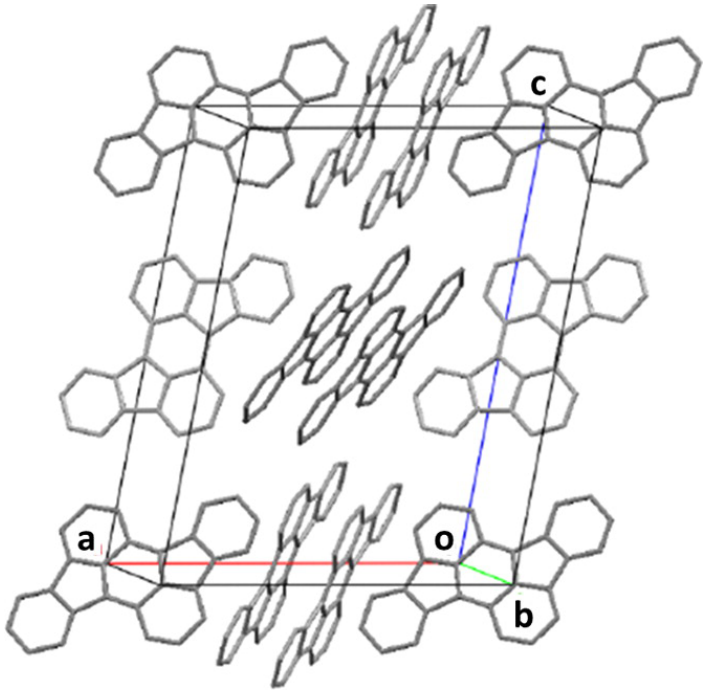

Figure 6.2.: Package of the molecules in the rubicene crystal, together with the crystal unit cell. The Bravais lattice is primitive monoclinic. The basis consists of 4 molecules, arranged in a parallel stacking structure.

Unit cell calculations yielded values of $a = 15.98$ Å, $b = 5.11$ Å, $c = 19.06$ Å and $\beta = 97.26°$ at 100 K and $a = 16.16$ Å, $b = 5.12$ Å, $c = 19.11$ Å and $\beta = 97.22°$ at 250 K, which are in good agreement with literature data.[61] Fractional atomic coordinates, isotropic or equivalent isotropic displacement parameters, selected geometric parameters and bond angles for both temperatures can be found in reference [57]. Since the structural results were almost identical for both temperatures, neither a phase transition nor a significant change in the crystal structure occurs in the temperature range between 100 K and 250 K. The crystallographic data for the structures have also been deposited with the Cambridge Crystallographic Data Centre.[151]

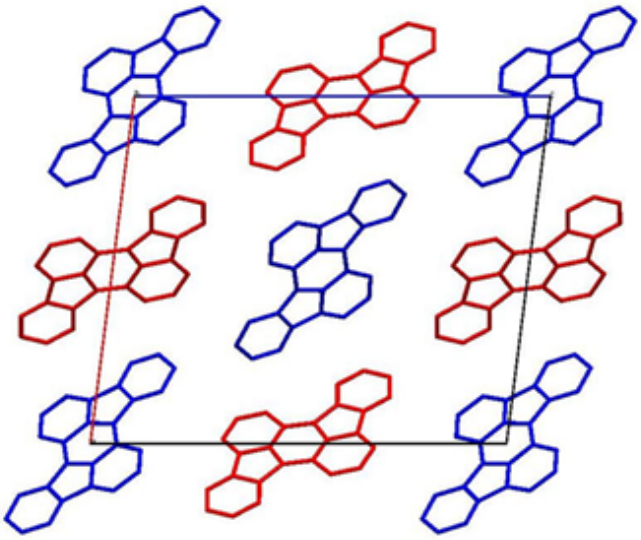

Figure 6.3.: Projection of the rubicene crystal structure along [010]. The molecules 1 are shown in blue color, the molecules 2 in red. The rubicene units pile up along [010] and form molecular stacks connected by π-stacking interactions.

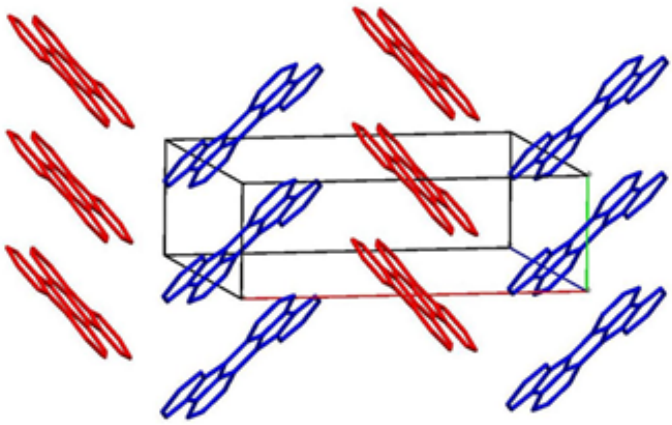

Figure 6.4.: Stacks of rubicene molecules form a fishbone-like stacking pattern with angles between the two different molecular units of 82.83° at 100K and 83.65° at 250 K.

6.4. Thermal Desorption Spectroscopy

As outlined above, thermal desorption spectroscopy can be applied to delineate the kinetics of adsorption and desorption of particles on and from substrates. In Fig. 6.5a-c desorption spectra of rubicene from silicon dioxide after different exposed amounts at 220 K are depicted. In this particular case the substrate surface was covered with a carbon layer, as described in section 5.3. For better visibility the spectra are plotted in three different figures for different coverage regimes. The exposed amounts of rubicene are described by the frequency changes of a quartz microbalance, which was positioned at the place of the substrate before the actual deposition at the substrate (see section 4.5). For rubicene a frequency change of 1 Hz equals a mean thickness change of 0.9 Å of deposited material. It should be emphasized at this point that the deposited amount equals the exposed amount only if the sticking coefficient is one. We will show below that this is not the case for rubicene on silicon dioxide in the low coverage regime.

In Fig. 6.5a a series of spectra for exposures between 2 Hz and 42 Hz are compiled. For very low exposure (2 Hz – 12 Hz) only a single peak is observed, designated as α-peak, which shifts to higher temperatures with increasing adsorbed amount. Above 12 Hz this peak increases further and shifts to even higher temperatures, but a second peak at approximately 30 K higher temperature, designated as β-peak, appears at the same time. With further coverage increase (Fig. 6.5b) the α-peak starts to decrease, while the β-peak still increases (42 Hz – 67 Hz). Finally, with even further coverage increase (50 Hz – 118 Hz) the α-peak totally disappears and the β-peak continues to increase with a common leading edge (Fig. 6.5c).

In order to interpret the specific behavior of the desorption spectra the actual amount of adsorbed/desorbed material needs to be determined. For this purpose the areas of the individual desorption spectra, which are proportional to the adsorbed/desorbed amount, were plotted versus the exposed amount as measured by the quartz microbalance (Fig. 6.6). The most remarkable result of this presentation is the increasing slope with increasing adsorbed amount. This means that the sticking coefficient for rubicene increases with increasing coverage. Usually, it is assumed that the initial sticking coefficient of organic molecules at and below room temperature is one.[152, 153] Apparently, this is not the case for the adsorption of rubicene on silicon dioxide. If we assume that the maximum slope (α_2) in Fig. 6.6 is close to one, the initial slope (α_1) is about 0.25. Considering this sticking coefficient we can convert the exposure values, given in Hz, into values for the adsorbed amount, described by the mean thickness (Å).

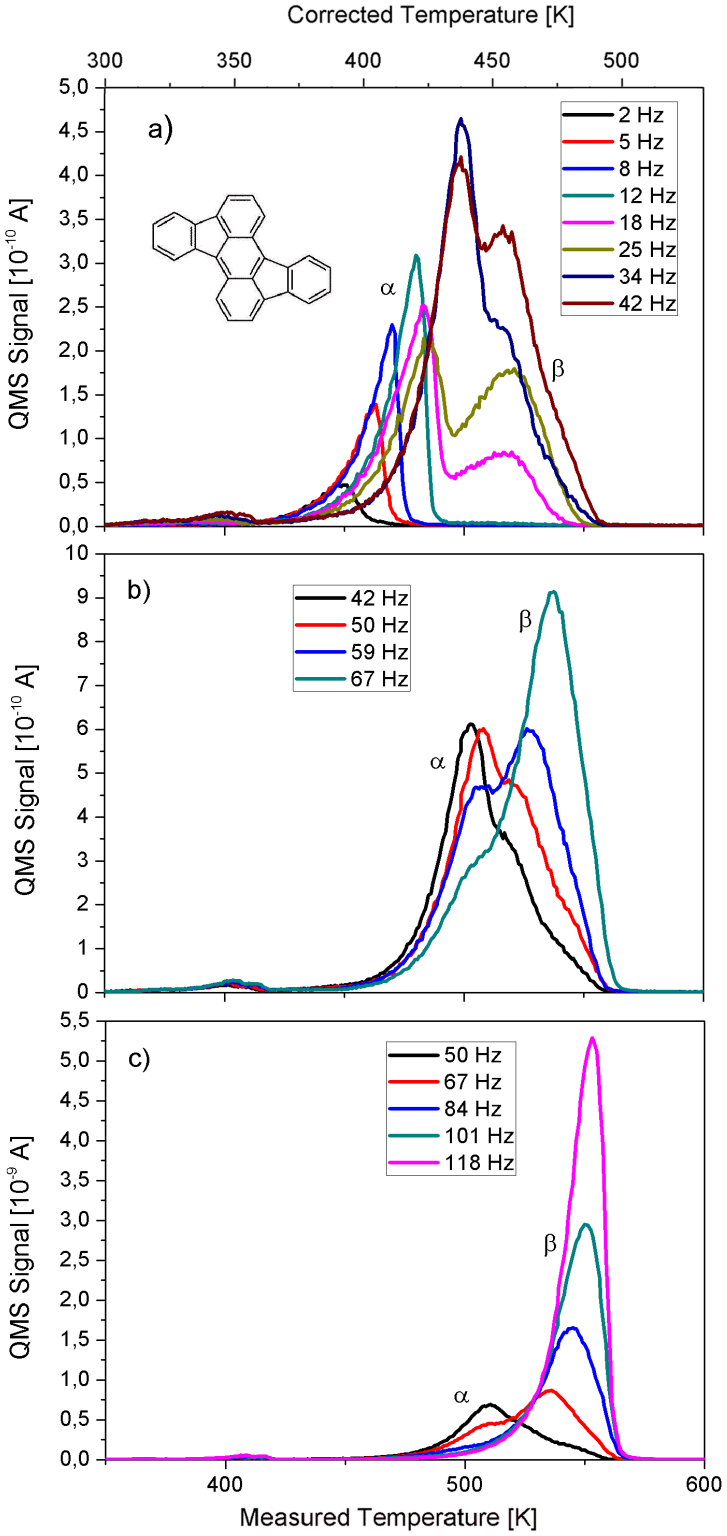

Figure 6.5.: Thermal desorption spectra of rubicene from carbon covered silicon dioxide for different exposures. Adsorption temperature T_{ad} = 220 K. Heating rate β_H = 1 K/s. The exposure is given in Hz, as determined by a quartz microbalance.

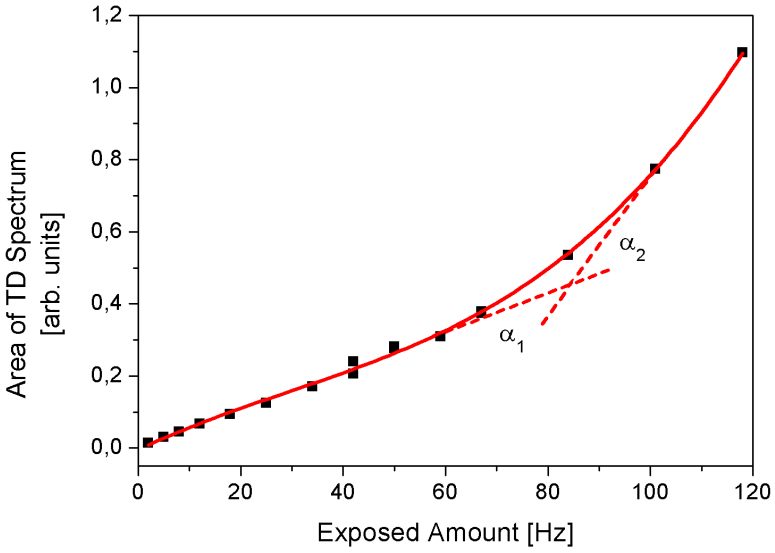

Figure 6.6.: TDS area for rubicene desorbed from carbon covered silicon dioxide as a function of the exposed amount, as measured by the quartz microbalance. Adsorption temperature: 220 K.

6.5. Influence of Surface Cleanliness

In order to check the influence of surface cleanliness on the adsorption behavior adsorption/desorption experiments on a silicon dioxide surface, which was cleaned by argon sputtering before each rubicene deposition, have been performed. A set of thermal desorption spectra is shown in Fig. 6.7. The result is similar to that on the carbon contaminated substrate. First, a single peak (α) at low temperature appears until at about 14 Hz a second peak (β) at higher temperatures starts to grow. The α-peak grows further to about double intensity, before it starts to decrease and finally disappears completely, whereas the β-peak continues to grow with exposure. The corresponding relationship between exposure and adsorbed amount is depicted in Fig. 6.8. Again, the slope of the coverage curve increases with increasing coverage. Assuming a slope of one in the high coverage regime yields an initial slope (initial sticking coefficient) of about 0.17. This is within the experimental error similar to that on the carbon covered substrate.

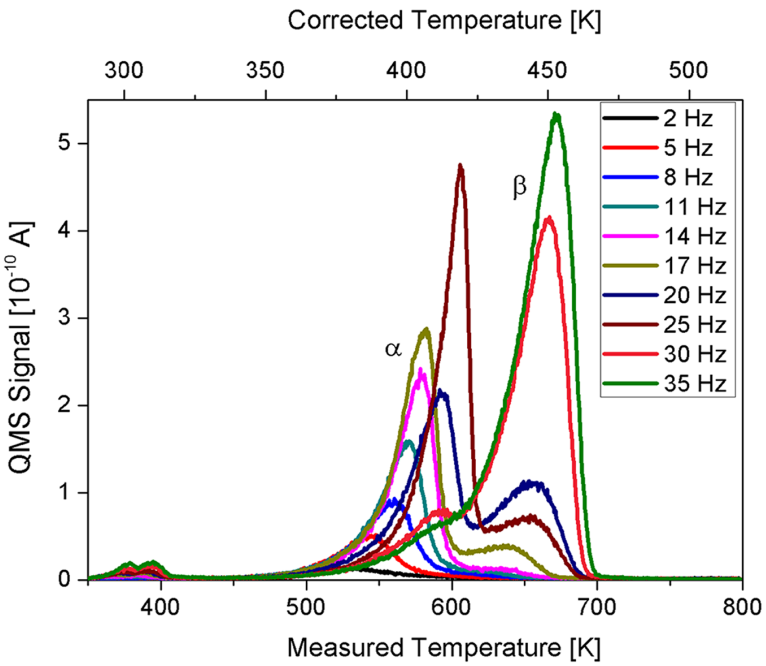

Figure 6.7.: Thermal desorption spectra of rubicene from sputter cleaned silicon dioxide for different exposures. Adsorption temperature T_{ad} = 220 K. Heating rate β_H = 1 K/s. The exposure is given in Hz, as determined by a quartz microbalance.

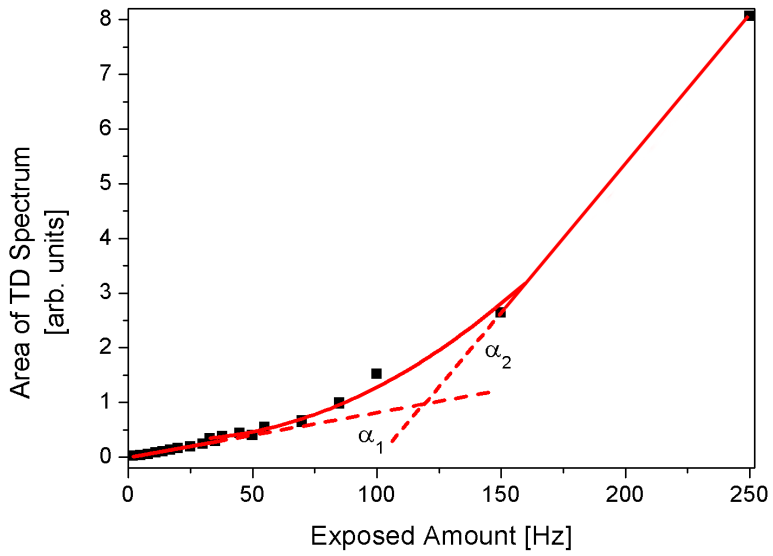

Figure 6.8.: TDS area for rubicene desorbed from sputter cleaned silicon dioxide as a function of the exposed amount, as measured by the quartz microbalance. Adsorption temperature: 220 K.

6.6. Temperature Correction and Heat of Evaporation Calculations

The desorption spectra for high rubicene coverage (Fig. 6.5c) show close to zero order desorption kinetics. From such spectra one can deduce the desorption energy, equivalent to the heat of evaporation. Unfortunately, as it is extensively described in section 4.6, the exact temperature of the substrate surface is not known, due to poor heat conductivity between the oxidized silicon wafer and the stainless steel heating plate. In order to obtain a reliable value for the heat of evaporation rubicene was adsorbed/desorbed directly on/from the steel plate sample holder, where the temperature is measured with the thermocouple. A corresponding desorption spectrum for an exposure of 100 Hz shows a peak maximum (T_p^{SS}) at about 390 K (Fig. 6.9). A comparison with Fig. 6.5a-c clearly shows the multilayer desorption peak from the silicon dioxide surface for 101 Hz exposure at 550 K (T_p^{Si}, see Fig. 6.5) and has therefore an error of 160 K. However, one can observe in that spectra a small peak at the true desorption temperature of 390 K, which stems from desorption from the tantalum foils, which are used to clamp the silicon wafer to the steel plate sample holder. Thus, it is possible to correct the temperature scale by assuming that at the adsorption temperature (T_{ad}), both the steel plate and the Si-wafer are at the same temperature, and that the temperature lag during heating shows a linear dependence. The correction formula then reads:

$$T_{corr} = T_{ad} + \left(\frac{T_p^{SS} - T_{ad}}{T_p^{Si} - T_0} \right) (T - T_{ad}) \tag{6.1}$$

Considering this correction, one obtains an easy way to calculate desorption energies and frequency factors.

The plot $\ln(R)$ vs $1/T$ for the corrected multilayer spectrum (101 Hz in Fig. 6.5) is shown in Fig. 6.10. Using equation (2.9) on page 22, this leads to a desorption energy of 1.47 eV from the slope and a frequency factor of $3{\times}10^{18}$ s^{-1} from the intercept with the y-axis. For the multilayer surface density the molecule density of the (001) plane of rubicene with a value of $2.4{\times}10^{14}$ molecules/cm^2 was used. The evaluation of the 12 Hz monolayer spectrum in Fig. 6.5a, assuming first order desorption (see eq. (2.8)), is shown in Fig. 6.11, and yields a desorption energy of 1.25 eV and a frequency factor of $3{\times}10^{16}$ s^{-1}. For this evaluation the monolayer density of flat lying rubicene molecules ($8.9{\times}10^{13}$ molecules/cm^2) was used. Repeating these calculations for the direct zero order desorption from the steel plate (Fig. 6.9) leads to a heat of evaporation of 1.49 eV. The discrepancy of about 18% between the desorption energy for rubicene as obtained on the SiO_2 surface and the stainless steel surface can be attributed to the poor temperature correction.

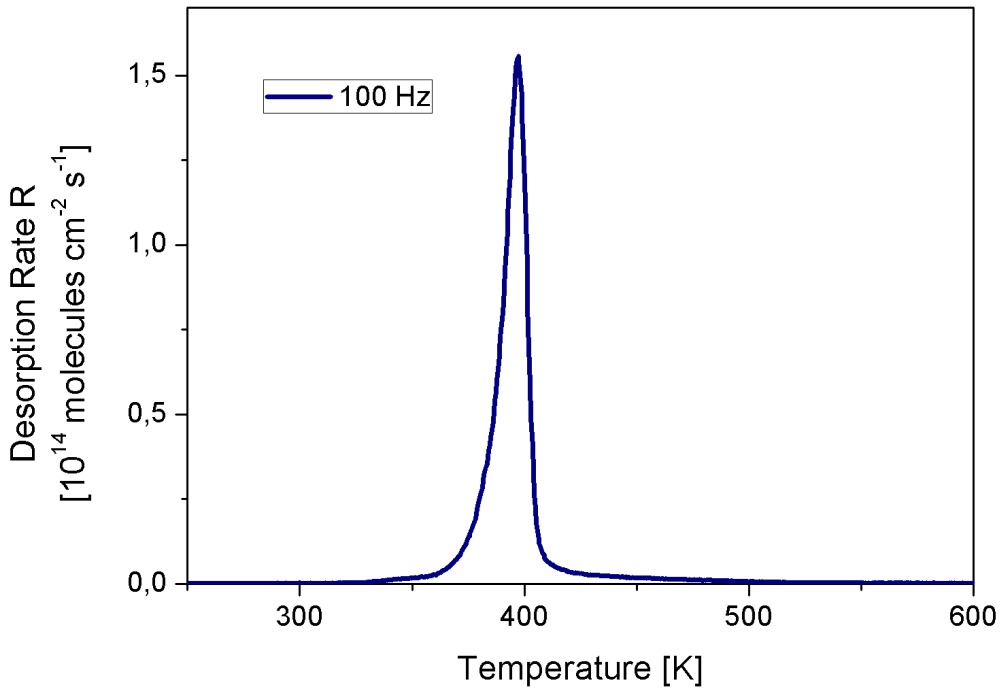

Figure 6.9.: Thermal desorption spectrum of rubicene from stainless steel after an exposure of 100 Hz equivalents. Adsorption temperature $T_{ad} = 220$ K. Heating rate $\beta_H = 1$ K/s. The peak maxiumum of this multilayer is at 390 K.

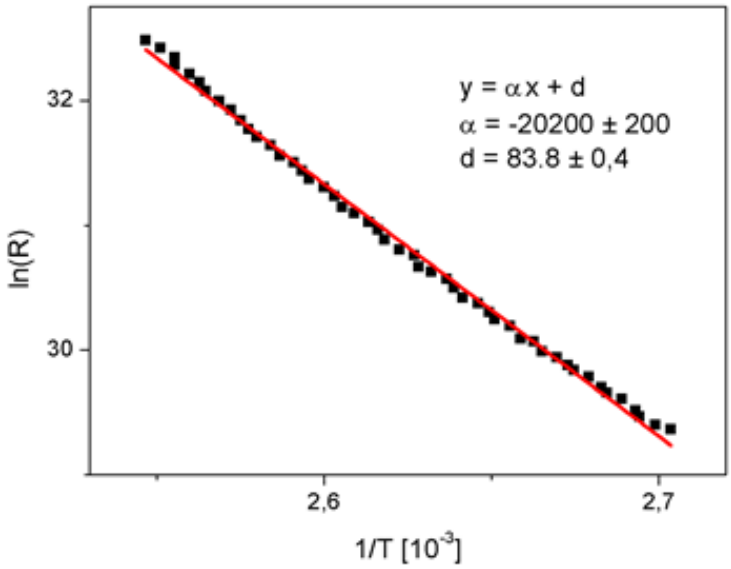

Figure 6.10.: Plot of $\ln(R)$ versus $1/T$ to determine the desorption energy and frequency factor for multilayer desorption

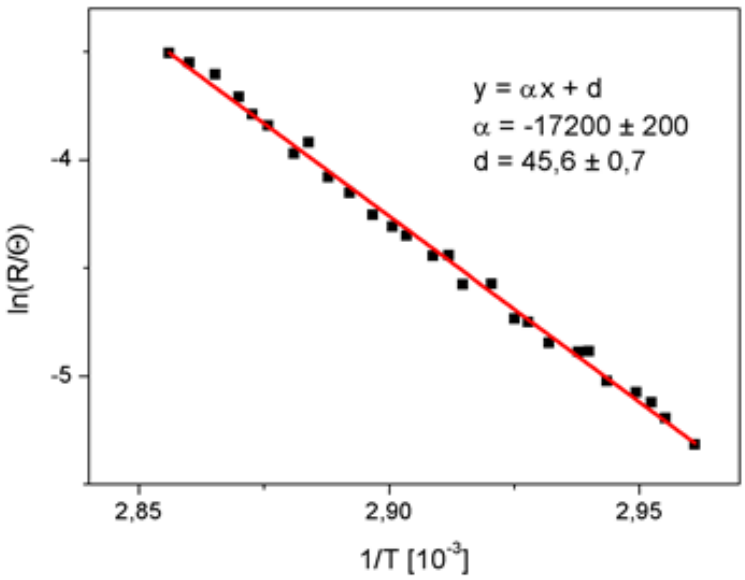

Figure 6.11.: Plot of $\ln(R/\Theta)$ versus $1/T$ to determine the desorption energy and frequency factor for monolayer desorption

6.7. Film Morphology and Dewetting

Thermal desorption spectroscopy has suggested that rubicene first forms two layers of flat lying molecules. With increasing deposition, however, these layers dewet and the molecules form islands. This could be proven by ex-situ atomic force microscopy. In Fig. 6.12 an AFM image of a rubicene film after an exposure of 250 Hz is shown, equivalent to a mean layer thickness of about 20 nm, considering the reduced sticking coefficient at low coverage. The film consists of randomly oriented islands with elongated shape. Interestingly, for very low coverage (e.g. 7 Hz, mean thickness: 0.16 nm), for which TDS reveals a layer-like monolayer film, ex-situ AFM shows again an island-like morphology (Fig. 6.13). This strange behavior can be explained by a dewetting process caused by the exposure of the sample to air. Such a venting induced dewetting has been recently demonstrated for the system hexaphenyl on mica.[100] Indeed, a desorption experiment on a 7 Hz rubicene film once performed directly after deposition and once performed after venting the vacuum chamber and re-evacuation, showed a dramatic difference (Fig. 6.14). Whereas in the first case one can see mainly desorption from the weakly adsorbed wetting layer, after venting only desorption from the more strongly bound islands is observed. In addition, the total area under the desorption spectrum has decreased by about 40% after venting. However, not only the exposure of the thin rubicene film to air changes the morphology, there is also a further gradual change of the morphology as a function of the storage time in air. This is shown in the AFM images for a

30 Hz film (mean thickness: 0.7 nm), which were obtained directly after venting the chamber and dismounting (Fig. 6.15) and after 24 hours (Fig. 6.16). Furthermore, it could be shown by AFM that for very thin films the storage of the sample in air results in a continuous decrease of the deposited amount. Particularly, a 7 Hz film was not visible anymore by AFM after storage in air for 5 days.

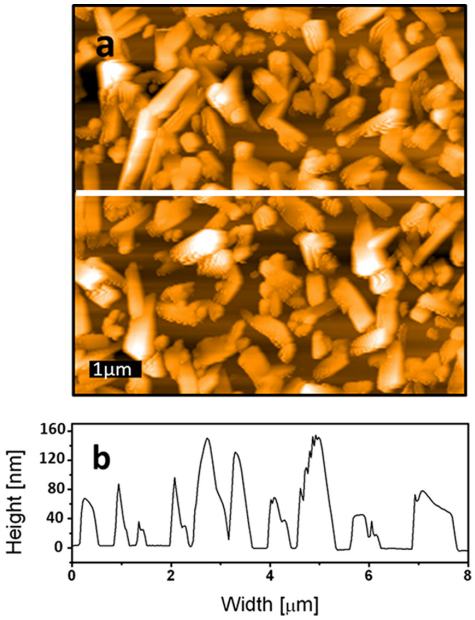

(a) Topography scan **(b)** Cross section along the white line in (a)

Figure 6.12.: AFM image (8×8 µm) of a rubicene film deposited at 300 K on silicon dioxide with a mean thickness of 20 nm

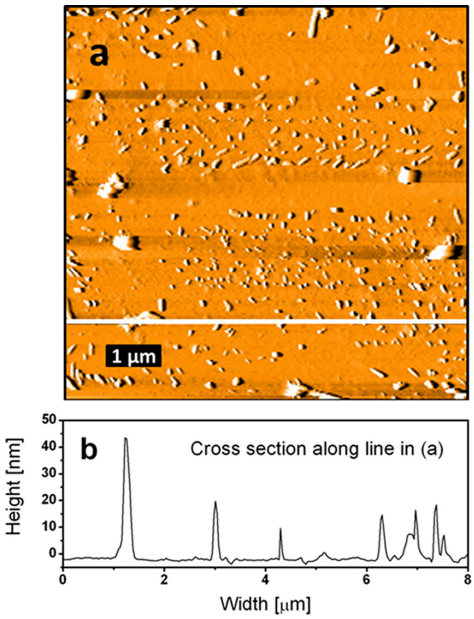

(a) Topography scan **(b)** Cross section along the white line in (a)

Figure 6.13.: AFM image (8×8 µm) of a 7 Hz rubicene film (mean thickness 0.16 nm) immediately measured after dismounting the sample from the vacuum chamber

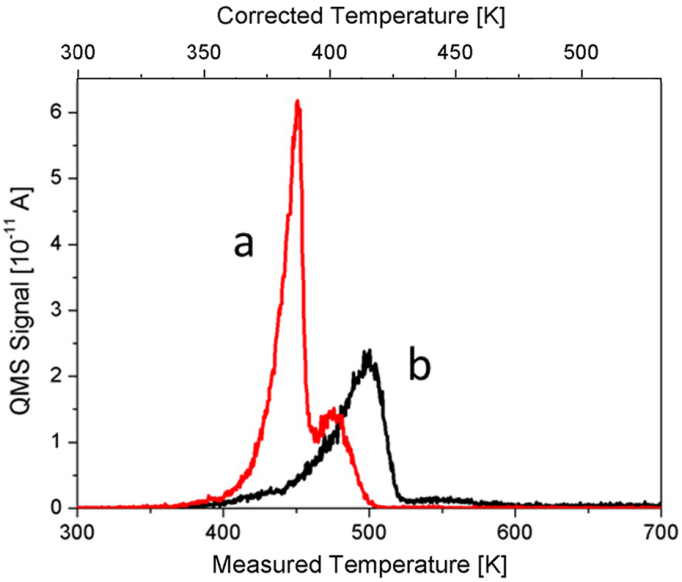

Figure 6.14.: Thermal desorption spectra for a 7 Hz rubicene film obtained directly after deposition (a) and for a film with the same exposure, but obtained after venting the vacuum system and re-evacuation (b)

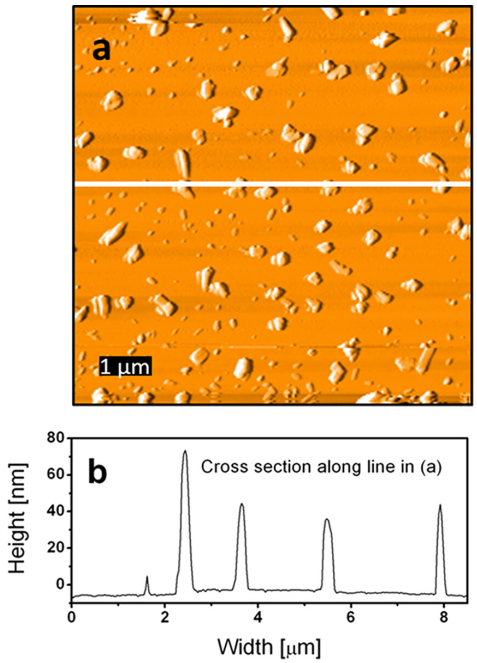

(a) Topography scan **(b)** Cross section along the white line in (a)

Figure 6.15.: AFM image (8.6×8.6 µm) of a rubicene film with an initial mean thickness of 0.7 nm, directly measured after deposition at 300 K and venting of the vacuum system

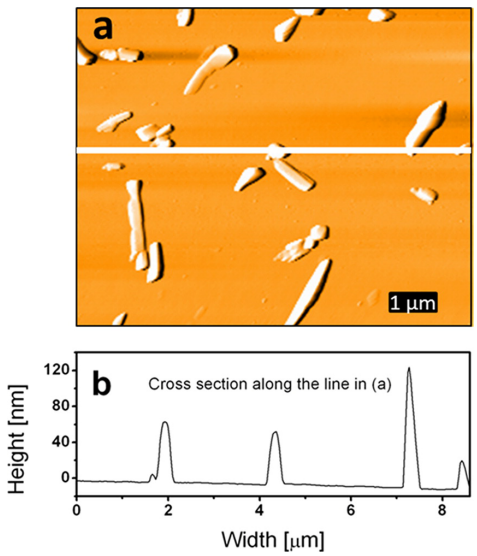

(a) Topography scan **(b)** Cross section along the white line in (a)

Figure 6.16.: AFM image (8.6×6.9 µm) of a rubicene film deposited at 300 K with an initial mean thickness of 0.7 nm measured 24 hours after venting

6.8. X-ray Diffraction on Thin Films

The crystallographic structure of a 20 nm thick film (corresponding to Fig. 6.12) was determined by X-ray diffraction. A specular scan ($\Theta/2\Theta$) scan is shown in Fig. 6.17, revealing that the crystallites are oriented with the (001) plane parallel to the substrate surface. However, from the large rocking width of about 6°, as depicted in the inset of Fig. 6.17, one has to conclude that the mosaicity of the rubicene crystals is large. Additional scans under different sample orientations (angle ψ) are shown in Fig. 6.18. Based on our crystal structure solution together with the observation of the (00l)-peaks within the specular diffraction, the alignment of the molecules relative to the substrate surface could be determined. The layers of molecules are formed parallel to the substrate surface (Fig. 6.19a). Within one layer the molecules are stacked parallel to each other so that they form parallel columns, while they are side-tilted within the columns (Fig. 6.19b). The slight displacement of different molecular layers during π-stacking is depicted in Fig. 6.20.

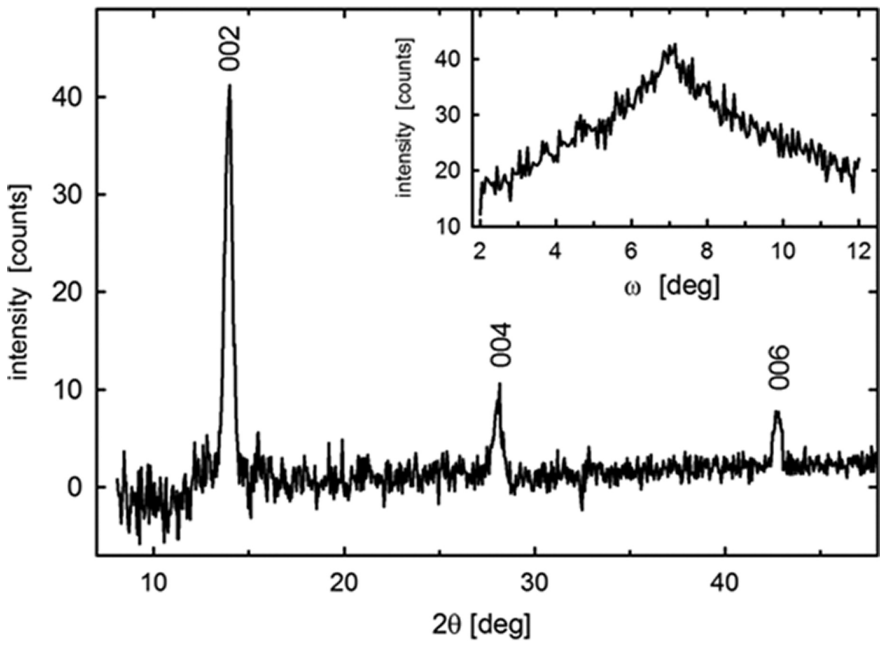

Figure 6.17.: Specular x-ray diffraction scan on a 20 nm thick rubicene film grown on SiO_2, using CrKα radiation. The inset displays the rocking curve of the 002 peak.

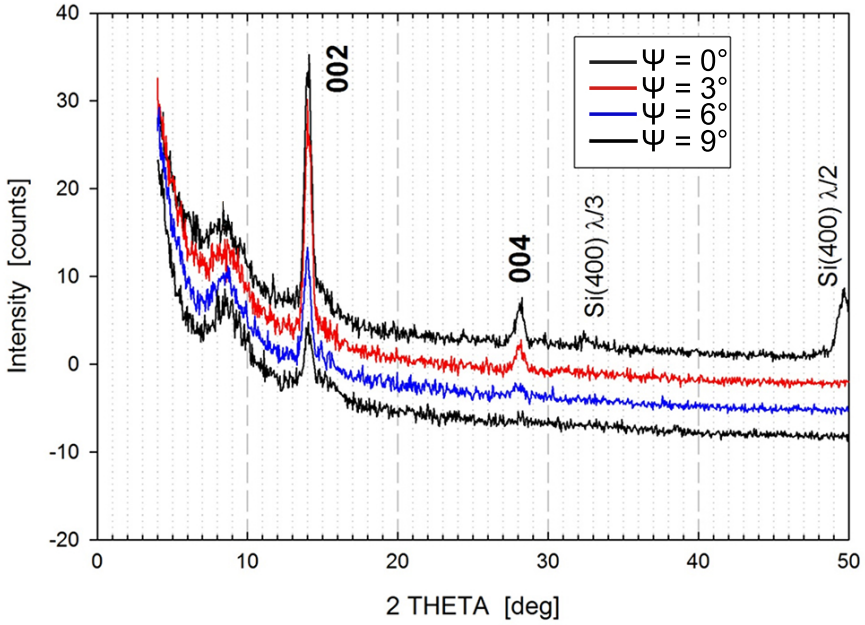

Figure 6.18.: Specular x-ray diffraction scan on a 20 nm thick rubicene film under different sample orientations ψ

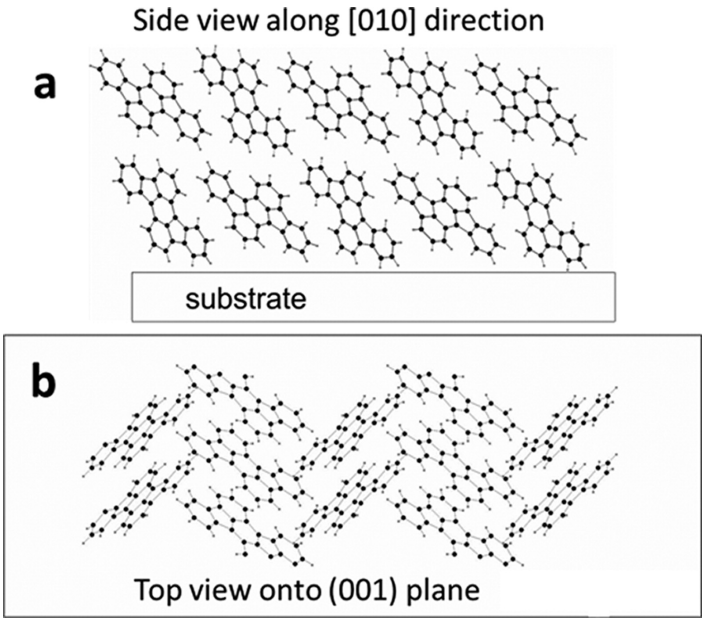

(a) Side view of two molecular layers along the [010] direction

(b) Top view onto the (001) plane of one molecular layer

Figure 6.19.: Molecule arrangements in a rubicene crystal

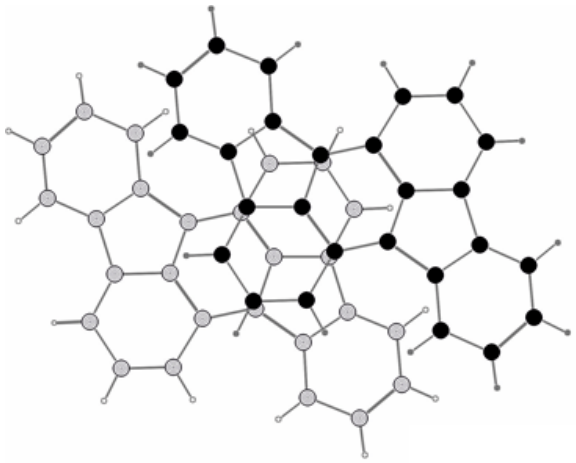

Figure 6.20.: π-π stacking of two rubicene molecules with a distance of 3.38 Å

6.9. Discussion

The initial layer formation of rubicene on silicon dioxide shows a quite peculiar behavior. Typically, on reactive surfaces small organic molecules form first a strongly bound wetting layer of lying molecules, on which then the multilayer forms, either consisting again of lying molecules or of standing molecules. Examples of the former film formation are quaterphenyl (4P) and hexaphenyl (6P) on Au(111) [90, 96], 6P on freshly cleaved mica [91, 92, 154], pentacene (5A) on Au(111) [94], or PTCDA on Ag(111) [97], to name just a few. An example of the latter layer growth is 5A on Si(111).[95] Contrary, on inert, flat substrates organic molecules tend to form films consisting of standing molecules, beginning already in the first layer, like for 6P on sputtered mica [91] or 5A on SiO_2 [56]. To distinguish between monolayer and multilayer formation quantitative thermal desorption spectroscopy can be used in addition to AFM and other spectroscopic methods. Particularly, the energetics and kinetics of film formation and decomposition can be studied successfully. Films of the above mentioned characteristics with a strongly bound wetting layer typically show two desorption peaks, one for multilayer desorption and another one for monolayer desorption at higher temperature. If the first layer already consists of standing molecules, due to weak interaction with the substrate, typically only one desorption peak is observed.[155]

In the case of rubicene desorption at low coverage first a single peak appears at relatively low temperature. After a particular coverage this peak starts to decrease and it is finally replaced by a desorption peak at higher temperature. Such a behavior for the first monolayer has not been observed before to the best of our knowledge. There is only one example in the literature where a similar desorption behavior was described, however involving the transition between a second layer and a multilayer. In that case hexaaza-triphenylene-hexacarbonitrile

(HATCN) was adsorbed on Au(111) [156] and Ag(111) [152]. In both cases a weakly bound second layer was formed on top of a strongly bound wetting layer, where the second layer was then incorporated at higher coverage into the multilayer by dewetting, from which the molecules desorbed at somewhat higher temperature.

The adsorption/desorption behavior of rubicene on/from silicon dioxide can be explained in the following way: In the sub-monolayer regime the molecules adsorb flat-lying on the inert SiO_2 substrate. This interaction is quite weak, the desorption energy is only 1.25 eV. Desorption of this layer appears already slightly above room temperature at around 370 K in the form of a single peak (α-peak) at low coverage. This single peak of asymmetric form shifts to higher temperature with increasing coverage, first with a common leading edge and finally even with the leading edge shifting to higher temperature. This desorption characteristic is an indication of first order desorption kinetics with attractive interactions between the molecules.[70] Desorption proceeds in form of a single peak up to an exposure of 12-15 Hz. According to the calibration of the quartz microbalance and the experimentally obtained initial sticking coefficient of about 0.25, the saturation of this single peak can be attributed to a coverage of about 0.3 nm mean thickness. This is evidence for a closed monolayer of flat lying molecules. The van der Waals thickness of aromatic molecules is roughly 3.5 Å.[148]

With further exposure a second desorption peak (β-peak) appears, shifted by about 30 K to higher temperature. At the same time the α-peak keeps on growing until it reaches saturation at a coverage equivalent to a double layer of lying molecules. The β-peak continually grows with increasing exposure, indicating desorption from a multilayer, while the α-peak decreases until it eventually totally disappears above an exposure of about 80 Hz. This is equivalent to a mean film thickness of 1.8 nm. This behavior can be interpreted as follows: After saturation of the first monolayer further impinging molecules adsorb in the second layer again flat on. However, this double layer is already metastable. Further adsorption on this double layer results in an unstable film and the molecules restructure from a flat-lying double layer to a standing arrangement, which is apparently energetically more favorable. Actually, the formation of a closed double layer before the formation of islands starts on this layer is not so uncommon. A few examples of such a layer growth are PTCDA on Ag(111) [97], HATCN on Au(111) [156] and sexiphenyl on Cu(110)(2x1)O [157].

The key point in the rubicene-SiO_2 system is that the binding energy of the molecules to the substrate (1.25 eV) is weaker than the binding energy between rubicene molecules in the bulk phase, which was calculated to be 1.47 eV. However, the diffusion probability of the flat-lying molecules in the sub-monolayer phase is not high enough to restructure the layer into 3D islands during heating, from where the molecules then would desorb at higher temperature. This latter behavior has been observed for 6P on sputtered mica.[100] Never-

theless, for higher coverage the tendency of dewetting in the system rubicene-SiO_2 is so high that the growth of smooth, thick films is very unlikely (see Fig. 6.12). The formation of a full monolayer of flat-lying molecules is only possible during growth in UHV. Exposure of a 7 Hz layer to air again results in a strong dewetting, as shown by AFM (Fig. 6.13). This was also verified by TDS, performed before and after venting with subsequent re-evacuation (Fig. 6.14). While before venting the desorption peak is at around 450 K (uncorrected), indicative of weakly bound molecules to the substrate, the desorption peak has shifted to 500 K after venting, indicative of desorption from 3D islands. Furthermore, the peak area after venting was reduced by about 40%, demonstrating the partial desorption during venting. A venting induced subsequent nucleation has been recently observed for the system 6P-mica.[100] It was assumed that upon venting water adsorbs on the sample surface and diffuses between film and substrate, such increasing the diffusion probability and/or decreasing the activation energy for nucleation. Such venting induced subsequent nucleation processes are in particular pronounced for very thin films. This should be taken into account whenever AFM images of such films are interpreted.

The quite weak bonding to the substrate (1.25 eV) and the rather low heat of evaporation of 1.47 eV, as obtained from TDS, has further consequences for the deposited rubicene film on SiO_2 when stored in air. A comparison of the morphology of a 30 Hz film (0.7 nm mean thickness) measured with AFM immediately after exposure to air (Fig. 6.15a) and after 24 h (Fig. 6.16a) shows significant differences. The film is composed of many small islands immediately after venting, with the largest islands having dimensions of about 300 nm in diameter and heights of about 50 nm (Fig. 6.15b). After storage in air for 24 h only few, large rectangular shaped islands are visible, with heights up to 120 nm (Fig. 6.16b). This phenomenon, known as Ostwald ripening, is again an indication of the weak bonding of the rubicene molecules at the rims of the 3D islands, leading to a quite dense 2D gas phase of rubicene monomers and hence to the growth of large islands at the expense of the small islands, according to the Gibbs-Thompson relation.[158] The process of Ostwald ripening and the partial evaporation of the film are relatively more pronounced on very thin films. A clear reduction of the island size after 30 days in air has been observed for the 0.7 nm thick film. Actually, on the 7 Hz film (mean thickness 0.16 nm, Fig. 6.15) no rubicene material whatsoever could be detected on the silicon dioxide after several days in air. Similar morphological changes of organic layers under ambient conditions have recently been observed also for naphthyl end-capped thiophenes deposited on mica.[159]

The morphology of thick films (20 nm mean thickness, Fig. 6.12) shows the existence of randomly oriented crystallites. With X-ray diffraction it was possible to identify that the structure of the small crystallites is identical to the bulk structure and that the crystallites are oriented with the (001) plane parallel to the substrate (Fig. 6.17). The arrangement of the rubicene molecules within the bulk crystal in two different views is shown in Fig. 6.19.

Rocking curve measurements (insert in Fig. 6.17) on this film revealed a quite high full width at half maximum of about 6°, indicating that the mosaicity of the film is rather large (significantly larger than for other organic films of rod like molecules, for example pentacene [160]).

Next, I would like to comment on some unusual features concerning the adsorption and desorption kinetics. The initial sticking coefficient of sufficiently large organic molecules is typically assumed to be one at and below room temperature.[152, 153] However, in this work it was clearly demonstrated that the sticking coefficient of rubicene on SiO_2 increases with increasing coverage, which excludes an initial sticking coefficient of one. Unfortunately, there exists little quantitative experimental and theoretical work in the literature on this subject, since all-atom molecular dynamics (MD) calculations of the adsorption dynamics of larger molecules are quite expensive. We are only aware of one theoretical work where the trapping dynamics of diindenoperylene (DIP) molecules on self-assembled monolayers (SAMs) have been studied, using MD simulations with MM3.[161] In that work the authors showed that the sticking coefficient depends on several parameters, e.g. on the incidence energy, the angle of incidence, the molecule orientation and the packing density of the SAM. Actually, these phenomena are well known for the adsorption of small molecules on rigid substrates, both for associative (e.g. CO) and dissociative adsorption (e.g. H2), for which a wealth of experimental and theoretical data is available.[162–164] Having these findings in mind we can at least speculate as to the reason of the rather low initial sticking coefficient for rubicene on silicon dioxide of about 0.2 (0.25 on the C-covered surface, 0.17 on the clean surface). The fundamental question is whether sufficient energy can be transferred to the substrate for accommodation within the interaction time. It was shown for the small molecule CO that the initial sticking coefficient on a variety of metal substrates decreases with increasing kinetic energy. Furthermore, the sticking coefficient decreases with decreasing adsorption energy.[165] This can be understood from simple classical arguments. The molecules have to transfer sufficient kinetic energy during the interaction with the surface to become trapped. The adsorption energy for the rubicene molecule ($C_{26}H_{14}$) on SiO_2 is 1.25 eV, which means that the binding energy per C atom is just about 50 meV. Thus it is not implausible that the initial sticking coefficient is not one. Another aspect is the orientation of the molecules in front of the surface during interaction with the surface. The influence of rotational energy on sticking has been shown by Batista *et al.* [166] for H_2O on ice and by Gardner *et al.* [167] for CO on ice substrates. It can be anticipated that the orientation effect will be even more pronounced for larger rigid molecules. Furthermore, the proper mass matching will be relevant for effective accommodation. This was shown, e.g. by McMaster *et al.* [168] for propane on platinum substrates. The authors explained the increase of the sticking coefficient with coverage by the better mass matching and a greater deformability

of the adlayer. Finally, precursor mediated adsorption should be taken into account.[169] In this scenario the molecule is first trapped in a weakly bound state where it can still move along the surface until final accommodation, or desorb again during the residence time in the precursor state. The interaction with islands and other imperfections on the surface will increase the accommodation, which again will lead to an increase of the sticking coefficient with coverage.

From the desorption spectra one can not only determine the desorption energy but also the frequency factor for desorption, according to equation (2.8). In particular, the frequency factor contains information on the kinetics of desorption. In our particular case we determine a frequency factor for the first-order desorption of the (sub)-monolayer phase of $\nu_1 \approx 10^{16}$ s^{-1}, and for the zero-order desorption from the multilayer phase $\nu_0 \approx 10^{18}$ s^{-1}. The lower frequency factor for the monolayer desorption might imply that the molecules in the (sub)-monolayer are more mobile than in the bulk phase prior to desorption.[106, 170]

6.10. Summary and Conclusion

The initial film formation of rubicene molecules on silicon dioxide exhibits a quite unusual behavior. First, a monolayer of flat lying molecules is formed, followed by a second layer of flat lying molecules. The desorption energy of these molecules is 1.25 eV. Deposition of further rubicene leads to a destabilization of this bilayer and to dewetting by the formation of 3D islands. The crystallographic structure of these islands is bulk like, with the (001) plane being parallel to the substrate. This leads to an arrangement of upright standing but tilted molecules. The desorption energy for the molecules in the 3D islands (heat of evaporation) is larger than that for the flat lying molecules in the wetting layer, namely 1.47 eV. This is the reason for the strong tendency of dewetting. Dewetting of the bilayer can also be induced by exposing such a layer to air. This has been shown by thermal desorption spectroscopy and atomic force microscopy. Furthermore, for the island-like film under ambient conditions Ostwald ripening was observed, leading to films composed of few, large crystalline islands. In the case of very thin films most of the material in the small islands even disappeared by evaporation within several days at room temperature.

A further peculiarity of the adsorption system rubicene/SiO_2 is related to the sticking coefficient. Contrary to common wisdom the initial sticking coefficient is not one, even at a substrate temperature of 220 K. An initial sticking coefficient of only 0.2 ± 0.05 (depending on the substrate conditions) was measured. This low value can be related to the relatively weak interaction energy between the molecules and the substrate. But other reasons connected with the adsorption dynamics can also play a role, e.g. orientational hindering, insuffi-

cient energy accommodation due to mass mismatch, or precursor mediated adsorption. This can be inferred from the fact that with increasing coverage the sticking coefficient increases, and probably approaches one for thicker films. Adsorption and desorption of rubicene on SiO_2 is only weakly depending on the substrate chemical composition. Accumulation of carbon on the surface, due to some dissociation of rubicene during sample heating, does neither significantly influence the shape of the desorption spectra nor the coverage dependence of the sticking coefficient. The reason for this is again the already weak interaction energy between rubicene and silicon dioxide, which is not further decreased by contaminations.

7 | Indigo

7.1. Introduction

Natural dyes such as indigo have been used for thousands of years by ancient cultures in India, China and Egypt to color textiles and food. Indigo is still the most commonly used dye today, thanks to jeans and their typical blue color. Originally it was obtained from the plants *Indigofera tinctoria* and *Isatis tentoria*, although with recent advancements in synthesis and fabrication it is almost exclusively produced artificially today.[171, 172] Despite the high level of awareness, the formation of highly-crystalline indigo films upon evaporation and the good charge transport properties have only been discovered recently.[60, 173] The combination of a reversible oxidation and reduction electrochemistry plus a low band gap makes this material behave as ambipolar semiconductor with fairly high mobilities of 0.01 cm^2/Vs. The low cost and low toxicity especially evoke high levels of interest for a new era of sustainable and bio-degradable materials for organic electronics.[174, 175]

The indigo molecule (IN, $C_{16}H_{10}N_2O_2$, see Fig. 7.1) shows a high planarity and forms a double cross-conjugated system with two electron donor groups and two acceptor groups with a central C=C double bond. Its deep blue color can be explained by the conformation of the two carbonyl groups with respect to the central C=C bond, as well as by the electronic arrangement of the heteroatom and its high polarisability.[177] During stacking each molecule is hydrogen bonded to four of its neighbors, while adjacent molecules are also π-stacked to each other.[45] Air-stable OFETs of indigoids on various substrates show field-effect mobilities and other functionalities inaccessible to conventional organic semiconductors and outperform many established materials in terms of operational stability.[43, 51–53]

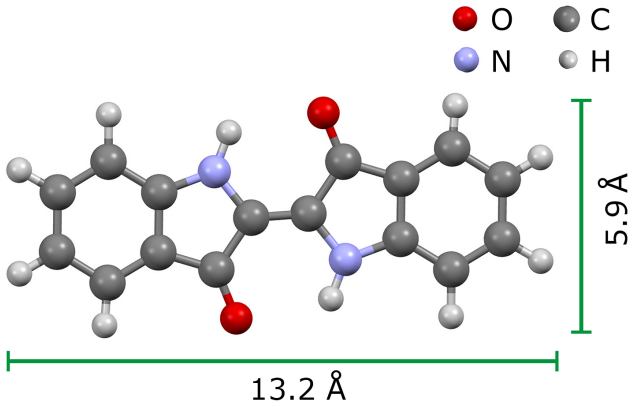

Figure 7.1.: Structure and van der Waals dimensions of the indigo molecule [148, 176]

In this chapter the initial growth behavior of thin indigo films on silicon dioxide and their suitability for possible applications in transistor fabrication will be investigated. High purity thin films were prepared under well-defined ultra-high vacuum conditions to study adsorption and desorption behavior via thermal desorption and Auger electron spectroscopy. In addition, film morphologies, air stability and crystalline orientations were examined with atomic force microscopy and X-ray diffraction.[1]

7.2. Experimental

For the following experiments indigo powder, provided by ALDRICH with a listed purity of 95%, was deposited, after proper outgassing, from a metal Knudsen cell heated to ≈490 K. Upon inserting the density of indigo (ρ = 1.50 g/cm^3) [59] into equation (4.3) on page 49, one obtains a frequency change of 1 Hz equaling a mean thickness change of 0.8 Å for the provided system. Once again, one should note that this relationship is only true, if the sticking coefficient of the indigo molecules on the silicon dioxide substrate as well as on the quartz crystal is unity, which is typically the case for organic molecules (and will later be confirmed by experimental data). Deposition rates varied between 6 ng/(min cm^2) and 270 ng/(min cm^2), equivalent to 0.04 nm/min and 1.8 nm/min.

Changes in the chemical composition of the film and substrate surface were analyzed and investigated via AES. Besides the anticipated silicon and oxygen peaks, carbon was observed as contaminant on the silica surface. It was possible to easily remove any carbon with 10 minutes of argon sputtering, however, any subsequent temperature treatment resulted in a

[1] As mentioned in section 1.4, large parts of this chapter emanate from a publication (Paper II, Ref. [68]) to which I have contributed as the leading author. For reasons of legibility I will avoid constant citation of this work in the following sections.

segregation of carbon atoms from the bulk and thus lead to additional carbon contamination during the heating process. An Auger analysis of deposited indigo films showed carbon, nitrogen and oxygen signals with no impurities (Fig. 7.2). Unfortunately, it was not possible to perform continuous Auger measurements during different stages of thin film growth, due to the destructive behavior of the electron beam on soft organic surfaces.

The mass spectrometer was tuned to mass 76 (most prominent fragment in the indigo cracking pattern) for thermal desorption analysis and the samples were heated linearly with a heating rate of 1 K/s (compare Sec. 3.1).

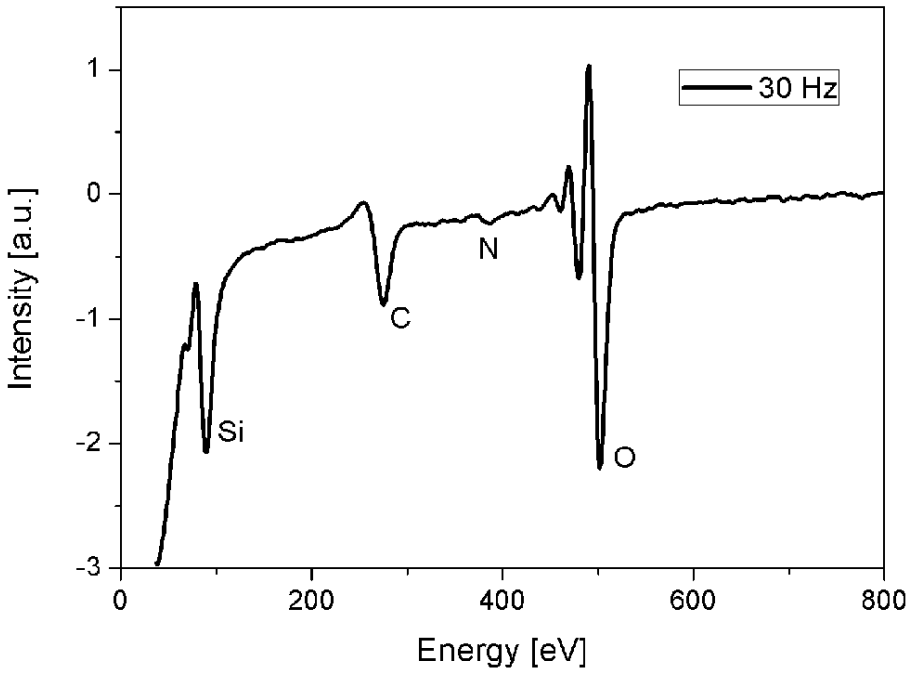

Figure 7.2.: Auger electron spectrum of an indigo film with a mean thickness of 2.4 nm on a SiO_2 substrate. Adsorption temperature T_{ad} = 220 K.

7.3. Adsorption and Desorption on/from carbon covered SiO_2

Fig. 7.4 displays desorption spectra of indigo from silicon dioxide for different exposed amounts at adsorption temperatures of 220 K. At this point I want to emphasize again, that after each deposition and subsequent desorption cycle, a specific amount of carbon will remain on the surface. Once an adequate amount of cycles is reached, the accumulated carbon reaches a saturation thickness above which no further decomposition can be observed

(Auger ratio $C_{272}/O_{510} \approx 0.18$). This stable and inert substrate was used for the adsorption and desorption experiments in this chapter.

Fig. 7.4a shows a series of spectra for very low exposures between 0.8 and 4.0 Å mean film thickness (see calibration of the coverage below). Initially, for exposures smaller than 0.8 Å, only a single peak at around 400 K (corrected temperature T_{corr} = 290 K, compare chapter 7.5) can be observed, designated as α-peak. For exposures between 0.8 and about 2.7 Å a second peak, designated as β-peak, appears at approximately 150 K (corrected value: 60 K) higher temperature. This is especially noteworthy, since TDS typically shows a single peak for monolayer desorption at high temperature which is followed by a second peak for multilayer desorption at lower temperatures for materials, which exhibit SK film formation.[155] With further increase in coverage the α-peak starts to decrease up to a point where it is not distinctively visible anymore at a coverage of about 9.6 Å. The β-peak increases meanwhile (1.6 - 4 Å) and, once the initial α-peak has disappeared, continues to increase with a common leading edge for higher coverages (9.6 - 52 Å), as can be seen in Fig. 7.4b. For high coverages, the small peak at 390 K, marked as Ta-peak, does not originate from desorption from the actual sample surface, it rather shows multilayer desorption from the tantalum foils, which are used to attach the silicon wafer onto the steel sample holder. Due to the good heat conductivity between those two materials and the direct connection to the thermocouple one can assume, that this early peak shows the true desorption temperature of indigo in the multilayer state. Therefore, this can be used to correct the temperature scale (see chapter 7.5 on page 96). Thus, the true desorption temperature of the α-peak is at around room temperature and that for the multilayer at about 350 - 400 K.

Taking only TDS measurements into consideration, one cannot distinguish between flat-lying and side-tilted molecules during initial film formation (α-peak), but it can safely be assumed, due to the low amount of adsorbed material, that at this point the interactions between the monomers on the surface are either non-existent or negligible. A densely packed monolayer of flat-lying indigo molecules would correspond to a mean thickness of about 3.5 Å, based on the van der Waals dimensions of the molecule.[148] Thus, the change of the desorption peak α into a more strongly bound state β, that occurs already at a mean thickness of below 1 Å, indicates the re-arrangement of the molecules way below a third of a monolayer. This re-arrangement can most probably be described by a dewetting process leading to the formation of islands, in which the molecules are more strongly bound than on the silicon surface. A behavior, where the molecules in the multilayer islands are more strongly bonded than in the wetting layer is quite unusual for organic materials and has only been observed in a few cases; for the first time by Jacob and Menzel for benzene on Ru(001) [178] and more recently also for bithiophene on Cu(110) [179]. In the laboratories of Graz University of Technology such a behavior was observed for rubicene on SiO_2 (see chapter 6.4 on page 69) and hexaaza-triphenylene-hexacarbonitrile (HATCN) on Au(111)

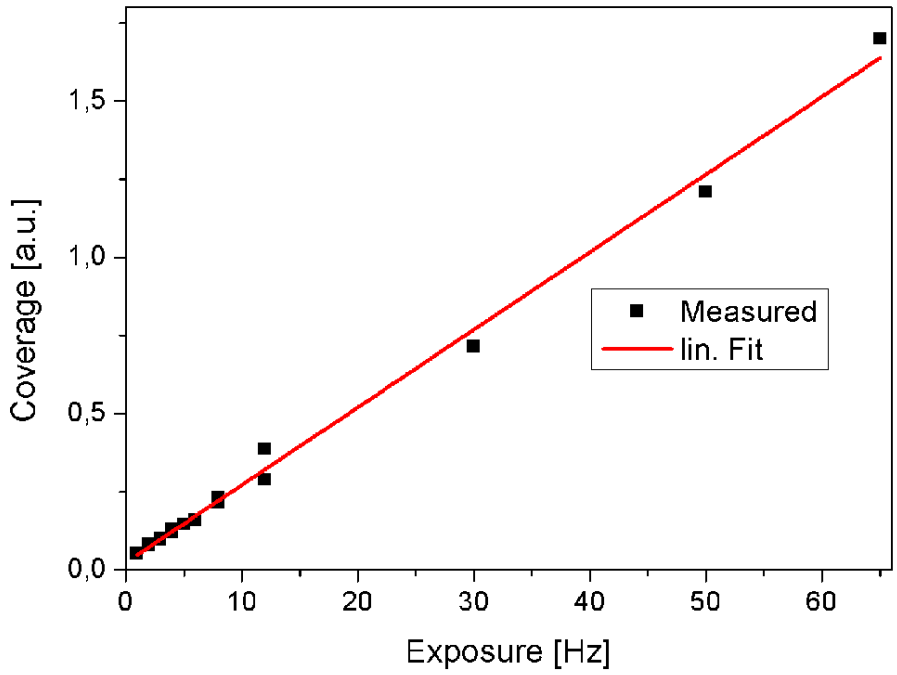

Figure 7.3.: TDS area for indigo desorbed from carbon covered silicon dioxide as a function of the exposed amount, as measured by the quartz microbalance

[156] and Ag(111) [152]. HATCN on Au(111) and Ag(111) forms a weakly-bonded second layer on top of a strongly bonded wetting layer. At higher coverages the second layer gets incorporated into the multilayer by dewetting, once more leading to desorption at higher temperatures.

If one wants to take a closer look at specific details of the desorption spectra and make arguments about dewetting and the formation of islands as a function of coverage, the need to evaluate the sticking coefficient arises. For this purpose one can integrate the area under the individual desorption spectra curves and therefore determine a parameter for the actual amount of adsorbed/desorbed material. This was plotted versus the exposed amount, as measured by the quartz microbalance, in Fig. 7.3. In both the sub-monolayer and multilayer regime the surface coverage increases linearly with the amount of exposed material, resulting in a constant slope. For organic molecules it is usually assumed that the initial sticking coefficient at and below room temperature is unity.[152, 153] Therefore, it stands to reason to assume a sticking coefficient of one for indigo on silicon dioxide. Considering this sticking coefficient, it is possible to convert the exposure values given in Hz into values for the adsorbed amount, described by the mean film thickness:

$$\boxed{1\ \text{Hz} \mathrel{\widehat{=}} 0.8\ \text{Å}}$$

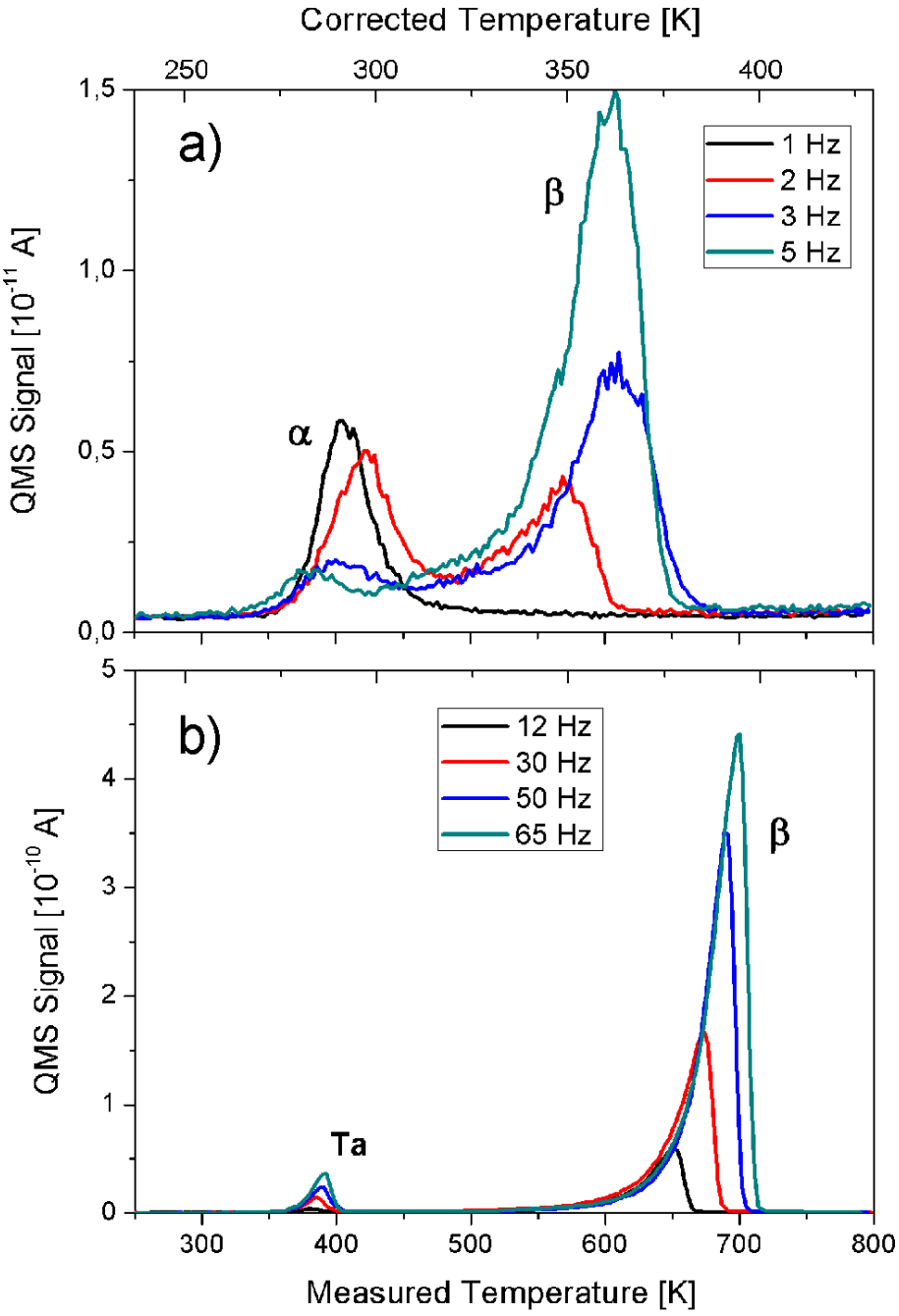

Figure 7.4.: Thermal desorption spectra of indigo from carbon covered silicon dioxide for different exposures. Adsorption temperature T_{ad} = 220 K. Heating rate β_H = 1 K/s. The exposure is given in Hz, as determined by a quartz microbalance. The small peak in (b) at 390 K (Ta) stems from desorption from the Ta mounting clamps.

7.4. Adsorption and Desorption on/from sputter cleaned SiO_2

In order to evaluate the influence of the underlying carbon layer and surface contamination in general, similar experiments as shown above were performed on a silicon dioxide surface that was cleaned by 10 minutes of argon sputtering (U = 500 V, I_e = 30 mA, p_{Ar} = 5×10^{-5} mbar) prior to each indigo deposition. The cleanliness was always checked by AES. A set of thermal desorption spectra is shown in Fig. 7.6. It is remarkable, that for a coverage up to 1.6 Å no desorption peaks can be observed at all. Impinging molecules get adsorbed onto the reactive surface and form chemical bonds that are so strong, that no desorption occurs for true surface temperatures of up to 430 K. The existence of some remaining adsorbed material after TDS was checked by AES. After further exposure a single peak (α) at around 450 K (corrected temperature T_{corr} = 307 K, compare chapter 7.5) appears, which saturates at a coverage of about 4.8 Å. After that a second peak (β) at higher temperatures starts to grow. Similar to the case of carbon covered SiO_2, the β-peak continues to grow with exposure, whereas the α-peak starts decreasing and disappears completely at, in this case, more than 6.4 Å mean film thickness.

The relationship between adsorbed and exposed amount of indigo on the sputter cleaned surface is shown in Fig. 7.5. Above 1.6 Å the relationship is once again clearly linear and it can therefore be assumed, that the sticking coefficient is unity. However, the intersection of the slope with the x-axis does not occur at zero, but rather at a coverage equivalent to 0.8 Å mean film thickness. This explains the small amount of decomposed indigo that stays on the sample after each desorption cycle, as it was described earlier. However, there is another remarkable phenomenon to be observed in Fig. 7.5. Up to about 1.6 Å no desorption takes place at all, but after a minute amount of additionally adsorbed indigo suddenly nearly all the adsorbed material desorbs (besides the remaining 0.8 Å). This suggests that at a particular coverage a rearrangement of some of the already adsorbed molecules has to take place, which leads to less strongly adsorbed particles, which can now desorb more easily.

To summarize the findings up to this point, the film formation and desorption behavior on the sputter cleaned surface can be described as follows: Initially, single molecules adsorb on the surface and form chemical bonds that proof to be so strong, that no desorption occurs below 800 K (430 K corrected temperature) and no desorption peak is visible in the TD spectra. As soon as a certain coverage threshold of about 2 Å mean thickness is reached, the probability of newly impinging molecules to land on top or in the vicinity of already adsorbed monomers becomes high enough, for a structural re-orientation to take place. It is suggested, that possibly dimers are formed, where each indigo molecule establishes hydrogen bonds to another indigo molecule. This newly created adsorbate is more weakly bonded

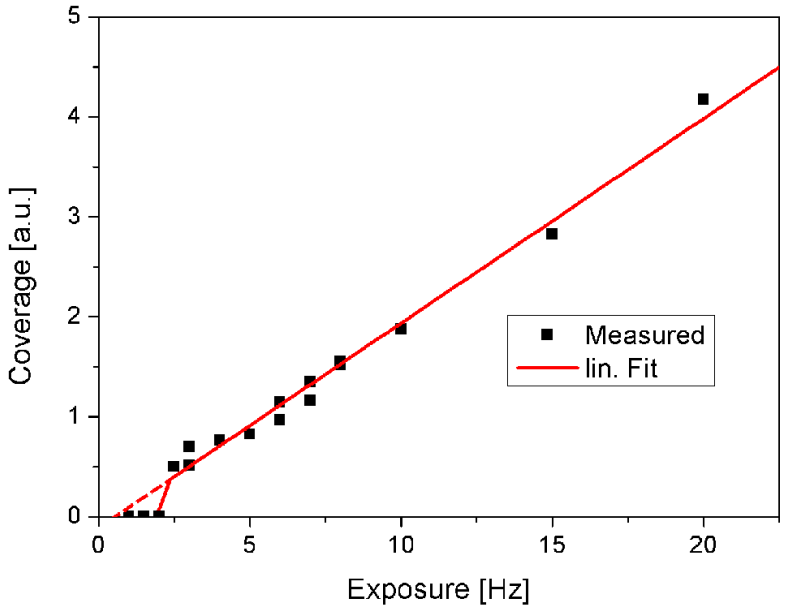

Figure 7.5.: TDS area for indigo desorbed from sputter cleaned silicon dioxide as a function of the exposed amount, as measured by the quartz microbalance

to the substrate due to the newly created hydrogen bonds between the active groups in the dimer. Situations where adsorbed molecules rearrange and form dimers with specific H-bonding interactions, thus causing increased diffusion on the surface have been reported by Mitsui *et al.* and Ranea *et al.* for water on Pd(111).[180, 181] With the available experimental capabilities it is of course not possible to present any evidence as to the type of the dimer or multimer formation. The most likely configuration is parallel π-stacking, where one molecule lies on top of another molecule. Furthermore, one should note, that such weakly bonded dimers can only be observed under vacuum conditions with liquid nitrogen cooling. Exposure to room temperature leads to immediate desorption, since the true desorption temperature for the α-adsorption state of indigo lies at around 300 K. At a coverage of 5.6 – 6.4 Å mean thickness dewetting sets in and island formation takes place, similarly to that on the carbon covered silicon oxide surface. The significantly higher saturation coverage of the α-state might be caused by the dimer formation. These dimers, although highly mobile, might not as easily become incorporated in nucleated islands compared to monomers. Discussions on this topic will resume in a later chapter, after island morphologies and island structures have been described in detail.

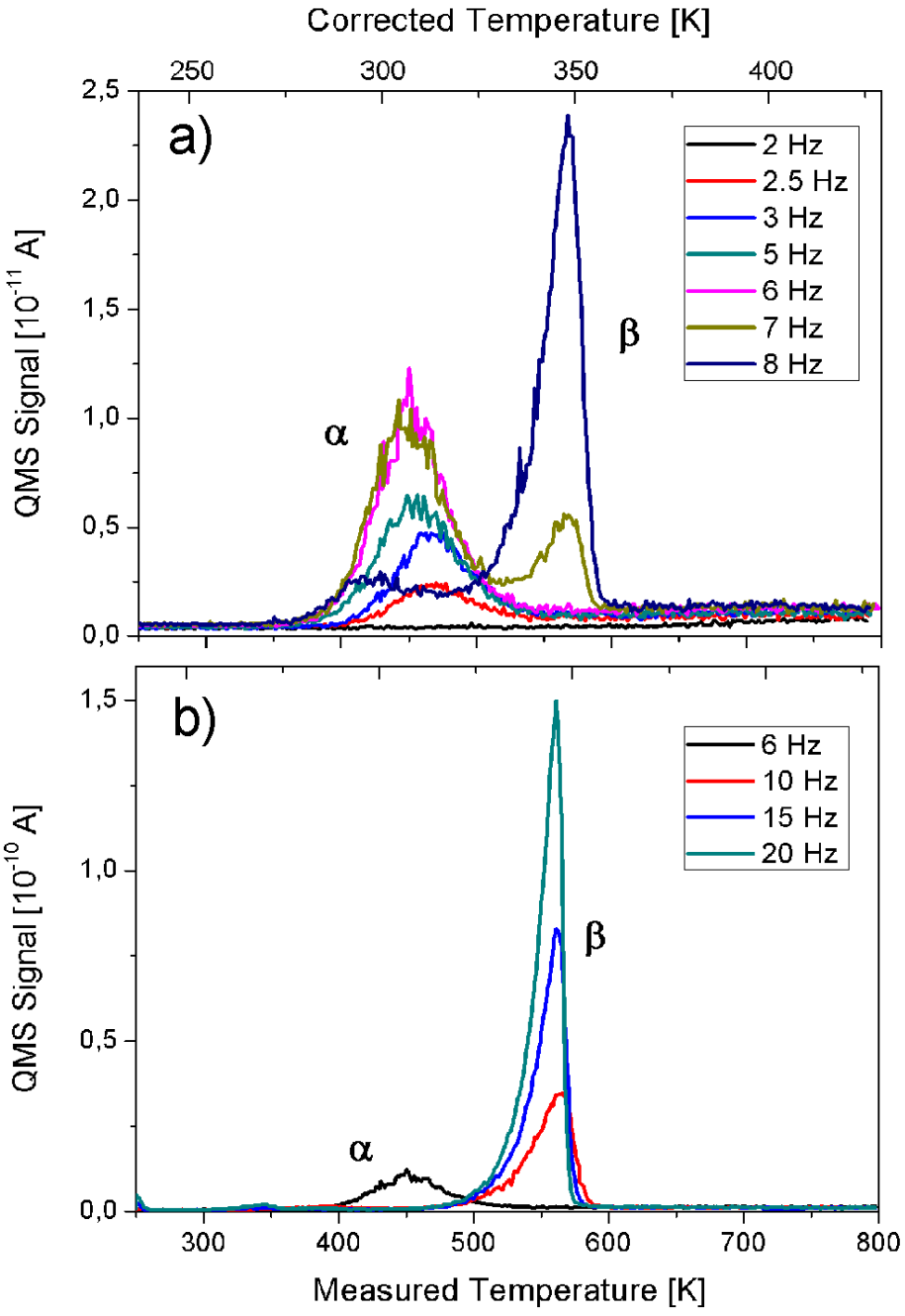

Figure 7.6.: Thermal desorption spectra of indigo from sputter cleaned silicon dioxide for different exposures. Adsorption temperature T_{ad} = 220 K. Heating rate β_H = 1 K/s. The exposure is given in Hz, as determined by a quartz microbalance.

7.5. Temperature Correction and Desorption Energies

Further evaluation of the desorption spectra for indigo films above a certain thickness (Fig. 7.4b) shows a common leading edge and a desorption maximum that shifts to higher temperatures for increasing coverage both on a carbon covered and on a sputter cleaned substrate (Figs. 7.4b and 7.6b). This specific behavior is characteristic for zero order desorption kinetics from multilayers. As described in an earlier chapter, the desorption energy can be deduced from equation (2.8) on page 21 for first and higher order desorption (Langmuir desorption) and from equation (2.9) for zero order desorption. Considering these two equations, a plot of the logarithm of the desorption rate $R(T)$ versus $1/T$ for zero order desorption and $R(T)/\Theta$ versus $1/T$ for first order desorption should yield a straight line, where the slope is equivalent to $-E_{des}/k_B$. However, and as already mentioned, the exact temperature of the sample surface during the experiments is not directly known, due to the poor heat conductivity between the silicon substrate and the stainless steel heating plate. In order to address this issue and to obtain a reliable value for the desorption temperature, experiments were conducted that featured multilayer adsorption and subsequent desorption of indigo directly onto/from the stainless steel sample holder, where the temperature is measured with a thermocouple. The corresponding desorption spectrum is shown in Fig. 7.7. One obtains a true multilayer (formed by 105 Hz exposure) desorption temperature of 400 K. Opposed to this, the multilayer peak on a carbon covered surface for 105 Hz exposure has a desorption temperature of 730 K (Fig. 7.4). Consequential, the temperature lag at this peak position calculates to 330 K. Thus one can correct the temperature scale in the same manner as in Sec. 6.6 by assuming that during adsorption both the steel plate and the SiO_2 substrate share the same temperature, and that the temperature lag during heating shows a linear dependence (compare equation (6.1) on page 73).

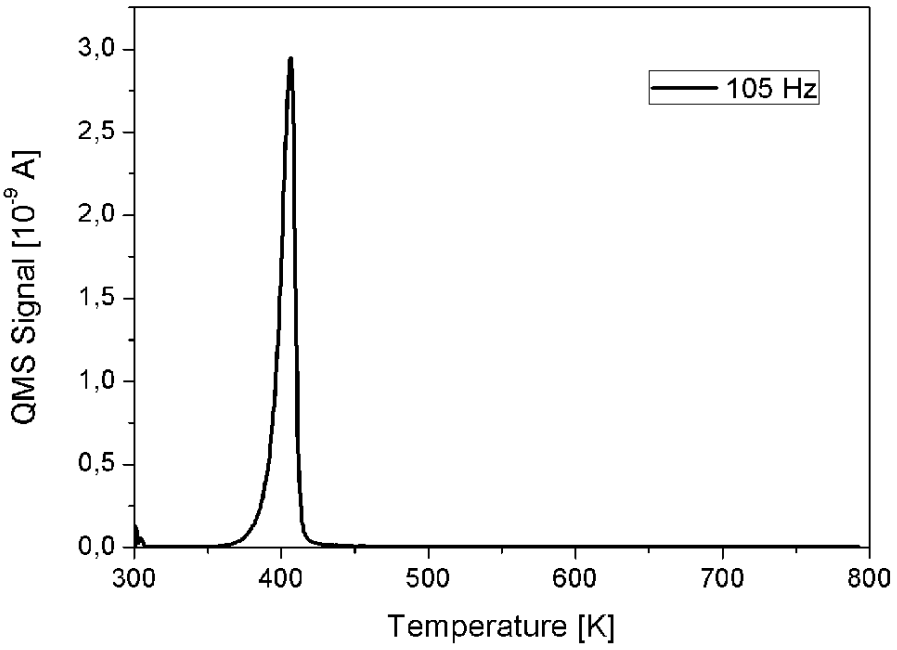

Figure 7.7.: Thermal desorption spectrum of indigo from the stainless steel sample holder

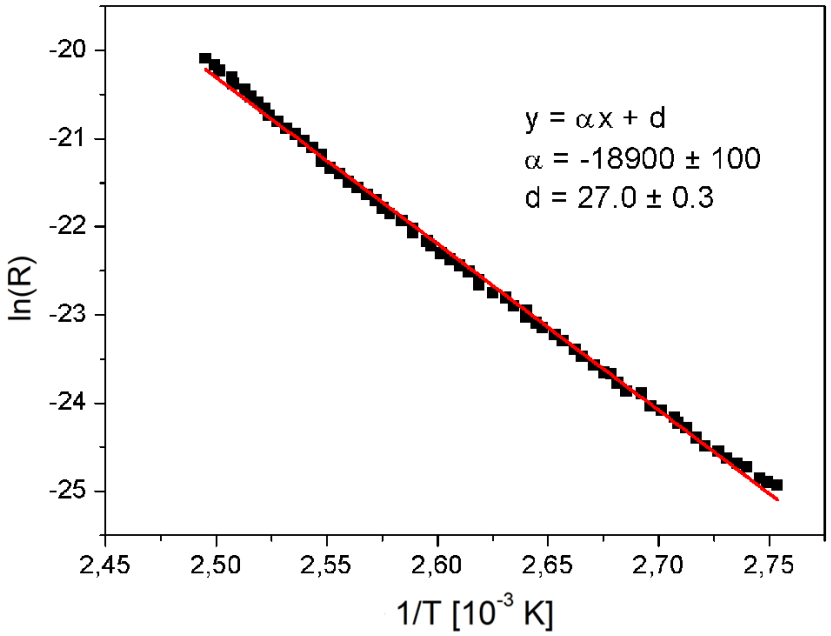

Figure 7.8.: Plot of $\ln(R)$ vs $1/T$ to determine the heat of evaporation of indigo

Calculations with the corrected temperature values yield a desorption energy of indigo from carbon covered SiO_2 (compare chapter 7.3) with a value of 1.67±0.05 eV, using the 50 Hz curve in Fig. 7.4b and the molecule density of indigo in the (100) plane with a value of 3.8×10^{14} molecules/cm^2. From the intercept of the linear fit with the y-axis one obtains a frequency factor of 1×10^{22} s^{-1} (see Fig. 7.9). By assuming first order desorption it was also possible to evaluate the desorption spectra in the monolayer and sub-monolayer regime (α-peak), assuming an equal discrepancy between the values for true and measured temperature. The evaluation of the 1 Hz spectrum in Fig. 7.4a yields a desorption energy E_{des} of 0.84±0.05 eV and a frequency factor ν of 6×10^{12} s^{-1} (see Fig. 7.10).

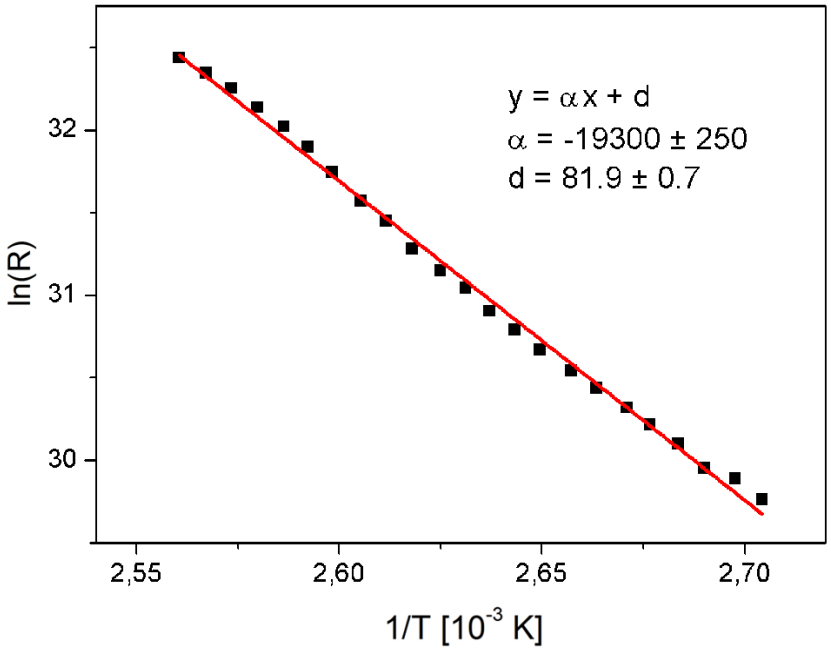

Figure 7.9.: Plot of $\ln(R)$ versus $1/T$ to determine the desorption energy for multilayer desorption of indigo from a carbon covered surface

Equivalent evaluation of the desorption energies and frequency factors for indigo desorption from a sputter cleaned substrate yields $E_{des} = 1.53$ eV and $\nu = 1.4\times10^{22}$ s^{-1} for the multilayer (see Figs. 7.6b and 7.11), as well as $E_{des} = 0.83$ eV and $\nu = 1.8\times10^{12}$ s^{-1} for the α-peak (see Figs. 7.6a and 7.12). The agreement of these values for the multilayer desorption energies and frequency factors between the sputtered and carbon covered substrate is not surprising. However, one would not expect agreement, within the margin of errors, for the α-peaks. Calculating the heat of evaporation directly from the desorption of indigo from the stainless steel plate yields a value of 1.63 eV (see Fig. 7.8). The discrepancy of about 2.5% between the desorption energy as obtained for indigo on the SiO_2 surface and the stainless steel surface can once again be attributed to uncertainties in the temperature correction.

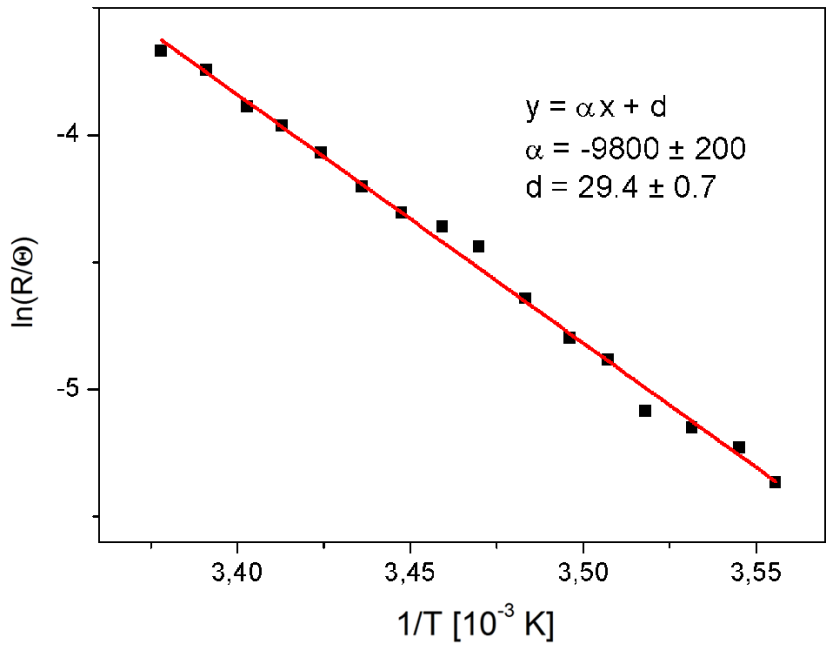

Figure 7.10.: Plot of $\ln(R/\Theta)$ versus $1/T$ to determine the desorption energy for monolayer desorption of indigo from a carbon covered surface

At first glance the large difference in the frequency factors for the α and β-peaks seems to be quite astonishing. However, considering the meaning of the pre-exponential factor according to transition state theory (TST, see chapter 2.6), this can easily be interpreted: The pre-exponential factor actually takes the change of all translational and internal degrees of freedom during desorption into account and is described by equation (2.11) on page 22. In the case of adsorption without an activation barrier for adsorption, the transition state is equal to the final state of the free molecules. Considering a particle, which is already highly mobile in the adsorbed state prior to desorption, i.e. the entropy is nearly the same in the adsorbed state and in the free state, the pre-exponential factor reduces to $\nu = \frac{k_B T}{h}$ $\approx 6{\times}10^{12}$ s^{-1} at room temperature. Thus, one can assume that this is largely fulfilled for desorption from the α-state. On the other hand, desorption from localized adsorption sites, as for example from kink sites of bulk materials, where the partition functions for translation and rotation approach unity, can lead to pre-exponential factors which are orders of magnitudes larger than 10^{13} s^{-1}. This has indeed been frequently observed for desorption from organic multilayer films.[155, 170, 182, 183]

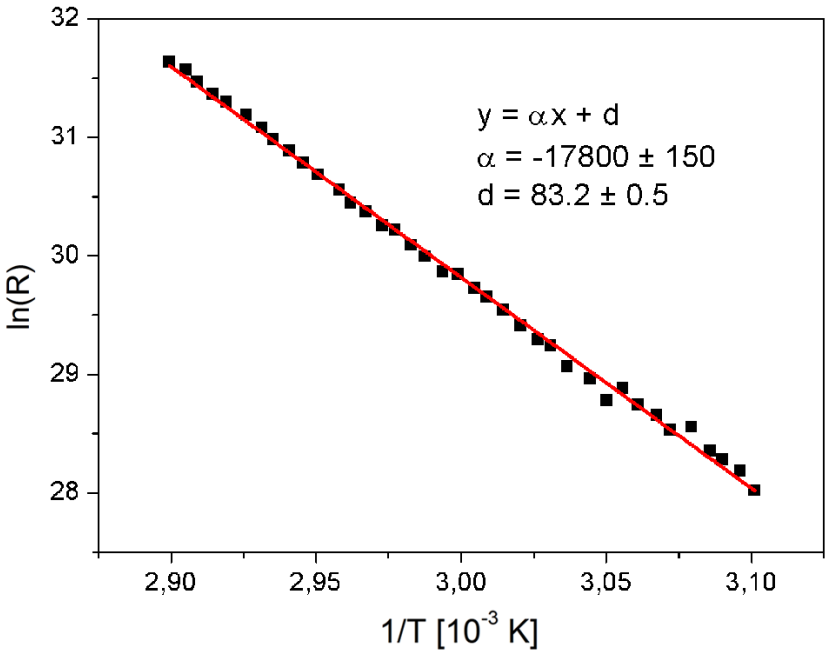

Figure 7.11.: Plot of $\ln(R)$ versus $1/T$ to determine the desorption energy for multilayer desorption of indigo from a sputter cleaned surface

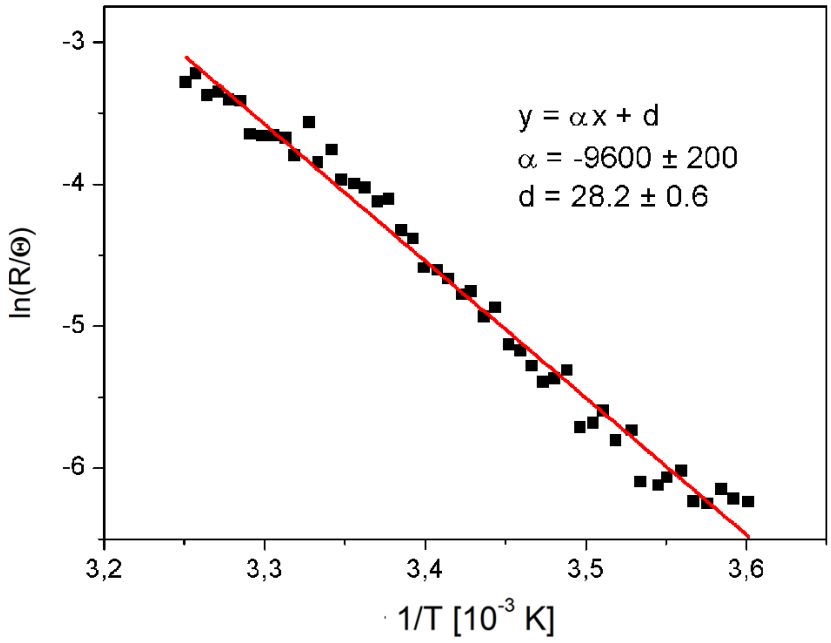

Figure 7.12.: Plot of $\ln(R/\Theta)$ versus $1/T$ to determine the desorption energy for monolayer desorption of indigo from a sputter cleaned surface

7.6. Surface Morphology

For a detailed look at the morphologies of indigo films and their correlations with the desorption spectra, ex-situ atomic force microscopy in tapping mode was used. In Fig. 7.14a an AFM image of an indigo film with a mean film thickness of 40 nm on a sputter cleaned surface is shown. The film consists of large, almost round islands with island heights between 50 and 100 nm, as shown in the cross section (Fig. 7.14b). After venting and storage under atmospheric conditions no further dewetting processes or morphology changes (Ostwald ripening) were observable. TDS spectra of indigo films on a sputter cleaned substrate taken before and after venting with subsequent re-evacuation showed significant material evaporation for the weaker bonded monolayer phase and only slight changes for the multilayer phase (Fig. 7.13). A comparison of the surface morphology for samples with 0.48 nm, 2.4 nm and 40 nm mean film thickness, measured with AFM immediately after exposure to air and then again 24 hours later, showed no changes in island size, shape or number. This suggests a stable configuration and complete immobilization of the indigo molecules once they are inherited into the bulk crystal structure, a discovery that is in good agreement with the high heat of evaporation (1.53 eV) found earlier. If one looks at an AFM image taken for an indigo film with the same mean film thickness on a carbon covered surface in Fig. 7.14c, one can see islands with similar shape, but clearly smaller and superior in number. The apparent island heights vary between 10 and 20 nm, as deduced from the cross-section in Fig. 7.14d. Apparently, in this case a continuous film already exists, so that the actual island height cannot be measured. Similarly, no changes in island size or shape were visible after sample storage under atmospheric pressure for multiple weeks. In consistency with the statements made earlier, the differences in island size, height and spacing can by described by an increased indigo dimer diffusion across the reactive silicon oxide surface compared to the monomer diffusion on a carbon covered surface. Spacing between individual islands on a sputter cleaned surface reaches up to a few hundred nanometers, which means that dimers can move very large distances until they finally get incorporated into an island and reach their stable configuration.

In Fig. 7.15a (sputter cleaned) and Fig. 7.15c (carbon covered) AFM pictures are shown for indigo films with a mean film thickness of 4.8 Å and 4 Å, respectively. Taking TDS measurement results into account, a mean film thickness of 4.8 Å on a sputter cleaned surface corresponds to the α-state, where the molecules form highly mobile dimers, but desorb already at room temperature. The small amount of material that can be seen is probably the result of some islanding of the α-state during warming to room temperature, prior to venting. However, on a carbon covered SiO_2 surface a mean indigo film thickness of 4 Å already corresponds to the β-state, which consists of stable islands. The cross-section (Fig. 7.15d)

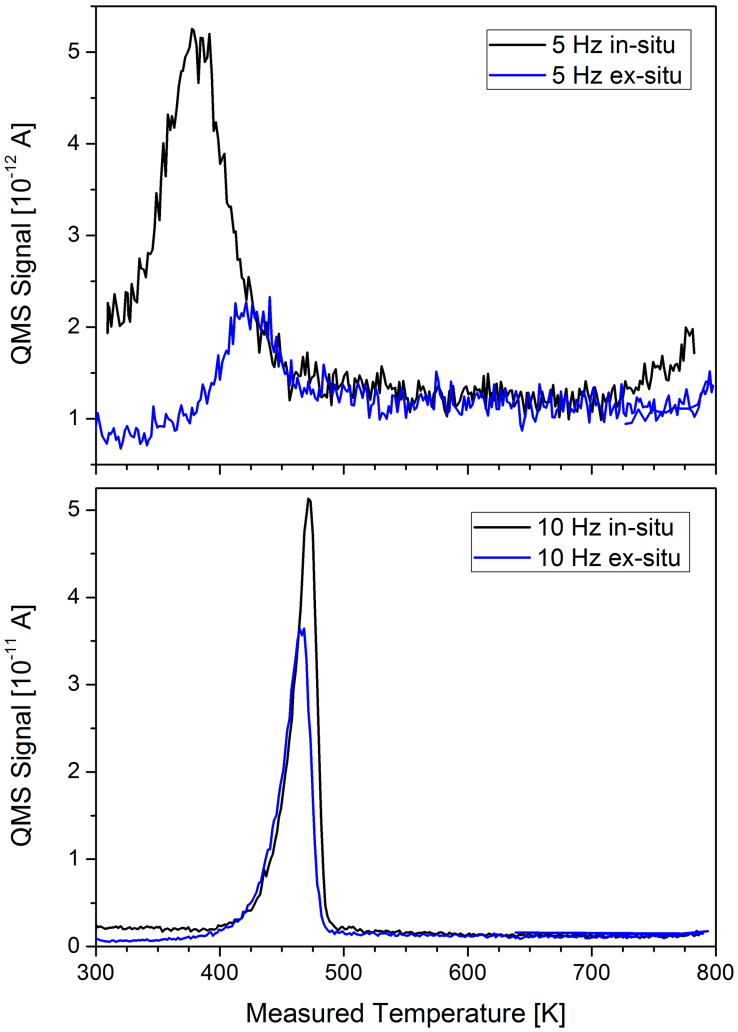

Figure 7.13.: Thermal desorption spectra of monolayer (top) and multilayer (bottom) indigo films before and after venting with subsequent re-evacuation

reveals heights between 5 and 15 nm. Integration over the island volumes provides a quite good agreement with the mean thickness as determined by the quartz microbalance. This corroborates the assumption, that in the β-state only negligible desorption takes place during warming to room temperature and venting.

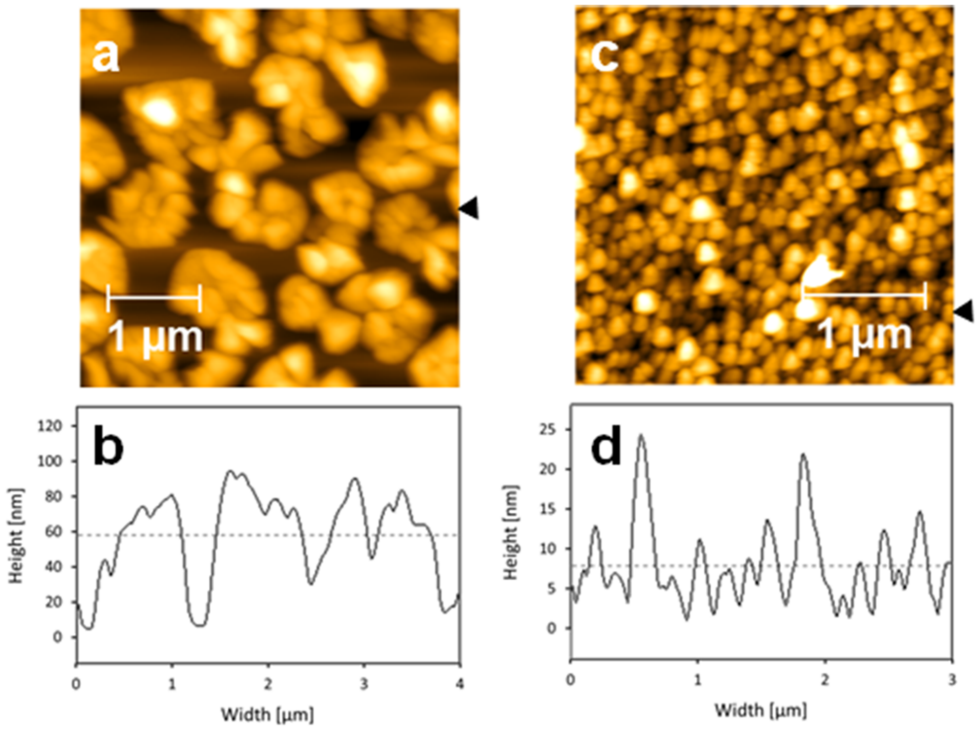

(a) 4×4 µm topography scan of a 40 nm thick indigo film on a sputter cleaned substrate

(b) Cross section along the line marked by the black arrow in (a)

(c) 3×3 µm topography scan of a 40 nm thick indigo film on a carbon covered substrate

(d) Cross section along the line marked by the black arrow in (c)

Figure 7.14.: AFM images of indigo films with a mean thickness of 40 nm on both sputter cleaned and carbon covered SiO_2. Substrate deposition temperature: 220 K. Deposition rate: 0.5 nm/min.

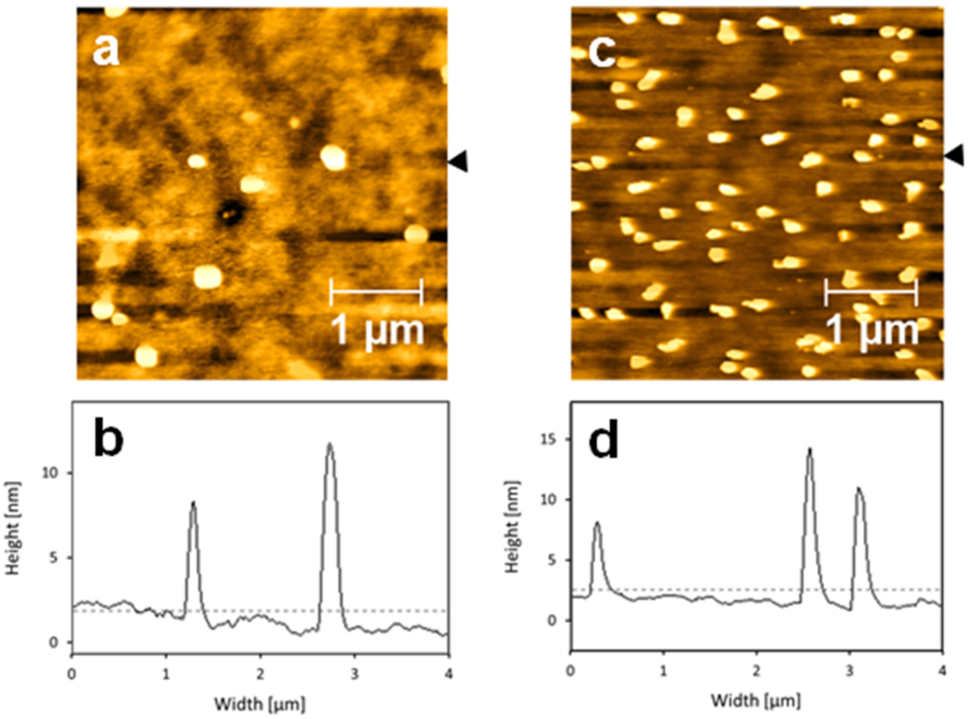

(a) 4×4 µm topography scan of a 0.48 nm thick indigo film on a sputter cleaned substrate

(b) Cross section along the line marked by the black arrow in (a)

(c) 4×4 µm topography scan of a 0.4 nm thick indigo film on a carbon covered substrate

(d) Cross section along the line marked by the black arrow in (c)

Figure 7.15.: AFM images of indigo films with mean thicknesses between 0.4 and 0.5 nm on both sputter cleaned and carbon covered SiO_2. Substrate deposition temperature: 220 K. Deposition rate: 0.5 nm/min.

7.7. Structural Characterization

Two polymorph crystal structures of indigo are known which are denoted as either polymorph A [59, 61, 176] or polymorph B [62, 184]. In both cases the lattice symmetries are the same (monoclinic, space group $P2_1/c$, two molecules within the unit cell) and even the packing of the molecules is nearly identical. The mass densities are slightly different with 1.50 g/cm^3 for polymorph A and 1.46 g/cm^3 for polymorph B. The packing of the molecules can be described by piles of stacked molecules where the aromatic planes of the indigo molecules are parallel to each other. In Fig. 7.16 three piles are shown, while only two molecules of a single pile are drawn. It is clearly visible, that the molecules of neighboring piles are tilted relative to each other. It is notable, that the distances of intermolecular hydrogen bonds (O ... H – N) are significantly shorter (2.17 Å) than typical intramolecular bonds (2.40 Å). The aromatic planes of stacked molecules are 3.40 Å separated from each other.

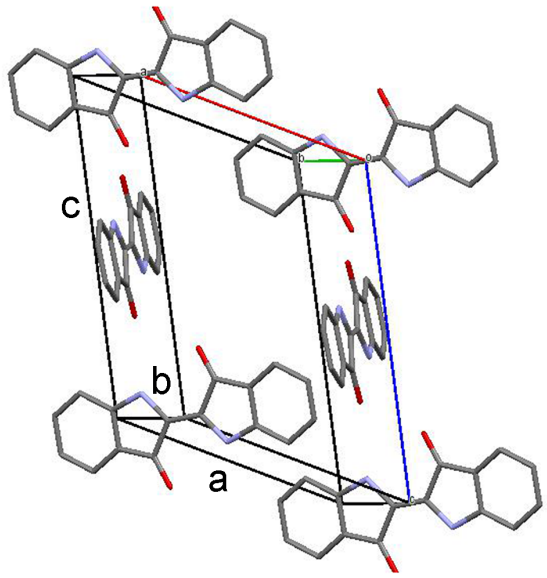

Figure 7.16.: Package of indigo molecules in the crystal together with the crystal unit cell

In the conducted experiments the crystallographic properties of two 40 nm thick indigo films on carbon covered and sputter cleaned SiO_2 substrates were determined by X-ray diffraction. A specular scan showed no observable peaks for a film grown on a sputter cleaned surface, hinting at completely random crystal orientation. However, on a carbon contaminated surface it was possible to see two reflections that can clearly be distinguished from the noise level at 2Θ angles of about 10.4 and 26.3 degrees (Fig. 7.17). A similar diffraction pattern has also been observed by Irimia-Vladu *et al.* for 75 nm thick indigo

films grown on an aliphatic tetratetracontane surface.[60] The type of polymorph cannot be unambiguously determined, since calculated peak positions of (100) and (210) of polymorph A as well as (-101) and (-212) for polymorph B fit well with the observed peak positions (compare Fig. 7.17). Despite different Laue indices for the Bragg peaks observed at 2Θ = 10.4° - (100) and (-101) - and for 2Θ = 26.3° - (210) and (-212) -, the orientation of the molecules relative to the substrate surface would be identical for both phases. In the first case the piles are aligned parallel to the substrate surface (Fig. 7.18a), while in the second case a molecular arrangement with some of the aromatic planes parallel to the substrate surface is observed (Fig. 7.18b). Additional pole figure measurements at these angles (see Fig. 7.19) show that the preferred orientations of the crystallites are weakly developed, a variation of ± 30° relative to the substrate surface is observed.

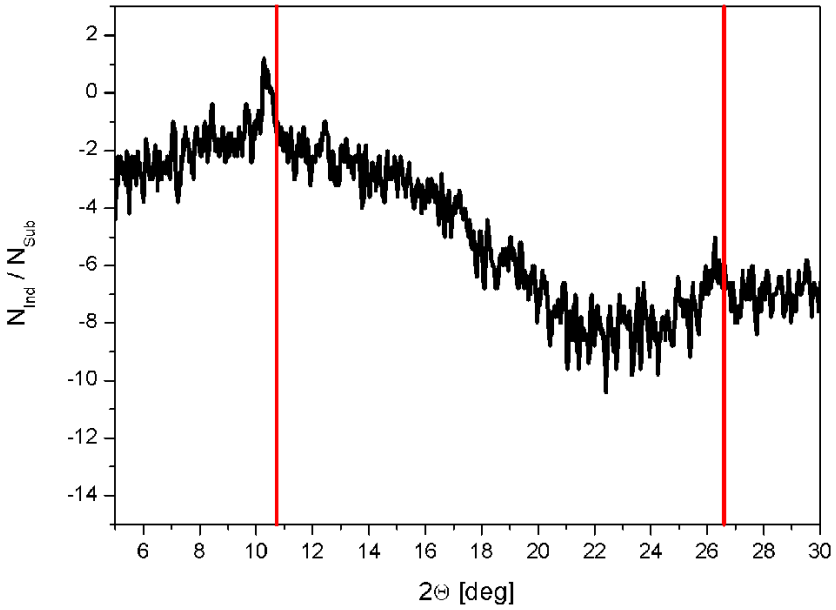

Figure 7.17.: Differential $\Theta/2\Theta$ scan for a 40 nm thick indigo film on a carbon covered SiO_2 substrate. The red lines indicate the nearest reflection angles of indigo powder in the α-phase (10.74° and 26.58°). [184]

One could speculate as to the reason for the different crystallization behavior of indigo on the sputter cleaned and carbon covered silicon oxide surface, and for the generally weaker tendency of these molecules to crystallize, as compared to rod-like organic molecules, e.g. pentacene [94, 95] or hexaphenyl [90–93]. It is reasonable to believe, that the main reason for this behavior is the fact, that the indigo molecules exhibit a chirality in the adsorbed state. Due to the missing mirror symmetry the achiral molecules in the gas phase become two-dimensional chiral after adsorption. As a consequence, when three dimensional islands have to be formed by diffusion-limited aggregation, only about half of the approaching molecules

will have the proper chirality to be incorporated without flipping the molecule. As we can see from the crystal structure (Fig. 7.16) a single indigo crystal is an enantiomerically pure crystal. All molecules within a crystal show the same handedness. Thus, a polycrystalline film will be a racemic conglomerate. It is obvious, that in such a case only small crystallites will develop.

The question remains, why no crystallinity can be observed at all for indigo on the sputter cleaned substrate. This might be correlated with the proposed formation of dimers in the adsorbed layer. Of course, the specific structure of such a dimer is not known, but under the assumption of a π-stacked dimer with four H-bonds, the two stacked molecules show different handedness, which makes it impossible to become incorporated into an enantiomeric crystal.

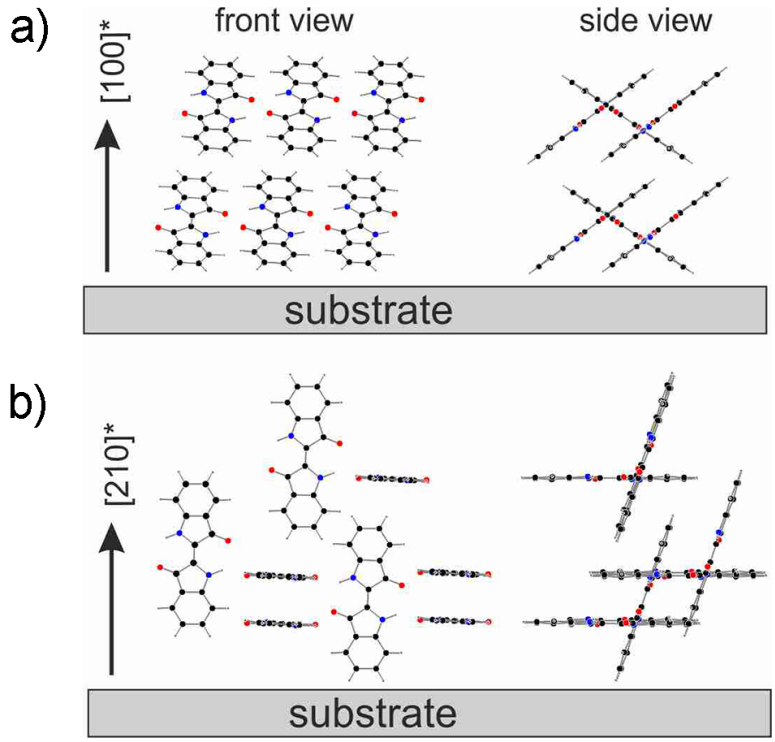

(a) Molecular arrangement of indigo molecules corresponding to the 2Θ peak at 10.4° in Fig. 7.17 viewed from the front (left) and side (right)

(b) Molecular arrangement of indigo molecules corresponding to the 2Θ peak at 26.3° in Fig. 7.17 viewed from the front (left) and side (right)

Figure 7.18.: Molecular arrangement of indigo molecules with respect to the substrate for the observed crystallographic orientations

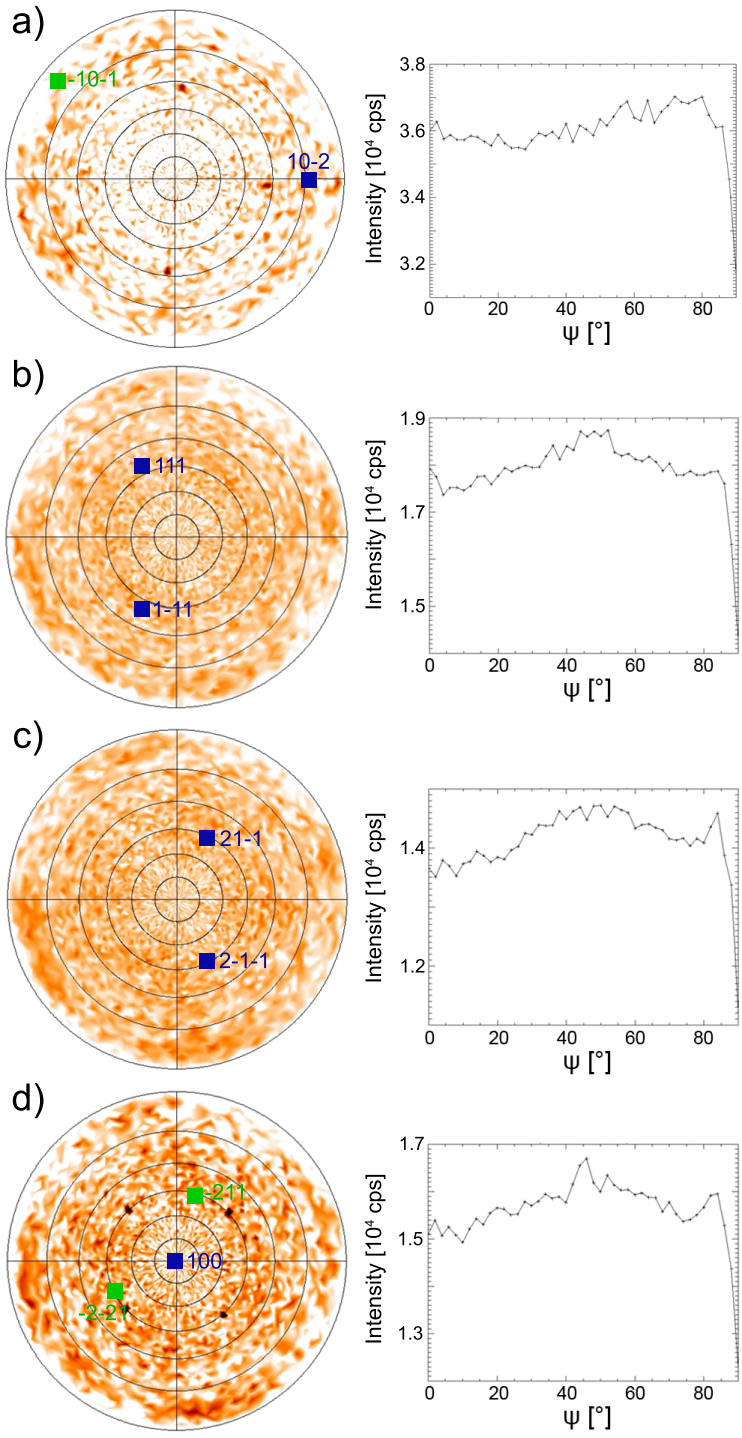

Figure 7.19.: XRD pole figure measurements and integrated ψ scans of indigo on SiO_2 taken from the four strongest reflections of indigo at 2Θ angles of 21.88° (a), 33.49° (b), 35.68° (c) and 37.1° (d). Every reflection can be explained by the (100) plane of indigo. Different intensities are represented by different orange scales where darker areas represent higher intensity.

7.8. Summary and Conclusion

In this chapter investigations on the initial film formation of indigo on multiple silicon dioxide substrates with the help of thermal desorption spectroscopy, atomic force microscopy and X-ray diffraction were shown. A comparison between sputter cleaned and carbon contaminated surfaces led to differences in diffusion behavior and island growth. In the first case the substrate is rather reactive and the indigo molecules are initially very strongly bonded and do not desorb from the surface in a temperature range of up to 430 K. After further adsorption possibly dimers are formed, which de-stabilize the bonding mechanism to the surface and lead to a weakly bonded α-state. Subsequently, at and above a certain coverage, the molecules dewet and form more strongly bonded three dimensional islands in the so called β-state. On the more inert, carbon covered substrates however, initially adsorbed indigo molecules form a similar metastable state, but dewet into islands at much lower coverage. All films with mean film thicknesses corresponding to the β-state were completely stable under atmospheric conditions. Films in the α-state could not be observed with AFM due to immediate desorption at room temperature. The sticking coefficient was found to be coverage independent and unity in all cases. Heat of evaporation calculations yielded desorption energies of 1.67±0.05 eV in the multilayer (β-state) and 0.84±0.05 eV in the monolayer regime (α-state) on a carbon covered and 1.53±0.05 eV (β-state) and 0.83±0.05 eV (α-state) on a sputter cleaned substrate. The frequency factors for desorption were determined to be about 1×10^{22} s^{-1} (carbon covered) and 1.4×10^{22} s^{-1} (sputter cleaned) for the β-state and 6×10^{12} s^{-1} (carbon covered) and 1.8×10^{12} s^{-1} (sputter cleaned) for the α-state. This hints at a quite localized desorption from the bulk state, but also at a high mobility of the molecules in the adsorbed state prior to desorption. Specular scans of a 40 nm thick film exhibited two weak diffraction peaks for carbon covered samples, which were located at 10.4 and 26.3 degrees. This can be dedicated to a weak crystallographic orientation along the (100) plane and (210) plane, respectively. Films on sputter-cleaned surfaces seem to be completely randomly orientated. The low tendency to crystallize at all can be traced back to the fact that adsorbed indigo molecules show chirality, which might hamper the correct incorporation of the molecules into the 3D crystal. The possible formation of special dimers on the sputter cleaned silicon oxide surface finally can make it even more difficult to form an enantiomeric crystal.

8 | Quinacridone

8.1. Introduction

Quinacridone (QA, $C_{20}H_{12}N_2O_2$, see Fig. 8.1), also known as linear trans-quinacridone [44], is a rod-like organic molecule of pink or red color with a molecular mass of 312.32 amu and an uncommonly high sublimation temperature of 535° C.[43] It consists of five linear-fused benzene rings and is often referred to as the H-bonded analogue to the very commonly studied pentacene molecule ($C_{22}H_{14}$). Liebermann *et al.* [185] were the first to synthesize quinacridone in the year 1935 and the discovery of its polymorphism and more efficient synthesis methods years later [43, 186–188] consequently led to simpler synthesis routes and has provoked considerable interest in both industry and academics ever since.[189] Its intense color and good solubility make the pigment highly popular for coating and coloring applications, e.g. as magenta printing ink. The scientific attention of quinacridone and other high-performance organic pigments is attributable to the formation of intermolecular hydrogen bonds leading to desirable charge mobilities and transport properties.[174]

In this chapter idiosyncrasies of quinacridone physical vapor deposition processes from various Knudsen cells will be explained. Thin films were grown on silicon dioxide substrates and analyzed by a multitude of spectroscopic methods, including thermal desorption spectroscopy, specular and grazing incidence X-ray diffraction and Raman spectroscopy.[1]

[1] As mentioned in section 1.4, large parts of this chapter emanate from a publication submitted to the Journal of Physical Chemistry C (Paper III, Ref. [69]) to which I have contributed as the leading author. Additional results are currently being prepared for publication (Paper IV).

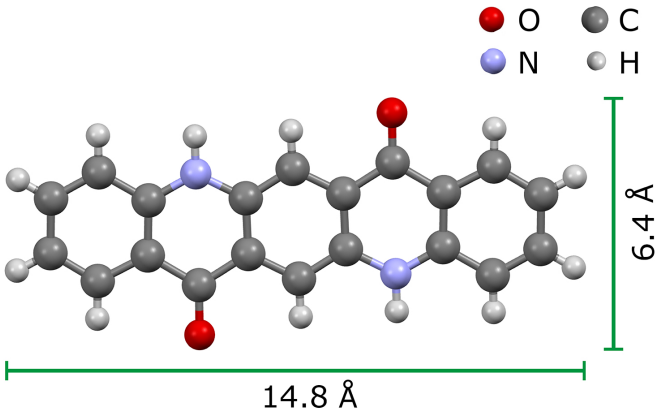

Figure 8.1.: Structure and van der Waals dimensions of the quinacridone molecule [34, 148]

8.2. Experimental

For all experiments in this chapter sublimation purified quinacridone, provided by Tokyo Chemical Industry with a purity of >99%, was used. Typically, the material was deposited, after proper outgassing, i.e., the evaporation of smaller and more volatile impurity molecules during the heating process, via physical vapor deposition from a stainless steel Knudsen cell heated to about 620 K. The inner diameter of the cell was 7 mm, the length 20 mm and the effusion hole diameter was 1 mm (compare Fig. 4.5 on page 51 and insert in Fig. 8.2). For several experiments it was necessary to switch to a glass Knudsen cell or other glass evaporation sources, which will be explained in more detail below. As substrate material, the already described silicon dioxide with a nominal thickness of 150 nm, that has been thermally grown on 525 µm thick Si(001) wafers, was used. The deposition process was conducted with a typical deposition rate of 105 ng/(min·cm^2), equivalent to 0.7 nm/min and controlled by a quartz microbalance, which could be placed intermittently at the sample position. The base pressure of the unbaked UHV chamber was typically 6×10^{-9} mbar. Furthermore, the whole sample stage was LN_2 cooled to 200 K during film deposition, if not stated otherwise.

An analysis of the chemical composition of the untreated substrate surface via AES revealed silicon and oxygen peaks originating from the substrate, with a slight carbon contamination on top. This carbon signal increased slightly as a consequence of repeated adsorption-desorption cycles. Such a carbon covered SiO_2 surface was used for the described experiments. An Auger analysis of vapor deposited quinacridone films showed the expected carbon, nitrogen and oxygen signals. Unfortunately, it was not possible to perform continuous Auger surveillance during different stages of the film growth process, due to the

destructive behavior of the electron beam on the organic films. After material deposition the samples were placed in front of a quadrupole mass spectrometer (QMS) tuned to typical cracking masses of quinacridone, i.e., either to 128 amu or 76 amu. When analyzing TD spectra of organic molecules with a QMS, cracking of the molecules in the ionization chamber of the spectrometer is unavoidable. This is due to electron impact induced fragmentation during the ionization process. Therefore, the cracking pattern depends on several QMS setting parameters. The measured cracking masses should not be mixed up with possible decomposition products entering the ionization chamber of the QMS after desorption from the surface.

8.3. Adsorption and Desorption of Quinacridone and its Decomposition Products on/from carbon covered SiO_2

Initially, thermal desorption experiments were carried out after physical vapor deposition of quinacridone on carbon covered SiO_2 from a metal Knudsen cell. The thermal desorption spectra of a 4.25 nm thick quinacridone film yielded a single desorption peak at, depending on the coverage, about 500 K (denoted γ, see red line in Fig. 8.2) when the QMS was tuned to a cracking mass of 128 amu. As already extensively described, the employed measurement setup does not provide a convenient way to measure the temperature directly at the SiO_2 surface, since the thermocouple is rather located at the backside of the sample and directly connected to the steel sample holder. However, the stainless steel mounting clamps are likewise subject to material deposition during the adsorption process, resulting in a small peak (labeled Ta) in the TDS curves where the organic molecules desorb from the metal. This is an indicator of the true desorption temperature ($\sim$500 K) and in good agreement with the conducted first order temperature correction (described in more detail in chapter 8.7). The corrected temperature values were plotted as top axis in all figures. The cracking fragment at 128 amu was chosen because it is very prominent in the quinacridone cracking pattern [146] and showed a reasonably good signal to noise ratio. Experimental limitations did not allow detecting the main mass of quinacridone or any other fragments higher than 200 amu. If there were only a single molecular species present on the surface, as one might assume from the red curve in Fig. 8.2, then the choice of cracking mass should have no significant influence and spectra for different cracking masses should be comparable. However, surprisingly, when tuning the QMS to the cracking mass 76 amu, a second peak at about 420 K (denoted β-peak, black line in Fig. 8.2) appeared, in addition to the expected peak at 500 K. A full TDS series consisting of multiple desorption spectra of thin quinacridone films from carbon covered

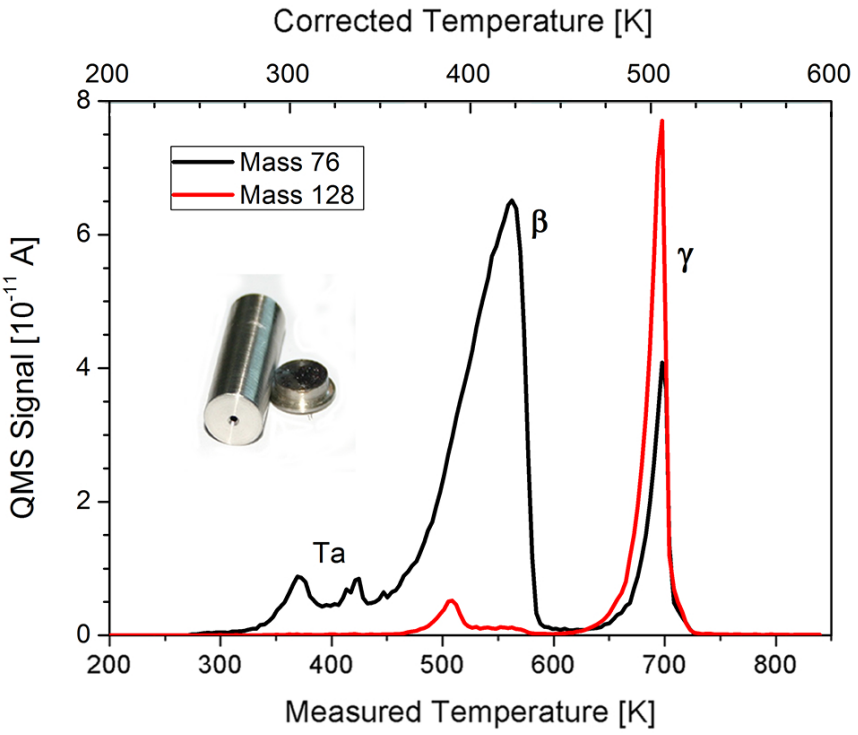

Figure 8.2.: Thermal desorption spectra for cracking masses of 76 amu (black) and 128 amu (red) of a 4.25 nm thick film which was grown on carbon covered silicon dioxide by evaporation of quinacridone from a stainless steel cell. Adsorption temperature T_{ad} = 200 K. Deposition rate A = 0.7 nm/min. Heating rate β_H = 1 K/s. The small peaks at 310 K, 340 K and 380 K stem from desorption from the Ta mounting clamps.

silicon dioxide is plotted for both masses in Fig. 8.3. The adsorption temperature was held constant at 200 K throughout all experiments. Fig. 8.3a shows a series of thermal desorption spectra of cracking mass 128 amu for exposures between 1.7 Å and 42.5 Å. Throughout all coverages one can once again observe a single desorption peak (γ-peak) at temperatures between 470 K and 520 K. The common leading edge between peaks of different coverages, the shift to higher temperatures of the peak maxima and the sudden cut-off are a clear sign of zero order multilayer desorption.[155] After tuning the mass spectrometer back to a cracking mass of 76 amu (Fig. 8.3b), one is, similar to Fig. 8.2, clearly able to see an additional desorption peak (β) at lower temperatures. This peak appears at roughly 100 K lower temperature, is slightly broader when compared to the γ-peak and shows signs of a common trailing edge. Additionally, for very low mean film thicknesses (between 1.7 Å and 8.5 Å total coverage) a metastable molecule configuration can be observed (α), that already shows slow desorption at 200 K. Mass spectrometry, XRD and GIXD investigations, which will be shown at a later point in this chapter, matched the α and β-peaks with indigo desorption. Taking

previous works on similar organic molecules into account [57, 68, 190, 191], it is assumed that the α-configuration consists of flat-lying and weakly bonded molecules. During this stage the β-peak is not yet visible. The molecules appear to be able to overcome the activation barrier for the reorientation process at layer thicknesses of more than 8.5 Å total coverage. The value of 8.5 Å corresponds to a layer thickness of about 6 Å if only the β-peak fraction is taken into account (see below). During the described reorientation process the very weakly bonded initial state of flat-lying molecules changes to a more stable and strongly bonded multilayer structure.

Due to the β-peak only appearing at certain cracking masses and the γ-peak being visible throughout all the masses in the quinacridone cracking pattern, one can disclose the existence of two distinctive molecules on the surface, independent of coverage. A second, weakly bonded molecule type with a different cracking pattern and, hence, a different desorption behavior is clearly present. Indeed, a full mass scan between 35 amu and 150 amu during desorption of the β and γ-peak, respectively, shows different cracking patterns (Fig. 8.4). The γ-peak and its cracking pattern are in good agreement with literature data of quinacridone [146] and it is therefore assumed that it corresponds to thermal desorption of pure quinacridone. This assumption is supported by several spectroscopic analyses, as will be shown below. Combining the cracking pattern of the β-peak with specular X-ray diffraction, Raman spectroscopy and GIXD made it possible to match this peak with indigo (IN, $C_{16}H_{10}N_2O_2$).[192] Indeed, multiple spectroscopic observations of a film corresponding to the β-peak agree reasonably well with data from chapter 7 describing the growth and desorption behavior of pure indigo films that were grown on SiO_2 under identical conditions. However, the spectroscopic data hint at the existence of an additional type of molecules in this film, although not observed in the TDS, which could be identified as carbazole (CA, $C_{12}H_9N$).[193]

Since all desorption spectra up to this point illustrate that the unaltered quinacridone molecules are significantly stronger bonded that the smaller decomposition products (100 K desorption temperature difference), it raised the question if a selected adsorption process is possible where the substrate is heated past the desorption temperature of the smaller molecules but still not high enough for the quinacridone molecules to desorb. This indeed proved to be successful for a substrate temperature of 400 K, as it can be seen in Fig. 8.5. (If the sample is held at a specific temperature for a longer period of time, then the measured temperature is roughly equal to the equilibrium temperature.) However, later results will show that this technique is not entirely convenient for the creation of pure quinacridone samples as many of the smaller particles present in the deposition flux decompose on the surface and form additional non-desorbing decomposition products.

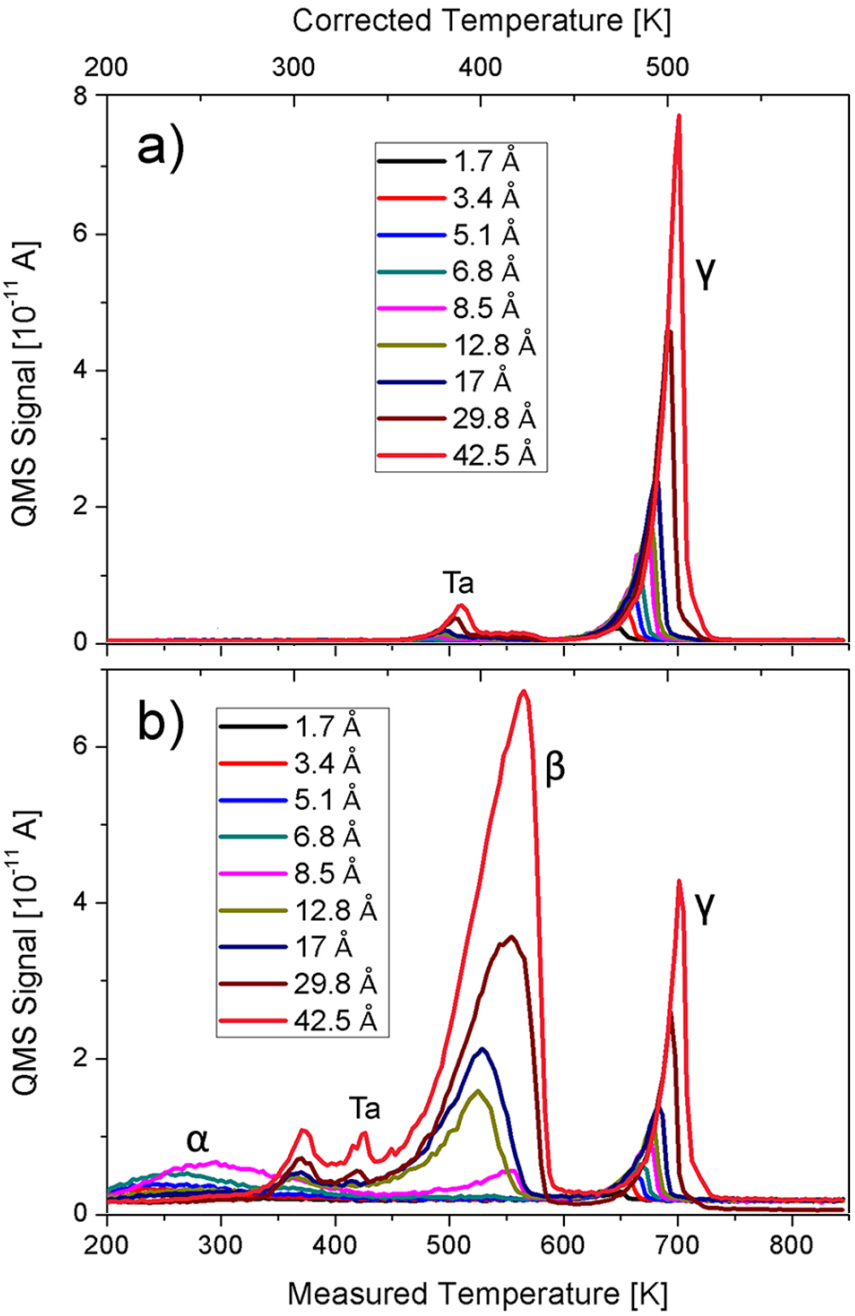

Figure 8.3.: Thermal desorption series of quinacridone from carbon covered silicon dioxide for different exposures, as determined by a quartz microbalance. The top picture (a) shows cracking mass 128, the bottom picture (b) cracking mass 76. Adsorption temperature: 200 K. Deposition rate: 2.6 Å/min. Heating rate: 1 K/s.

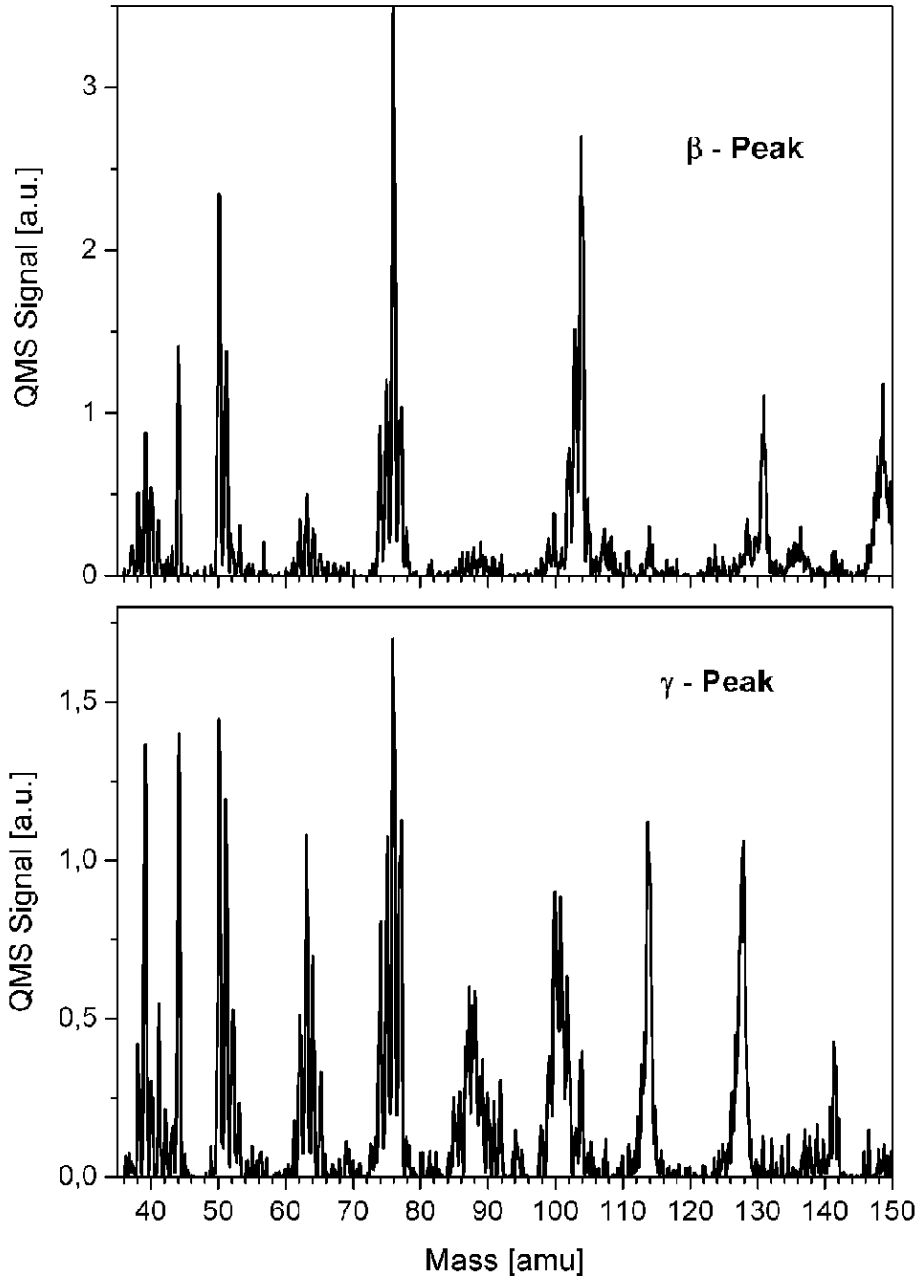

Figure 8.4.: Accumulated mass spectra (cracking spectra) of the desorption flux in the range of 350 K – 450 K (β-peak) and 470 K- 530 K (γ-peak). Sweep rate: 0.2 s/amu. A 3 nm thick film, prepared by evaporation of quinacridone from a stainless steel Knudsen cell was used for this experiment. Heating rate: 1 K/s. Adsorption temperature: 200 K.

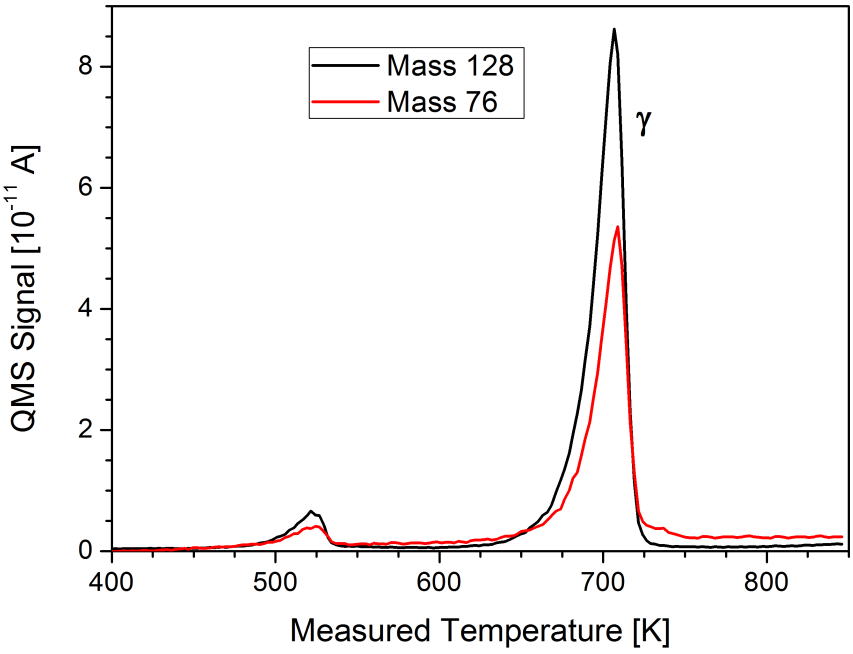

Figure 8.5.: Thermal desorption spectra for cracking masses of 128 amu (black) and 76 amu (red) of a 6.6 nm thick film which was grown on carbon covered silicon dioxide at an elevated substrate temperature of $T_{ad} = 400$ K

8.4. Adsorption and Desorption of Quinacridone and its Decomposition Products on/from sputtered SiO_2

For the sputter cleaned SiO_2 substrate multilayer desorption up to a mean thickness of 21.3 Å was investigated, as shown in Fig. 8.6. It should be mentioned once more that for these experiments the surface was sputter cleaned after each TDS. The γ-desorption peaks in this case likewise exhibit zero order desorption kinetics. The discrepancy between the desorption behavior from a C-covered substrate and the measurements shown in Fig. 8.6 is caused by the formation of a strongly bonded wetting layer on the rather reactive SiO_2. Up to a mean film thickness of 3.4 Å, which roughly corresponds to one monolayer of lying molecules [148], no material desorption can be observed at all during heating to 600 K, neither for a cracking mass of 128 amu nor for a cracking mass of 76 amu. However, the subsequent desorption from the multilayer is not significantly influenced by the initial condition of the silicon dioxide surface, once the full wetting layer has been formed.

To summarize the thermal desorption results it is therefore convenient to describe the

film formation and desorption behavior on sputter cleaned silicon dioxide as follows: Initially, single molecules of both indigo and quinacridone adsorb on the surface and form chemical bonds that prove to be so strong, that no desorption occurs up to 600 K. As soon as a certain coverage threshold of 3.4 Å mean thickness is reached, which corresponds to one full monolayer of lying molecules, the influence of the reactive silicon dioxide surface has been overcome and newly impinging molecules can adsorb on the soft organic layer. This described process does not occur on a non-sputtered substrate due to the already existing carbon atoms undertaking the function of a wetting layer. Subsequently both the indigo and quinacridone molecules form separate multilayer islands with different desorption temperatures and bonding strengths. Desorption evaluations of quinacridone show multilayer growth on top of the wetting layer with strong binding and clear zero order desorption. The indigo molecules on the other hand first form a very weakly bonded monomer layer on top of the already existing wetting layer. At a coverage threshold of roughly 6-7 Å – assuming a molecule ratio of 63±5% indigo and 37±5% quinacridone in the deposition flux (see below) – a dewetting process occurs where the indigo monomers reorientate into subsequently growing islands. This initial weakly bonded α-state compares reasonably well with the desorption kinetics of purified indigo on SiO_2, as described in the previous chapter.

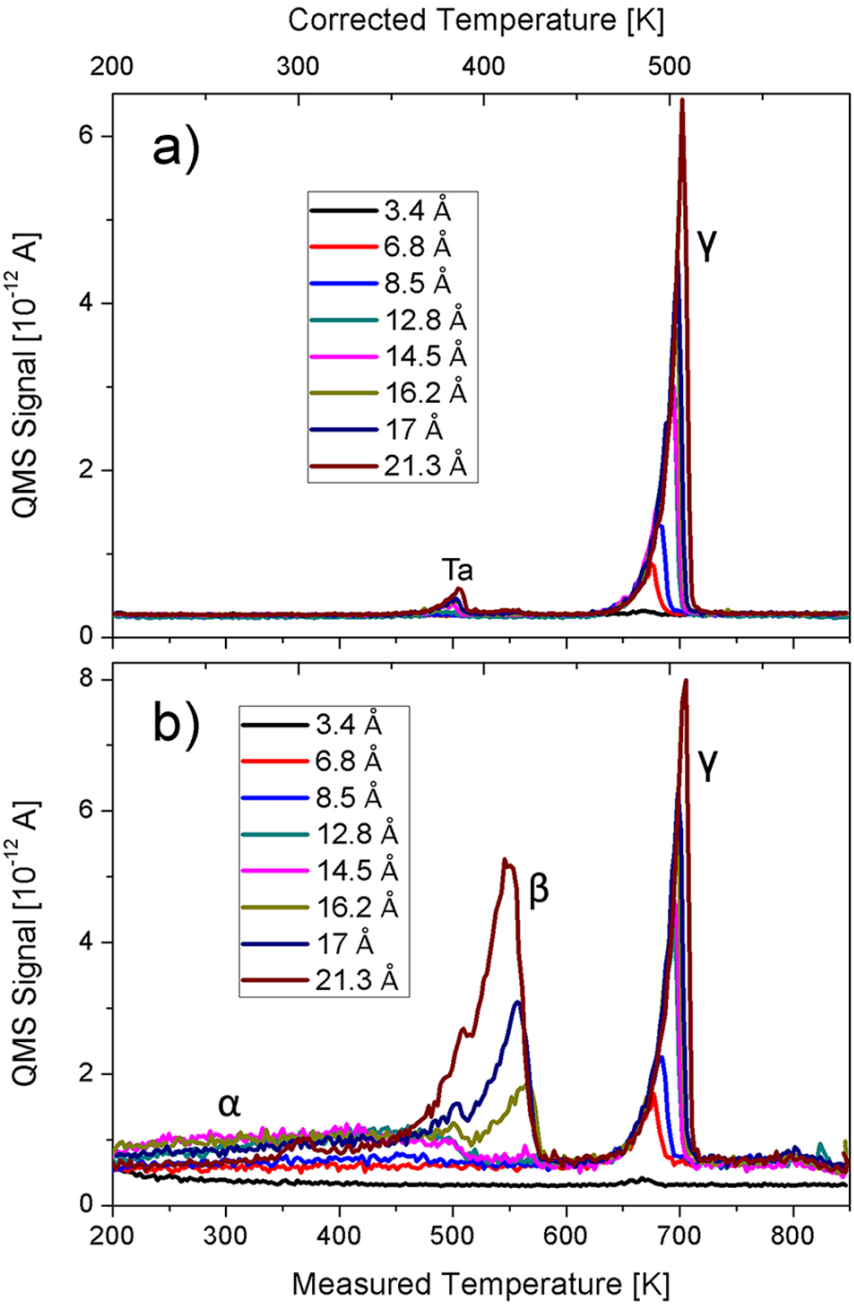

Figure 8.6.: Thermal desorption series of quinacridone from sputter cleaned silicon dioxide for different exposures, as determined by a quartz microbalance. The top picture (a) shows cracking mass 128, the bottom picture (b) cracking mass 76. Adsorption temperature: 200 K. Deposition rate: 4.1 Å/min. Heating rate: 1 K/s.

8.5. Separating the Different Molecule Types with the Help of a Secondary Sample Holder

At this point, the question arises whether indigo is generated on the silicon dioxide surface during heating of a pure quinacridone film or whether this type of molecules is already effusing from the stainless steel Knudsen cell. To address this issue, the following experiments have been performed: After the growth of a thin film with the described physical vapor deposition from the stainless steel Knudsen cell, a second sample holder with an identical Si/SiO_2 wafer, held at room temperature, was put in front of the primary sample (compare Fig. 4.5 on page 51). Heating this primary sample to 425 K exclusively caused the molecules corresponding to the β-peak to desorb while the more strongly bonded quinacridone remained (see Fig. 8.5). The employed geometry (1.0 cm distance between the two 1 cm^2 large samples, assuming a cosine desorption distribution) allowed about 1/3 of the desorbed molecules to re-adsorb on the stationary sample, which turned out to be a convenient way to create films with solely weakly bonded indigo and/or other decomposition molecules (β-peak). After breaking the vacuum this stationary sample was installed on the heatable sample holder and a TDS was performed as soon as UHV conditions were reached. The desorption spectrum of this film was similar in shape to the original β-peak, demonstrating that this molecular species remains unchanged during the described re-adsorption and subsequent desorption (see Fig. 8.8a).

Applying a similar experimental procedure, material corresponding to the γ-peak was deposited on the stationary sample and a TDS was performed after venting and re-evacuation. In this case, solely the γ-peak appeared in the desorption spectrum (see Fig. 8.8b), confirming that the β-peak is not a result of quinacridone decomposition during sample heating. Thus, the indigo observed in the desorption spectra (Fig. 8.2 and Fig. 8.6) must have originated from the stainless steel Knudsen cell. Indeed, a full mass spectrum between 35 amu and 200 amu of the deposition flux leaving the metal Knudsen cell (see Fig. 8.7) confirmed the existence of prominent cracking fragments from both indigo (β-peak) and quinacridone (γ-peak) molecules.

Thermal decomposition (pyrolysis), dissociation and isomerization processes involving collisions of organic molecules with hot surfaces are commonly observed and well characterized in the field of organic chemistry.[194, 195] Apparently, quinacridone seems to be particularly prone to such decomposition processes, due to its high sublimation temperature.[196] However, only sparse reports exist involving cracking and/or restructuring of chemical bonds with the subsequent formation of new and stable molecules for quinacridone-based and other H-bonded materials. Haucke *et al.* [197] described a smooth and homogenous transition from indigo to epindolidione in the vapor phase, if the former is heated to 733 K under vacuum con-

ditions. Berg *et al.* [185] observed decreasing mobilities for quinacridone organic field-effect transistors grown in vacuum after repeated temperature gradient sublimation preparation circles.

After having verified that a decomposition process takes place in the stainless steel Knudsen cell the question arises as to the quantitative ratio of the effusing molecules, corresponding to the β- and γ-peak. Despite the fact that both species exhibit common cracking masses (e.g. 76 amu), one has to be aware that the intensities of the different desorption peaks depend on the detailed measurement conditions and no statements can be made on the actual distribution and relative amount of the molecules on the samples. To address this issue, AFM measurements were performed on films prepared with the method described above, consisting either of material corresponding to the β or γ-peak, respectively (see Fig. 8.9). Evaluation of the cross sections of the island-like films allowed a quantitative determination of the effusion rates. Mean island heights of 10±2 nm (only β-peak molecules) and 4±1 nm (only γ-peak molecules), respectively, combined with the fact that some γ-peak material decomposes upon the initial heating to 425 K, results in a flux ratio of 63±5 % indigo to 37±5 % quinacridone. All given mean thickness values in this chapter correspond to the total amount of adsorbed material, hence including both molecules. The molecular ratio given above should therefore be taken into account if the two types of molecules were to be analyzed separately.

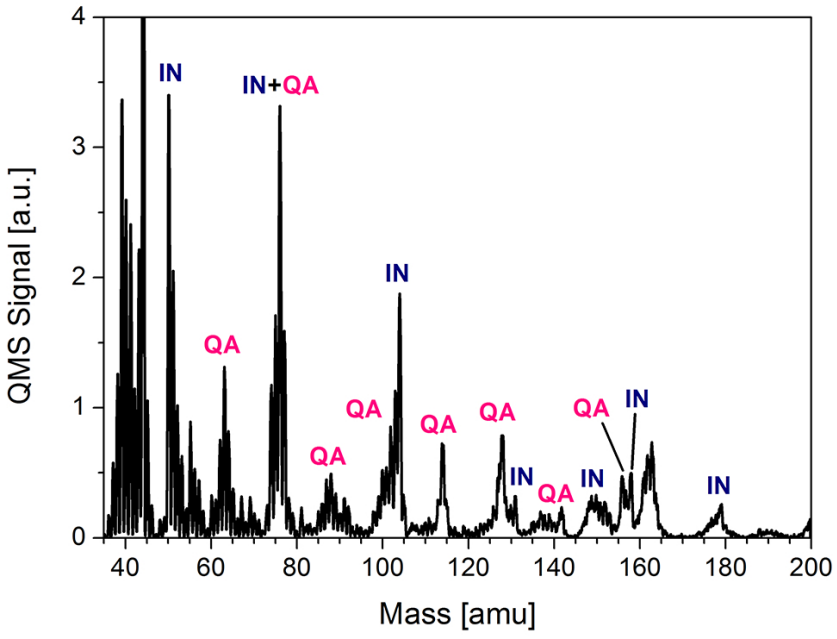

Figure 8.7.: Cracking spectrum of the stainless steel Knudsen cell deposition flux. Knudsen cell temperature: 650 K.

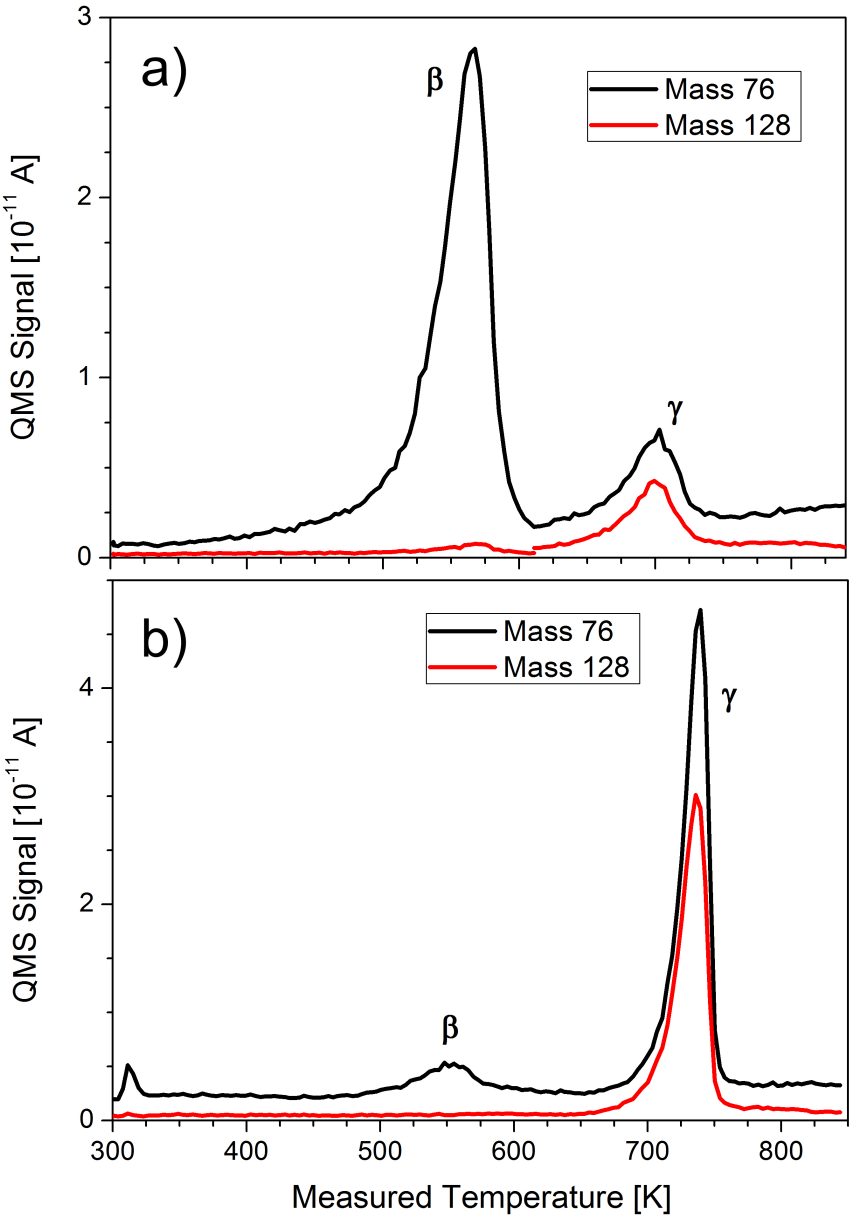

Figure 8.8.: Thermal desorption spectra for cracking masses of 76 amu (black) and 128 amu (red) of two films that were grown with the help of a secondary sample holder and which only consist of the β-peak (a) and γ-peak (b), respectively. For both films about 85 nm material was evaporated onto the primary sample. However, the resulting thickness values are significantly lower (∼10 nm and ∼4 nm, respectively), as it was determined by AFM.

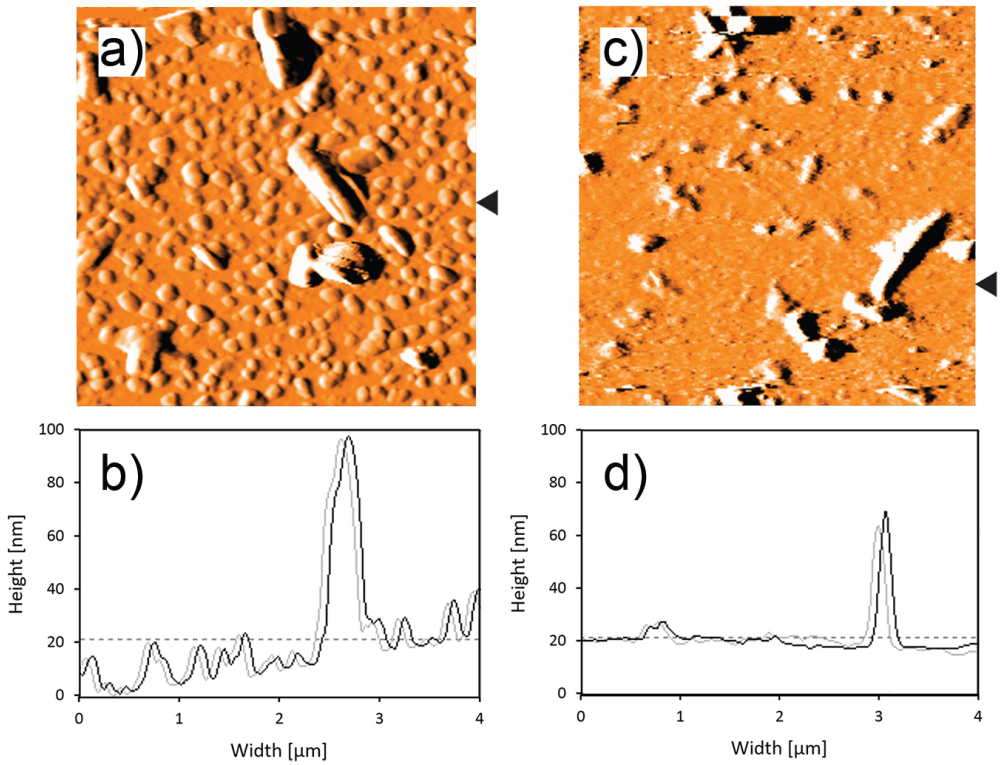

(a) AFM micrograph (4 µm × 4 µm) of a film consisting of molecules corresponding to the β-peak grown via desorption and re-adsorption onto a secondary sample holder

(b) Cross section along the line marked by the black arrow in (a)

(c) AFM micrograph (4 µm × 4 µm) of a film consisting of molecules corresponding to the γ-peak grown via desorption and re-adsorption onto a secondary sample holder

(d) Cross section along the line marked by the black arrow in (c)

Figure 8.9.: AFM images of films with only one molecule type present

8.6. Influence of the Knudsen Cell Type on the Evaporation of Quinacridone

In a first attempt to quantify and describe the chemical cracking process and to confirm the coexistence of different types of molecules on the surface despite the fact that only purified quinacridone is present in the Knudsen cell, the deposition process was repeated with various Knudsen cells and different evaporation sources. In order to check the purity of the quinacridone source material and to, therefore, rule out possible contaminations, a 18 nm thick quinacridone film was grown on a silicon dioxide sample via Langmuir evaporation

from an open quartz glass tube (see inset in Fig. 8.10) in a separate vacuum chamber. The sample was then again installed in the UHV chamber and analyzed via thermal desorption. As shown in Fig. 8.10, only the γ-peak appears in the desorption spectrum, indicating that the employed material is indeed pure and that no material decomposition occurs in that case. In the case of Langmuir evaporation (or free evaporation) [198] the sublimed molecules can be deposited at the substrate surface without any further collision in between. Contrary, in the evaporation from a Knudsen cell the sublimed molecules hit many times the inner cell wall before they leave the small effusion hole. For our particular stainless steel Knudsen cell dimensions, a distance of 5 cm between sample and Knudsen cell orifice and a typical deposition flux of 105 ng/(min cm^2) calculations result in about 400 collisions of a sublimed particle with the inner walls before escaping through the effusion hole. This corroborates the assumption of a thermally activated decomposition process within the metal Knudsen cell.

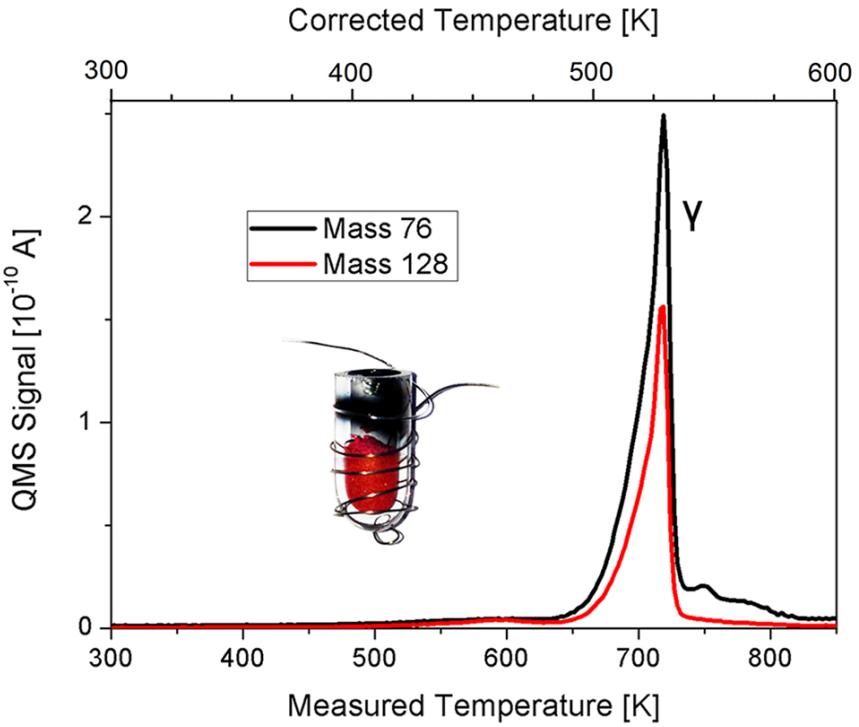

Figure 8.10.: Thermal desorption spectrum for an 18 nm thick quinacridone film deposited from a glass evaporation cell (Langmuir evaporation). Substrate temperature: 300 K.

As a next step, it comes to answer the question whether the decomposition of quinacridone occurs due to a possible catalytic behavior of stainless steel or whether it can be reproduced in other Knudsen-like evaporation cells. To this end, a special glass cell of Knudsen type

was employed. This cell featured a diameter of about 10 mm with a 3 mm wide nozzle. Wiring of the resistive heating filament (0.5 mm thick Ta-wires) around the cell was done in different ways, either by focusing on the nozzle area (inset in Fig. 8.11a) or on the backside of the cell (inset in Fig. 8.11b). To discuss differences in the deposition behavior of this glass cell compared to a typical metal Knudsen cell, one needs to first recall the physical processes happening within such a cell. Clearly, the limited wiring of the heating filament, combined with the poor heat conductivity of quartz glass lead to a strongly varying temperature distribution along the long cell axis, contrary to the required uniform heating of an ideal Knudsen source. In the first case, the nozzle area is, due to its smaller cross-section, significantly hotter than the residual cell walls. Due to the missing wiring at the backside we can, in turn, assume, that the back wall, where all the material leaving a Knudsen cell in a straight path typically comes from, is significantly colder in comparison and does therefore not contribute to any material deposition whatsoever. Instead, all molecules that eventually leave the cell in a direction where they can reach the sample surface need to have at least surpassed one collision under low angle with the higher temperature cell wall in the nozzle area. Actually, the temperature of the nozzle is much higher than needed to just evaporate the material. Therefore, the thermally activated cracking process of quinacridone molecules can be expected to occur more likely in such an excessively hot nozzle. Indeed, deposition from a glass Knudsen cell featuring dense wiring near the nozzle area resulted in the complete cracking of every single quinacridone molecule, hence only the β-peak being visible in the TDS spectrum (Fig. 8.11a). In contrary, the usage of a glass Knudsen cell with a colder nozzle and a heated backside again showed partial cracking, comparable to results from a metal cell, and different molecular species were once again present on the sample (Fig. 8.11b).

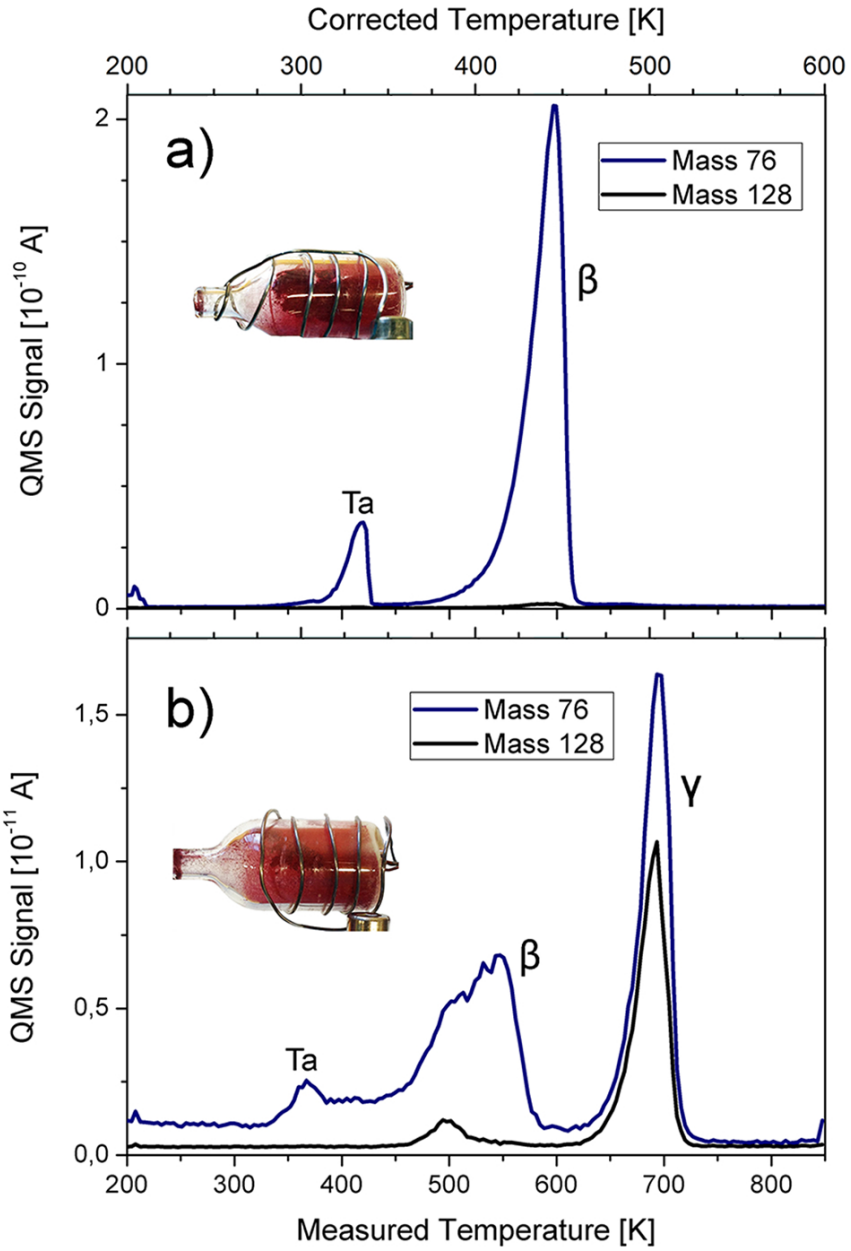

Figure 8.11.: Thermal desorption spectra for quinacridone films deposited from a glass Knudsen-type cell with dense wiring near the nozzle (a) and after removal of said wiring and increased heating at the backside (b). The nominal film thicknesses are 5 nm in plot (a) and 2.5 nm in plot (b). Adsorption temperature: 200 K.

8.7. Sticking Coefficient

In order to discuss the formation of islands as a function of coverage, dewetting and possible interactions of the two molecules on the surface, one needs to evaluate the relationship between impinging and desorbing molecules. A plot of the amount of material that was deposited onto the sample versus the amount of desorbed material is a good indicator of how likely molecules are to stick to the surface. For this purpose the area under the individual desorption curves was integrated and plotted versus the exposed amount, as measured by the quartz microbalance. Fig. 8.12 shows this relationship for the β-peak and Fig. 8.13 for the γ-peak. On a carbon covered substrate both the quinacridone (red curve in Fig. 8.13) and the molecules resulting from the cracking process (red curve in Fig. 8.12) show a surface coverage that increases linearly with the amount of exposed material. Initially, one would assume that this corresponds to a sticking coefficient of unity throughout all coverage ranges. However, the constant buildup of carbon residue on the substrate surface, which was already described in chapter 5.3, disproves this assumption and leaves only one possible explanation: Quinacridone as well as both its cracking products desorb only partially from an already carbon covered substrate while leaving a certain percentage of molecules behind, which will then dissociate upon further heating and remain as carbonic residue on the surface. The sticking coefficient curve does then consequently show a linear increase for all exposures, but is nonetheless smaller than unity by the fraction that is left behind.

On sputtered SiO_2 both types of molecules initially show a very small sticking coefficient which starts to increase slightly at around 10-20 Å of total exposure. However, even for high coverages neither quinacridone nor indigo/carbazole reach a slope that is equal to that on carbon covered substrates. This can be explained by the formation of a strongly bond wetting layer (less material desorption at small coverages) on the one hand and a sticking coefficient smaller than unity on the other hand. This is a peculiar situation since the sticking coefficient of large and rod-like organic molecules is generally assumed to be unity for higher coverages at and below room temperature.[152, 153] However, some comparable adsorbate/substrate systems exist where sticking coefficients smaller than one have been reported throughout all coverage regimes (compare the discussion made in chapter 6.9). A possible explanation for the reduced sticking in the observed system is an orientation mismatch on the smooth silicon dioxide surface , i.e. 'upright' molecules are unable to 'lie down' when approaching the surface due to their rigid structure and get scattered elastically. The carbon surface in turn is much softer enabling molecules to hit-and-stick independent of their original orientation. However, this does not explain the reduced sticking at coverages of multiple layers and further simulations (e.g. through molecular dynamics) are necessary to fully understand this phenomenon.

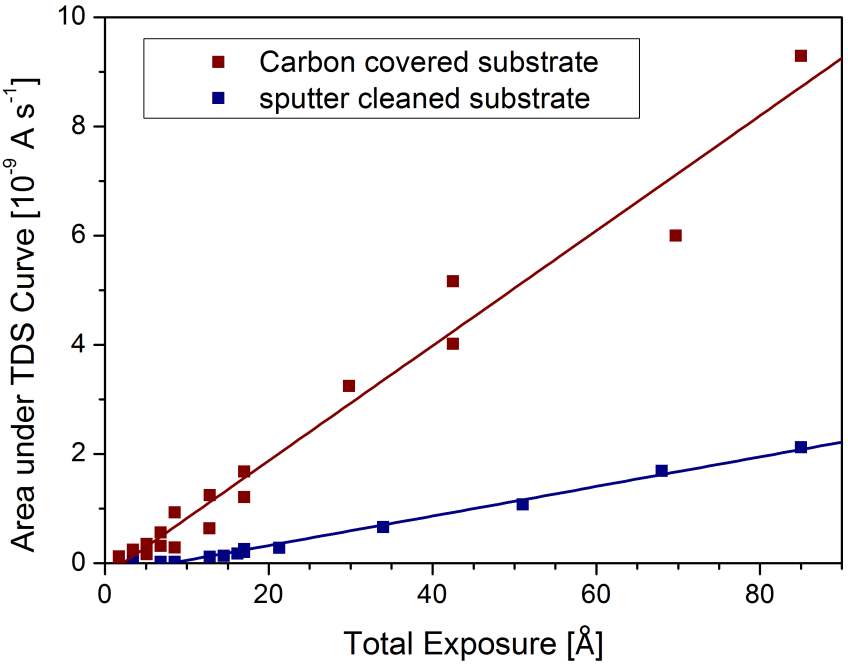

Figure 8.12.: Area under the TDS curves for the first molecule type (β-peak) desorbed from carbon covered and sputter cleaned silicon dioxide as a function of the total exposed amount, as measured by a quartz microbalance

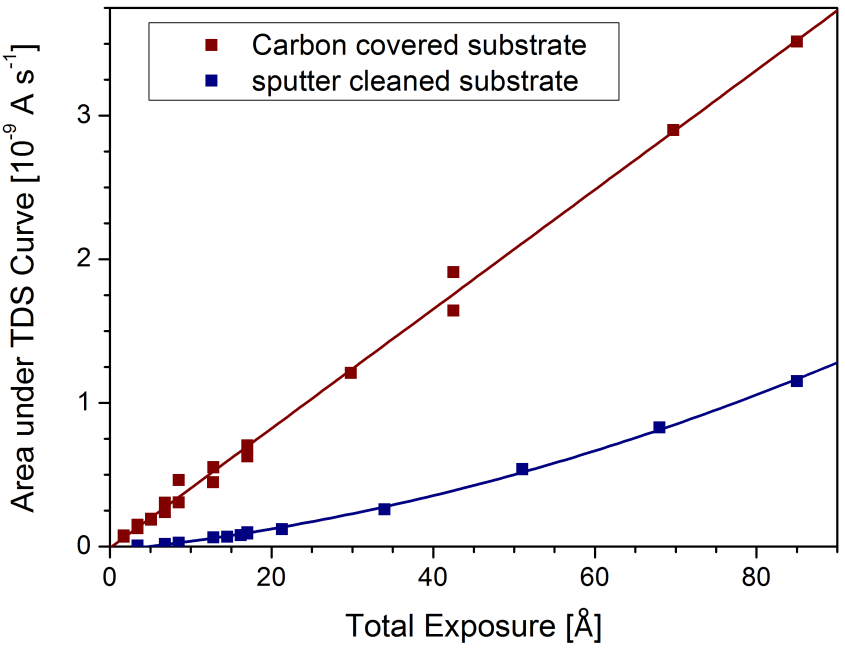

Figure 8.13.: Area under the TDS curves for the second molecule type (γ-peak) desorbed from carbon covered and sputter cleaned silicon dioxide as a function of the total exposed amount, as measured by a quartz microbalance

8.8. Temperature Correction and Desorption Energy Calculations

Same as in previous chapters, there exists a temperature lag between the surface and the temperature measured by the thermocouple, caused by the contact resistance between the heated steel plate and the silicon wafer and the bad heating conductivity of the latter. A thermal desorption spectrum of an 11 nm (130 Hz) thick quinacridone film that was directly grown on the stainless steel plate shows a true γ-peak desorption temperature T_p^{SS} of 530 K (Fig. 8.14). Similar to TDS experiments from SiO_2, it is possible to see a desorption of indigo and other quinacridone cracking products (β-peak) at a temperature of 410 K when tuning the quadrupole mass spectrometer to a cracking mass of 76 amu. The multilayer γ-peak of quinacridone on a carbon covered SiO_2 surface for 100 Hz exposure (8.5 nm mean film thickness) has a maximum desorption temperature T_p^{Si} of 715 K, which results in an error of 185 K at the point of maximum desorption. Applying correction formula (6.1) on page 73 results in corrected temperature values, which have been plotted as top axis in all thermal desorption figures.

The plot $\ln(R)$ vs $1/T$ for the corrected multilayer spectrum (4.25 nm mean thickness) is shown in Fig. 8.15. Taking the Polanyi-Wigner equation into account, one obtains a desorption energy E_{des} of 2.1±0.1 eV from the slope of the linear fit. From the intercept of the slope with the y-axis one obtains a pre-exponential or frequency factor ν of $1\times10^{19\pm1}$ s^{-1}. A second and less error-prone option is to calculate the desorption energy, which is in this case equivalent to the heat of evaporation, by evaluating the $\ln(R)$ vs. $1/T$ plot for the multilayer peak that was directly desorbed from the stainless steel sample holder. Doing so results in a value of 2.0±0.1 eV for the desorption energy and in a frequency factor of $1\times10^{18\pm1}$ s^{-1} (see Fig. 8.16). The discrepancy between the desorption energy as obtained from the stainless steel surface and the desorption energy of molecules from the silicon dioxide substrate can be attributed to uncertainties in the temperature correction.

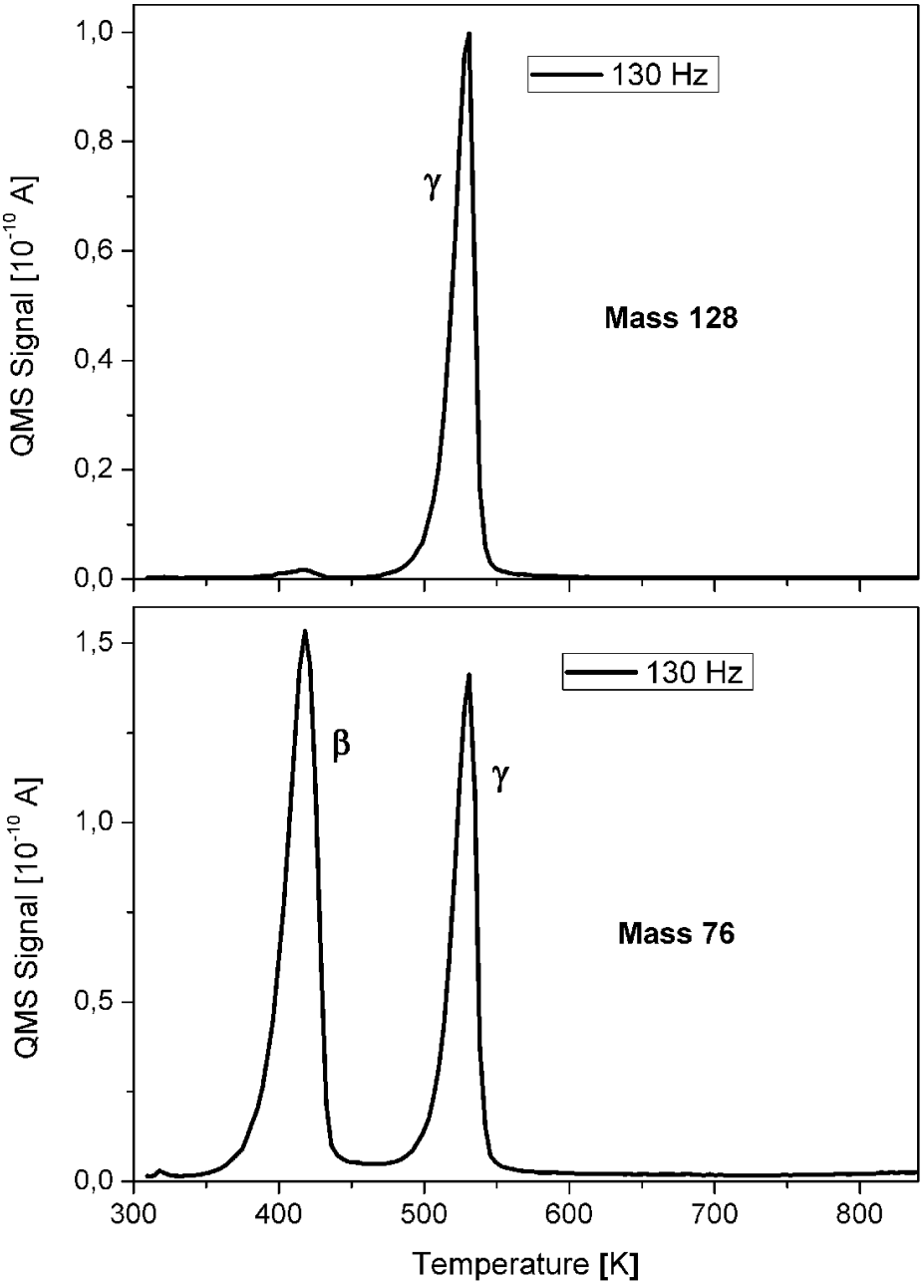

Figure 8.14.: Thermal desorption spectra of quinacridone from the stainless steel sample holder. The exposure is given in Hz, as determined by a quartz microbalance. Adsorption temperature: 200 K. Heating rate: 1 K/s.

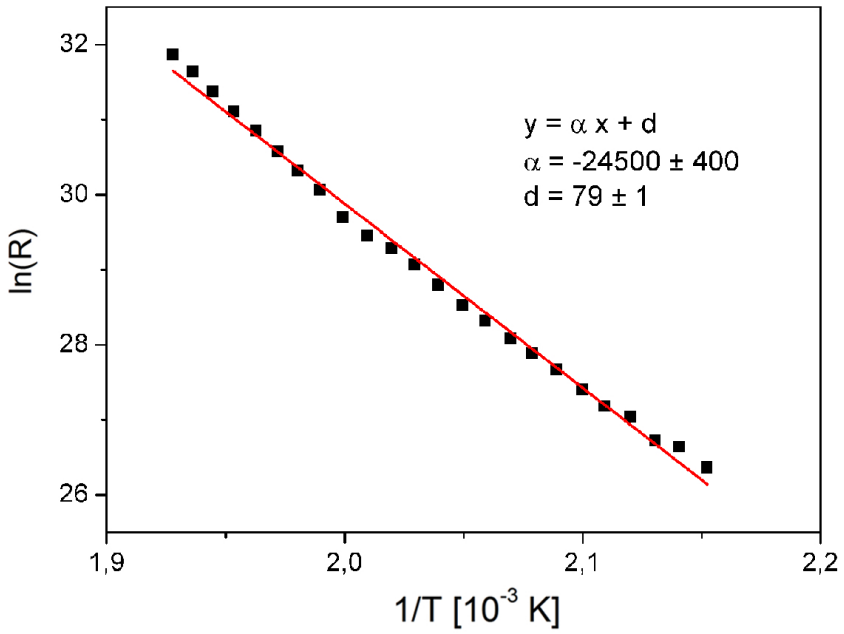

Figure 8.15.: Plot of $\ln(R)$ versus $1/T$ to determine the desorption energy for multilayer desorption of quinacridone on a carbon covered silicon dioxide surface

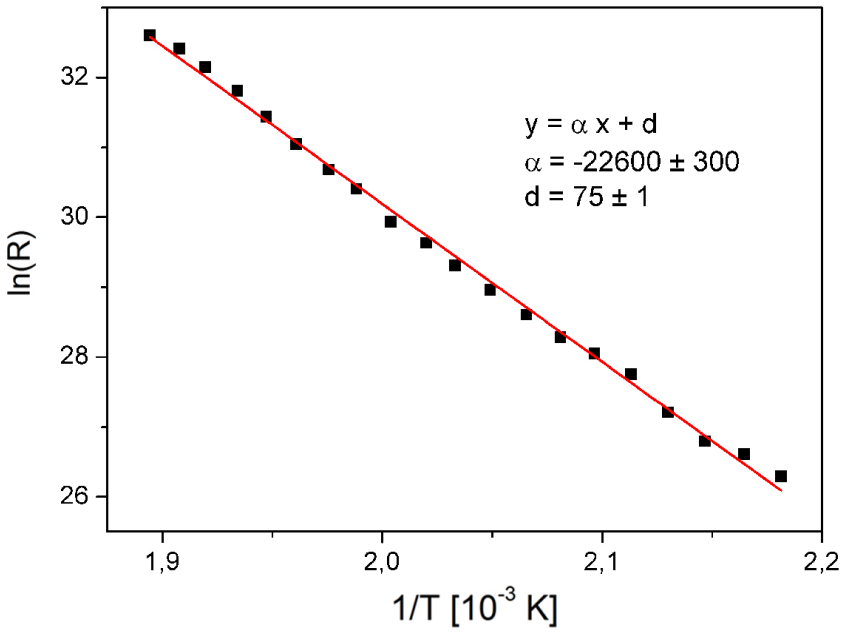

Figure 8.16.: Plot of $\ln(R)$ vs $1/T$ to determine the heat of evaporation of quinacridone multilayer desorption from the stainless steel sample holder

8.9. Surface Morphology

In order to take a closer look at the morphologies of the obtained films and for a possible morphological confirmation of the separate molecule types on the surface, ex-situ atomic force microscopy was used. All images were taken in tapping mode to not damage the sensitive organic films and plotted using derived data. In order to distinguish quinacridone islands from islands consisting of other molecules, it was necessary to create samples with either just quinacridone or just the decomposed molecules present. Samples with no quinacridone molecules adsorbed, i.e. samples with indigo and possible other decomposition products, were prepared by using the glass Knudsen cell described above with enhanced heating filament wiring near its opening (Fig. 8.11a). Additionally, similar films were prepared via partial material desorption (β-peak) from one SiO_2 sample and subsequent adsorption onto another sample, as described above. Both methods produced comparable films and will therefore not be distinguished in the following. Moreover, all samples above a certain thickness that were produced by either of these methods displayed a deep blue color visible to the bare eye. Pure quinacridone samples (with a bright pink color) could be manufactured by using the original metal Knudsen cell and heating the substrate to 425 K during the adsorption process, resulting in an immediate desorption of the weakly bonded smaller molecules.

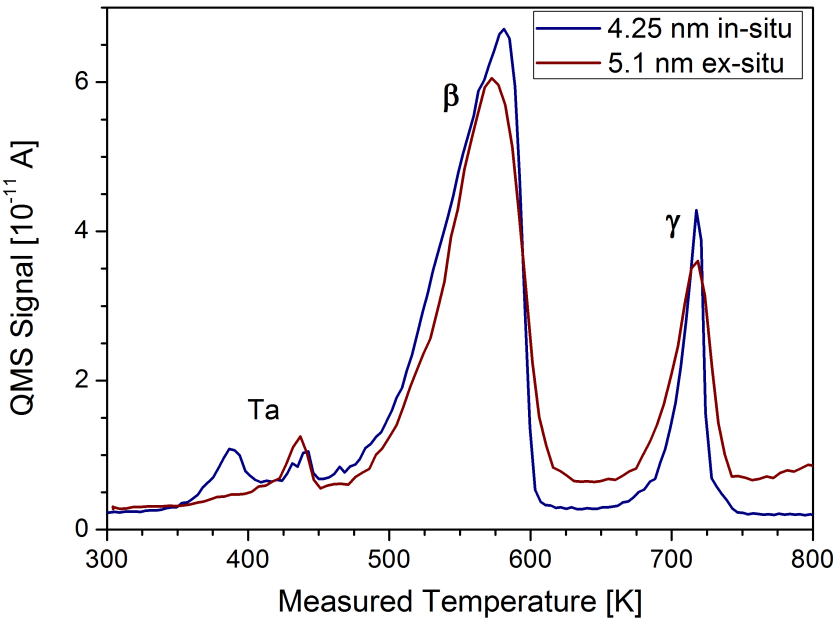

Figure 8.17.: Thermal desorption spectra of a 50 Hz (4.25 nm) quinacridone film measured in-situ (blue) and of a 60 Hz (5.1 nm) film measured after venting and subsequent re-evacuation (red)

All grown thin films experienced slight material evaporation of both molecule types upon venting, as can be seen in Fig. 8.17. A desorption spectrum of a 50 Hz (4.25 nm) thick film taken in-situ compares roughly to the desorption spectrum of a 60 Hz (5.1 nm) thick film after venting and subsequent re-evacuation. From these two spectra one can calculate that after normalization the net material loss through venting amounts to about 10%. Therefore, the evaporated amounts are rather small and no subsequent Ostwald ripening or other morphology changes occurred after storage under atmospheric conditions for at least 90 days, independent of molecule type and thickness. A comparison of surface morphologies for films of 5 nm, 60 nm, and 120 nm mean film thickness, as measured by AFM immediately after exposure to air and after 24 hours, showed no changes in island size, shape, or number. This suggests that molecules within multilayer islands are immobile on the surface and show a stable configuration once they are incorporated into their respective bulk crystal structures.

Figure 8.18 shows AFM images of three thin films on silicon dioxide with either all types of molecules (a), pure quinacridone (b) or solely indigo and other decomposed molecules (c) being present. Figure 8.18a shows a 42.5 nm thick film that was deposited from the metal Knudsen cell. Therefore, multiple types of molecules have been adsorbed and subsist on the surface. A multitude of islands is apparent, either round or slightly elongated, with heights up to 200 nm (cross-section Fig. 8.18b). Samples grown from the special glass deposition cell or via substrate heating, as depicted in Figs. 8.18c-e, show similarly shaped islands with comparable mean heights. Interestingly, for the pure films it was not possible to observe the elongated islands as found for the mixed film. Initially the hope was to be able to correlate the two different island morphologies to the different types of molecules. While this might still be true, the different experimental conditions for the individual film fabrication (e.g. 425 K substrate temperature during quinacridone deposition, high nozzle temperature during indigo film preparation) might be responsible for this failure.

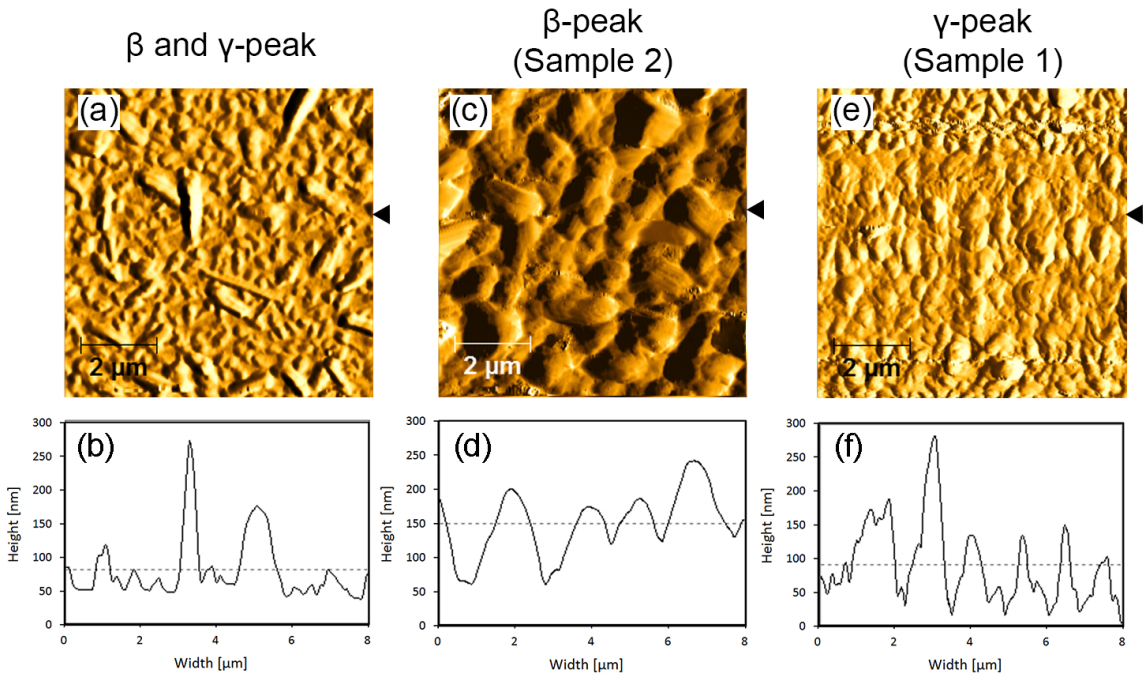

(a) AFM micrograph (8 µm × 8 µm) of a quinacridone film containing additional cracking molecules on silicon dioxide deposited from a metal Knudsen cell at 200 K substrate temperature. Nominal thickness: 42.5 nm. Deposition rate: 0.7 nm/min.

(b) Cross section along the line marked by the black arrow in (a)

(c) AFM micrograph (8 µm × 8 µm) of a 85 nm thick film of the smaller cracking molecules, assumed to be mainly indigo, on silicon dioxide. The film was deposited from a glass Knudsen cell with enhanced heating near the opening. Substrate deposition temperature: 200 K. Deposition rate: 0.7 nm/min.

(d) Cross section along the line marked by the black arrow in (c)

(e) AFM micrograph (8 µm × 8 µm) of a quinacridone film on silicon dioxide deposited from a metal Knudsen cell at a substrate temperature of 425 K. For this film, material equivalent to a nominal thickness of 170 nm was deposited onto the sample, but partial desorption caused the resulting layer to be significantly thinner (estimated thickness: 63 nm). Deposition rate: 0.7 nm/min.

(f) Cross section along the line marked by the black arrow in (e)

Figure 8.18.: AFM images of different films containing quinacridone and/or additional molecules which result from thermal decomposition

8.10. Structural Characterization

Quinacridone is a molecule with a planar conformation that crystallizes within the space group $P2_1/c$ with two molecules per unit cell. In the literature, up to seven different polymorph structures of linear trans-quinacridone have been reported.[199–208] However, only the β and γ-polymorphs (not to be mixed with the β and γ desorption peaks) are commercially important due to α-quinacridone transitioning either fully or partially into γ-quinacridone at elevated temperatures.[196, 209] From the crystal bulk structure it is apparent, that each molecule is connected to two neighboring molecules in the α and β-phase and to four neighboring molecules in the γ-phase via intermolecular hydrogen bonds between the carbonyl and imino groups.[210] These comparatively strong bonds allow for a high thermal stability and a high melting point. Full crystallographic data of the bulk structure has only sparsely been published due to difficulties of crystal growth in solution and due to the typically insufficient quality of vapor deposited crystals.[34, 43, 49]

In my own experiments the crystallographic properties of two differently prepared films grown on SiO_2 with a thickness of 63 nm (sample 1) and 85 nm (sample 2), respectively, was investigated by using both specular and grazing-incidence X-ray diffraction. A specular scan of the first sample, grown from a metal Knudsen cell at a substrate temperature of 425 K, showed multiple out-of-plane reflections for scattering vectors q_z between 0.3 $Å^{-1}$ and 2.2 $Å^{-1}$ (Fig. 8.19). A comparison with calculated diffraction data from powder cell measurements [211, 212] matches the peaks at 0.42 $Å^{-1}$ and 0.84 $Å^{-1}$ with (002) and (004) orientations of the quinacridone β-polymorph structure and peaks at 0.44 $Å^{-1}$ and 0.89 $Å^{-1}$ with (001) and (002) crystal orientations of the α-polymorph. Therefore, quinacridone molecules seem to exclusively arrange in crystallographic orientations where the (00l) planes are parallel to the substrate. Fig. 8.20 shows the packing of both the α and β crystallographic phases. Interestingly, there exist clear additional reflections which could not be attributed to any quinacridone net planes. Namely, reflections at 1.38 $Å^{-1}$, 1.42 $Å^{-1}$ and 1.63 $Å^{-1}$ are indications of the presence of p-sexiphenyl (6P, $C_{36}H_{26}$) [213] and/or other oligophenylenes. However, there is no evidence of such molecules in the thermal desorption or mass spectra. It is assumed that the occurrence of 6P is due to additional thermal decomposition and reaction of the impinging molecules at the relatively high substrate temperature of 425 K. During the growth process of this sample quinacridone molecules as well as all the described decomposition products in the Knudsen cell (indigo, carbazole) are present in the deposition flux. However, the latter cannot form a stable phase at a substrate temperature of 425 K and either instantly desorb or undergo further thermal decomposition. From a chemical point of view, both the break-off of CO and NH_3 molecules is quite likely, leading to a possible explanation of the formation of oligophenylenes from indigo, carbazole and quinacridone

molecules. The newly formed molecules have to be thermally stable on the surface at elevated temperatures, restricting the possible oligophenylenes to p-sexiphenyl and larger molecules.

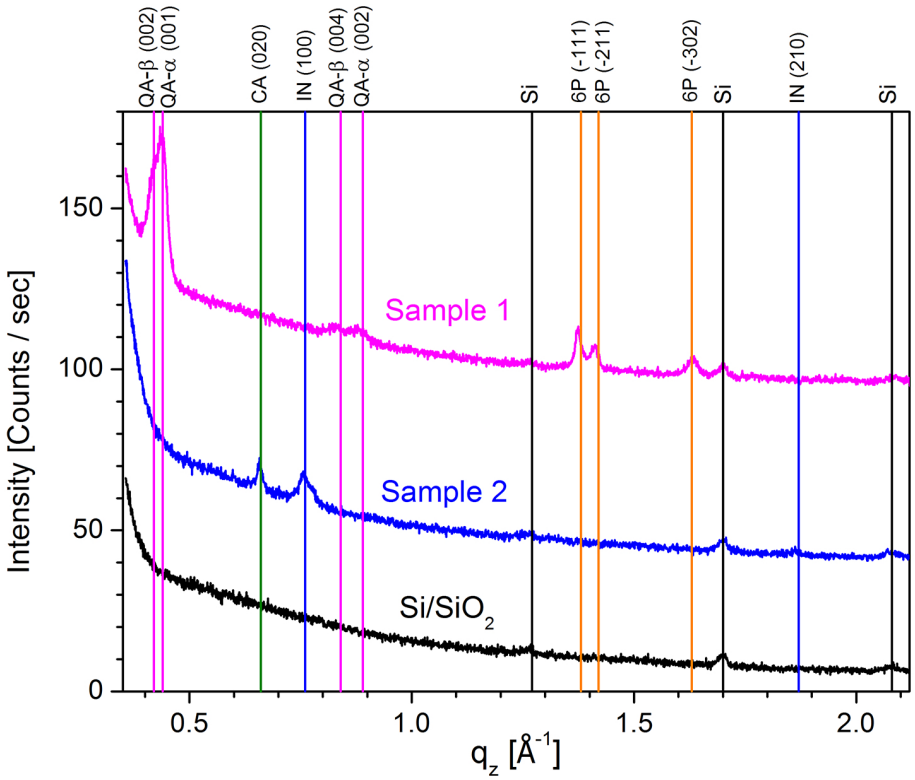

Figure 8.19.: Specular X-ray diffraction pattern for a bare Si/SiO_2 substrate (black), a 63 nm thick quinacridone film with additional 6P reflections (Sample 1, pink, compare to Fig. 8.18e) and for a 85 nm thick film consisting of indigo and carbazole (Sample 2, blue, compare to Fig. 8.18c). Data are vertically shifted for better visibility.

Berg *et al.* [185] conducted similar experiments with 105 nm thick quinacridone films grown by vacuum sublimation on SiO_2 substrates. XRD peaks corresponding to α-(001), α-(002), β-(002) and β-(004) orientations were found, in accordance with my own experiments. In both phases molecules are orientated almost perpendicular to the substrate with their long axis tilted by only 10° and 20° with respect to the surface normal. Furthermore, it was shown that the relative peak distribution changes with increasing substrate temperature for the simple reason that the α-phase is metastable and that it can transform into a β-polymorph at elevated temperatures.[34] The α-polymorph was found to be favored for thin films with 11 nm nominal thickness. Therefore, it makes sense to assign α to an interface-near substrate induced thin film phase while the β-polymorph is dominant within the bulk phase. Additionally, Sytnyk *et al.* [35] recorded XRD patterns of quinacridone micro- and

nanocrystals synthesized at various temperatures, and observed molecular arrangements that correspond to the α and β-polymorph throughout the measured temperature range.

The second film (sample 2) was prepared by using the special glass cell mentioned above with increased heating near the nozzle for the deposition process where desorption hinted at indigo. Indeed, a specular XRD scan (shown in Fig. 8.19) clearly links the peaks at 0.76 $Å^{-1}$ and 1.87 $Å^{-1}$ to indigo corresponding to orientations where the (100) and (210) planes, respectively, are parallel to the substrate. Note that this findings agrees well with indigo results in chapter 7.7 on page 105. However, for this film again a special reflection appears in the XRD (0.66 $Å^{-1}$) which cannot be attributed to indigo. Extensive literature search showed that this reflection could be matched with a multitude of possible quinacridone cracking products [214–217], of which the (020) orientation of carbazole seems most likely if the entirety of the available spectroscopic data is taken into account.

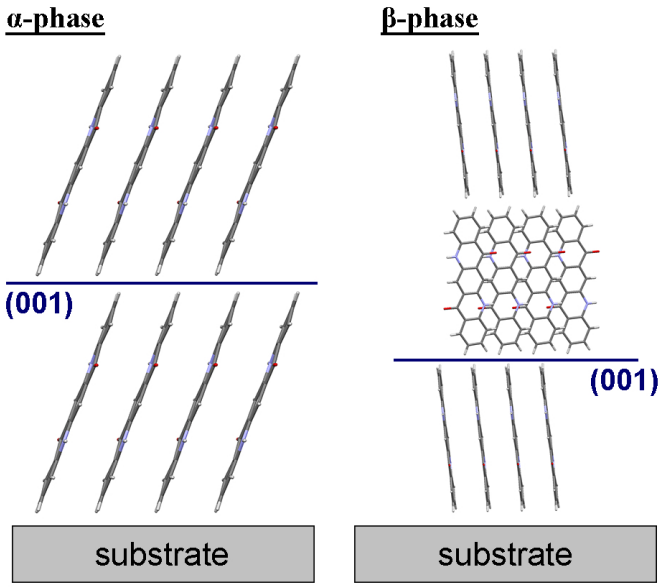

Figure 8.20.: Preferred orientation of quinacridone molecules packing within the α- and β-polymorph with the (00l)-planes parallel to the substrate.[62, 176]

In order to provide support for the conclusions drawn from the specular X-ray diffraction data and to obtain additional information on the in-plane molecule arrangement grazing incidence X-ray diffraction at BESSY II was carried out on the same samples as described before. Fig. 8.21 shows two-dimensional GIXD images with an incidence wavelength of 1 Å and under an incidence angle of 0.13°. Numerous in-plane and out-of-plane reflections confirm the existence of a variety of molecular species and additionally crystalline phases with different crystallographic orientations. The superimposed white lines represent the highest

intensity reflections of quinacridone and p-sexiphenyl (top) as well as indigo and carbazole (bottom) taken from literature values (CSD-Codes QNACRD06, QNACRD07, ZZZNTQ01, INDIGO01, INDIGO02, CRBZOL01).[34, 62, 176, 213, 214] A detailed assignment list is given in Tab. 8.1.

As expected, when looking at a sample with both the β- and γ-peak present almost no crystallinity can be seen under the same measurement conditions as in Fig. 8.21 (see top part of Fig. 8.22). This is most likely caused by hindrances in the bulk structure formation due to the presence of the respective other molecule and the desire of different molecules to form contrasting crystallographic structures. Only when significantly increasing the integration time to 60 minutes can reflections be seen (bottom part of Fig. 8.22). When comparing the GIXD pattern to Tab. 8.1, it becomes apparent that all four types of molecules coexist in the thin film in a polycrystalline arrangement.

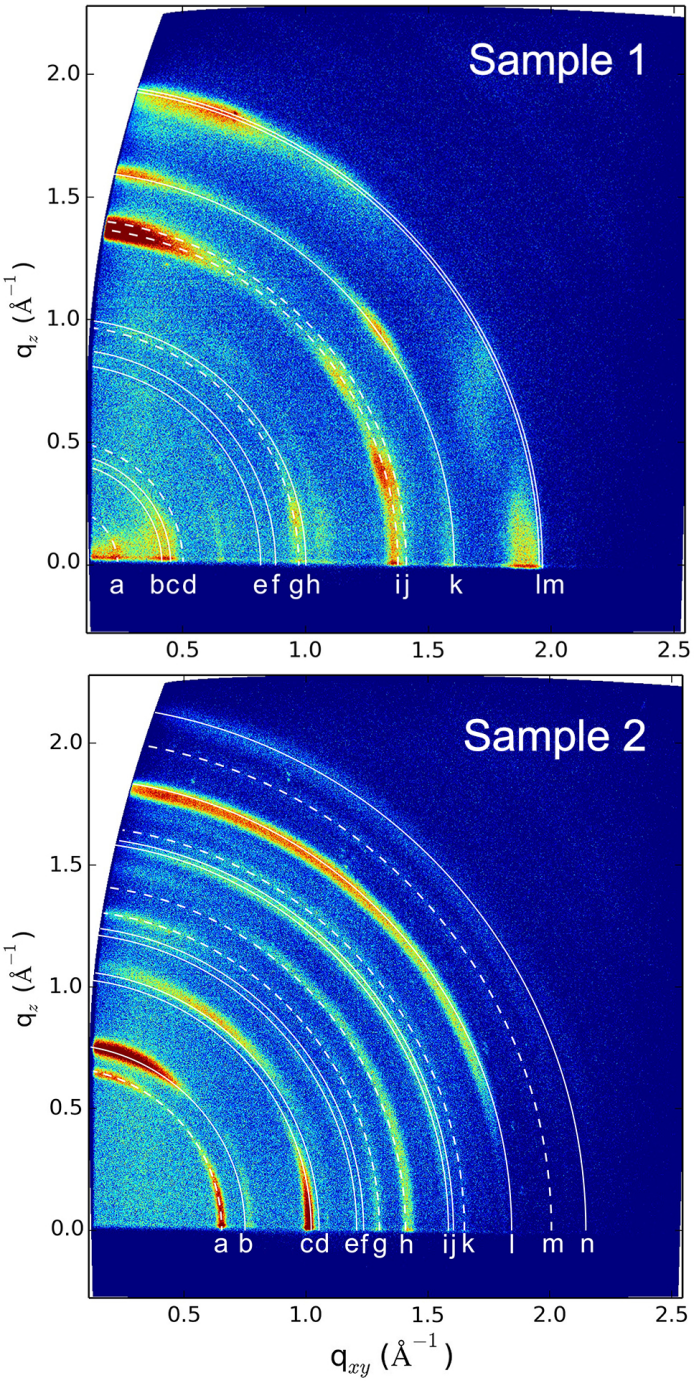

Figure 8.21.: 2D-GIXD patterns of a 63 nm thick quinacridone film (Sample 1, top) and a 85 nm thick film solely consisting of cracking molecules (Sample 2, bottom). The white lines depict Debye-Scherrer rings of selected net planes of quinacridone (solid), p-sexiphenyl (dashed), indigo (solid), and carbazole (dashed); for detailed information see Tab. 8.1

Table 8.1.: Crystallographic reflections of p-sexiphenyl, quinacridone, carbazole and indigo that are in good agreement with the observed GIXD reflection spots

		q [Å^{-1}]	Molecule	Phase	Net Plane (*hkl*)
Sample 1	a	0.24	p-Sexiphenyl		(100)
	b	0.42	Quinacridone	β	(002)
	c	0.44	Quinacridone	α	(001)
	d	0.48	p-Sexiphenyl		(200)
	e	0.84	Quinacridone	β	(004)
	f	0.89	Quinacridone	α	(002)
	g	0.97	p-Sexiphenyl		(400)
	h	1.00	Quinacridone	α	(01-1)
	i	1.38	p-Sexiphenyl		(-111)
	j	1.42	p-Sexiphenyl		(-211)
	k	1.59	Quinacridone	β	(011)
	l	1.95	Quinacridone	β	(1-1-2)
	m	1.98	Quinacridone	α	(1-12)
Sample 2	a	0.66	Carbazole		(020)
	b	0.76	Indigo	A+B	(100)
	c	1.03	Indigo	B	(-102)
	d	1.06	Indigo	A	(-102)
	e	1.24	Indigo	A	(011)
	f	1.26	Indigo	B	(011)
	g	1.31	Carbazole		(040)
	h	1.40	Carbazole		(111)
	i	1.58	Indigo	A	(111)
	j	1.61	Indigo	B	(2-1-1)
	k	1.65	Carbazole		(210)
	l	1.87	Indigo	A+B	(210)
	m	1.98	Carbazole		(211)
	n	2.15	Indigo	A	(211)

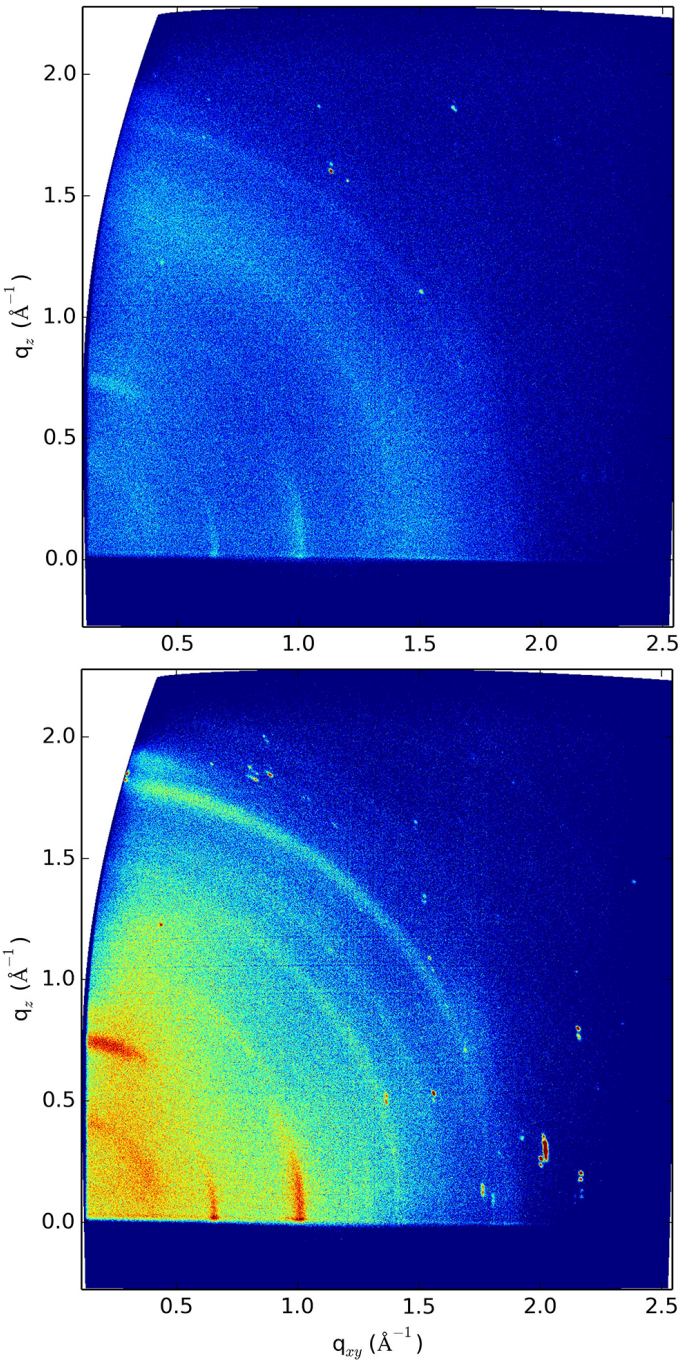

Figure 8.22.: 2D-GIXD patterns of a 45 nm thick quinacridone film containing additional cracking molecules deposited from a metal Knudsen cell at 200 K substrate temperature. The top picture was taken under the same measurement conditions as Fig. 8.21 while the bottom picture featured a significantly longer integration time.

8.11. Raman Spectroscopy

To interpret the results and features observed so far and for more information about the chemical composition of the thin organic films, Raman spectroscopy was employed on the two samples that were used for AFM, specular XRD and GIXD investigations before (compare Figs. 8.18, 8.19, and 8.21). Both samples were irradiated with monochromatic light with a wavelength of 325 nm yielding a multitude of scattering peaks, as shown in Fig. 8.23. I want to stress that the absolute peak intensities of the Raman modes in Fig. 8.23 are arbitrary values that depend on the molecular orientations within the samples. This finding was not elaborated in further detail, since the focus here lies on a qualitative sample analysis. The quinacridone sample which was grown at a high substrate temperature (Sample 1, pink) showed strong features at wavenumbers between 1550 cm^{-1} and 1650 cm^{-1} and certain peaks in the area of 1350 cm^{-1} that agree reasonably well with powder measurements and literature values of quinacridone (see Fig. 8.24 and Tab. 8.2).[218] Differences between thin film and powder measurements may, in this case, be explained by (a), the presence or dominant behavior of different polymorphs or (b), an increased amount of intermolecular hydrogen bonds within the thin film compared to powder samples.

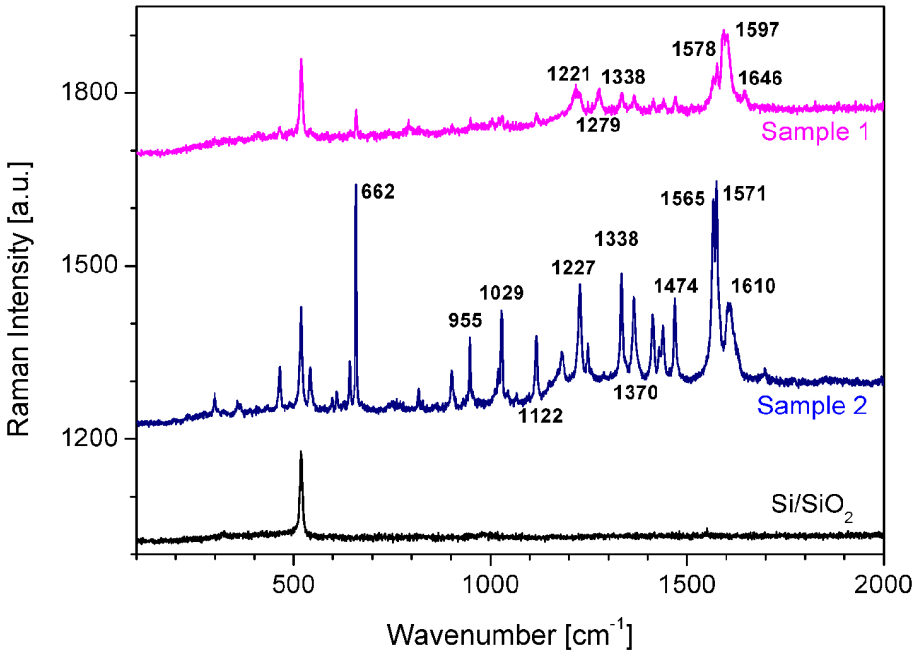

Figure 8.23.: Raman spectra of a bare Si/SiO_2 substrate (black), a 63 nm thick quinacridone film (Sample 1, pink) and of a 85 nm thick film consisting of indigo and carbazole (Sample 2, blue)

Additional peaks at 1221 cm^{-1} and 1279 cm^{-1} agree very well with p-sexiphenyl Raman excitations.[219] The second sample (Sample 2, blue) shows a thoroughly different fingerprint with multiple excitations, due to no quinacridone but rather indigo and possible additional cracking molecules being present. Features at 1227 cm^{-1}, 1370 cm^{-1}, 1474 cm^{-1}, 1565 cm^{-1}, 1571 cm^{-1} and 1610 cm^{-1} as well as additional smaller peaks, can be matched with Raman excitations of indigo powder (see Fig. 8.24 and Tab. 8.2). Certain peaks, most notably at 662 cm^{-1}, 1029 cm^{-1} and 1122 cm^{-1}, are neither originating from quinacridone, nor from indigo vibrations, again corroborating our claim of the existence of at least one additional cracking molecule. They are in good agreement with carbazole literature data.[220]

Table 8.2.: Observed 325 nm excited Raman features compared with powder excitations of indigo (IN) and quinacridone (QA) and possible matches of the remaining features with literature data of p-sexiphenyl (6P, [219]) and carbazole (CA, [220])

	Observed Thin Film Raman Shift [cm^{-1}]	Observed Powder Raman Shift [cm^{-1}]	Closest Raman Shift from Literature [cm^{-1}]	Molecule
Sample 1	1221		1220	6P
	1279		1278	6P
	1338	1323		QA
	1578	1558		QA
	1597	1591	1594	QA / 6P
	1646	1646		QA
Sample 2	662		658	CA
	1029		1017	CA
	1122		1105	CA
	1227	1224	1226	IN / CA
	1338		1338	CA
	1370	1360		IN
	1474	1459	1483	IN / CA
	1565	1569		IN
	1571	1580	1575	IN / CA
	1610	1624	1629	IN / CA

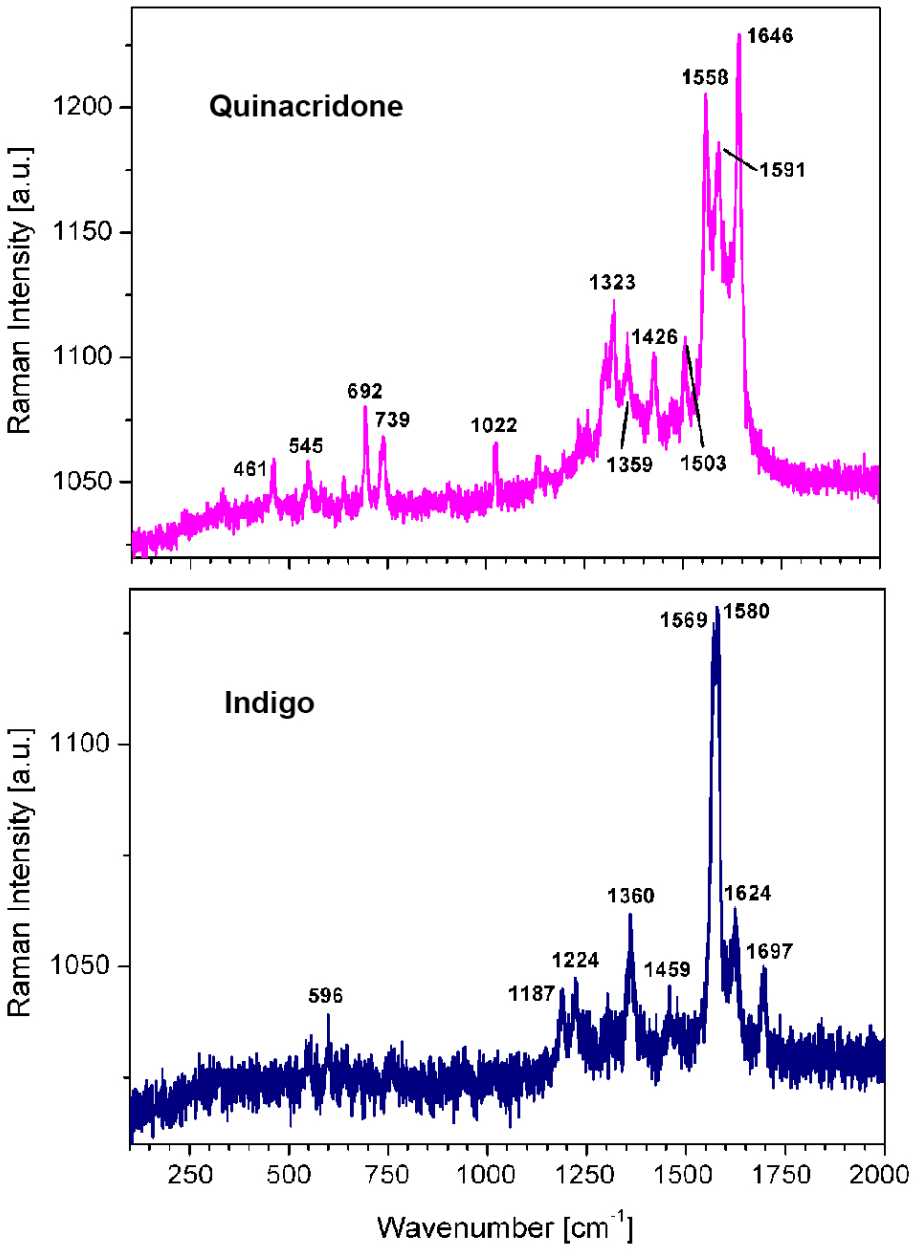

Figure 8.24.: Raman spectra of quinacridone (pink) and indigo (blue) powder samples upon irradiation with a wavelength of 325 nm

8.12. Summary and Conclusion

In this chapter, some idiosyncrasies in the context of the preparation of thin quinacridone films upon employing Knudsen cell deposition in ultra-high vacuum were described. Since quinacridone exhibits a comparably high sublimation temperature, due to the existing hydrogen bonds, this causes partial decomposition in the Knudsen cell during evaporation, which impedes the formation of pure quinacridone films. A variety of spectroscopies were used to unravel the thermally activated fragmentation and decomposition in the Knudsen cell by analyzing the effusion flux and the composition and structure of the deposited film. By using thermal desorption spectroscopy it could unambiguously be demonstrated that at least two different species were deposited on a silicon dioxide substrate upon evaporation of quinacridone from a stainless steel Knudsen cell. In addition to quinacridone which desorbed at about 500 K (γ-peak), a second desorption peak (β-peak) appeared already at a temperature of 410 K, which could be attributed to indigo. Additionally, for very low mean film thicknesses a metastable indigo configuration could be observed, which shows slow desorption at 200 K. The desorption energy and frequency factors were calculated to 2.1±0.1 eV and $1\times10^{19\pm1}$ s^{-1}, respectively. Experiments on sputtered silicon dioxide suggest the formation of a non-desorbing wetting layer and a sticking coefficient of less than unity for this configuration. With special experimental methods it was possible to prepare films which exclusively consist of molecules corresponding to either the β-peak or the γ-peak, respectively. This was realized by desorbing and re-adsorbing only one molecule type onto a second sample positioned opposite to the primary sample. Additionally, it was possible to prepare similar films with only one molecular species on the surface by either using a special Knudsen-like glass cell or by quinacridone deposition at elevated substrate temperatures. The latter films were subsequently analyzed by atomic force microscopy, specular and grazing-incidence X-ray diffraction and Raman spectroscopy. These methods verified the existence of quinacridone and indigo in the respective samples. However, additional decomposition products were found which could not be observed in the desorption spectra. In the film corresponding to the β-peak carbazole was detected in addition to indigo, while the film corresponding to the γ-peak displayed p-sexiphenyl, most likely created through further thermal decomposition processes at the hot substrate surface, in addition to quinacridone. These findings were supported by grazing-incidence and Raman spectroscopy. Pure quinacridone films could be prepared only upon using a Langmuir evaporation source (free evaporation). All films were stable, showed only slight material evaporation upon venting and no significant morphology changes after storage in air. The conducted studies highlight that these findings are of relevance for choosing the proper deposition techniques for organic molecules with high sublimation temperature, in particular for hydrogen-bonded molecules.

9 | Epindolidione

9.1. Introduction

Epindolidione ($C_{16}H_{10}N_2O_2$, see Fig. 9.1) is a rod-like organic molecule of orange or bright yellow color that consists of four linear-fused benzene rings and which is commonly used as synthetic pigment. It can be regarded as the H-bonded analogue to the well-known and intensively studied tetracene ($C_{18}H_{12}$). Similar to the already discussed indigo and quinacridone pigments, epindolidione shows strong intermolecular interactions and forms high crystal lattice energy solids due to the interplay between intermolecular hydrogen-bonds and π-π- stacking interactions.[44, 221] Despite a number of recent studies which demonstrate the promising potential of epindolidione thin films for highly air-stable organic field-effect transistors with high hole-mobilities [35, 43, 53, 222, 223], almost no spectroscopic data is available for this specific molecule.

Epindolidione has at least two polymorphic forms that are obtained upon sublimation. Despite being chemically equivalent they do define if the pigment is of orange or bright yellow color. Both polymorphs were present in the material provided by the work group of Dr. Glowacki from the university of Linz. After proper purification by sublimation the powder was evaporated onto Si/SiO_2 wafers via physical vapor deposition from a stainless steel Knudsen cell under ultra-high vacuum conditions.

The main motivation to study epindolidione during my thesis was a direct result from the thoroughly explained fragmentation process of quinacridone molecules within a Knudsen cell and the initial suspicion that epindolidione might be an end product of the thermally activated cracking process since its isomer indigo is clearly present. To disprove this sus-

picion it was necessary to perform mass spectrometry, as well as XRD, GIXD and Raman spectroscopy investigations.

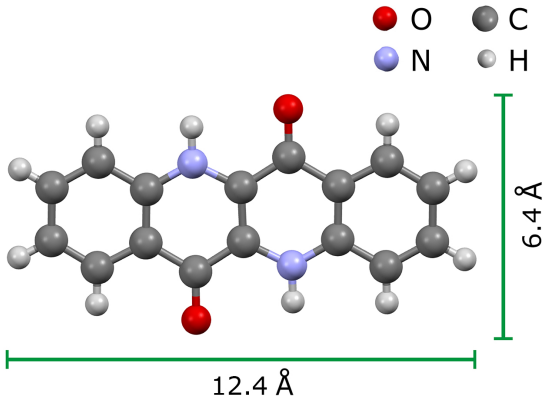

Figure 9.1.: Structure and van der Waals dimensions of the epindolidione molecule [148]

9.2. Thermal Desorption Spectroscopy

The first step of evaluating epindolidione thin film characteristics was the thermal desorption analysis of a 100 Hz thick film that was grown on carbon covered SiO_2. For this experiment the film thickness can only be represented in the frequency change of a quartz microbalance upon mass accumulation, since no reliable density values for epindolidione are available in the literature and equation (4.3) on page 49 is therefore not applicable. However, since most organic materials have densities between 1.3 g/cm^3 and 1.5 g/cm^3, a similar value is assumed for epindolidione and 100 Hz deposition then calculates to roughly 8.5 nm mean film thickness. Additionally, no temperature correction was conducted, meaning that solely the measured temperature is plotted versus the QMS signal. However, the temperature lag between sample surface and heating plate was most likely similar to measurements mentioned in chapter 8.3. Fig. 9.2 shows a single steep desorption peak with its maximum at T_m $\approx$ 580 K. Earlier peaks at 330 K and 400 K are assumed to be measurement artifacts, while the peak at 455 K can be associated with material desorptiom from the tantalum holding clamps. Once again, this can be used to estimate the true desorption temperature.

Since no secondary SiO_2 desorption peak is visible in Fig. 9.2, neither at higher nor at lower temperature than the main peak, it can be concluded that epindolidione films, which reach a thickness of multiple layers, show only a single desorbing phase and no observable wetting layer formation. Of course, no statements can be made on monolayer and submonolayer thick films and whether this phase consists of lying or standing molecules. This question will be addressed with additional spectroscopic methods in the following chapters.

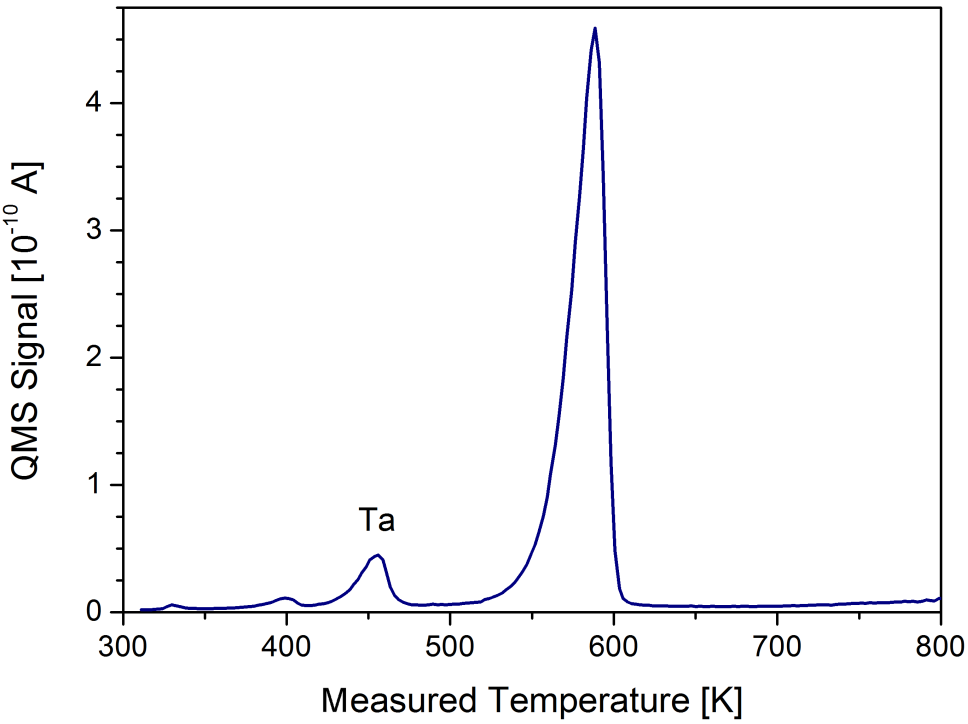

Figure 9.2.: Thermal desorption spectrum of epindolidione from carbon covered silicon dioxide for an exposure of 100 Hz, as determined by a quartz microbalance. Adsorption temperature T_{ad} = 200 K. Deposition rate A ≈ 3 Å/min. Heating rate β_H = 1 K/s. The small peak at 450 K likely originates from desorption from the Ta mounting clamps.

9.3. Cracking Mass Analysis

A full mass spectrum which was taken during the desorption process of epindolidione from silicon dioxide is shown in Fig. 9.3. It is apparent that no significant similarities can be found upon comparison with the cracking phase in chapter 8.3 (see the top part of Fig. 8.4 on page 117), which was - as mentioned in the introduction - the main motivation to investigate epindolidione characteristics. Therefore, just the mass spectra alone make it safe to say that epindolidione molecules take no part in the fragmentation processes which are described in chapter 8.3.

The spectrum in Fig. 9.3 still proves to be interesting, since no cracking mass analysis of epindolidione is available from literature data. Strong fragmentation masses can be found at 76 amu, 50 amu, 102 amu, 63 amu and 157 amu, as well as smaller peaks at 130 amu, 88 amu, 44 amu, 151 amu, 117 amu and 114 amu (sorted by intensity).

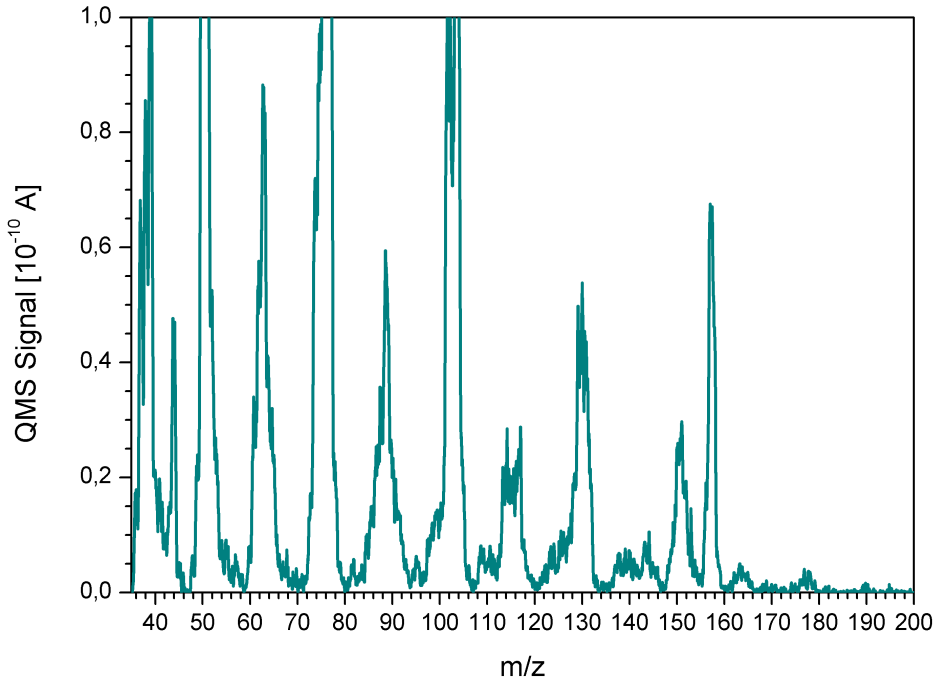

Figure 9.3.: Cracking mass analysis of the epindolidione desorption peak in Fig. 9.2. The plot shows a single mass spectrum in the temperature range of 550-600 K.

9.4. Surface Morphology

Atomic force microscopy of a roughly 85 nm (deposition equivalent to 1000 Hz frequency change) thick epindolidione film (see Fig. 9.4) shows a multitude of small and round islands with heights up to 30 nm. From the mean island height and the film thickness it can be concluded that the space inbetween islands cannot be associated with the substrate. Since there is also only a single desorption phase visible in the TDS spectrum it is reasonable to assume that epindolidione forms large cohesive island structures on a slightly carbon covered SiO_2 substrate. Morphology changes during the venting process or after storage under air have not been investigated and no statements can be made regarding this issue.

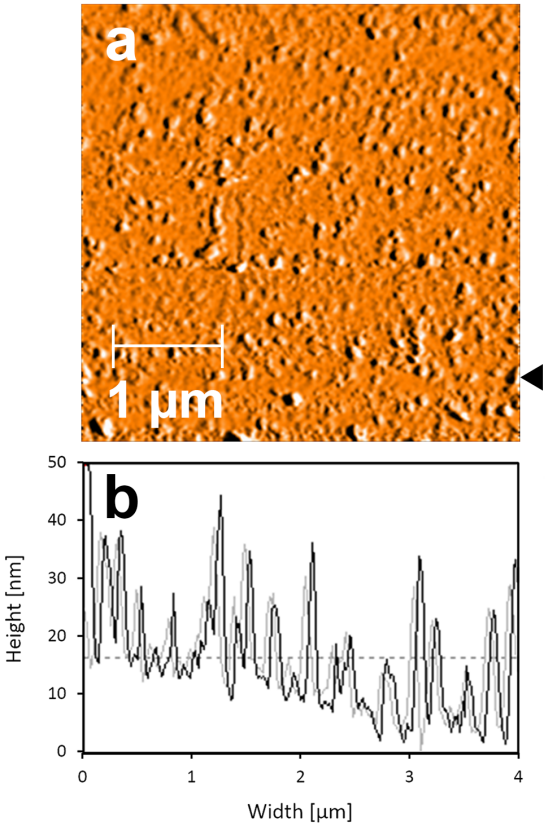

(a) Topography scan

(b) Cross section along the line marked by the black arrow in (a)

Figure 9.4.: 4×4 µm AFM image of an ∼85 nm thick epindolidione film on carbon covered SiO_2. Substrate deposition temperature: 200 K. Deposition rate: ≈ 3 Å/min.

9.5. Structural Characterization

For the epindolidione molecule neither unit cell dimensions (either measured or calculated) nor powder diffraction patterns are available in any of the common databases (e.g. [212]). Therefore, measuring X-ray diffraction patterns of epindolidione, both with a specular and a grazing incidence setup, was of key interest. Contrary to powder diffraction investigations of indigo and quinacridone, which were performed at the same apparatus under identical measurement conditions, epindolidione powder produces unusually broad peaks in the Θ/2Θ-scan (compare Fig. 9.5). With the help of the Scherrer equation

$$\tau = \frac{K\lambda}{\beta \cos(\Theta)} \tag{9.1}$$

where K is a dimensionless shape factor with a value of 0.9 and λ is the used X-ray wavelength (1.54 Å), one can calculate the mean crystallite size τ from the Bragg-angle Θ and the line broadening at half maximum intensity (β). Doing so for the main features in Fig. 9.5 leads to relatively small crystallite domains of 12.9 nm for the peak at 7.0° and 7.4 nm for the peak at 26.8°. The broad peak shape can therefore be directly traced back to the very fine epindolidione powder and its preparation.

The two already mentioned and most distinctive peaks at 7.0° and 26.8° are equivalent to plane separations of 12.68 Å and 3.31 Å, respectively, corresponding to a fully upright standing configuration in the first case and flat-lying molecules in the latter case (compare Fig. 9.1).

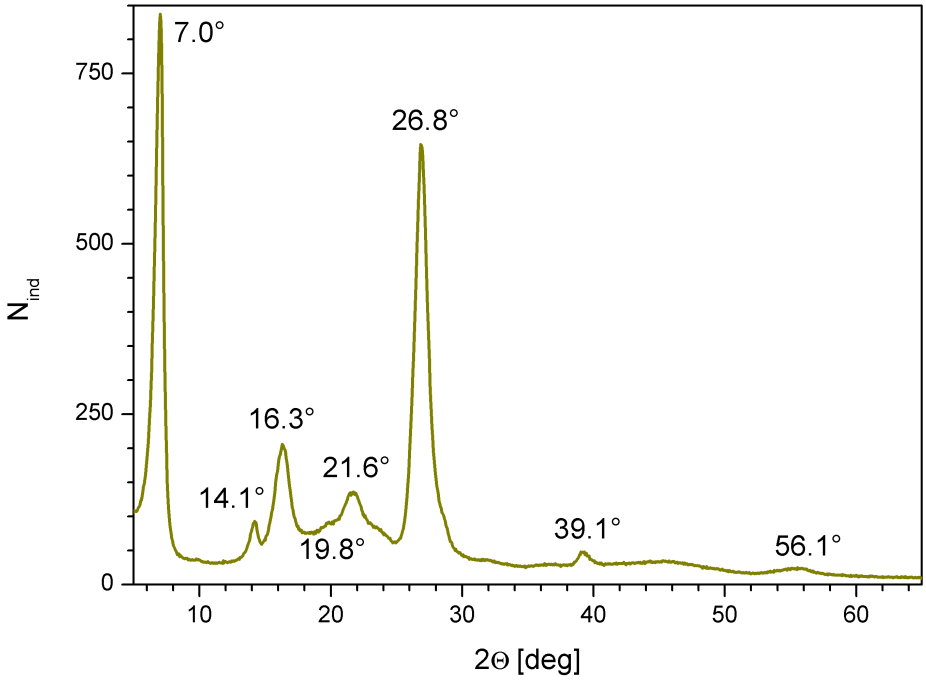

Figure 9.5.: Specular X-ray diffraction pattern for an epindolidione powder sample

The diffraction pattern of an ∼85 nm thick film (Fig. 9.6) only displays a single peak at 7.1°, implicating that molecules solely arrange in an upright-standing configuration when grown on silicon dioxide substrates. This coincides very well with the single desorption peak plotted in Fig. 9.2. Similarly, the 2D-GIXD pattern of the very same sample (Fig. 9.7) only features a small number of reflections, which can be attributed to a configuration of standing molecules with the (100)-plane parallel to the substrate (q_z=0.5 Å^{-1}, d=12.6 Å) and additional reflections from π-π-stacking (q_z=1.9 Å^{-1}, d=3.3 Å).

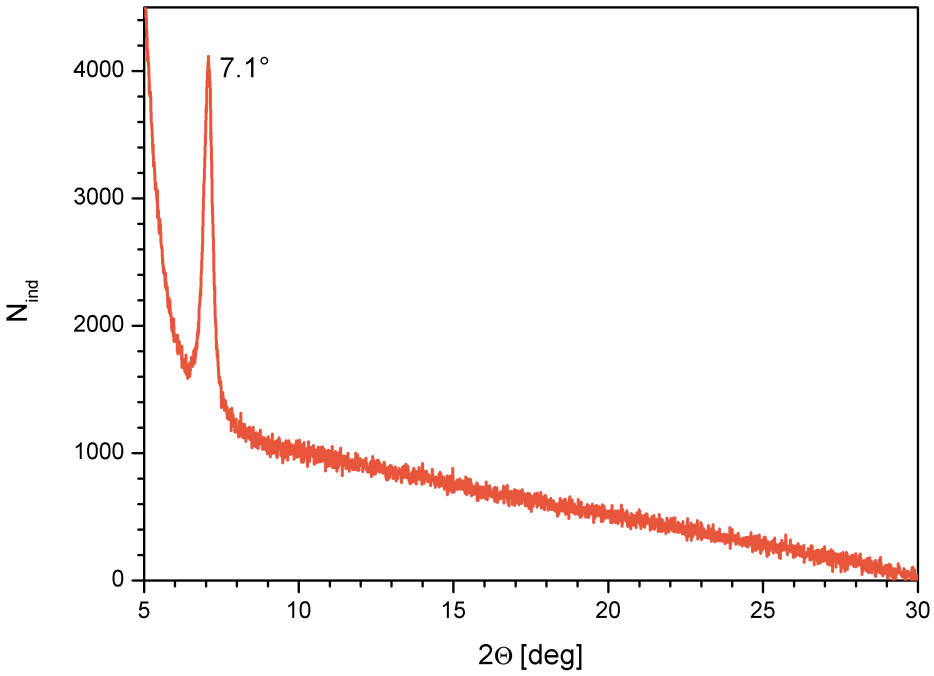

Figure 9.6.: Specular X-ray diffraction pattern for an ∼85 nm thick epindolidione film

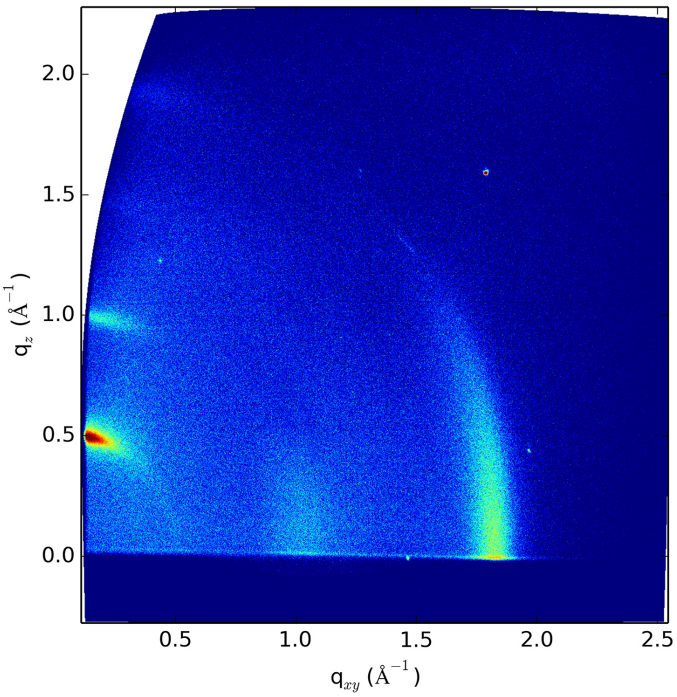

Figure 9.7.: 2D-GIXD pattern of a ∼85 nm thick epindolidione film

9.6. Raman Spectroscopy

Figure 9.8 shows Raman scattering excitations of an epindolidione powder sample, irradiated with a wavelength of 325 nm. In addition to the peak at 1364 cm^{-1}, a broad peak can be seen between 1550 cm^{-1} and 1650 cm^{-1}, which most likely consists of multiple overlapping excitations. The latter can in similar fashion be observed for indigo and quinacridone samples (compare Fig. 8.23 on page 143) and are associated with C=O and C=C stretching vibrations.[224]

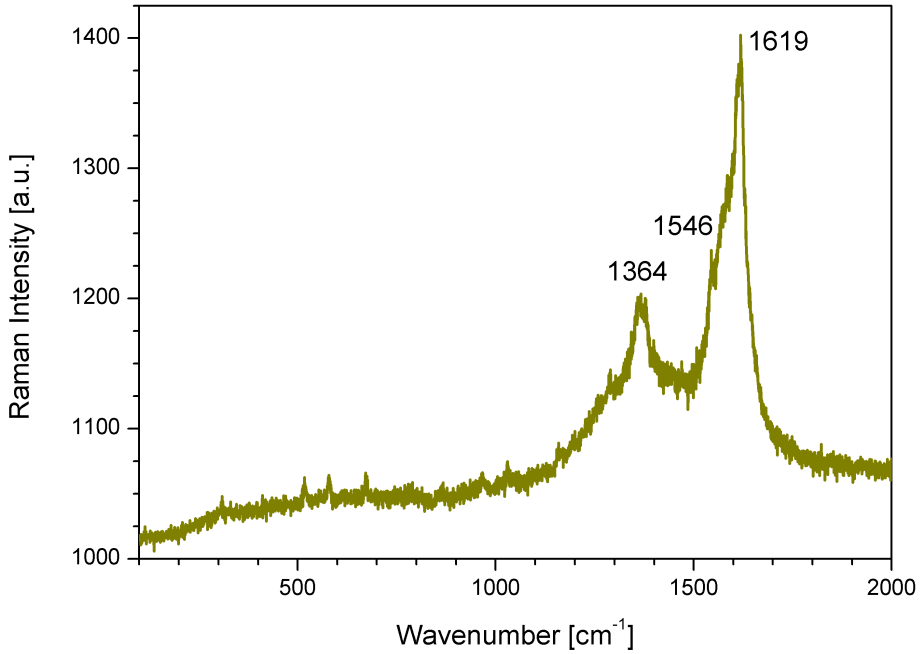

Figure 9.8.: Raman features of an epindolidione powder sample

9.7. Summary and Conclusion

Epindolidione has recently been established as an interesting pigment with a number of possible applications in organic devices. Despite its promising outlook, almost no scientific publications exist which focus on this specific molecule or any of its derivatives. With the help of TDS, AFM, XRD, GIXD and Raman spectroscopy a number of spectroscopic investigations were presented in this chapter, both for powder and thin film samples. It could be shown that epindolidione thin films consist of fully upright standing molecules ((100)-plane parallel to the substrate) and feature a single desorption peak at around 450 K. No connections were found with the quinacridone cracking phase in chapter 8. The powder samples show strong features at 7.0°, 16.3° and 26.8° in a specular Θ-2Θ-scan and prominent Raman excitation vibrations at wavenumbers of 1364 cm^{-1}, 1546 cm^{-1} and 1619 cm^{-1}.

10 | Summary

This dissertation demonstrates how important precise deposition conditions and substrate preparations are for the growth behavior of thin organic semiconductor films. Four different disc- and rod-like organic molecules have been investigated on carbon covered as well as sputter cleaned silicon dioxide substrates with a focus on initial film formation. Thin films were evaporated in an ultra-high vacuum setup via physical vapor deposition from metal and/or glass evaporation cells onto 1×1 cm^2 large Si/SiO_2 samples and subsequently analyzed. Thermal desorption spectroscopy (TDS) was utilized to study growth behavior as well as monolayer and multilayer desorption characteristics for various coverages. Additionally, Auger electron spectroscopy (AES) was used in-situ to evaluate chemical compositions of thin films and to check for surface impurities. Thin films were analyzed ex-situ with atomic force microscopy (AFM), X-ray diffraction (XRD) and grazing-incidence X-ray diffraction (XRD) as well as Raman spectroscopy. The obtained results can be summarized as follows:

- The initial film formation of **rubicene** molecules on silicon dioxide exhibits a quite unusual behavior. Initially, two full layers of flat-lying molecules are formed which subsequently dewet into three dimensional islands upon further material deposition. The crystallographic structure of these islands was found to be bulk like, with the (001) plane being parallel to the substrate, resulting in an arrangement of upright standing but tilted molecules. The strong tendency to dewet is caused by a larger desorption energy for the molecules in the 3D islands compared to initial flat-lying molecules. Furthermore, for the island-like film under ambient conditions Ostwald ripening was observed. In the case of very thin films most of the material in the small islands even disappeared by evaporation within several days at room temperature. A further peculiarity concerns the initial sticking coefficient of rubicene on SiO_2 with

only a value of 0.2±0.05, which is attributable to relatively weak interactions between the molecules and the substrate surface. Only weak dependencies on the substrate chemical composition were reported. Accumulation of carbon on the surface did neither significantly influence the shape of the desorption spectra nor the coverage dependence of the sticking coefficient.

- For **indigo** significant differences in diffusion behavior and island growth were observed between sputter cleaned and carbon contaminated surfaces. In the former case the substrate is rather reactive and the indigo molecules are initially very strongly bonded and show no desorption. After further material adsorption possibly dimers are formed, which de-stabilize the bonding mechanism to the surface and lead to a weakly bonded first state. Subsequently, at and above a certain coverage, the molecules dewet and form more strongly bonded three dimensional islands. However, on the more inert carbon covered substrates initially adsorbed indigo molecules form a similar metastable state, but dewet into islands at much lower coverage. The sticking coefficient was found to be coverage independent and unity in all cases. X-ray diffraction on a 40 nm thick film exhibited two weak diffraction peaks for carbon covered samples, which can be dedicated to weak crystallographic orientations along the (100) and (210) planes, respectively. Films on sputter-cleaned surfaces seemed to be completely randomly orientated.

- Detailed investigations on the **quinacridone** film formation on silicon dioxide substrates revealed idiosyncrasies in the deposition process when using Knudsen or Knudsen-like evaporation cells. The unusually high sublimation temperature of quinacridone combined with a large number of inner wall collisions in the Knudsen cell promotes partial dissociation of the quinacridone molecules. By using thermal desorption spectroscopy it could unambiguously be demonstrated that at least two different species were deposited on a silicon dioxide substrate upon evaporation of quinacridone from a stainless steel Knudsen cell. In addition to the quinacridone desorption peak at about 500 K, a second desorption peak was found at lower temperature, which could unambiguously be allocated to indigo and other decomposition products. Additionally, for very low mean film thicknesses a metastable indigo configuration was found. Experiments on sputtered silicon dioxide suggest the formation of a non-desorbing wetting layer and a sticking coefficient of less than unity for this configuration. With special experimental methods it was possible to prepare and analyze films which exclusively consist of only one molecular species. Experimental methods such as atomic force microscopy, specular and grazing-incidence X-ray diffraction and Raman spectroscopy verified the existence of quinacridone, indigo, carbazole and additional para-hexaphenyl in the respective samples. The latter is most likely formed by further thermal decom-

position on the surface at elevated substrate temperatures and is not present in the Knudsen cell effusion flux. Pure quinacridone films could be prepared only upon using a Langmuir evaporation source.

- For **epindolidione** both powder and thin film measurements were conducted since almost no spectrographic investigations exist which focus on this specific molecule or any of its derivatives. It could be shown that epindolidione thin films consist of fully upright standing molecules in a configuration where the (100)-plane is parallel to the substrate. A single thermal desorption peak was found at around 450 K. The powder samples show strong features at 7.0°, 16.3° and 26.8° in a specular Θ-2Θ-scan and prominent Raman excitation vibrations at wavenumbers of 1364 cm^{-1}, 1546 cm^{-1} and 1619 cm^{-1}.

Table 10.1 provides an overview of desorption energies and pre-exponential factors of the investigated molecules for different surface preparations.

Table 10.1.: Desorption energies E_{des} and pre-exponential factors ν for some of the studied organic molecules

Material	Surface Preparation	Layer Type	E_{des} [eV]	ν [s^{-1}]
Rubicene	C-covered	Multilayer	1.47	3×10^{18}
	C-covered	Monolayer	1.25	3×10^{16}
Indigo	C-covered	Multilayer	1.67	1×10^{22}
	C-covered	Monolayer	0.84	6×10^{12}
	sputter-cleaned	Multilayer	1.53	1×10^{22}
	sputter-cleaned	Monolayer	0.83	2×10^{12}
Quinacridone	C-covered	Multilayer	2.1	1×10^{19}

In general, it can be concluded that neither of the four investigated molecules shows layer-by-layer growth on silicon dioxide substrates, which would be desirable for transistor fabrication. Nevertheless, many interesting facets and previously unreported aspects were described, illustrating how different conditions at the initial stages of film growth can have formidable influence on subsequent layers and thin films. The gathered results and drawn conclusions in this thesis are of significant relevance for the application of organic molecules in novel organic electronic devices.

The thesis was part of the research project 'Initial Stages of Organic Film Growth' (project number P 23530) financed by the Austrian Science Fund FWF. Close cooperation has been carried out with members of project TRP 239, entitled 'In-situ Characterization of Organic Semiconductor Devices'.

Part III.

Supplemental

A. List of Conference Contributions

1. *Initial Growth and Desorption Studies of H-Bonded Organic Semiconductors on SiO_2 Substrates*, B. Scherwitzl, R. Resel and A. Winkler, 7th School on Organic Electronics, 14. - 18.09.2015, Como, Italy (Poster presentation)

2. *Idiosyncrasies of Physical Vapor Deposition Processes from Various Knudsen Cells for Quinacridone Thin Film Growth on SiO_2*, B. Scherwitzl, R. Resel and A. Winkler, 79th Annual DPG Spring Meeting, 15. - 20.03.2015, Berlin, Germany (Talk given by B. Scherwitzl)

3. *Thin Film Growth Analysis of Quinacridone on SiO_2*, B. Scherwitzl, R. Resel and A. Winkler, 2nd International Winterschool on Bioelectronics BioEl2015, 28.02 - 07.03.2015, Kirchberg, Austria (Poster presentation)

4. *Initial Film Growth Studies of Indigo on SiO_2*, B. Scherwitzl, R. Resel and A. Winkler, 64th Annual Meeting of the Austrian Physical Society, 24. - 27.09.2014, Pöllau, Austria (Talk given by B. Scherwitzl)

5. *Film Growth, Adsorption and Desorption Kinetics of Indigo on SiO_2*, B. Scherwitzl, R. Resel and A. Winkler, International Conference of Physics Students ICPS, 10. - 17.08.2014, Heidelberg, Germany (Talk given by B. Scherwitzl)

6. *Initial Film Growth Studies of Indigo on SiO_2*, B. Scherwitzl, R. Resel and A. Winkler, 15th Joint Vacuum Conference, 15. - 20.06.2014, Vienna, Austria (Poster presentation)

7. *Film Growth, Adsorption and Desorption Kinetics of Indigo on SiO_2*, B. Scherwitzl, R. Resel and A. Winkler, 78th Annual DPG Spring Meeting, 30.03. - 04.04.2014, Dresden, Germany (Talk given by B. Scherwitzl)

8. *Film Growth, Adsorption and Desorption Kinetics of Indigo on SiO_2*, B. Scherwitzl, R. Resel and A. Winkler, 1st International Winterschool on Bioelectronics BioEl2014, 22.02. - 01.03.2014, Kirchberg, Austria (Talk given by B. Scherwitzl)

9. *Initial Steps of Rubicene Film Growth on Silicon Dioxide*, B. Scherwitzl, W. Lukesch, A. Hirzer, J. Albernig, G. Leising, R. Resel and A. Winkler, 19th International Vacuum Congress IVC-19, 09. - 13.09.2013, Paris, France (Poster presentation)

10. *Initial Steps of Indigo Film Growth on Silicon Dioxide*, B. Scherwitzl, R. Resel and A. Winkler, 63th Annual Meeting of the Austrian Physical Society, 03. - 06.09.2013, Linz, Austria (Talk given by B. Scherwitzl)

11. *Initial Steps of Rubicene Film Growth on Silicon Dioxide*, B. Scherwitzl, W. Lukesch, A. Hirzer, J. Albernig, G. Leising, R. Resel and A. Winkler, 77th Annual DPG Spring Meeting, 10. - 15.03.2013, Regensburg, Germany (Poster presentation)

12. *Initial Growth of Rubicene on Silicon Oxide*, B. Scherwitzl, W. Lukesch, A. Winkler, 62nd Annual Meeting of the Austrian Physical Society, 18. - 21.09.2012, Graz, Austria (Poster presentation)

Bibliography

[1] M. Pope and C. E. Swenberg, *Electronic Processes in Organic Crystals and Polymers* (Oxford University Press on Demand, 1999).

[2] F. Ebisawa, T. Kurokawa, and S. Nara, *J. Appl. Phys.* **54**, 3255–3259 (1983).

[3] A. Tsumura, H. Koezuka, and T. Ando, *Appl. Phys. Lett.* **49**, 1210–1212 (1986).

[4] A. J. Lovinger and L. J. Rothberg, *J. Mater. Res.* **11**, 1581–1592 (1996).

[5] C. D. Dimitrakopoulos and P. R. L. Malenfant, *Adv. Mater.* **14**, 99 (2002).

[6] L. Wang, M.-H. Yoon, G. Lu, Y. Yang, A. Facchetti, and T. J. Marks, *Nature Mat.* **5**, 893–900 (2006).

[7] M. Kaltenbrunner, T. Sekitani, J. Reeder, T. Yokota, K. Kuribara, T. Tokuhara, M. Drack, R. Schwödiauer, I. Graz, S. Bauer-Gogonea, S. Bauer, and T. Someya, *Nature* **499**, 458–463 (2013).

[8] M. Kaltenbrunner, M. S. White, E. D. Głowacki, T. Sekitani, T. Someya, N. S. Sariciftci, and S. Bauer, *Nat. Commun.* **3**, 770 (2012).

[9] T. Sekitani, U. Zschieschang, H. Klauk, and T. Someya, *Nat. Mater.* **9**, 1015–1022 (2010).

[10] S. R. Forrest, *Nature* **428**, 911–918 (2004).

[11] N. T. Kalyani and S. J. Dhoble, *Sust. Energ. Rev.* **16**, 2696–2723 (2012).

[12] G. Kranzelbinder and G. Leising, *Rep. Prog. Phys.* **63**, 729 (2000).

[13] J. H. Burroughes, D. D. C. Bradley, A. R. Brown, R. N. Marks, K. Mackay, R. H. Friend, P. L. Burns, and A. B. Holmes, *Nature* **347**, 539–541 (1990).

[14] C. W. Tang and S. A. VanSlyke, *Appl. Phys. Lett.* **51**, 913–915 (1987).

[15] C. P. Jarrett, R. H. Friend, A. R. Brown, and D. M. De Leeuw, *J. Appl. Phys.* **77**, 6289–6294 (1995).

[16] H. Stubb, E. Punkka, and J. Paloheimo, *Mater. Sci. Rep.* **10**, 85–140 (1993).

[17] B. Crone, A. Dodabalapur, A. Gelperin, L. Torsi, H. E. Katz, A. J. Lovinger, and Z. Bao, *Appl. Phys. Lett.* **78**, 2229–2231 (2001).

[18] H. E. Katz, *J. Mater. Chem.* **7**, 369–376 (1997).

[19] P. Ostoja, S. Guerri, S. Rossini, M. Servidori, C. Taliani, and R. Zamboni, *Synthetic Met.* **54**, 447–452 (1993).

[20] A. Dodabalapur, L. Torsi, and H. E. Katz, *Science* **268**, 270–271 (1995).

[21] C. D. Dimitrakopoulos, A. R. Brown, and A. Pomp, *J. Appl. Phys.* **80**, 2501–2508 (1996).

[22] M. J. Panzer, C. R. Newman, and C. D. Frisbie, *Appl. Phys. Lett.* **86**, 103503 (2005).

[23] Y.-Y. Lin, D. J. Gundlach, S. F. Nelson, and T. N. Jackson, *Electron Devic. Lett.* **18**, 606–608 (1997).

[24] F.-J. Meyer zu Heringdorf, M. C. Reuter, and R. M. Tromp, *Nature* **412**, 517–520 (2001).

[25] S. Steudel, D. Janssen, S. Verlaak, J. Genoe, and P. Heremans, *Appl. Phys. Lett.* **85**, 5550–5552 (2004).

[26] Y.-Y. Lin, D. J. Gundlach, S. F. Nelson, and T. N. Jackson, *IEEE C. Elec. Devices* **44**, 1325–1331 (1997).

[27] R. Friend, J. Burroughes, and T. Shimoda, *Phys. World* **12**, 35–40 (1999).

[28] A. Facchetti, Y. Deng, A. Wang, Y. Koide, H. Sirringhaus, T. J. Marks, and R. H. Friend, *Angew. Chem.* **112**, 4721–4725 (2000).

[29] L. Jiang, Y. Fu, H. Li, and W. Hu, *J. Am. Chem. Soc.* **130**, 3937–3941 (2008).

[30] T. W. Kelley, P. F. Baude, C. Gerlach, D. E. Ender, D. Muyres, M. A. Haase, D. E. Vogel, and S. D. Theiss, *Chem. Mater.* **16**, 4413–4422 (2004).

[31] Q. Tang, L. Jiang, Y. Tong, H. Li, Y. Liu, Z. Wang, W. Hu, Y. Liu, and D. Zhu, *Adv. Mater.* **20**, 2947–2951 (2008).

[32] A. A. Virkar, S. Mannsfeld, Z. Bao, and N. Stingelin, *Adv. Mater.* **22**, 3857–3875 (2010).

[33] T. Jentzsch, H. J. Juepner, K.-W. Brzezinka, and A. Lau, *Thin Solid Films* **315**, 273–280 (1998).

[34] E. F. Paulus, F. J. J. Leusen, and M. U. Schmidt, *Cryst. Eng. Comm.* **9**, 131–143 (2007).

[35] M. Sytnyk, E. D. Głowacki, S. Yakunin, G. Voss, W. Schöfberger, D. Kriegner, J. Stangl, R. Trotta, C. Gollner, S. Tollabimazraehno, G. Romanazzi, Z. Bozkurt,

M. Havlicek, N. S. Sariciftci, and W. Heiss, *J. Am. Chem. Soc.* **136**, 16522–16532 (2014).

[36] U. Keller, K. Müllen, S. De Feyter, and F. C. De Schryver, *Adv. Mater.* **8**, 490–493 (1996).

[37] I. Javed, Z. Zhang, T. Peng, T. Zhou, H. Zhang, M. I. Khan, Y. Liu, and Y. Wang, *Sol. Energ. Mat. Sol. C.* **95**, 2670–2676 (2011).

[38] B. Mahns, F. Roth, A. König, M. Grobosch, M. Knupfer, and T. Hahn, *Phys. Rev. B* **86**, 035209 (2012).

[39] S. Verlaak, S. Steudel, P. Heremans, D. Janssen, and M. S. Deleuze, *Phys. Rev. B* **68**, 195409 (2003).

[40] J. A. Venables, G. D. T. Spiller, and M. Hanbucken, *Rep. Prog. Phys.* **47**, 399 (1984).

[41] R. Ruiz, B. Nickel, N. Koch, L. C. Feldman, R. F. Haglund Jr., A. Kahn, F. Family, and G. Scoles, *Phys. Rev. Lett.* **91**, 136102 (2003).

[42] J. Lee, L. G. Kaake, J. H. Cho, X.-Y. Zhu, T. P. Lodge, and C. D. Frisbie, *J. Phys. Chem. C* **113**, 8972–8981 (2009).

[43] E. D. Głowacki, M. Irimia-Vladu, M. Kaltenbrunner, J. Gsiorowski, M. S. White, U. Monkowius, G. Romanazzi, G. P. Suranna, P. Mastrorilli, T. Sekitani, S. Bauer, T. Someya, L. Torsi, and N. S. Sariciftci, *Adv. Mater.* **25**, 1563–1569 (2013).

[44] H. M. Smith, *High Performance Pigments* (Wiley, 2002).

[45] L. Serrano-Andrés and B. O. Roos, *Chem. Eur. J.* **3**, 717–725 (1997).

[46] M. U. Schmidt, T. Schmiermund, and M. Bolte, *Cryst. Struct. Commun.* **62**, 37–40 (2006).

[47] R. Johnson, *US Pat.* **4197404A** (1978).

[48] M. Urban, *US Pat.* **5614014A** (1995).

[49] G. Lincke, *Dyes Pigments* **44**, 101–122 (2000).

[50] J. J.-A. Chen, T. L. Chen, B. Kim, D. A. Poulsen, J. L. Mynar, J. M. J. Fréchet, and B. Ma, *ACS Appl. Mater. Inter.* **2**, 2679–2686 (2010).

[51] E. D. Głowacki, G. Voss, L. Leonat, M. Irimia-Vladu, S. Bauer, and N. S. Sariciftci, *Isr. J. Chem.* **52**, 540–551 (2012).

[52] M. Irimia-Vladu, E. D. Głowacki, G. Voss, S. Bauer, and N. S. Sariciftci, *Mater. Today* **15**, 340–346 (2012).

[53] E. D. Głowacki, M. Irimia-Vladu, S. Bauer, and N. S. Sariciftci, *J. Mater. Chem. B* **1**, 3742–3753 (2013).

[54] E. Zojer, N. Koch, P. Puschnig, F. Meghdadi, A. Niko, R. Resel, C. Ambrosch-Draxl, M. Knupfer, J. Fink, J. L. Bredas, and G. Leising, *Phys. Rev. B* **61**, 16538 (2000).

[55] J. Locklin, M. E. Roberts, S. C. B. Mannsfeld, and Z. Bao, *J. Macromol. Sci. Pol. R.* **46**, 79–101 (2006).

[56] R. Ruiz, D. Choudhary, B. Nickel, T. Toccoli, K.-C. Chang, A. C. Mayer, P. Clancy, J. M. Blakely, R. L. Headrick, S. Iannotta, and G. G. Malliaras, *Chem. Mater.* **16**, 4497–4508 (2004).

[57] B. Scherwitzl, W. Lukesch, A. Hirzer, J. Albering, G. Leising, R. Resel, and A. Winkler, *J. Phys. Chem. C* **117**, 4115–4123 (2013).

[58] Database of Standards and References, *NIST*, (2011) `http://webbook.nist.gov/chemistry/`.

[59] P. Süsse, M. Steins, and V. Kupcik, *Zeitschr. Kristall.* **184**, 269–274 (1988).

[60] M. Irimia-Vladu, E. D. Głowacki, P. A. Troshin, G. Schwabegger, L. Leonat, D. K. Susarova, O. Krystal, M. Ullah, Y. Kanbur, M. A. Bodea, V. F. Razumov, H. Sitter, S. Bauer, and N. S. Sariciftci, *Adv. Mater.* **24**, 375–380 (2012).

[61] H. von Eller, *Bull. Soc. Chim. Fr.*, 1433–1438 (1955).

[62] P. Süsse and A. Wolf, *Naturwissenschaften* **67**, 453–453 (1980).

[63] C. K. Kim and C. A. Maggiulli, *J. Heterocyclic Chem.* **16**, 1651–1653 (1979).

[64] E. D. Głowacki, L. Leonat, M. Irimia-Vladu, R. Schwödiauer, M. Ullah, H. Sitter, S. Bauer, and N. S. Sariciftci, *Appl. Phys. Lett.* **101**, 023305 (2012).

[65] J. Mizuguchi, T. Sasaki, and K. Tojo, *Z. Krist.-New Cryst. St.* **217**, 249–250 (2002).

[66] B. E. Deal and C. R. Helms, *The Physics and Chemistry of SiO_2 and the Si-SiO_2 Interface* (Springer US, 2013).

[67] S. Verhavebeke, M. Meuris, A. Kelleher, M. M. Heyns, R. F. de Keersmaecker, M. P. Murrell, and C. J. Sofield, in Proc. Electrochem. Soc. Fall Meeting, Phoenix, Arizona (1991).

[68] B. Scherwitzl, R. Resel, and A. Winkler, *J. Chem. Phys.* **140**, 184705 (2014).

[69] B. Scherwitzl, C. Röthel, A. O. F. Jones, B. Kunert, I. Salzmann, R. Resel, G. Leising, and A. Winkler, *J. Phys. Chem. C.* (accepted Aug. 2015).

[70] R. I. Masel, *Principles of Adsorption and Reaction on Solid Surfaces*, Vol. 3 (John Wiley and Sons, 1996).

[71] D. Frenkel and B. Smit, *Understanding Molecular Simulation: From Algorithms to Applications* (Elsevier Science, 2001).

[72] K. Y. Foo and B. H. Hameed, *Chem. Eng. J.* **156**, 2–10 (2010).

[73] E. Umbach, K. Glöckler, and M. Sokolowski, *Surf. Sci.* **402**, 20–31 (1998).

[74] W. Gebauer, M. Bässler, R. Fink, M. Sokolowski, and E. Umbach, *Chem. Phys. Lett.* **266**, 177–183 (1997).

[75] W. Gebauer, C. Väterlein, A. Soukopp, M. Sokolowski, and E. Umbach, *Thin Solid Films* **284**, 576–580 (1996).

[76] M. Dell'Angela, T. Anniyev, M. Beye, R. Coffee, A. Föhlisch, J. Gladh, T. Katayama, S. Kaya, O. Krupin, J. LaRue, A. Møgelhøj, D. Nordlund, J. K. Nørskov, H. Öberg, H. Ogasawara, H. Öström, L. G. M. Pettersson, W. F. Schlotter, J. A. Sellberg, F. Sorgenfrei, J. J. Turner, M. Wolf, W. Wurth, and A. Nilsson, *Science* **339**, 1302–1305 (2013).

[77] K. Oura, V. G. Lifshits, A. A. Saranin, A. V. Zotov, and M. Katayama, *Surface Science: An Introduction* (Springer Berlin, 2003).

[78] H. P. Bonzel, „Mass Transport by Surface Self-Diffusion“, in *Surface Mobilities on Solid Materials* (Springer, 1983), pp. 195–241.

[79] R. Gomer, *Rep. Prog. Phys.* **53**, 917–1002 (1990).

[80] A. G. Naumovets and Y. S. Vedula, *Surf. Sci. Rep.* **4**, 365–434 (1985).

[81] A. G. Naumovets, *Surf. Sci.* **299**, 706–721 (1994).

[82] M. Henzler and W. Göpel, *Oberflächenphysik des Festkörpers* (Vieweg+ Teubner Verlag Wiesbaden, 1991).

[83] G. Ehrlich and F. G. Hudda, *J. Chem. Phys.* **44**, 1039–1049 (1966).

[84] R. L. Schwoebel and E. J. Shipsey, *J. Appl. Phys.* **37**, 3682–3686 (1966).

[85] C. Teichert, G. Hlawacek, A. Winkler, P. Puschnig, and C. Draxl, „Ehrlich-Schwoebel Barriers and Island Nucleation in Organic Thin-Film Growth“, in *Small Organic Molecules on Surfaces* (Springer, 2013), pp. 79–106.

[86] J. Venables, *Introduction to Surface and Thin Film Processes* (Cambridge University Press, 2000).

[87] E. Bauer, *Z. Kristallogr.* **110**, 372–394 (1958).

[88] H. G. Rubahn, H. Sitter, G. Horowitz, and K. Al-Shamery, *Interface Controlled Organic Thin Films*, Springer Proceedings in Physics (Springer Berlin Heidelberg, 2009).

[89] M. Möbus and N. Karl, *Thin Solid Films* **215**, 213–217 (1992).

[90] T. Haber, S. Müllegger, A. Winkler, and R. Resel, *Phys. Rev. B* **74**, 045419 (2006).

[91] P. Frank, G. Hlawacek, O. Lengyel, A. Satka, C. Teichert, R. Resel, and A. Winkler, *Surf. Sci.* **601**, 2152–2160 (2007).

[92] A. Andreev, G. Matt, C. J. Brabec, H. Sitter, D. Badt, H. Seyringer, and N. S. Sariciftci, *Adv. Mater.* **12**, 629–633 (2000).

[93] F. Balzer and H.-G. Rubahn, *Appl. Phys. Lett.* **79**, 3860–3862 (2001).

[94] C. B. France, P. G. Schroeder, J. C. Forsythe, and B. A. Parkinson, *Langmuir* **19**, 1274–1281 (2003).

[95] P. Kury, K. R. Roos, D. Thien, S. Möllenbeck, D. Wall, M. Horn-von Hoegen, and F.-J. Meyer zu Heringdorf, *Org. Electr.* **9**, 461–465 (2008).

[96] S. Müllegger, I. Salzmann, R. Resel, and A. Winkler, *Appl. Phys. Lett.* **83**, 4536–4538 (2003).

[97] L. Kilian, E. Umbach, and M. Sokolowski, *Surf. Sci.* **573**, 359–378 (2004).

[98] D. Walton, *J. Chem. Phys.* **37**, 2182–2188 (1962).

[99] G. Hlawacek, P. Puschnig, P. Frank, A. Winkler, C. Ambrosch-Draxl, and C. Teichert, *Science* **321**, 108–111 (2008).

[100] L. Tumbek, C. Gleichweit, K. Zojer, and A. Winkler, *Phys. Rev. B* **86**, 085402 (2012).

[101] T. A. Witten Jr and L. M. Sander, *Phys. Rev. Lett.* **47**, 1400 (1981).

[102] J. A. Venables and H. Brune, *Phys. Rev. B* **66**, 195404 (2002).

[103] D. Kandel and E. Kaxiras, *Phys. Rev. Lett.* **75**, 2742 (1995).

[104] L. Tumbek and A. Winkler, *Surf. Sci.* **606**, L55–L58 (2012).

[105] D. Kandel, *Phys. Rev. Lett.* **78**, 499 (1997).

[106] K. A. Fichthorn and R. A. Miron, *Phys. Rev. Lett.* **89**, 196103 (2002).

[107] K. K. Kolasinski and K. W. Kolasinski, *Surface Science: Foundations of Catalysis and Nanoscience* (Wiley, 2012).

[108] D. Menzel, „Desorption phenomena“, in *Interactions on metal surfaces* (Springer, 1975), pp. 101–142.

[109] V. P. Zhdanov, *Surf. Sci. Rep.* **12**, 185–242 (1991).

[110] A. Redondo, Y. Zeiri, J. J. Low, and W. A. Goddard III, *J. Chem. Phys.* **79**, 6410–6415 (1983).

[111] E. K. Grimmelmann, J. C. Tully, and E. Helfand, *J. Chem. Phys.* **74**, 5300–5310 (1981).

[112] P. A. Redhead, *Vacuum* **12**, 203–211 (1962).

[113] G. Ehrlich, *Adv. Catal.* **14**, 255–427 (1963).

[114] D. A. King, *Surf. Sci.* **47**, 384–402 (1975).

[115] E. Habenschaden and J. Küppers, *Surf. Sci.* **138**, L147–L150 (1984).

[116] D. Briggs and J. T. Grant, *Surface analysis by Auger and X-ray photoelectron spectroscopy* (IM Publications, 2003).

[117] V. K. Pecharsky and P. Y. Zavalij, *Fundamentals of Powder Diffraction and Structural Characterization of Materials*, Vol. 2 (Springer, 2009).

[118] P. P. Ewald, *Acta Crystall. A-Crys.* **25**, 103–108 (1969).

[119] M. Birkholz, *Thin Film Analysis by X-ray Scattering* (John Wiley & Sons, 2006).
[120] S. K. Chatterjee, *X-Ray Diffraction: Its Theory and Applications* (PHI Learning, 2010).
[121] I. Salzmann and R. Resel, *J. Appl. Crystallogr.* **37**, 1029–1033 (2004).
[122] P Müller-Buschbaum, *Anal. Bioanal. Chem.* **376**, 3–10 (2003).
[123] K. Mittal and K. Lee, *Polymer Surfaces and Interfaces: Characterization, Modification and Application* (Taylor & Francis, 1997).
[124] G. H. Vineyard, *Phys. Rev. B* **26**, 4146 (1982).
[125] Y. Yoneda, *Phys. Rev.* **131**, 2010 (1963).
[126] D. A. Long, *The Raman Effect: A Unified Treatment of the Theory of Raman Scattering by Molecules* (John Wiley and Sons Ltd, 2002).
[127] E. Smith and G. Dent, *Modern Raman Spectroscopy: A Practical Approach* (John Wiley & Sons, 2013).
[128] Nanosurf AG, *Nanosurf easyScan 2 AFM Operating Instructions* (2011).
[129] STAIB Instruments, *STAIB Cylindrical Mirror Analyzer Manual* (2012).
[130] P. Hofmann, *Surface Physics: An Introduction* (Philip Hofmann, 2013).
[131] M. Knudsen, *Ann. Phys.* **333**, 75–130 (1909).
[132] M. A. Herman and H. Sitter, *Molecular Beam Epitaxy: Fundamentals and Current Status*, Springer Series in Materials Science (Springer Berlin Heidelberg, 2012).
[133] G. Sauerbrey, *Physik* **155**, 206–222 (1959).
[134] Inficon, *Front Load Single and Dual Sensors Operating Manual* (2014).
[135] S. Hofmann and J. H. Thomas III, *J. Vac. Sci. Technol. B* **1**, 43–47 (1983).
[136] T. Hattori, Y. Hisajima, H. Saito, T. Suzuki, H. Daimon, Y. Murata, and M. Tsukada, *Appl. Phys. Lett.* **42**, 244–246 (1983).
[137] J. H. Thomas III and S. Hofmann, *J. Vac. Sci. Technol. A* **3**, 1921–1928 (1985).
[138] R. Sherman and W. Whitlock, *J. Vac. Sci. Technol. B* **8**, 563–567 (1990).
[139] M. Hollerer, „AFM Morphology Investigation of Pentacene OFETs at the Semiconductor-Metal Contact“, Master Thesis (Graz University of Technology, Graz, 2015).
[140] R. Lassnig, *Private Communication*.
[141] M. P. Seah and S. J. Spencer, *Surf. Interface Anal.* **33**, 640–652 (2002).
[142] M. P. Seah and S. J. Spencer, *J. Vac. Sci. Technol. A* **21**, 345–352 (2003).
[143] P. Swift, *Surf. Interface Anal.* **4**, 47–51 (1982).
[144] A. Erko, I. Packe, C. Hellwig, M. Fieber-Erdmann, O. Pawlizki, M. Veldkamp, and W. Gudat, in Synchrotron Radiation Instrumentation - Eleventh US National Conference, Vol. 521, 1 (AIP Publishing, 2000), pp. 415–418.

[145] D. Kriegner, E. Wintersberger, and J. Stangl, *J. Appl. Crystallogr.* **46**, 1162–1170 (2013).

[146] Japan AIST/NIMC Database, *Spectrum* **MS-NW-9353**.

[147] H. Lee, Y. Zhang, L. Zhang, T. Mirabito, E. K. Burnett, S. Trahan, A. R. Mohebbi, S. C. B. Mannsfeld, F. Wudl, and A. L. Briseno, *J. Mater. Chem. C* **2**, 3361–3366 (2014).

[148] A. Bondi, *J. Phys. Chem. A* **68**, 441–451 (1964).

[149] `http://www.chemspider.com/Chemical-Structure.60779.html` (visited on 09/05/2015).

[150] G. R. Desiraju and A. Gavezzotti, *Acta Cryst. B* **45**, 473–482 (1989).

[151] Cambridge Crystallographic Data Centre, 12 Union Road, Cambridge CB2 1EZ, U.K.; Supplementary publication no. CCDC 913540 (rubicene, 100 K) and CCDC 913541 (rubicene, 250 K).

[152] P. Frank, T. Djuric, M. Koini, I. Salzmann, R. Rieger, K. Müllen, R. Resel, N. Koch, and A. Winkler, *J. Phys. Chem. C* **114**, 6650–6657 (2010).

[153] S. Müllegger, O. Stranik, E. Zojer, and A. Winkler, *Appl. Surf. Sci.* **221**, 184–196 (2004).

[154] F. Balzer and H.-G. Rubahn, *Appl. Phys. Lett.* **79**, 3860–3862 (2001).

[155] A. Winkler, „Thermal Desorption of Organic Molecules“, in *Interface Controlled Organic Thin Films* (Springer, 2009), pp. 29–36.

[156] P. Frank, N. Koch, M. Koini, R. Rieger, K. Müllen, R. Resel, and A. Winkler, *Chem. Phys. Lett.* **473**, 321–325 (2009).

[157] A. J. Fleming, F. P. Netzer, and M. G. Ramsey, *J. Phys.: Condens. Matter* **21**, 445003 (2009).

[158] L. Ratke and P. W. Voorhees, *Growth and Coarsening: Ostwald Ripening in Material Processing* (Springer, 2002).

[159] F. Balzer, M. Schiek, I. Wallmann, A. Schäfer, A. Lützen, and H.-G. Rubahn, *Proc. SPIE, Nanophotonic Materials VIII* **8094**, 809409 (2011).

[160] B. Nickel, R. Barabash, R. Ruiz, N. Koch, A. Kahn, L. C. Feldman, R. F. Haglund, and G. Scoles, *Phys. Rev. B* **70**, 125401 (2004).

[161] A. P. Kaushik and P. Clancy, *Surf. Sci.* **605**, 1185–1196 (2011).

[162] K. D. Rendulic and A. Winkler, *Surf. Sci.* **299**, 261–276 (1994).

[163] T. Matsushima and K. Shobatake, *J. Molec. Catal. A: Chemical* **315**, 135–147 (2010).

[164] J. C. Tully, *Ann. Rev. Phys. Chem.* **51**, 153–178 (2000).

[165] S. Kneitz, J. Gemeinhardt, and H.-P. Steinrück, *Surf. Sci.* **440**, 307–320 (1999).

[166] E. R. Batista, P. Ayotte, A. Bilić, B. D. Kay, and H. Jónsson, *Phys. Rev. Lett.* **95**, 223201 (2005).

[167] D. O. N. Gardner, A. Al-Halabi, and G.-J. Kroes, *J. Phys. Chem. B* **108**, 3540–3547 (2004).

[168] M. C. McMaster, S. L. M. Schroeder, and R. J. Madix, *Surf. Sci.* **297**, 253–271 (1993).

[169] J. F. Weaver, A. F. Carlsson, and R. J. Madix, *Surf. Sci. Rep.* **50**, 107–199 (2003).

[170] K. R. Paserba and A. J. Gellman, *Phys. Rev. Lett.* **86**, 4338 (2001).

[171] M. Shahid, Shahid-ul-Islam, and F. Mohammad, *J. Clean. Prod.* **53**, 310–331 (2013).

[172] E. Steingruber, *Ullm. Enc. Ind. Chem.* **19**, 55 (2000).

[173] E. D. Glowacki, L. Leonat, G. Voss, M. Bodea, Z. Bozkurt, M. Irimia-Vladu, S. Bauer, and N. S. Sariciftci, *Proc. Spie* **8118**, 81180M (2011).

[174] M. Irimia-Vladu, P. A. Troshin, M. Reisinger, L. Shmygleva, Y. Kanbur, G. Schwabegger, M. Bodea, R. Schwödiauer, A. Mumyatov, J. W. Fergus, V. F. Razumov, H. Sitter, and N. S. Sariciftci, *Adv. Funct. Mater.* **20**, 4069–4076 (2010).

[175] M. J. Robb, S.-Y. Ku, F. G. Brunetti, and C. J. Hawker, *J. Polym. Sci. A1* **51**, 1263–1271 (2013).

[176] E. A. Gribova, G. S. Zhdanov, and G. A. Golder, *Crystallogr. Rep.* **1**, 53–60 (1956).

[177] M. Klessinger and W. Lüttke, *Tetrahedron* **19**, 315–335 (1963).

[178] P. Jakob and D. Menzel, *Surf. Sci.* **220**, 70–95 (1989).

[179] G. Koller, R. I. R. Blyth, S. A. Sardar, F. P. Netzer, and M. G. Ramsey, *Surf. Sci.* **536**, 155–165 (2003).

[180] T. Mitsui, M. K. Rose, E. Fomin, D. F. Ogletree, and M. Salmeron, *Science* **297**, 1850–1852 (2002).

[181] V. A. Ranea, A. Michaelides, R. Ramirez, P. L. de Andres, J. A. Vergés, and D. A. King, *Phys. Rev. Lett.* **92**, 136104 (2004).

[182] M. Roos, A. Breitruck, H. E. Hoster, and R. J. Behm, *Phys. Chem. Chem. Phys.* **12**, 818–822 (2010).

[183] S. L. Tait, Z. Dohnálek, C. T. Campbell, and B. D. Kay, *J. Chem. Phys.* **122**, 164708 (2005).

[184] F. Kettner, L. Hüter, J. Schäfer, K. Röder, U. Purgahn, and H. Krautscheid, *Acta Crystallogr., Sect. E: Struct. Rep. Online* **67**, 2867 (2011).

[185] D. Berg, C. Nielinger, W. Mader, and M. Sokolowski, *Synthetic Met.* **159**, 2599–2602 (2009).

[186] G. D. Potts, W. Jones, J. F. Bullock, S. J. Andrews, and S. J. Maginn, *J. Chem. Soc. Chem. Commun.* **22**, 2565–2566 (1994).

[187] S. S. Labana and L. L. Labana, *Chem. Rev.* **67**, 1–18 (1967).

[188] H. Liebermann, H. Kirchhoff, W. Gliksman, L. Loewy, A. Gruhn, T. Hammerich, N. Anitschkoff, and B. Schulze, *Liebigs Ann. Chem.* **518**, 245 (1935).

[189] P. Pollak, *Prog. Org. Coat.* **5**, 245–253 (1977).

[190] S. Müllegger and A. Winkler, *Surf. Sci.* **600**, 1290–1299 (2006).

[191] S. Müllegger, I. Salzmann, R. Resel, G. Hlawacek, C. Teichert, and A. Winkler, *J. Chem. Phys.* **121**, 2272–2277 (2004).

[192] NIST Mass Spectrometry Data Center, *Spectrum* **MS-341442**.

[193] NIST Mass Spectrometry Data Center, *Spectrum* **MS-113349**.

[194] C. Puglisi, L. Sturiale, and G. Montaudo, *Macromolecules* **32**, 2194–2203 (1999).

[195] F. O. Rice, *J. Am. Chem. Soc.* **53**, 1959–1972 (1931).

[196] F. H. Chung and R. W. Scott, *J. Appl. Cryst.* **4**, 506–511 (1971).

[197] G. Haucke and G. Graness, *Angew. Chem. Int. Ed. Engl.* **34**, 67–68 (1995).

[198] L. I. Maissel and R. Glang, *Handbook of Thin Film Technology* (McGraw-Hill Book Company, 1983).

[199] A. D. Reidinger and W. S. Struve, *Chem. Abstr.* **53**, 1777d (1959).

[200] W. S. Struve, *Chem. Abstr.* **53**, 1777f (1959).

[201] C. W. Manger and W. S. Struve, *Chem. Abstr.* **53**, 1777f (1959).

[202] E. E. Jaffe, *Eur. Pat.* **305328** (1989).

[203] E. E. Bäbler, F.Jaffe, *Eur. Pat.* **530143** (1993).

[204] R. S. Tyson and L. Schapiro, *Ger. Pat.* **2435219** (1975).

[205] W. Deuschel, H. W. Gundel, and E. Dauback, *Chem. Abstr.* **59**, 14143e (1963).

[206] H. R. Schweizer, *Chem. Abstr.* **70**, 30042 (1969).

[207] K. Hashizume, M. Miyatake, M. Shigemitsu, I. Kumano, H. Katsura, and M. Ohshima, *Br. Pat.* **1243652** (1968).

[208] A. P. Wagener, *Chem. Abstr.* **77**, 90071r (1972).

[209] G. Lincke and H.-U. Finzel, *Cryst. Res. Technol.* **31**, 441–452 (1996).

[210] H. Fukunaga, D. G. Fedorov, M. Chiba, K. Nii, and K. Kitaura, *J. Phys. Chem. A* **112**, 10887–10894 (2008).

[211] N. Panina, F. J. J. Leusen, F. F. B. J. Janssen, P. Verwer, H. Meekes, E. Vlieg, and G. Deroover, *J. Appl. Cryst.* **40**, 105–114 (2007).

[212] Cambridge Crystallographic Data Centre, 12 Union Road, 689 Cambridge CB2 1EZ, U.K.

[213] K. N. Baker, A. V. Fratini, T. Resch, H. C. Knachel, W. W. Adams, E. P. Socci, and B. L. Farmer, *Polymer* **34**, 1571–1587 (1993).

[214] M. Kurahashi, M. Fukuyo, A. Shimada, A. Furusaki, and I. Nitta, *Bull. Chem. Soc. Jpn.* **42**, 2174–2179 (1969).

[215] O. Dideberg, L. Dupont, and J. M. André, *Acta Crystallogr. B Struct. Crystallogr. Cryst. Chem.* **28**, 1002–1007 (1972).

[216] M. A. Rodriguez and S. D. Bunge, *Acta Crystallogr. E Struct. Rep.* **59**, o1123–o1125 (2003).

[217] H. R. Luss and D. L. Smith, *Acta Crystallogr. B Struct. Crystallogr. Cryst. Chem.* **28**, 884–889 (1972).

[218] C. Binant, B. Guineau, and A. Lautie, *Spectrochim. Acta* **45**, 1279–1287 (1989).

[219] H. Ohtsuka, Y. Furukawa, and M. Tasumi, *Spectrochim. Acta* **49**, 731–737 (1993).

[220] A. Bree and R. Zwarich, *J. Chem. Phys.* **49**, 3344–3355 (1968).

[221] H. Zollinger, *Colour Chemistry: Synthesis, Properties and Applications of Organic Dyes and Pigments* (John Wiley-VCH Publishers, 2002).

[222] E. D. Głowacki, G. Romanazzi, C. Yumusak, H. Coskun, U. Monkowius, G. Voss, M. Burian, R. T. Lechner, N. Demitri, G. J. Redhammer, N. Sünger, G. P. Suranna, and N. S. Sariciftci, *Adv. Funct. Mater.* **25**, 776–787 (2014).

[223] E. D. Glowacki, R. R. Tangorra, H. Coskun, D. Farka, A. Operamolla, Y. Kanbur, F. Milano, L. Giotta, G. Farinola, and N. S. Sariciftci, *J. Mater. Chem. C* **3**, 6554–6564 (2015).

[224] E. del Puerto, C. Domingo, J. V. Garcia Ramos, and S. Sanchez-Cortes, *Langmuir* **30**, 753–761 (2014).